Applied Research Laboratory

Technical Report

Process-Structure-Property Relationships of Micron Thick Gadolinium Oxide Films Deposited by Reactive Electron Beam-Physical Vapor Deposition (EB-PVD)

by

Daniel A. Grave and Dr. Douglas E. Wolfe

PENNSTATE

The Pennsylvania State University
The Applied Research Laboratory
P.O. Box 30
State College, PA 16804

Process-Structure-Property Relationships of Micron Thick Gadolinium Oxide Films Deposited by Reactive Electron Beam-Physical Vapor Deposition (EB-PVD)

By
Daniel A. Grave and Dr. Douglas E. Wolfe

Technical Report No. TR 14-010
December 2014

Supported By:

Penn State Applied Research Laboratory, Exploratory and Foundational Research Program

REPORT DOCUMENTATION PAGE

Form Approved
OMB No. 0704-0188

PLEASE DO NOT RETURN YOUR FORM TO THE ABOVE ORGANIZATION.

1. REPORT DATE *(DD-MM-YYYY)*	2. REPORT TYPE	3. DATES COVERED *(From - To)*
06-18-15	Technical Report	December 14-June 2015

4. TITLE AND SUBTITLE
Process-Structure-Property Relationships of Micron Thick Gadolinium Oxide Films Deposited by Reactive Electron Beam-Physical Vapor Deposition (EB-PVD)

5a. CONTRACT NUMBER

5b. GRANT NUMBER

5c. PROGRAM ELEMENT NUMBER

6. AUTHOR(S)
Daniel A. Grave
Douglas E. Wolfe

5d. PROJECT NUMBER

5e. TASK NUMBER

5f. WORK UNIT NUMBER

7. PERFORMING ORGANIZATION NAME(S) AND ADDRESS(ES)
Applied Research Laboratory
The Pennsylvania State University
PO Box 30
State College, PA 16804

8. PERFORMING ORGANIZATION REPORT NUMBER
TR 14-010

9. SPONSORING/MONITORING AGENCY NAME(S) AND ADDRESS(ES)
Defense Advance Research Projects Agency
Tactical Technology Office
675 N. Randolph Street
Arlington, VA 22203-2114
Attn: Kevin Massey

10. SPONSOR/MONITOR'S ACRONYM(S)
DARPA

11. SPONSOR/MONITOR'S REPORT NUMBER(S)

12. DISTRIBUTION/AVAILABILITY STATEMENT
Approved for Public Release: distribution unlimited

13. SUPPLEMENTARY NOTES

14. ABSTRACT
See attached

15. SUBJECT TERMS

16. SECURITY CLASSIFICATION OF:			17. LIMITATION OF ABSTRACT	18. NUMBER OF PAGES	19a. NAME OF RESPONSIBLE PERSON
a. REPORT	b. ABSTRACT	c. THIS PAGE			Douglas E. Wolfe
Unclassified	Unclassified	Unclassified	UU	281	19b. TELEPHONE NUMBER *(Include area code)* 814-865-0316

20151210104

The Pennsylvania State University

The Graduate School

College of Earth and Mineral Sciences

PROCESS-STRUCTURE-PROPERTY RELATIONSHIPS OF MICRON THICK GADOLINIUM OXIDE FILMS DEPOSITED BY REACTIVE ELECTRON BEAM-PHYSICAL VAPOR DEPOSITION (EB-PVD)

A Dissertation in

Materials Science & Engineering

by

Daniel A. Grave

Submitted in Partial Fulfillment
of the Requirements
for the Degree of

Doctor of Philosophy

December 2014

The dissertation of Daniel A. Grave was reviewed and approved* by the following:

Douglas E. Wolfe
Associate Professor of Materials Science & Engineering
Associate Professor of Engineering Science & Mechanics
Dissertation Co-Adviser
Chair of Committee

Joshua A. Robinson
Assistant Professor of Materials Science & Engineering
Dissertation Co-Adviser

James H. Adair
Professor of Materials Science & Engineering
Professor of Biomedical Engineering and Pharmacology

Michael A. Lanagan
Professor of Engineering Science & Mechanics

Suzanne Mohney
Professor of Materials Science & Engineering
Chair of the Intercollege Graduate Degree Program in Materials Science and Engineering

*Signatures are on file in the Graduate School.

Abstract

Gadolinium oxide (Gd_2O_3) is an attractive material for solid state neutron detection due to gadolinium's high thermal neutron capture cross section. Development of neutron detectors based on Gd_2O_3 requires sufficiently thick films to ensure neutron absorption. In this dissertation work, the process-structure-property relationships of micron thick Gd_2O_3 films deposited by reactive electron-beam physical vapor deposition (EB-PVD) were studied. Through a systematic design of experiments, fundamental studies were conducted to determine the effects of processing conditions such as deposition temperature, oxygen flow rate, deposition rate, and substrate material on Gd_2O_3 film crystallographic phase, texture, morphology, grain size, density, and surface roughness. Films deposited at high rates (> 5 Å / s) were examined via x-ray diffraction (XRD) and Raman spectroscopy. Quantitative phase volume calculations were performed via a Rietveld refinement technique. All films deposited at high rates were found to be fully monoclinic or mixed cubic / monoclinic phase. Generally, increased deposition temperature and increased oxygen flow resulted in increased cubic phase volume. As film thickness increased, monoclinic phase volume generally increased. Grazing incidence x-ray diffraction (GIXRD) depth profiling analysis showed that cubic phase was only present under large incidence angle (large penetration depth into the film) measurements, and that after a certain point, only monoclinic phase was grown. This was confirmed by transmission electron microscopy (TEM) analysis in conjunction with selected area diffraction (SAD).

Deposition of a pure cubic phase film was possible at high deposition rates for film thickness less than 50 nm under a deposition temperature of 250 °C and 200 sccm

O_2 flow. However, this film was shown to be under significant compressive stress of 1.7 GPa by XRD residual stress measurements. Thick (1 μm) pure cubic phase films were deposited by lowering the deposition rate to < 1 Å / s, and increasing the deposition temperature to 650 °C. This was attributed to both increased adatom mobility as well as reduction in compressive stress as measured by the wafer curvature technique. Based on this information, a large compressive stress was hypothesized to cause the formation of the monoclinic phase. Therefore, an experiment was designed to introduce compressive stress into the Gd_2O_3 films via ion beam assisted deposition (IBAD). This allowed for systematic increase in compressive stress while keeping a large adatom diffusion length on the film surface. It was shown that the films could be completely transformed from the cubic to monoclinic phase with applied compressive stress of -777 MPa for the deposition conditions considered, confirming the existence of a stress-induced phase transition.

Crystallographic texture evolution in the Gd_2O_3 films was investigated for different substrate types. At high rates, it was shown that films deposited on different substrates (quartz, silicon, sapphire, and GaN) all had similar θ-2θ diffraction patterns, suggesting that films grew similarly on different substrates due to the low adatom mobility. However, significant differences in texture were observed for films deposited at low rates (< 1 Å / s) and high temperature (650 °C) on different substrates. For evaluation of in-plane texture in the Gd_2O_3 films, pole figure analysis was performed. Mixed phase films deposited at high rates and low temperature showed weak out-of-plane texture and random in-plane texture. Mixed phase films deposited at high temperatures possessed a fiber texture (strong out-of-plane texture), but lacked the necessary adatom

mobility to develop in-plane texture. For single phase cubic films grown under low rates of deposition, out-of-plane texture was observed on quartz substrates. However, weak and strong in-plane textures were observed for sapphire and GaN substrates, respectively. The use of ion bombardment resulted in the formation of moderate biaxial texture for films grown on quartz. For films grown on sapphire, a very strong biaxial texture was achieved with ion bombardment which adds additional energy to the system.

The effects of processing on the structure, composition, and interfacial chemistry of the Gd_2O_3 films were investigated. The results showed that films primarily adhered to the Structure-Zone models with a few exceptions. The deviation from the Structure-Zone model was explained by the combined effects of columnar growth, shadowing, and adatom mobility. At low deposition temperatures, decreasing oxygen flow resulted in increased film density due to higher adatom mobility. Films deposited at this temperature were characterized by small (10 – 15 nm) nanocrystalline grains with some porous disordered regions. As the deposition temperature was raised to 650 °C, a dense nucleation region was observed and the films were highly crystalline with larger grain size. After the approximately 200 nm dense nucleation region, columnar growth was observed as the film grew thicker. Porosity formed between the growing columns due to shadowing effects. The effects of processing on the interfacial layer size of Gd_2O_3 films deposited on silicon were investigated. The size and structure of the interfacial layer was dependent upon the deposition conditions. Generally, higher oxygen flow and higher deposition temperature led to larger interfacial layer size and a more undulating interface. The interfacial reaction was determined to proceed as a result of intermixing of the SiO_x layer with the Gd_2O_3 layer to form the Gd-Si-O interface during deposition. Films

deposited on GaN possessed excellent interfacial characteristics with near heteroepitaxial growth and no apparent interfacial layer. Ion beam assisted deposition was shown to result in significant densification of the film structure and elimination of the columnar morphology. Lastly, the O : Gd ratio of the Gd_2O_3 films was investigated using EDS and XPS, and showed that the processing conditions had significant effects on the film composition. Increasing temperature was found to decrease the O : Gd ratio. Increasing oxygen flow was found to increase the O : Gd ratio for films deposited at low temperatures, but had little effect for films deposited at high temperature due to the fact that adatom mobility was significantly more affected by oxygen flow at lower temperatures.

The dielectric properties of Si(111) / Gd_2O_3 / Ti / Au MOS capacitors were investigated. Moisture absorption in Gd_2O_3 films was found to result in both increased dielectric loss (10x) and inflated dielectric constant values (~40 %). Heat treatment of the films at 100 °C resulted in outgassing of moisture, reduction in dielectric constant, and excellent frequency dispersion of the dielectric constant over a range of 10 kHz – 1 MHz. The effect of film processing on the dielectric constant was systematically investigated. Tuning of the dielectric constant from a value of 11 to a value of 24 was possible by manipulating the structure and crystallographic phase of the material via the processing conditions. Capacitance-voltage (C-V) and conductance-voltage (G-V) characteristics of GaN / AlGaN / Gd_2O_3 / Ti / Au MOS capacitors were investigated. The effects of processing on fixed oxide charge, trapped oxide charge, and density of interface states were evaluated. Single phase cubic films deposited at low rates with near heteroepitaxial growth were shown to have the lowest density of trapped charge.

Additionally, threshold instability in the C-V curve as well as a non-volatile charge trapping effect was observed. Conduction mechanisms in Gd_2O_3 films were studied through current-voltage-temperature (I-V-T) measurements. A number of mechanisms were found to govern conduction in Gd_2O_3 films across a wide measurement temperature and electric field range including ohmic conduction, Schottky Emission, Poole-Frenkel emission, and space charge limited conduction. For Poole-Frenkel emission, the trap heights of 1.03 eV and 1.25 eV were found for the cases of gate and substrate injection, respectively. Schottky barrier height at the Si (111) / Gd_2O_3 interface and Gd_2O_3 / Ti / Au interface was found to be 0.56 eV and 0.54 eV, significantly lower than the expected barrier height value. For GaN / AlGaN / Gd_2O_3 / Ti / Au capacitors, the Schottky barrier height at the GaN / AlGaN / Gd_2O_3 interface was found to be 0.79 eV and the Poole Frenkel trap height was 0.46 eV. The performance of GaN / AlGaN / Gd_2O_3 / Ti / Au high electron mobility transistors (MOS-HEMTs) was investigated with emphasis on necessary device performance for radiation detection. Gd_2O_3 films deposited at 650 °C led to devices with good switching characteristics including an on/off ratio of $\sim 10^9$ and subthreshold swing as low as 88 mV. However, significant hysteresis and threshold voltage instability was observed for the Gd_2O_3 MOS-HEMTs.

Finally, the response of GaN / AlGaN / Gd_2O_3 / MOS-HEMTs to gamma and neutron radiation was investigated. The devices showed sensitivity to both types of radiation. For devices with 1 μm thick Gd_2O_3 films, the neutron response was not improved over the control device. Devices with 10 μm thick films showed significantly increased neutron detection. However, the neutron response was larger than the expected theory, suggesting that added signal due to γ-radiation may have been collected.

List of Figures

Appendix Figures:

List of Tables

Tables in Appendix:

Acknowledgements

First and foremost, I would like to thank my advisor, Dr. Douglas Wolfe for his guidance during the span of my Ph.D work. His support and encouragement were instrumental for the achievement of the dissertation goals and for my growth as a professional researcher. I have learned many things under his mentorship and hope to have the honor of working with him in the future. Thank you.

I would like to thank my dissertation co-advisor and committee member Dr. Joshua Robinson for his substantial contributions and helpful scientific discussions. I would also like to thank my other committee members, Dr. Michael Lanagan and Dr. James Adair for their suggestions and guidance.

I would like to acknowledge the staff members in the ARL Advanced Coatings Department who have helped tremendously throughout the course of this work. I would like to extend a special thanks to Thomas Medill who initially trained me on the Denton EB-PVD system and provided countless hours of technical assistance as well as valuable insight into thin film processing and many other areas. I would like to thank Anna Stump for her extensive help with materials characterization. I would also like to express my gratitude to Scottie Showers for his help in the lab. I would like to thank the fellow graduate students (Michael Schmitt, Michael Reedy, Nan Butler, and Joyce Lin) and undergraduates in the Advanced Coatings laboratory that I have worked with over the years.

I would like to acknowledge the Electro-Optics Center (EOC) of Penn State. It was a pleasure working with Dr. David Snyder, Zachary Hughes, Kathleen Trumbull, Greg Pastir, and Dillon Nichols. Their work in electrical fabrication and characterization

was essential towards the dissertation work. I would also like to acknowledge the work done by the staff at the Penn State University Radiation Science and Engineering center, most notably by Brenden Heidrich. I would also like to acknowledge the modeling work performed by Dr. Igor Jovanovic and Ed Cazalas which provided useful insight into the radiation induced phenomena. I would like to acknowledge the technical staff at MRI and MCL, especially, Dr. Xiaojun Weng who was instrumental to the TEM work.

I am extremely thankful to my parents, Ilan and Yarona Grave, and my sister, Lidar. Without their continued support, I would not be where I am today and achieving these goals would not have been possible. Thank you. I would like to express a sincere thanks to my friends, you know who you are.

Lastly, I would like to thank the Defense Threat Reduction Agency (DTRA) which sponsored this research under contract number DTRA01-03-D-0010-0022 and the Eric Walker fellowship program of the Applied Research Laboratory at the Pennsylvania State University for allowing me this great opportunity.

Chapter 1

Introduction

Detection of special nuclear materials (SNM) has been of interest since the inception of nuclear technology. Special nuclear materials decay by spontaneous fission which results in neutron emission. As a result, efficient neutron detectors are needed to detect nuclear weapons technology and deter proliferation of illegal nuclear material. Significant research has advanced radiation technology through the introduction and optimization of ionization chambers, proportional counters, scintillation detectors, photomultiplier tubes, and semiconductor diode detectors.[1] However, no technology has emerged as a viable replacement to the costly state-of-the-art ^{3}He gas-filled proportional detector. Gadolinium-based materials are particularly attractive for solid state neutron detection due to gadolinium's high thermal neutron capture cross section.[1] Despite the attractiveness of Gd_2O_3 for solid state neutron detection, little work has been achieved on understanding of the relevant process-structure-property relationships of the material for use in radiation detection.

The basis for incorporation of Gd_2O_3 into a neutron detector relies on the Gd atom – neutron interaction. Absorption of a neutron by a Gd nucleus results in a number of interactions, one of which is the simultaneous emission of a conversion electron and a gamma ray.[2] Figure 1.1 shows the schematic drawings for two different types of detector test structures that both operate on the basis of this reaction. In Figure 1.1a, the Gd_2O_3 film is deposited on a silicon substrate and electrical contacts are made to the front and back. Due to Gd_2O_3's insulating nature, if enough conversion electrons-hole pairs are created and swept to the device terminals under an applied bias, it is possible to measure

an electrical current. This phenomenon is known as radiation induced conductivity (RIC) and has been observed experimentally in other oxide systems.[3] The low cost and ease of scalability of silicon electronics makes this detector very appealing if adequate neutron detection efficiencies can be met.

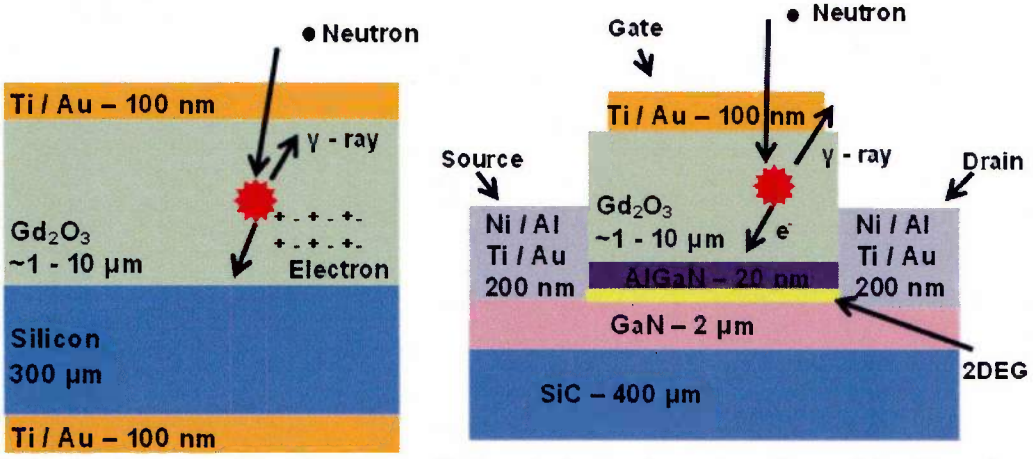

Figure 1.1. Schematic showing radiation test structures based on (a) silicon-based electronics and (b) AlGaN/GaN based electronics. Figures not drawn to scale.

Another promising class of materials for radiation detection is based on the group IIIa-nitride compound semiconductors: aluminum nitride (AlN), gallium nitride (GaN), and their alloy, AlGaN. Polarization of the GaN/AlGaN system induces a high density of electrons called the 2 dimensional electron gas (2DEG) at the interface between the two materials.[4] These electrons contain extremely high mobilities due to the absence of ionized impurity scattering and are very sensitive to external charge. Incorporation of GaN/AlGaN semiconductor quantum well (QW) structures with radiation sensitive materials such as Gd_2O_3 that generate charged particles in the presence of radiation could be ideal for enabling the future development of highly sensitive, miniature detector architectures. The test structure pictured in Figure 1.1b is a high electron mobility transistor (HEMT) based on the AlGaN / GaN system. Each test structure is composed of

source and drain materials (known as ohmic contacts), a gate metal (Ti/Au), and a gate dielectric (Gd_2O_3). The current in the 2DEG channel is modulated by applying a bias to the gate. Therefore, in addition to the current collection measured between drain and gate as a result of neutron interaction in the gate dielectric, charge injection into the highly sensitive 2DEG can result in a much higher collection efficiency by monitoring the drain-source current during irradiation.

Since neutron absorption is directly linked to film density and volume, thick films are needed to ensure proper capture of reaction products. Indeed, the mean free path of a neutron in Gd_2O_3 is approximately 7.7 μm.[5] However, since Gd_2O_3 has gained interest as a candidate for the replacement of SiO_2 in the metal oxide semiconductor field effect transistor (MOSFET), the deposition of Gd_2O_3 films reported in the literature have been for either epitaxial or polycrystalline films with thicknesses below 100 nm.[6–8] Therefore, many of the difficulties and issues associated with the deposition of thick films have not yet been addressed.

As film thickness increases, film structural stability becomes a much larger issue due to increased intrinsic growth stresses.[9] The effects of grain growth, film porosity, crystallographic texture, phase, and surface roughness on film properties must be considered. Stability at the interface between the film and the substrate becomes critical with increasing film thickness as to avoid cracking or film delamination. Increased probability of incorporated microscopic defects into the film may add difficulty in maintaining stoichiometry and can significantly alter film electrical, optical, and structural properties. Understanding the cause and role of these defects will allow for improved film quality and device performance. In addition to neutron detection, thick

Gd_2O_3 films have potential for use in other technological fields. For instance, Gd_2O_3 is a promising candidate for use in optical coating systems due to its large experimentally measured band gap and transparency in the ultraviolet spectrum.[10–12] Possible applications include UV anti-reflective coatings[13] and photoluminescent phosphors.[14]

Prior to the development of a neutron radiation detector, the properties of thick Gd_2O_3 films must be well understood and device performance characterized and optimized for radiation detection. Therefore, the goals for this work are three-fold:

1) Develop process-structure-property relations of micron thick Gd_2O_3 films deposited by reactive electron beam-physical vapor deposition (EB-PVD).
    a. Create a process window for deposition of Gd_2O_3 films by investigating deposition parameters such as substrate type, substrate temperature, oxygen flow, deposition rate, and ion beam power.
    b. Determine the effects of processing on the crystallographic phase, texture, crystallite size, surface roughness, density, composition, and interfacial structure of the Gd_2O_3 films.
    c. Determine the effects of processing and structure on the film electrical and optical properties.
2) Investigate the electrical properties and performance of thick Gd_2O_3 film incorporation into silicon-based MOS capacitors and GaN / AlGaN high electron mobility transistors (HEMTs).
3) Assess the fundamental interaction of neutron and gamma radiation with Gd_2O_3 microelectronic devices.

To address these goals, the outline for the thesis will be as follows:

Chapter 2 will provide background material for the basis of the work. It will begin with an overview of current state of the art radiation detectors and the advantages and disadvantages of the proposed gadolinium oxide detector. This will be followed by background material on the structure, properties, and phase stability of gadolinium oxide. After this, a description of film deposition processes, with particular emphasis on the growth of films by electron beam physical vapor deposition will be covered. This will lead into an overview on previous deposition of Gd_2O_3 thin films in the literature. The last section will cover electrical properties of oxide films and associated microelectronic device performance.

Chapter 3 will discuss the experimental methods used to perform this work. The first section will describe the electron beam physical vapor deposition system used in this work and outline the deposition process. An overview of the materials characterization techniques used in this work will then be given. Next, the techniques used to fabricate the microelectronic Gd_2O_3 devices and the electrical characterization methods will be discussed. Finally, an overview of the radiation testing set up and procedure will be reviewed. The chapter will end with a description of the design of experiments used in the dissertation work.

Chapter 4 is a discussion of the process phase relationships observed in the Gd_2O_3 films deposited under a range of deposition conditions. θ-2θ X-ray diffraction (XRD) analysis was used to investigate the effect of deposition temperature, oxygen flow rate, film thickness, and substrate on the crystallographic phase, orientation, and crystallite size of Gd_2O_3 films. Quantitative Rietveld analysis was employed in order to determine

phase volume. Grazing incidence x-ray diffraction (GIXRD) was used to identify a thickness dependent crystallography in the Gd_2O_3 films through depth profiling.

Chapter 5 will provide evidence for the deposition of micron thick single phase cubic Gd_2O_3 films. This was linked to the effects of adatom mobility and residual stress on the Gd_2O_3 film phase stability. Demonstration of a stress induced phase change using ion beam assisted deposition will be presented. Finally, pole figure analysis was employed to determine the in and out-of-plane orientation of the Gd_2O_3 films.

In chapter 6, the effects of film processing on Gd_2O_3 film morphology, composition, and interfacial chemistry will be presented and related to the crystallographic phase and texture results from chapters 4 and 5. Scanning electron microscopy (SEM) was used to examine the morphology, grain size, and thickness of the films and related to the Structure-Zone model.[15] Atomic force microscopy (AFM) was used to characterize the surface roughness. Transmission electron microscopy (TEM) was used for film structure determination, phase identification, interfacial structure, and composition. Energy dispersive spectroscopy (EDS) and X-ray photoelectron spectroscopy (XPS) were used to investigate the Gd / O ratio of the films. The results from the materials characterization techniques were correlated with film processing.

In chapter 7, the effects of film processing and structure on the electrical properties of the Si(111) / Gd_2O_3 / Ti / Au and GaN / AlGaN / Gd_2O_3 / Ti / Au MOS capacitors were examined. Current-voltage-temperature (I-V-T) measurements were performed to investigate the leakage current and conduction mechanisms present within the devices. Capacitance-Voltage (C-V) techniques were used to examine frequency dependent dielectric properties such as dielectric constant and dielectric loss. The device

performance of GaN / AlGaN / Gd_2O_3 / Ti / Au HEMTs with respect to the requirements for neutron detection was examined. Finally, the response of the HEMT devices to gamma and neutron radiation was studied.

Chapter 8 will provide a bulleted summary of the important conclusions that resulted from this work and will then conclude with directions for future work. This will include discussion of fundamental research pertaining to optimizing the structure and properties of the Gd_2O_3 films through processing. Suggestions will be given to improve the performance of the Gd_2O_3 electronic devices. Furthermore, interesting new pathways for scientific exploration that originated from the dissertation work will be explored.

Chapter 2

Background

The literature review in this chapter will begin with a discussion on the current state-of-the-art in neutron detection and comparisons will be made to the gadolinium oxide (Gd_2O_3) based device discussed in this work. Next, the phase stability of bulk Gd_2O_3 will be reviewed. Specific detail will be given to phase transitions observed in rare earth oxides due to temperature, pressure, and ion irradiation. This will be followed by a general overview of oxide thin film deposition coupled with a literature review on the deposition of Gd_2O_3 thin films and their properties. Lastly, dielectric properties and charge transport in Gd_2O_3 microelectronic devices will be discussed and related to neutron detection.

2.1. Radiation detection

Detection of gamma and neutron radiation has been of interest since the inception of nuclear technology. As a result, significant research has advanced radiation technology through the introduction and optimization of ionization chambers, proportional counters, scintillation detectors, photomultiplier tubes, and semiconductor diode detectors.[1] Helium-3 (^3He) has been the benchmark for new neutron radiation sensitive materials since its first use in detectors in 1955, and has been widely available commercially for nearly 40 years.[1] Although ^3He detectors can reach efficiencies of 80% using high pressure and expensive high purity ^3He gas, long term stability issues resulting from gas leakage and electronegative poisoning can reduce ^3He detectors efficiencies to 10-15%.[16] In addition, the high voltages required for operation, large detector footprint,

high pressures, and sensitivity to micro-phonics make the detector undesirable for air transport and field deployment. Silicon-based solid-state detectors have also been developed which improve upon the robustness, power consumption, and energy resolution compared to their scintillator and ionization chamber counterparts.[1] Recently, boron-10 (^{10}B) doped solid state materials have also shown promise for neutron detection, and have demonstrated higher detection efficiencies than their He^3 counterpart under the same conditions.[17]

As shown in Figure 2.1, semiconductor-based solid state detection has superior energy resolution as compared to gas proportional detectors and scintillators. This higher energy resolution allows for distinguishing between various radiological threats too difficult to resolve using other techniques – especially when the signatures are of low intensity.

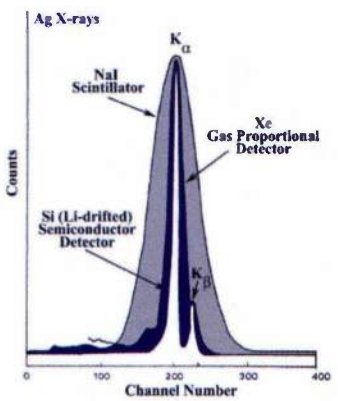

Figure 2.1. Energy spectrum of detectors illustrating superior energy resolution of the semiconductor-based detection method.[1]

A figure of merit for neutron sensitive materials is the capture cross section (measured in *barns* ($10^{-28}m^2$)) and is a direct indicator of the probability of interaction between a neutron and isotope of choice; thus, as the cross section increases so does the

probability of interaction. Materials for radiation detection are chosen based on this intrinsic property, of which ^{3}He, ^{10}B, ^{6}Li, and ^{157}Gd exhibit some of the largest cross sections for thermal neutrons.[1]

Figure 2.2a demonstrates the cross section of these elements as a function of neutron kinetic energy.[18,19] Helium-3, boron-10, and lithium-6 exhibit large thermal neutron cross sections (5333b, 3840b, 940b, respectively), but it is gadolinium that exhibits the largest thermal neutron capture cross section - elemental Gd ~ 49700b and ^{157}Gd ~ 259000b. The interaction of a neutron with any of the aforementioned elements results in the ejection of one or more charged particles and gamma radiation (Figure 2.2b). Because of its large capture cross section, gadolinium based materials represent an attractive choice for the active material in a neutron detector.

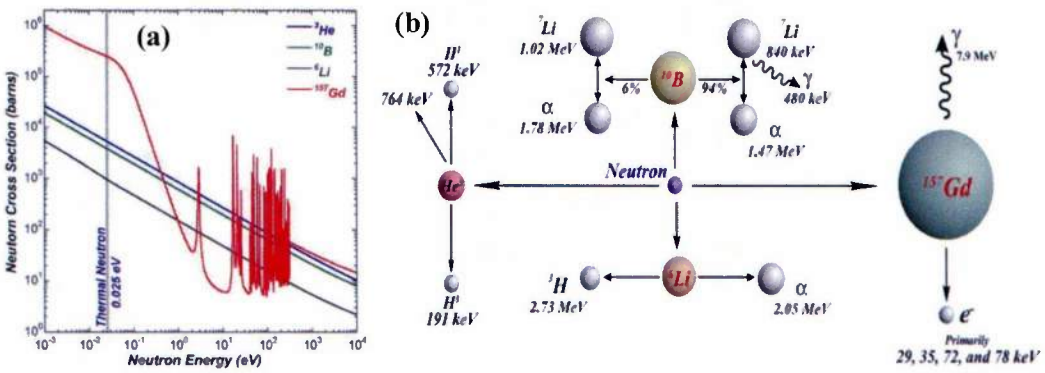

Figure 2.2. (a) Neutron capture cross section of gadolinium-157, boron-10, lithium-6, and helium-3 as a function of neutron energy, and (b) products associated with the neutron/element reaction (right). Note the large neutron cross section range as a function of neutron energy for ^{157}Gd.[20]

Figure 2.3 directly compares current scintillator and silicon-based solid state detectors with the Gd_2O_3-based test structure fabricated in this study. For typical

scintillators, as shown in Figure 2.3a, a gamma ray is absorbed by the scintillator material, which re-emits the absorbed energy in the form of a visible light photon (i.e., gamma ray is converted into detectable light). The light photon is subsequently converted to an electron (photoelectric effect), which undergoes multiplication (photo-electrons) to generate a measurable electrical pulse.

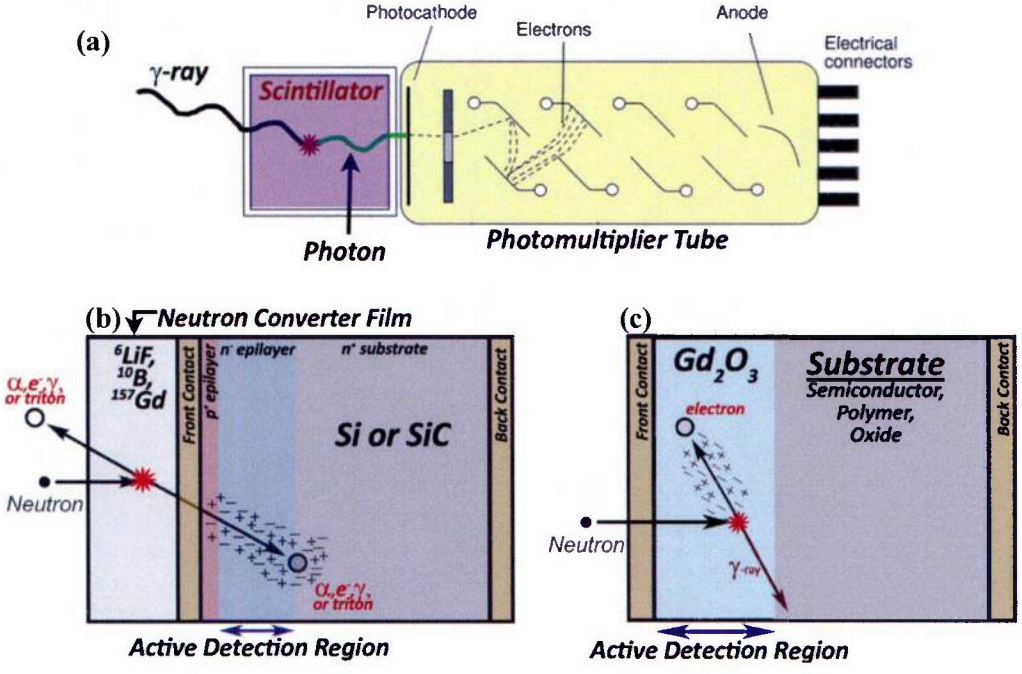

Figure 2.3. Schematic representations of (a) scintillator solid state detector, (b) silicon-based state-of-the-art solid state detector, and (c) Gd_2O_3 solid state device.

The ideal scintillator material has linear conversion (light yield proportional to energy over a wide range), is transparent to its own emission wavelength for increased light collection, has induced luminescence with short decay times for fast signal responses, and can be made large enough to facilitate component fabrication. Unfortunately, no single material meets all these requirements. Generally, a scintillator material (such as NaI, or

oxide-based single crystal) having good linearity and high light output, will have a slow response time. A more detailed description on scintillators is provided by Birks.[21] Charged particle interactions within a scintillator will also create light photons. By adding a neutron converter such as those shown in Figure 2.3b, scintillators can be used as neutron detectors. The primary disadvantage of this type of neutron detector is the poor energy resolution, efficiency degradation due to electron backscattering and color center formation, long decay times, and slow response. Thermal neutron detection efficiency of most scintillators is good. However, temperature sensitivities, the required photomultiplier tube and required high operating voltages, result in poor robustness, which significantly limits fieldability for many applications.

Current state-of-the-art semiconductor detectors require converter films on top of a semiconductor PiN or Schottky diode as illustrated in Figure 2.3b.[22,23] The probability of signal generation in the material resulting from incident neutron interaction is directly proportional to the density of the material, neutron flux, absorption cross section, and surface area of the detector. Consequently, for a given material quality, sensitivity is dictated by the size (area and volume) of the detector. While silicon and germanium detectors have shown good energy resolution, they require significant cooling to reduce electronic noise in the detector. Silicon carbide and diamond-based detectors have shown great promise for radiation hard, room temperature solid state detectors; however, to date, no detector larger than 5 mm^2 has been reported.[24,25] Detector size has been limited by material quality and defects. The required thickness of the semiconductor drift (collection) region can be prohibitively large. Detection of neutrons (and charged particles) is heavily dependent on the ability to collect as much signal as possible before

the neutron exits the back side of the detector. Impurities, crystalline structure, and defects in a material can detrimentally affect the ability to achieve collection widths required for high energy particle detection. Additionally, commercial SiC devices require bias voltages on the order of 1000 V to achieve collection widths of μm. They also undergo extensive detector fabrication processes and are extremely expensive (~ $10,000 for a one 2-inch wafer).[26]

A major influence on sensitivity comes from the properties of the converter film, and current state-of-the-art solid state detectors require that the chemical, structural, and thickness characteristics of the converter material be optimized for neutron detection. Highly reactive materials that generate charged particles (α, ^{3}H, or protons) are required for efficient detection of neutrons. The coating performance is a strong function of film microstructure, and thus processing parameters. Impurities in boron-based converter films have been reported to significantly reduce converter film sensitivity, and it can be expected that this effect will be similar in other films of interest.[27,28,29] To date, research has focused on the optimization of converter film thickness; however, little has been accomplished on structural and impurity optimization of the films.

The Gd_2O_3 based solid state system developed in this dissertation and shown in Figure 2.3c requires no converter film because the active, Gd_2O_3 film converts neutron radiation and detects the interaction simultaneously. Due to Gd_2O_3's insulating nature, as electron-hole pairs are created in the film and swept to the device terminals under an applied bias, it is possible to measure an electrical current. This phenomenon is known as radiation induced conductivity (RIC).[30] 100% of the charge associated with a neutron-gadolinium (n/Gd) interaction (i.e. conversion efficiency) should be measured in this

active layer solid state detector, which results in increased detection efficiency, as opposed to 50% in the solid state detectors which employ a Gd conversion layer. This is due to the emission of the reaction products, gamma ray and conversion electron, at 180° away from each other. Furthermore, gadolinium oxide (Gd_2O_3) is stable at high temperatures under oxidizing environments, and thus an attractive alternative to the environmentally unstable, pure Gd metal. Gd_2O_3 has also been applied to polymer-based substrate materials at room temperature, can be doped with other rare earth oxide materials allowing for tailorability. Also, it can be used for applications where visible transparency is important (i.e., protective eyewear, windshields, building windows and architecture, road signs, etc).[22] However, for development of a Gd_2O_3 based thick film neutron detector, an understanding of the process-structure-property relationships of Gd_2O_3 is necessary to synthesize high quality films.

2.2. The crystal structure of gadolinium oxide (Gd_2O_3)

The rare earth metals include the lanthanide elements (atomic number Z=57-71), scandium (atomic number Z=21) and yittrium (atomic number Z=39).[31] The metals received their name because most of them were originally isolated from rare minerals in the 18th and 19th centuries although many of the elements are not particularly rare in the present day. The lanthanides have typically been segregated into two groups, the light rare earth elements (Z=57-63) and the heavy rare earth elements (Z=64-71). Most of the rare earths have electronic configuration $[Xe]6s^24f^*$ with the 5d orbital remaining vacant and the electrons filling into the 4f orbital.[32] Gadolinium is an exception with electronic configuration $[Xe]6s^24f^75d^1$ to retain a half-filled f-orbital. Gadolinium is a malleable

and ductile silvery-white metal. The crystal structure of gadolinium under ambient conditions is hexagonal close packed (HCP) until 1262 °C, where it transforms to a body centered cubic (BCC) structure. The density of Gd is approximately 7.89 gm / cm^3 and the melting point is 1312 °C.[33]

Rare earth metals are typically extremely reactive with oxygen.[34] Therefore, the rare earth oxides have extremely high stability in oxidizing environments and under high temperatures. Most binary rare earth oxides employ an ion with a trivalent state with formula R_2O_3 where R is a rare earth metal, though divalent and tetravalent states are possible. The trivalency of the cations and similarity in ionic radii allow for significant solid substitution of rare earth elements for each other into various lattices, and is the reason why multiple rare earth elements are often found in the same minerals.

The phase stability of the rare earth binary oxides at ambient temperature and pressure depends on the cation and anion radius ratios.[35] Figure 2.4 displays the phase diagram of the binary rare earth oxides under standard pressure.[36] The following phases are typically found for rare earth oxides at temperatures below 2300 °K: the hexagonal (A) phase (space group P32/m), the monoclinic (B) phase (space group C2/m), and the cubic bixbyite (C) phase (space group Ia3). The small rare earth cations typically favor the C or B phase at ambient conditions while the larger cations favor the A phase. As shown in Figure 2.2, for bulk Gd_2O_3 under standard pressure, the low temperature thermodynamically stable phase is the cubic (C) structure. Between 1472 and 2373 °K, Gd_2O_3 exists in the monoclinic (B) phase. Above 2373 °K, Gd_2O_3 is reported to be of the hexagonal (H) phase (space group P63/mmc). Another phase transition to the cubic (X) phase (Im3m) has been observed at slightly higher temperatures before the melting

temperature. For the remainder of this dissertation, reference to the cubic phase will be exclusively towards the bixbyite (C) (space group Ia3) phase as it is the only cubic phase observed in this work.

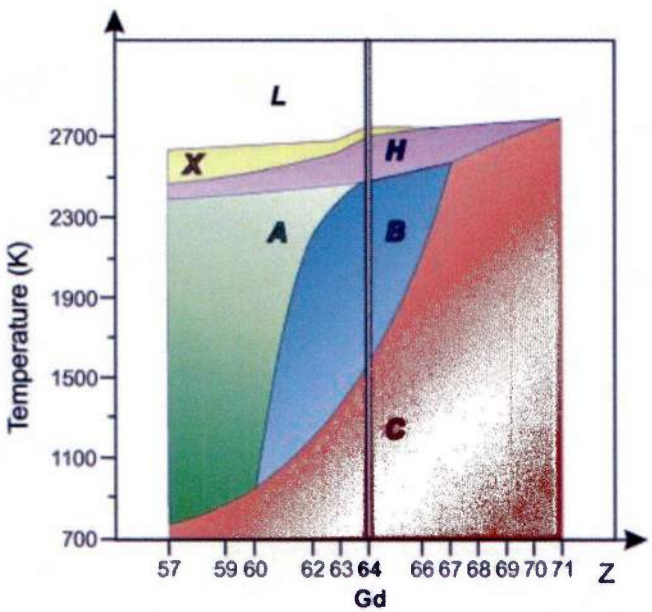

Figure 2.4. Phase diagram for rare earth binary oxides as a function of cation atomic number under standard pressure.[36]

It is important to note the difference in the crystal structures of the Gd_2O_3 phases since they are vastly different from one another and may possess significant differences in their properties. The cubic bixbyite (C) Gd_2O_3 structure shown in Figure 2.5a, space group Ia3, is identical to the fluorite lattice structure, except with one fourth of the anion sites vacant. It contains 32 metal atoms and 48 oxygen atoms per unit cell. The resulting coordination is six for gadolinium and four for oxygen. The monoclinic Gd_2O_3 structure shown in Figure 2.3b, space group C2/m, has sevenfold coordination of the cation, with three unique Gd sites. The oxygen site is four, five, or six coordinated.

(a) Cubic (C) Phase (Ia3)

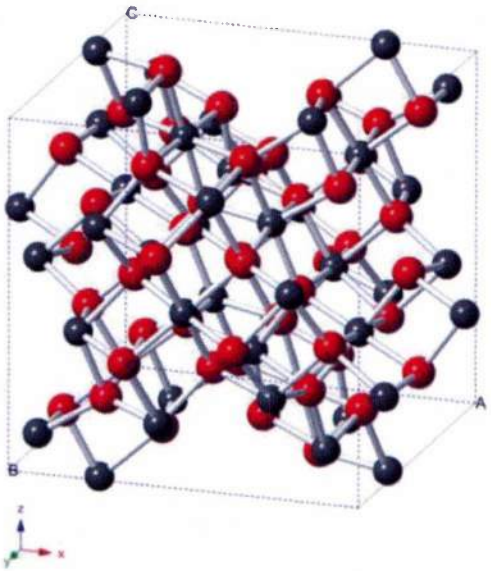

Oxygen Coordination (4)

Gadolinium Coordination (6)

(b) Monoclinic (B) Phase (c2/m)

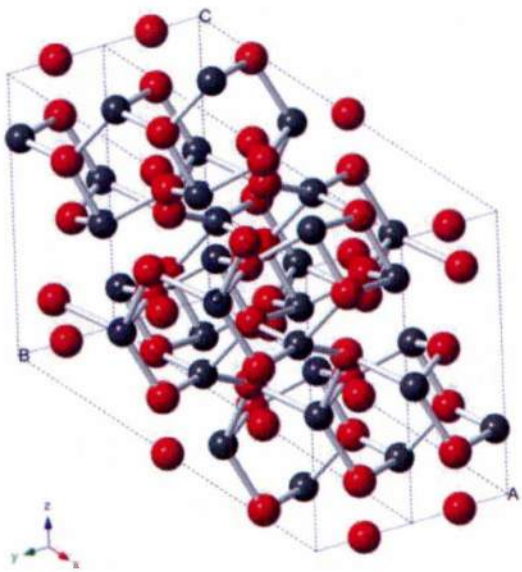

Oxygen Coordination (4, 5, 6)

Gadolinium Coordination (7)

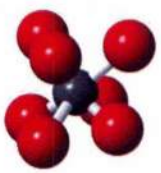

Figure 2.5. Crystal structures of Gd_2O_3 in (a) cubic C phase (space group Ia3) and (b) monoclinic B phase (space group C2/m). The oxygen and gadolinium coordination for each phase is shown next to the unit cells. Red corresponds to oxygen atoms and gray corresponds to gadolinium atoms.

The cubic to monoclinic phase transition is reconstructive with bond breaking, accompanied by a change in the Gd coordination from six to seven as well as a decrease in the molar volume by approximately 8%. The hexagonal (A) phase, space group P32/m, has Gd in seven coordination while the oxygen is four and five coordinated. The change in molar volume between the A and B phase is relatively small, approximately 2%. Unsurprisingly, the C→B transformation has been reported to be irreversible while the B→A transformation is reversible.[37] As a result, while Gd_2O_3 can exist at room temperature in either the monoclinic or the cubic phase, the hexagonal phase cannot be quenched in at room temperature. Table 2.1 provides select properties of cubic and monoclinic Gd_2O_3. One possible advantage that the monoclinic phase has over the cubic phase for neutron detection is its greater density. An increased number of gadolinium atoms in the same volume provide an increased probability of neutron absorption which could increase detector efficiency. However, the poor symmetry of the monoclinic phase may result in worse packing density and potentially undesirable electrical properties in thin film form.

Table 2.1. Properties of Gd_2O_3 bulk ceramic at standard pressure

	Cubic (C)	**Monoclinic (B)**
Space group	Ia3	C2/m
Temperature (°C)	<1250	>1250
Density (g / cm^3)	7.62	8.35
Unit Cell Volume (10^6 pm^3)	1264.27	432.43
Lattice parameter (Å)	a = 10.81	a = 14.06, b = 3.57, c = 8.76

2.3. Phase transitions in bulk Gd_2O_3

Since the structure of the Gd_2O_3 phases are quite different from one another and may possess different properties, it is important to understand what dictates the phase

stability of the material. In addition to temperature, phase transitions in Gd_2O_3 have also been induced due to shock[38], pressure[37,39], and ion irradiation.[36] For instance, the dependency of Gd_2O_3 phase on pressure was studied via a diamond anvil experiment.[39] Gd_2O_3 powder was placed inside a diamond anvil cell and hydrostatic pressure was applied. An irreversible phase transition from the cubic (C) phase to the hexagonal (A) phase was observed between 7 and 15 GPa. After release of the pressure, a spontaneous transformation occurred to the B phase as shown by the diffraction patterns in Figure 2.6. The authors correlated this pressure induced phase transition to the relative lattice energies of the three phases.

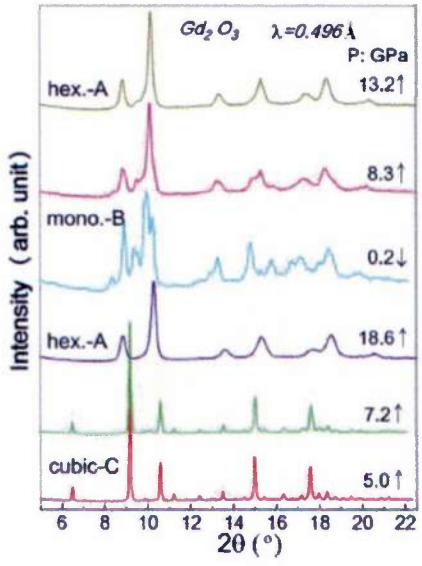

Figure 2.6. Diffraction pattern showing phase change from C phase to A phase with increasing pressure and formation of B phase upon pressure release.[37]

Phase transformations in Gd_2O_3 have also been observed by ion irradiation. Very recently, the C→B transformation was induced in Gd_2O_3 via means of swift heavy ion irradiation (2.25 GeV Au ions).[36] The exact nature of the phase transition was not

identified but the authors attributed it to a possible combination of thermal effects, defects, strain, and changes in oxygen content. The polymorphic nature of Gd_2O_3 has important implications for thin film growth of the material. Since thin film growth is a non-equilibrium process, metastable phase formation can occur. Manipulation of film phase stability through processing can be employed to tune the resulting film structure, properties, and performance.

2.4. Thin film growth

As discussed in section 2.1, development of the solid state detector requires growth of Gd_2O_3 films with sufficient thickness to capture a large portion of incident neutrons. The mean free path of neutrons in Gd_2O_3 is approximately 7.7 μm.[5] Therefore, relatively thick films (> 1 μm) are needed to ensure proper neutron absorption. Electron beam-physical vapor deposition (EB-PVD) provides efficient means of depositing high quality films with fast growth rates (up to 100 nm / min). Furthermore, EB-PVD is a versatile technique that can produce high quality films.

2.4.1. Electron beam-physical vapor deposition (EB-PVD)

The electron beam-physical vapor deposition (EB-PVD) process is illustrated in Figure 2.7. The source material is placed within a water cooled crucible within the deposition chamber. The chamber is then evacuated and an electron beam is formed as a result of thermionic emission from a tungsten filament. The electron beam is directed at the source material causing evaporation. Increasing the current through the tungsten filament results in an increase in the number of electrons impinging upon the source

material; this in turns increases the rate of evaporation. The electron beam gun is electromagnetically deflected according to the Lorentz force towards the evaporant material, in which enough kinetic energy is imparted by the beam of electrons into the material to cause evaporation. Due to the change in localized pressure, the atoms then rise and deposit on the substrate. The process is performed under sufficient vacuum (typically greater than 10^{-3} Torr) to ensure large mean free path of the evaporated species. EB-PVD of gadolinium oxide can either be performed via a direct method where the Gd_2O_3 material is evaporated directly onto the substrate from the oxide source or through a reactive method where the gadolinium metal is evaporated and reacted with background oxygen gas to form an oxide film on the substrate surface.

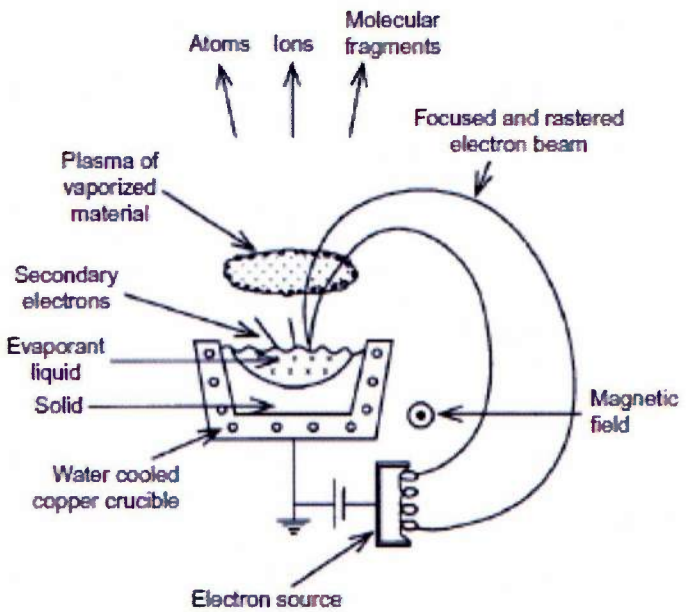

Figure 2.7. Schematic of electron beam-physical vapor deposition process.[40]

2.4.2. Atomistic description of thin film growth

Thin film processing determines the manner in which the evaporated atoms condense on the substrate and form the resulting film structure. Therefore, development of process-structure-property relationships for thin films must begin with an understanding of how the processing parameters affect growth at an atomistic level. Film growth by EB-PVD can be described in the following steps:

1) The evaporated species absorb on the film surface
2) The adsorbed species diffuse along the film surface until they are incorporated in the film
3) A reaction occurs between the adsorbed species forming chemical bonds (chemisorption)
4) Nucleation and Growth
5) Film develops morphology and structure
6) Diffusion within bulk film or interfacial reaction with the substrate

Adjusting the processing parameters can impact each of the above steps. Beginning with step 1, the evaporated atoms can either adsorb on the film or substrate surface or they can be re-evaporated (Figure 2.8). The atoms that initially adsorb are weakly bonded to the substrate or film (physisorption). At this point, these atoms can desorb, diffuse across the surface, or condense as part of the growing film. The desorption rate is a function of the bonding energy between the film and substrate, surface temperature, and arrival rate of the incoming atoms. Atoms that do not desorb and are mobile on the film surface are called adatoms and are responsible for the film growth.

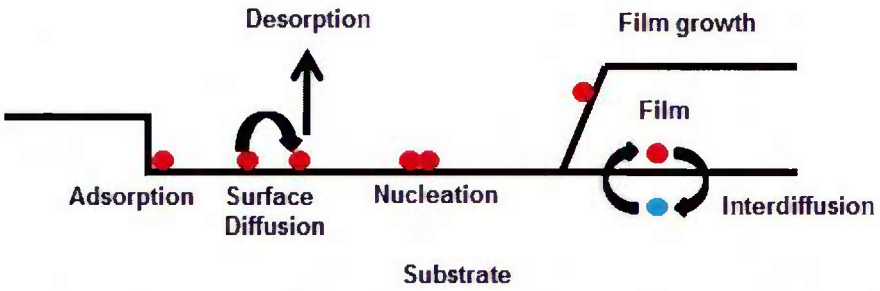

Figure 2.8. Schematic showing the stages of film growth.[41]

Each adatom sits within an energy well on the surface of the substrate or film. This well is separated by an energy barrier from adjacent energy wells by some barrier. The atoms oscillate within the wells due to thermal oscillation. If an atom acquires enough energy to overcome the barrier, it may hop to an adjacent site resulting in surface diffusion (step 2). The surface mobility and diffusion length of the adatoms are determined by a number of factors. For instance, as the substrate temperature increases, the surface mobility increases due to an increased hopping rate. However, too high of a substrate temperature can result in increased desorption which has the ability to limit surface mobility as well. If the evaporant flux to the film surface is high or a background gas is present, the adatoms may collide with another atom, which reduces the surface mobility and diffusion length. Therefore, a lower evaporation rate and lower gas flow is favorable for higher surface mobility.

The adatoms condense on the surface by losing energy through the formation of chemical bonds, also known as chemisorption (step 3). This can occur through bonding to the substrate, bonding to the film, collision with other adatoms, or bonding at preferential nucleation sites (defects, steps, grain boundaries, etc.). Addition of atoms to the growing surface creates additional surface energy. Therefore, nuclei of a critical size

must be formed in order to stabilize the film. The nucleation rate is controlled by the processing parameters. Increased deposition temperature results in an increased critical nuclei size and a lower nucleation rate. Higher deposition rates result in a decreased critical nuclei size which leads to an increase in nucleation rate.

The initial stages of film nucleation and growth are dominated by minimization of surface energy, or more specifically; the surface energy of the substrate free surface (γ_s), the surface energy of the film free surface (γ_f), and the surface energy of the substrate/film (γ_i) interface. Three different types of growth modes exist depending on the magnitudes of these surface energies. If $\gamma_s > \gamma_{f+} \gamma_{i,}$ then the film will wet the surface to lower the surface energy and the film will grow layer by layer (Frank van der Merwe growth). If $\gamma_s < \gamma_{f+} \gamma_{i,}$ then the atoms will be more strongly bound to each other, and form three dimensional islands (Volmer-Weber growth). Lastly, when γ_s is approximately equal to $\gamma_{f+} \gamma_{i,}$ the films will undergo mixed growth, where they initially grow layer by layer, and then form islands after a few monolayers are deposited (Stranski-Karstanov growth). At this point, it is more appropriate to move towards a macroscopic description of thin film growth to explain the formation of film structure and morphology (step 5).

2.4.3. Macroscopic description of thin film growth and Structure-Zone model

While evaporated thin films are initially accurately described by the growth modes described in section 2.4.2, once films reach a certain thickness, they may be described by the Structure-Zone model. The Structure-Zone model was first introduced by Movchan and Demchisin[42] and subsequently modified by Thornton[43] and Messier.[15]

The Structure-Zone model given by Thornton as a function of pressure and substrate temperature is shown in Figure 2.9. It is important to note that the Structure-Zone model is only applicable to polycrystalline and amorphous films as there are no zones in epitaxial thin films.

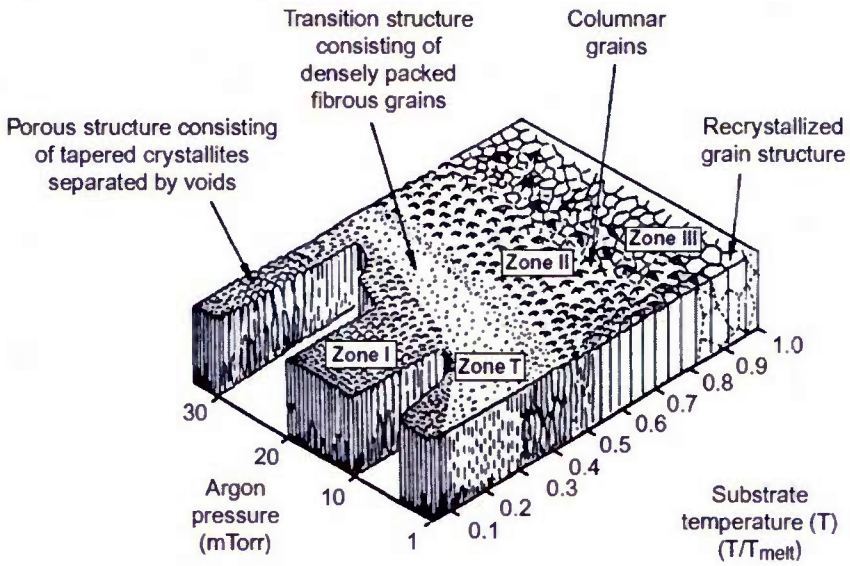

Figure 2.9. Structure-Zone model for vapor deposited coatings.[44]

Zone 1, where the deposition temperature, T, is < 0.2 of the melting temperature, T_m, is characterized by thin (10 - 20 nm), fibrous, columnar grains separated by voids. This structure arises from low adatom mobility and shadowing effects, meaning that open boundaries between the columns are formed and cannot be filled in due to the low mobility. As the films grow thicker, the columns may span the full length of the film thickness, but the grain size within the column can still remain small (< 20 nm) or the column may even contain amorphous material.[40]

Zone T, where $T < 0.4\ T_m$, is similar to that of Zone 1 with small fibrous grains. However, there is less voiding due to the slight increase in surface diffusion. Due to the small nanometer sized grains, this structure has a large grain boundary volume. Zone T is an intermediate step between Zones 1 and 2, and is typically observed in sputtered films rather than evaporated films.

Zone 2, where $T < 0.7\ T_m$, exhibits a columnar microstructure with wide columns. In this region, surface diffusion is a dominating factor in film growth. The added surface mobility allows for densification of the columnar boundaries, which reduces the voiding within the film. The grain size increases, and the crystallinity is improved. The increased surface mobility allows for the atoms to rearrange themselves in low energy orientations. Indeed, certain crystallographic planes may grow faster than others due to reduced surface energy, and from this, preferred orientation or texture may arise.

In zone 3, where $T > 0.7\ T_m$, substantial surface and bulk diffusion occurs. This results in significant grain growth and densification leading to an equiaxed grain structure. The columns may consist of single crystals that span the entire length of the film thickness.

While the Structure-Zone model has been accurate in predicting the structure of numerous vapor deposited materials, it is a phenomenological model and therefore, it should be taken simply as a guide. It is possible that exceptions to the model exist depending on the type of material being deposited and variations in the film processing conditions. No previous work had been completed on the applicability of the Structure-Zone model to Gd_2O_3 films until the author's work[45], which will be discussed in great detail in chapter 6.

2.4.4. Residual stress in thin films

With the development of film structure and increased film thickness, the residual stress of thin films becomes an important consideration. Residual stress is defined as the stress remaining in a thin film after the growth process. Residual stresses are important because they can affect the structure[46] and properties of thin films.[47] Residual stresses in thin films are a summation of the intrinsic, extrinsic, and epitactic components of residual stresses. Intrinsic residual stresses refer to stresses that arise in the material during the growth process. This can be affected by numerous factors including the density of the film, nucleation and growth, grain size, crystallographic texture, phase transitions, defects, atom impingement, surface morphology, and compositional differences. Extrinsic stresses are due to external factors such as coefficient of thermal expansion (CTE) mismatch between the film and substrate, lattice mismatch, and interfacial structure / chemistry. Epitactic stresses are stresses that arise due to epitaxy and can be disregarded for amorphous or polycrystalline films. It is difficult to measure the intrinsic components of residual stress due to the complexity and number of contributing mechanisms. Extrinsic stresses, however, can generally be estimated since CTE mismatch is typically the major contribution to extrinsic stress. The effects of residual stress on Gd_2O_3 thin films were found to have a significant effect on film phase stability and will be discussed in detail in chapter 5.

2.5. Gadolinium oxide (Gd_2O_3) thin films

Gadolinium oxide films have been investigated thoroughly as a replacement for SiO_2 as a gate dielectric as a result of the downscaling of complementary metal-oxide-

semiconductor (CMOS) devices. Therefore, most of the published work on the deposition of Gd_2O_3 until this point has been focused on the deposition of less than 100 nm thick films for use as high K gate dielectrics. Several different methods have been used to deposit Gd_2O_3 films including electron beam-physical vapor deposition (EB-PVD)[7], pulsed laser deposition (PLD)[48], chemical vapor deposition (CVD)[49], atomic layer deposition[50], and magnetron sputtering[51] on a variety of substrate materials. Deposition of amorphous[6], epitaxial[52], and polycrystalline[8] Gd_2O_3 films has been observed and will be discussed in greater detail in the following sections.

2.5.1. Epitaxial gadolinium oxide films

Thin film epitaxial Gd_2O_3 deposited on silicon has been extensively investigated for microelectronic use. For very thin (4.5 nm) Gd_2O_3 films deposited on silicon (111) by molecular beam epitaxy (MBE), growth of the cubic bixbyite phase with a two dimensional in-plane epitaxial relationship is observed due to the small lattice mismatch.[53] Epitaxial Gd_2O_3 on Si(111) exhibits an A/B twinning relationship where B orientation is related to the substrate A by a 180° rotation around the surface normal. Epitaxial relationships have also been found to exist for Gd_2O_3 grown on Si(100) and Si(110).[53] The leakage currents for the Si / Gd_2O_3 / Pt metal-oxide-semiconductor (MOS) capacitors were found to be 0.4, 0.5, and 4.5 mA / cm^2 for Si(001), Si(111), and Si(110) substrates, respectively.

Gd_2O_3 films were also grown epitaxially by electron beam physical vapor deposition (EB-PVD) under ultrahigh vacuum (UHV) conditions on GaAs(100) substrates.[54] The Gd_2O_3 film grew in the bixbyite phase and was (110) oriented with

single domain epitaxy. These films were characterized by a breakdown field of 4 MV / cm and possessed leakage currents of ~10^{-9} A / cm^2 at zero bias.

Gd_2O_3 films have also been grown epitaxially on GaN substrates in cubic[55], monoclinic[56], and hexagonal[57] structures. A 76 nm thick cubic Gd_2O_3 film was grown epitaxially on GaN via metalorganic chemical vapor deposition (MOCVD) with orientation $Gd_2O_{3(111)} \parallel GaN_{(0001)}$. The large bond length mismatch resulted in a film with a high density of dislocations. This reduced the breakdown field of the oxide to 0.3 MV / cm. The dielectric constant of the film was 11.4.[55] Another group reported the growth of 10 nm thick single crystal monoclinic Gd_2O_3 heteroepitaxially on GaN with orientational relationship $Gd_2O_{3(-402)} \parallel GaN_{(0001)}$.[56] These films possessed a low leakage current of 4.6 x 10^{-9} A / cm^2 at 1 MV / cm and a dielectric constant of ~17. Another study succeeded in stabilizing the high temperature hexagonal (H) phase using epitaxy on a GaN substrate.[57] They deposited a 3 nm thick hexagonal film with epitaxial relationship $Gd_2O_{3(0001)} \parallel GaN_{(0001)}$. The film possessed a significantly higher dielectric constant of 24. The ability to grow cubic, monoclinic, and hexagonal Gd_2O_3 films through epitaxy highlights the polymorphic nature of Gd_2O_3, which must be taken into consideration for processing of polycrystalline Gd_2O_3 films.

2.5.2. Polycrystalline gadolinium oxide films

The growth of thin polycrystalline Gd_2O_3 has been shown to yield cubic, monoclinic, and mixed phase films.[58] 100-300 nm thick polycrystalline Gd_2O_3 films deposited by metalorganic chemical vapor deposition (MOCVD) on silicon(111) and fused quartz substrates resulted in cubic Gd_2O_3 with C(222) texture. The C(222) texture

was attributed to the minimization of surface energy. In another study, ~30 nm thick polycrystalline Gd_2O_3 films deposited on Si(001) substrates by magnetron sputtering deposition exhibited mixed cubic and monoclinic phases.[8] An increase in the deposition temperature from 450 °C to 570 °C resulted in an increase of the monoclinic phase, and change from C(222) texture to M(-402) texture. The transition to monoclinic phase was accompanied by a significant decrease in the dielectric constant from 17 to 9 and an increase in the leakage current by nearly one order of magnitude (from 2 to 13 mA / cm^2 at -6 V). In comparison, Li et al. investigated the effect of oxygen concentration on the properties of ~70 nm thick polycrystalline Gd_2O_3 films deposited on Si(100) by magnetron sputtering deposition at a deposition temperature of 650 °C.[51] An increase in the amount of cubic phase was observed with increasing oxygen partial pressure. However, the dielectric constant for all deposited films was approximately 12, regardless of oxygen content, suggesting no correlation of dielectric constant to crystal structure which is in contrast to Yue et al.[8] As shown by these studies, thin film structure and properties can differ significantly depending upon deposition methods and processing parameters.

Another important consideration for growth of Gd_2O_3 films on silicon substrates are interfacial reactions. Wu et al.[59] observed an amorphous silicate interfacial layer between the silicon substrate and a 30 nm thick Gd_2O_3 film deposited by direct EB-PVD. Annealing at 900 °C in oxygen for 2 minutes resulted in a complicated multilayer structure consisting of oxide layers, silicate layers, and SiO_2 rich layers. It has been suggested that ultra-high vacuum (UHV) may be necessary to grow Gd_2O_3 without an

interfacial layer on silicon.[60] Furthermore, the extended time required for deposition of thick films needed for neutron detection could result in additional interfacial reactions.

2.5.3. Amorphous Gd_2O_3 films

Gd_2O_3 films have also been deposited in the amorphous phase without long range order. One study showed that a 4.6 nm thick amorphous Gd_2O_3 film deposited by direct electron beam physical vapor deposition resulted in improved surface roughness over epitaxial thin films.[6] The leakage current density was also improved by 3 orders of magnitude, 10^{-6} A at 1 V. The dielectric constant of this film was found to be 14. The author is not aware that any other reports regarding amorphous Gd_2O_3 films, possibly suggesting that Gd_2O_3 may crystallize fairly easily during thin film growth.

2.5.4. Phase transitions in thin film Gd_2O_3 during growth

In section 2.5.1, it was shown that epitaxial stabilization of metastable Gd_2O_3 phases was possible. Interestingly, a number of reports have detailed the existence of phase transitions due to changes in film thickness. During the epitaxial growth of Gd_2O_3 on Ge, Molle et al. reported initial growth of the thermodynamically stable cubic phase followed by a transition to the monoclinic phase above a critical film thickness of 8.8 nm.[61] This was attributed to strain, but the mechanism was not investigated further. In another study, Gd_2O_3 films deposited on GaN (0001), transformed from the hexagonal phase to the cubic phase at a critical film thickness of approximately 3-4 nm.[62] A similar phase transition from hexagonal to monoclinic phase was observed when the film

thickness increased from 2 nm to 6 nm for single crystal Gd_2O_3 deposited on GaAs (111).[63]

Naturally, differences in Gd_2O_3 phase volume have resulted in various film morphologies and electrical properties. Recently, a study investigated the effect of film thickness in very thin epitaxial layers grown on Si(111).[64] A large increase in dielectric constant was found (13 to 20) for very small thicknesses (below 8 nm) as compared to thicker films. This was attributed to a possible strain induced structural change into the monoclinic phase before eventual relaxation into the bulk cubic phase, which is the reverse direction of the transition mentioned previously by Molle.[61] The aforementioned results suggest that the strain and residual stress in Gd_2O_3 films can alter the phase, and therefore, the properties of the Gd_2O_3 films. Indeed, we will show in chapter 5 that residual stress plays a crucial role in determining the phase stability of Gd_2O_3 films.

Understanding the mechanisms that govern structural and crystalline growth in Gd_2O_3-based films may be essential towards optimizing film properties for a specific application, such as radiation detection. Furthermore, the change in molar volume from cubic Gd_2O_3 to the monoclinic phase is approximately 8%. For films with sufficient thicknesses, transformations with such drastic changes in volume may result in cracking or failure. Since solid state neutron radiation detection devices incorporating Gd_2O_3 may utilize films that are several microns thick, the ability to control the phase and resulting properties of thick films is highly desirable.

2.6. Dielectric properties

The metal-oxide-semiconductor (MOS) capacitor consists of a semiconductor substrate, insulating film, and a metal electrode referred to as a gate as shown in Figure 2.10. The MOS capacitor is not widely used by itself in modern electronics, but is instead sandwiched between two p-n junctions to form a MOS transistor. However, measurement of MOS capacitor properties can provide significant information about film properties through study of the dielectric properties and conduction mechanisms within the devices.

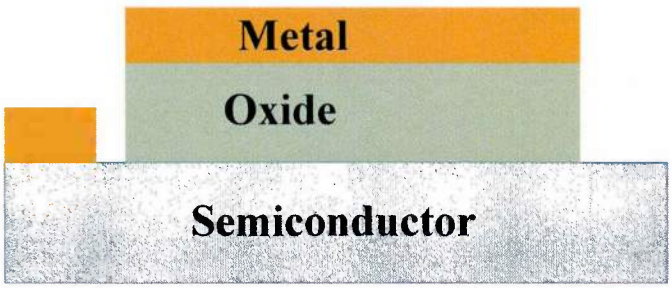

Figure 2.10. Schematic of a MOS capacitor.

Characterization of the dielectric properties of MOS capacitors can yield information about the film dielectric constant, dielectric loss, and the types of defect present within the material. In a C-V measurement, a voltage is applied to the gate metal and the capacitance is measured. A typical capacitance-voltage (C-V) curve of a MOS capacitor with an n-type semiconductor substrate is shown in Figure 2.11. The MOS capacitor undergoes three distinct modes of operation when the bias is swept to sufficient voltages. When the bias attracts the majority charge carriers, the capacitance measured is the capacitance across the dielectric film only and the MOS device is in accumulation.

With the device in accumulation, the dielectric constant of the film can be calculated provided the thickness of the film and area of the device are known. When the bias begins to force majority charge carriers away, the MOS device enters depletion and the capacitance decreases. The capacitance decreases due to the depletion of charge at the oxide-semiconductor interface. After all of the charge carriers have been depleted from the semiconductor, the minority carriers begin to accumulate at the interface, forming an inversion layer.

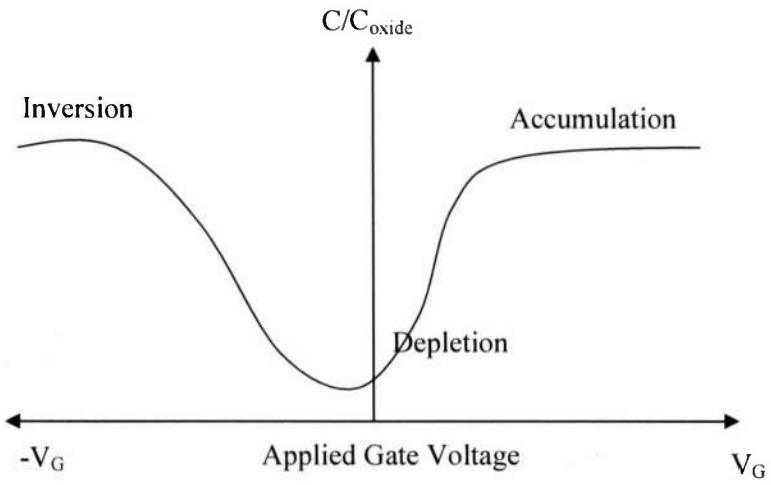

Figure 2.11. C-V curve for a MOS capacitor with n-type substrate showing three regions of capacitor operation.

Since charges in the oxide cause a shift in the gate voltage required to reach the threshold condition, the C-V measurement can provide information about the fixed oxide charge, oxide trapped charge, mobile charge, and interface trapped charge. A shift in the flatband voltage can be attributed directly to the presence of fixed oxide charge within the film. Fixed oxide charge is often a result of oxygen vacancies or broken bonds. The

presence of hysteresis as shown in the CV curve in Figure 2.12 can be attributed to either mobile charges within the oxide or interface trap states. Interface traps typically cause "smearing out" of the C-V curve, meaning that the transition from accumulation to depletion is no longer sharp. Combining the C-V measurement with conductance-voltage (G-V) measurement enables extraction of interface state density.

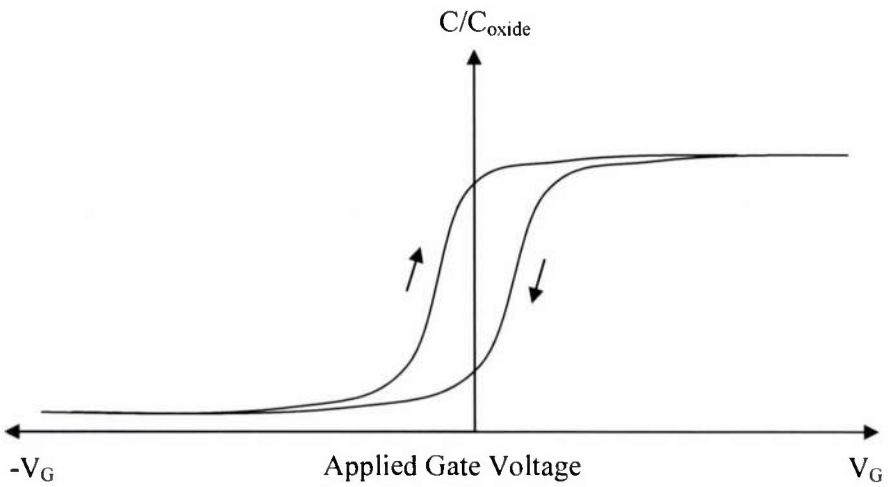

Figure 2.12. Hysteresis in CV curves as a result of trapped oxide charge.

2.7. Conduction in metal oxides

Understanding how Gd_2O_3 conducts charge is extremely important for optimization of a neutron detector to improve charge transport and detection efficiency. Metal oxides can be conducting, semiconducting, or insulating. Like the other rare earth oxides, Gd_2O_3 is a dielectric insulator with a large bandgap (5.4 eV or greater).[65]

The measured current in a MOS capacitor can be the result of a number of different conduction mechanisms. Charge carriers within an oxide can either be intrinsic, meaning they belong to the insulator, or extrinsic, meaning they are injected from the

electrodes. For intrinsic charge carriers, the conduction is ohmic and the charge carrier density is low.

Extrinsic conduction leads to two types of conduction mechanisms in the MOS structure. The first is where the electrodes act as an infinite source of electrons. In this case, conduction is governed by the bulk of the oxide. The second type of conduction is where the electrodes limit carrier injection into the oxide. These two types of conduction are referred to as bulk-limited and electrode-limited conduction.

A schematic detailing energy level transitions for different conduction mechanisms is shown in Figure 2.13.[66] The bulk limited conduction mechanisms include hopping conduction[67], space charge limited current[68], and Frenkel-Poole conduction.[69] The electrode limited mechanisms include Schottky (thermionic) emission[70], tunneling[66], and Fowler-Nordheim effect.[71]

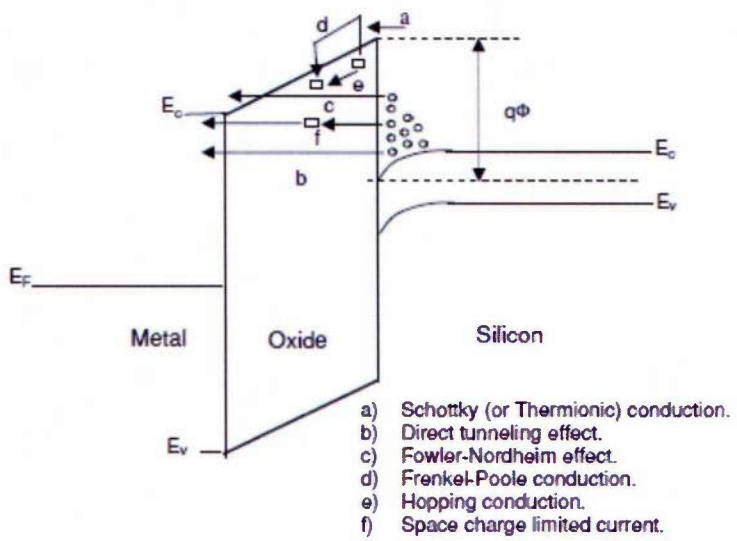

Figure 2.13. Energy level transitions for different conduction mechanisms. E_v is the valence band, E_c is the conduction band, E_f is the Fermi level, and $q\phi$ is the Schottky barrier height.[66]

2.7.1. Bulk-limited conduction mechanisms

In bulk-limited conduction, at low fields, the I-V characteristics should be ohmic as long as the electrode can readily supply carriers. This is generally explained by hopping conduction, where electrons move from one trap to the other without excitation into the conduction band as shown in Figure 2.13e. The ohmic current saturates when all carriers can be driven through the insulator for an applied bias. Hopping conduction can, however, be non-ohmic in nature when carrier distribution throughout the oxide grows due to increasing temperature or voltage.

2.7.1.1. Space charge limited conduction (SCLC)

Space charge is defined as electrical charge distributed through the oxide. This charge is thought of as a continuum of charge rather than specific electrical point charges. Essentially, an electron cloud is created throughout the material creating a space charge region. This typically only occurs in dielectrics because in metals, this charge is quickly neutralized.

If leakage throughout the dielectric is bulk limited, the characteristics of the current flow are governed by electrons in the conduction band. The concentration of charge carriers in the conduction band are largely affected by the energy of the trap levels, the concentration of trap levels, and the injection of electrons into these traps. Typically, it is quite difficult to elevate electrons into the conduction band by thermal transition or tunneling due to large energy barriers. However, if the oxides have a large trap density, electrons can be activated into the conduction band with small activation energies as shown in Figure 2.13f. Space charge limited conduction is typically observed

in room temperature or below since a low density of charge carriers causes charge unbalance quite easily. However, due to increased charge trap density in rare earth oxides, this can also be observed at high temperatures in these materials.

For SCLC, the current voltage relationship will be proportional to $J \sim V^n$ where n = 2 for discrete traps. If traps are distributed in the middle of the band gap, then n may be greater than 2. In order to fit the curve to SCLC mechanism, log (J) versus log (V) is plotted. The resulting plot will be linear with the slope equal to the exponent n if the SCLC mechanism is dominant.

2.7.1.2. Frenkel-Poole conduction

For Frenkel-Poole conduction, we will again assume the case of perfect ohmic contacts that are able to inject charge without any potential barriers at the electrode film interface. Electrons are trapped in localized states within an insulator and require thermal fluctuations to reach the conduction band. Once an electric field is applied, the charge carriers escape their trap state by overcoming a potential barrier into the conduction band as shown in Figure 2.13d. Once in the conduction band, the electrons can move into a lower energy trap state. This mechanism is, therefore, thermally activated and governed according to equation 2.1:

$$J = (qN_C\mu)E_{ox}\left[\frac{-q(\phi-\sqrt{qE_{ox}/\pi\varepsilon_r\varepsilon_0}}{k_BT}\right] \qquad \text{Eq 2.1}$$

where J is the current density, q is the electronic charge, N_c is the density of states in the conduction band, μ is the electronic drift mobility, E_{ox} is the electric field across the oxide, π is a constant, ϕ is the trap energy level, ε_r is the oxide dielectric constant, ε_0 is

the permittivity of free space, k_B is Boltzmann's constant, and T is the measurement temperature.

In a large electric field, however, the electron does not need as much thermal energy to overcome the potential barrier and escape to the conduction band. For fitting the Frenkel-Poole curves, log (J/E) is plotted vs $E^{1/2}$. This gives a linear plot. The accuracy of this plot can be checked by calculating the dielectric constant from the given slope. If the calculated dielectric constant is reasonably close to the measured dielectric constant, it is likely that Frenkel-Poole is the dominating conduction mechanism.

2.7.2. Electrode-limited conduction mechanisms

2.7.2.1. Schottky emission

The interface between two materials may have a potential barrier known as a Schottky barrier as shown in Figure 2.13a. Similar to the case of Frenkel-Poole conduction, application of a bias will allow the charge carries to overcome this barrier. This mechanism is also thermally activated. Schottky conduction can be shown by the equation 2.2:

$$J = A^* T^2 exp\left[\frac{-q(\phi - \sqrt{qE_{ox}/4\pi\varepsilon_r\varepsilon_0}}{k_B T}\right] \qquad \text{Eq 2.2}$$

where J is the current density, A* is the Richardson constant, T is the measurement temperature, q is the electronic charge, ϕ is the Schottky barrier height, E_{ox} is the electric field across the oxide, π is a constant, k_B is Boltzmann's constant, ε_r is the oxide dielectric constant, and ε_0 is the permittivity of free space. By plotting log (J) versus $E^{1/2}$, one can derive the linear slope of the graph and calculate the dielectric constant. Similar

to Frenkel-Poole, the accuracy of the dielectric constant can be checked to determine if Schottky emission is a dominating conduction mechanism

2.7.2.2. Fowler-Nordheim tunneling

Fowler-Nordheim Tunneling is another electrode-limited or interface-limited conduction mechanism. Instead of overcoming a potential barrier in the classical sense, the charge carriers are tunneled through from the electrode Fermi level directly into the conduction band as shown in Figure 2.13c. Fowler-Nordheim tunneling is governed according to the equation 2.3:

$$J_{FN} = \left(\frac{q^3E^2}{8\pi h\phi_B}\right) * \exp\left(\frac{-8\pi\sqrt{2qm_{ox}}}{3hE}\phi_B^{3/2}\right) \qquad \text{Eq 2.3}$$

where J is current density, q represents the elementary charge, E represents the applied electric field within the insulator, π is a constant, $\phi_B$is the voltage barrier that an electron must overcome to move from atom to atom within the insulator, m_{ox} is the effective mass of an electron in the insulator, and h is Planck's constant.

To check for this conduction mechanism, log (J/E^2) versus -1/V is plotted. A linear region suggests the presence of Fowler-Nordheim Tunneling. Since there is no temperature dependence for FN tunneling, any thermal gradient cannot be attributed to this conduction mechanism.

Chapter 3

Experimental methods

This chapter discusses the experimental methods used to perform the dissertation work in detail. The first section covers the basics of film deposition by reactive electron beam-physical vapor deposition as well as details about the processing conditions. The second section covers the materials characterization techniques used to analyze the Gd_2O_3 films. Then, a brief description of the electrical test structure fabrication process is given. Finally, the electronic characterization and radiation testing techniques employed will be discussed.

3.1. Film Deposition

3.1.1. Electron beam-physical vapor deposition (EB-PVD)

A schematic of EB-PVD equipment used for the Gd_2O_3 depositions is shown Figure 3.1. The vacuum chamber (Denton Vacuum, Inc. (DV-SJ/26)) is approximately 30 inches high and 26 inches wide with a volume of approximately 0.3 m^3. The chamber and most of the components within it are made of stainless steel. The inside of the chamber is covered with aluminum foil to keep contaminants from adsorbing to the chamber walls and to assist with easy chamber clean-up. There are two window ports on the chamber door and one port on the side for viewing of the deposition process. Glass plates are placed over the viewports to prevent film deposition since they are inexpensive and easily removable. The substrate holder was a 6" diameter stainless steel platen used to accommodate the various substrates during the deposition process.

Within the deposition chamber, a stainless steel heater with a molybdenum element was used for elevated temperature depositions. A vapor shield is used to protect the inside of the heater walls from evaporant material deposition. The upper temperature limit of the heater is 650 °C. There are four water-water cooled graphite crucibles (25 cubic centimeters) contained in the source manifold.

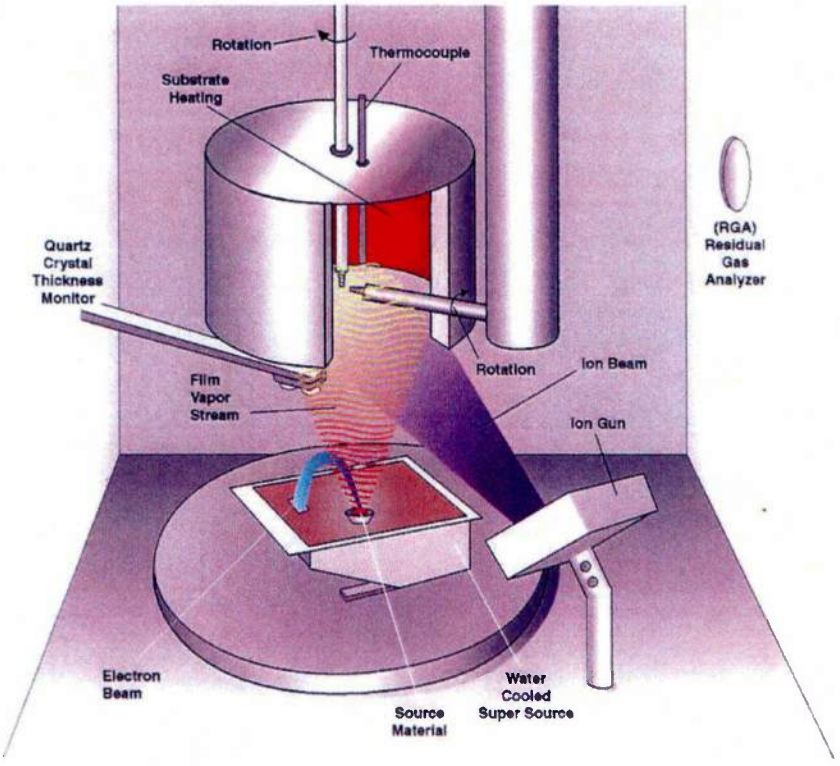

Figure 3.1. Schematic of the Denton vacuum EB-PVD system.

When one crucible is exposed to the 270° deflected electron beam, the other three remain shielded by the copper housing. The four crucibles allow for the deposition of thick films which require more material than is available in one crucible without the need to vent the chamber. Additionally, the other crucibles can be used to deposit multilayers of different materials. The electron beam (Temescal model STIH-270-2MB) is generated

from an emitter assembly which consists of a beam former and an electron-emitting tungsten filament.

3.1.2. Reactive electron-beam physical vapor deposition

Gadolinium oxide (Gd_2O_3) films were deposited on heavily doped, 2" diameter 0.002–0.008 Ω-cm resistivity, n-type (111) silicon wafers (Silicon Inc.), 9 x 9 mm GaN / AlGaN quantum well structures, 2" diameter sapphire C-cut wafers, and 1" x 1" quartz substrates (Ted Pella Inc.) via reactive electron beam physical vapor deposition. Prior to Gd_2O_3 film deposition, the substrates were cleaned in an acetone bath for four minutes, followed by an iso-propanol (IPA) bath for 1 min. The substrates were then rinsed with de-ionized water and dried with high purity (99.9999%) N_2 gas. The silicon samples were etched in diluted HF solution (BOE 6:1) for 30 seconds before being rinsed with DI water and dried with N_2. The samples were then placed in the substrate holder. The mask is shown in Figure 3.2. There are four locations for 2" diameter wafers (Si or sapphire), one location for the 1"x1" quartz substrate and seven locations for 9 x 9 mm pieces typically used for GaN / AlGaN or Si(111).

A gadolinium metal ingot (Hefa Rare Earth), purity 99.99%, weighing between 25 and 30 g was placed in a graphite crucible and used as the evaporant material. Additional crucibles were used for depositions requiring films thicker than 5 μm as the source material would begin to oxidize during the deposition resulting in a smaller melt pool (and thus lower flux) and a distortion of the vapor plume leading to non-uniform film deposition. Therefore, when the melt pool began to shrink, the crucible was changed to provide a fresh pot with unoxidized Gd metal to maintain the Gd flux. Two quartz

crystals were installed in the crystal thickness monitor before every deposition for measuring *insitu* film thickness.

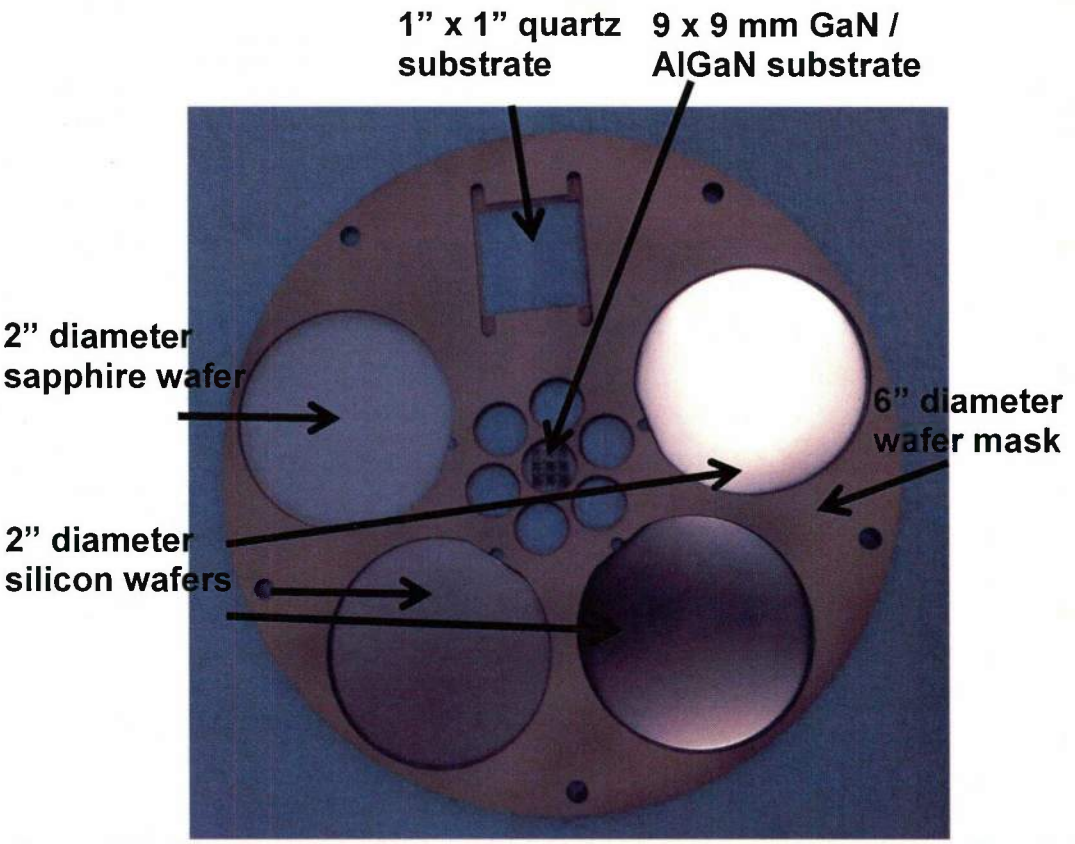

Figure 3.2. Digital image showing the substrate holder used in Gd_2O_3 EB-PVD experiments which can accommodate four 2" wafers, one 1" x 1" substrate, and seven 9 x 9 mm substrates.

After the samples were loaded into the deposition chamber and positioned within the heater, the chamber was first evacuated using a mechanical pump to a pressure of approximately 10^{-3} Torr. Subsequently, the base pressure was pumped below 6×10^{-6} Torr by use of a cryogenic pump. Cold water was flowed throughout the chamber walls to keep the chamber cooled and to prevent damage. During elevated temperature deposition, the sample temperature was ramped up and the samples allowed

to soak at temperature for 10 minutes before starting the deposition process. Ultra high purity O_2 (99.9999%) was introduced to the chamber through an inlet tube 15 seconds before opening of the deposition shutter. This was done to allow the Gd metal atoms to react with oxygen to form the gadolinium oxide, i.e. reactive EB-PVD. Select depositions where more oxygen was required involved flowing additional oxygen through the ion beam manifold. The deposition pressure varied between 10^{-4} and 10^{-6} Torr depending on O_2 flow rate (10-200 sccm) whereas the deposition temperature was varied between ambient and 650 °C depending on experimental conditions. The source to substrate distance was 12.5 inches (31.75 cm). In situ film thickness was monitored through use of a quartz crystal thickness monitor (QCM) in conjunction with the IC 6000 deposition controller. The IC-6000 allows for the programming of up to 6 different film programs with 37 adjustable parameters. While the IC-6000 has the capability to run in automated mode, all depositions in this work were performed in manual mode. In manual mode, the operator controls the electron beam current and resulting deposition rate. During the deposition process, the deposition rate, gas flow, chamber pressure, and source material were constantly monitored.

3.1.3. Direct electron beam-physical vapor deposition

Select depositions were completed via a direct evaporation method utilizing a Gd_2O_3 source rather than Gd metal. The Gd_2O_3 source material (Cerac Inc., 99.99% purity) consisted of a large number of small pellets packed into a graphite crucible. The Gd_2O_3 and Gd source material after extended deposition in oxygen environments are shown in Figure 3.3.

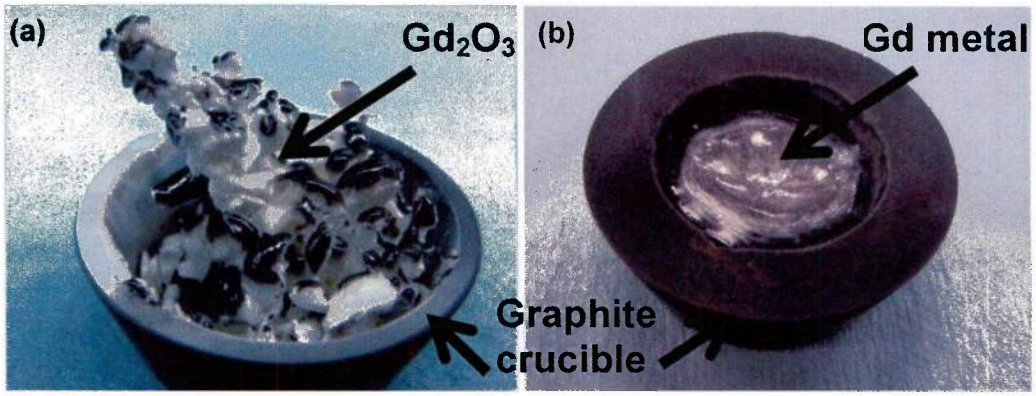

Figure 3.3. Digital images of (a) Gd_2O_3 and (b) Gd source material after direct and reactive evaporations, respectively.

As can be seen in Figure 3a, during the direct evaporation of Gd_2O_3, substantial dendritic growth is observed as well oxygen deficiency in the source material characterized by the metallic black outerlayer. The dendritic growth has potential to cause a distorted vapor plume resulting in an uneven film thickness, composition, texture, and morphology. Therefore, most of the work in this thesis focused on reactive deposition of Gd metal with oxygen due to the good, uniform melt pool during evaporation as shown by the divot in the Gd source material in Figure 3b. The dendritic growth in the Gd_2O_3 source material could possibly be a result of phase transformation within the Gd_2O_3 from the cubic to the monoclinic phase which was discussed in section 2.2, and has a molar volume change of approximately 9%. To mitigate this behavior and to minimize the change in plume geometry, a rod source could be used during evaporation.

3.1.4. Ion beam assisted deposition (IBAD)

Select depositions utilized ion beam assistance using a Denton CC-101 cold cathode ion source. The CC-101 is able to produce ion beams of Ar^+, N^+ and O^+. The

ions are used to bombard the substrate during deposition to increase adatom mobility, increase film density, control crystallographic orientation, and impart stress into the film. Gas is introduced into the ion beam source (IBS) chamber where it is ionized by a high voltage field between the cathode and anode. An extraction grid, a 100 mm diameter meshed stainless steel grid, covers the IBS exit port. As the ionized gas exits the IBS, the extraction grid serves as an electron getter. It collects the electrons which in turn creates a potential that helps accelerate the ionized species towards the substrate.

3.2. Materials characterization

A variety of analytical materials characterization techniques were used to determine the phase, structure and properties of the Gd_2O_3 films. X-ray diffraction (XRD) was used for the determination of film crystallographic structure, film texture, and residual stress. Raman spectroscopy was used to assist in phase identification. Scanning electron microscopy (SEM) was use to characterize top surface and fracture surface morphology as well as extract film thickness. Atomic force microscopy (AFM) was used to investigate film surface roughness. Transmission electron microscopy (TEM) in conjunction with energy dispersive x-ray spectroscopy (EDS) and electron energy loss spectroscopy (EELS) was used to analyze film structure, orientation, and interfacial chemistry. EDS was also used during SEM analysis to evaluate bulk Gd / O ratio in the films. X-ray photoelectron spectroscopy (XPS) was used to evaluate chemical state and Gd / O ratio of the Gd_2O_3 films. A wafer curvature technique was used to measure the film residual stress. UV-Vis spectroscopy and ellipsometry were used to determine the band gap and refractive index of the films, respectively.

3.2.1. Scanning electron microscopy (SEM)

SEM is essential for the analysis of film microstructure and morphology. Both top surface and fracture surfaces of the Gd_2O_3 films were studied. Two field effect scanning electron microscopes were used for analysis of the Gd_2O_3 films. SEM (JEOL 6700F) surface morphology was used in conjunction with Clemex Vision analytical software for grain size determination. Clemex allows for automated analysis of grain size based on image contrast. Ten SEM images (magnification 50000x) were obtained from various locations on the sample surface for determining the average grain size. A LEO 1530 FESEM was also used for surface and fracture surface characterization when higher resolution images were required.

3.2.2. Transmission electron microscopy (TEM)

TEM was used to analyze the structure, interfacial chemistry, and phase of the Gd_2O_3 films. TEM cross-sectional specimens were prepared using conventional mechanical polishing followed by Ar ion milling in a PIPS ion thinner. Cross-sectional TEM, selected area diffraction (SAD), scanning transmission electron microscopy (STEM), energy dispersive x-ray spectroscopy (EDS), and electron energy loss spectroscopy (EELS) were performed in a JEOL-2010F field-emission TEM/STEM equipped with a EDAX XEDS system and a Gatan Enfina 1000 EELS system. Both XEDS and EELS were performed under STEM mode using an electron probe with a nominal size of 0.5 nm. The EEL spectra were collected with a dispersion of 0.2 eV/channel and a resolution of ~1.4 eV. The semiconvergence angle was 7.25 mrad and the collection angle was 6.92 mrad for the EELS acquisition. High-angle annular

dark-field (HAADF) STEM images were collected with an inner detector radius of 63.5 mrad. The microscope operation energy was 200 kV for all studies. TEM work was performed by Daniel Grave and Dr. Xiaojun Weng, Materials Research Institute, Penn State University.

3.2.3. Focused ion beam (FIB)

Focused ion beam was used to investigate the cross sections of select Gd_2O_3 films when traditional wafer cleaving methods and fracture surfaces were not sufficient. An FEI Quanta 200 3D dual beam FIB was used to prepare the cross sections. Before ion milling, a metallic protective layer was applied to the film in order to create a clean cross section. The cross sections were milled using a 30kV Ga ion beam. Subsequent to cross section preparation, the samples were studied via SEM.

3.2.4. Atomic force microscopy (AFM)

AFM (Digital Instruments Dimension 3100) was used for evaluation of surface morphology and roughness analysis. The AFM was operated in tapping mode under ambient conditions. AFM scans were completed over 1 μm^2, 5 μm^2, and 10 μm^2 areas on the sample surface. Additionally, select scans were completed on a Bruker Dimension Icon AFM using PeakForce tapping mode, a novel technique where the tapping oscillation is performed at frequencies significantly below the cantilever resonance (which extends cantilever lifetime). Scanasyst AFM tips with a resonance frequency of 50 - 90 kHz and a spring constant of 0.4 N/m were used.

3.2.5. X-ray diffraction (XRD)

A number of X-ray diffraction techniques were used in this work for analysis of film phase, preferred orientation, crystalline grain size, residual stress, and texture evolution. θ-2θ scans were performed on the Gd_2O_3 films using a Phillips MRD-XRD, type PW3040/00. A copper anode was used as the x-ray source. Scans were collected from a 2θ angle of 10 degrees to 90 degrees with operating voltage / current of 40kV / 45 mA. The step size was 0.02° and the time step was 1 second. The x-ray beam was set for 1.2 mm x 10 mm horizontal and vertical divergence, respectively. When higher resolution was needed for the θ-2θ scans, select samples were scanned over the same 2θ range using a Phillips Empyrean diffractometer with a PIXcel 3D detector.

Scherrer's formula[72] was used to determine and correlate the XRD crystallite size with the measured grain size of the films:

$$D = \frac{K\lambda}{B\cos\theta} \qquad 3.1$$

where D is the grain size, K is the shape factor, λ is the X-ray wavelength, B is the difference in the instrumental broadening and crystallite size broadening, and θ is the Bragg angle. K was taken to be 0.9 and λ to be 1.54056 Å for Cu radiation. The instrument broadening contribution obtained from a diffraction pattern of a standard packed Si powder was subtracted from the full width half maximum (FWHM) of the analyzed peaks.

For films deposited on single crystal substrates, diffraction peaks from the substrate were observed if the film thickness was small enough. Therefore, the x-ray depth of penetration for Gd_2O_3 was calculated using the mass attenuation coefficient of Gd_2O_3. Figure 3.4a displays the film thickness from which 99% of the intensity originates

for a given angle 2θ. Figure 3.4b shows the X-ray penetration depth at angle 28.4° 2θ, the substrate peak for Si(111). As can be seen from this graph, one can expect to see some diffraction from the substrate up until a Gd_2O_3 film thickness of approximately 1.5 μm. For sapphire wafers which have a substrate peak at approximately 41 degrees, one can expect to see diffraction from the substrate for film thicknesses of approximately 3 μm.

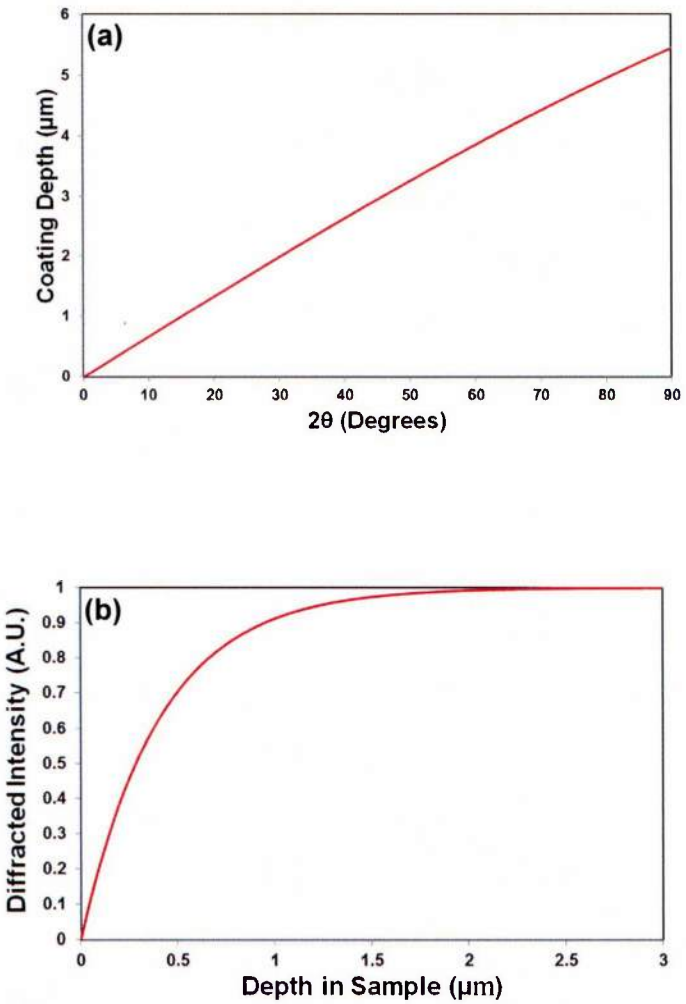

Figure 3.4. (a) Gd_2O_3 film thickness from which 99% of the intensity originates as a function of angle 2θ and (b) percentage of diffracted intensity as a function of Gd_2O_3 film thickness at the Si(111) peak position.

Grazing incidence (GIXRD), or 2θ-only, X-ray diffraction scans were also performed using a Phillips X'Pert MRD-XRD, type PW3040/00, diffractometer. In 2θ-only scans, the incident angle of diffraction is held constant, and only the detector moves. This gives diffraction from other planes which are not just oriented parallel to the substrate surface. In a perfectly randomly oriented sample, the peak positions and relative intensities from both the θ/2θ and 2θ-only scans would match. However, significant texturing is observed in some of the deposited Gd_2O_3 films, and therefore, 2θ scans can yield significant information about the film structure and orientation. Additionally, since the incident angle of diffraction is controlled, the depth of penetration can be varied. Scans were performed at incedence angles of 1, 2, 5, 10, and 15 ° for depth profiling of the Gd_2O_3 films. This is especially useful for the deposited Gd_2O_3 films since a thickness dependent crystallography was observed.

Pole figure measurements were also performed on select Gd_2O_3 films to determine both out-of-plane and in-plane texture. The scans were performed using a Phillips X'Pert MRD-XRD, type PW3040/00, diffractometer. Pole figures were taken using sample tilts of 0 – 85° in 5° steps with azimuthal rotation from 0 – 355° with a step size of 1° and step time of 1 second. The operating voltage / current were 40 kV / 45 mA, respectively. The x-ray beam was set for 1.2 mm x 10 mm horizontal and vertical divergence, respectively

3.2.6. Raman spectroscopy

Raman spectroscopy (WiTec alpha300 Confocal Raman instrument) was used to observe changes in the vibrational modes of the Gd_2O_3 films to assist in phase identification. A laser beam with wavelength 488 nm was directed at the deposited films, and the light from the illuminated spot was collected in a lens and dispersed onto a detector. The shift in the laser was used to identify the vibrational modes in the material which gives information about its phase, residual stress, and crystallinity. The wavelength of the excitation laser used was 488 nm combined with a 100 × objective yielding a lateral resolution of 325 nm. Integration times were 1 min with a laser power of 25 mW.

3.2.7. Energy dispersive x-ray spectroscopy (EDS)

Energy dispersive x-ray spectroscopy (EDS) was used to determine the Gd / O ratio in the Gd_2O_3 films. Fractured sections of Gd_2O_3 films deposited on Si(111) were attached to a large 2" diameter stainless steel stub, which can hold up to 12 samples at one time, for EDS characterization. The samples were then sputter coated with carbon. Silver paste was applied to make a conducting path from the Gd_2O_3 film to the stub. The stub was mounted in the ESEM FEI 2000 chamber and then evacuated and the sample surface was imaged. Three EDS scans were taken at different points on the sample for a collection period of 1 minute and averaged to determine the Gd / O ratio. The oxygen and gadolinium concentrations were measured relative to a Gd_2O_3 "standard" 99.99% pure pellet (Cerac). A few considerations must be taken into account. There may be some differences in the local environment in the chamber whenever the chamber is

vented and then reloaded. Therefore, it is only accurate to compare samples that are measured under the same conditions. Secondly, the electron beam may penetrate films that are too thin resulting in skewed data. The additional silicon peak for these samples may affect the accuracy of the recorded values. Thirdly, these measurements should be regarded as semi-quantitative since the "standard" may not necessarily be stoichiometric Gd_2O_3. Nevertheless, under the same chamber conditions, EDS provides a means to compare the Gd / O ratio of the Gd_2O_3 films as a function of processing conditions.

3.2.8. X-ray photoelectron spectroscopy

XPS can yield additional information about the stoichiometry of the Gd_2O_3 films. It also can give information about the bonding state in the films. XPS was performed on a Kratos Axis Ultra XPS (Kratos Analytical Inc., Chestnut Ridge, NY) using Aluminum Kα (1486.6 eV) as the radiation source. The photoelectrons were analyzed at a take-off angle normal to the sample plane. Survey scans were recorded for each sample with a pass energy of 80 eV and step size of 1 eV. An Ar ion beam was used for depth profiling. Survey scans were repeated periodically throughout the film thickness until the substrate had been reached. XPS measurements were carried out by Vince Bojan and Tad Daniels, Materials Research Institute, Penn State.

3.2.9. UV-Vis spectroscopy

UV-Vis spectroscopy is an optical characterization technique which allows the measurement of transmittance through the sample. Optical transmission measurements in the wavelength range of 800–190 nm were made on select Gd_2O_3 films deposited on

quartz substrates using a PerkinElmer Lambda 950 UV/Vis/NIR spectrometer in order to measure the optical band gap value. From this data, $(\alpha h\upsilon)^2$ as a function of $h\upsilon$ was plotted, where α is the absorption coefficient and $h\upsilon$ is the photon energy. A tangential line to the absorption edge was drawn to obtain the optical band gap value.

3.2.10. Ellipsometry

Ellipsometry is an optical characterization technique that is used to determine film thickness and refractive index. A Gaertner L116C variable angle ellipsometer was used to determine the refractive index of the Gd_2O_3 films. The measurement setup involves the illumination of the sample with a 1 mW Ne-He 632.8 nm laser. The laser light was then reflected into the detector, and the change in polarization of the light was measured. The measurements were taken at a 50° angle of incidence. Five measurements across the wafer were taken to obtain the refractive index distribution of the Gd_2O_3 films.

3.2.11. Residual stress by wafer curvature method

To investigate the relationship between the residual stress state of the films and the phase stability, a wafer curvature technique was used to measure the residual stress. The wafer curvature technique allows for the measurement of total residual stress in thin films, namely the sum of the intrinsic and extrinsic stresses. A Tencor Flexus 2320 laser wafer curvature system was used to measure the radius of curvature of the silicon and sapphire wafers before and after film deposition for residual stress calculations. A schematic of the measurement is shown in Figure 3.5.

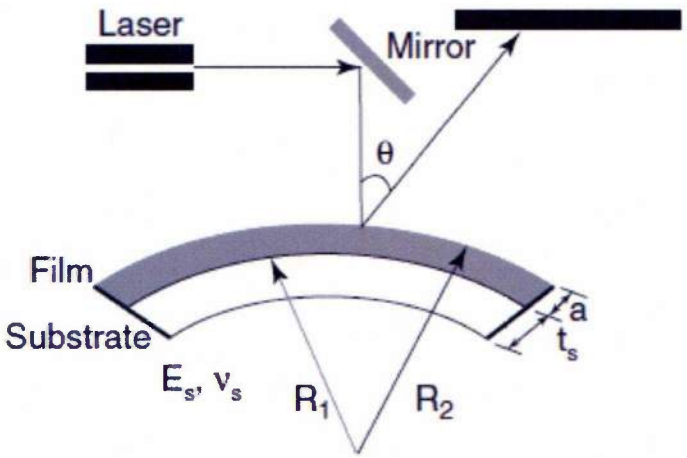

Figure 3.5. Schematic of wafer curvature measurement using Tencor Flexus 2320.[73]

The laser is scanned across the film surface and reflected back to a photodetector. 45mm (90%) of the (50.8 mm) wafer diameter was measured to avoid edge effects. Assuming a biaxial stress state and a coating thickness much smaller than the substrate, we employed Stoney's equation[74] to calculate the residual stress:

$$\sigma = \frac{E_s t_s^2}{6(1-\nu_s)a}\left(\frac{1}{R_2} - \frac{1}{R_1}\right)$$

where $E_s/(1-\nu_s)$ is the biaxial modulus of the substrate, t_s is the substrate thickness, a is the film thickness, and R_2 and R_1 are the radii of curvature after and before deposition. This method assumes a uniform stress state across the entire film.

3.3. Electrical test structure fabrication

Microelectronic devices based on silicon and GaN / AlGaN electronics were fabricated for both electrical characterization and radiation testing. Si (111) / Gd_2O_3 / Ti / Au MOS capacitors were fabricated using a shadow mask and were used to extensively study the effects of processing on the electrical properties of the Gd_2O_3 films. GaN /

AlGaN / Gd_2O_3 / Ti / Au MOS capacitors and high electron mobility transistors (HEMT) were also fabricated using clean room fabrication techniques. These will be discussed in more detail in the following sections.

3.3.1. Gd_2O_3 / Si(111) MOS capacitor fabrication

Subsequent to film deposition, select samples deposited on Si(111) were chosen for electrical fabrication. Metal-oxide-semiconductor (MOS) capacitor structures were fabricated by depositing 20 nm Ti / 200 nm Au contacts on top of the Gd_2O_3 films with a Kurt J. Lesker Lab 18 electron beam evaporator through a shadowmask making circular contacts with diameters of 1.5 mm and 3 mm. The Ti/Au multilayer was deposited on the edge of the wafer (where no oxide film was deposited) to create an adequate bottom contact. Figure 3.6a shows a schematic of the cross section and Figure 3.6b shows a digital image of the top view of the device.

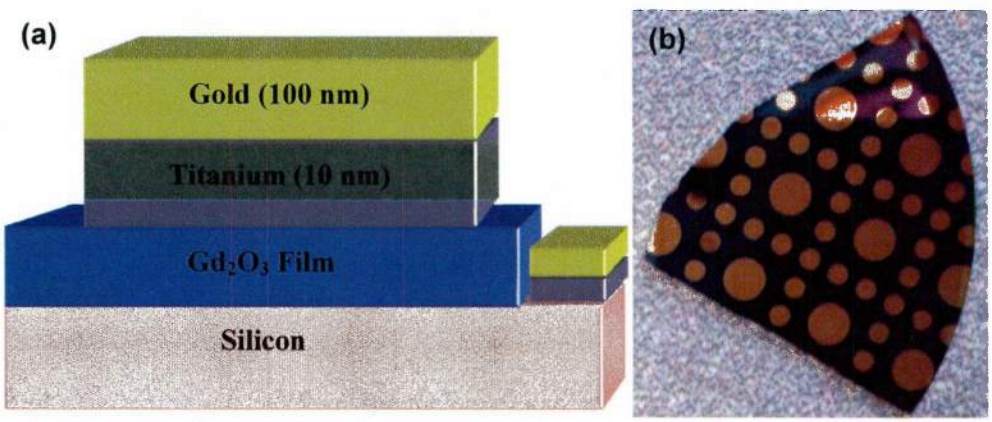

Figure 3.6. (a) Cross Sectional Schematic of Si / Gd_2O_3 / Ti / Au MOS capacitor and (b) digital image of top view of Si / Gd_2O_3 / Ti / Au MOS capacitor. The small and large circular contacts are 1.5 mm and 3 mm in diameter, respectively.

3.3.2. GaN / AlGaN quantum well structures

Microelectronic devices based on GaN / AlGaN quantum well structures were fabricated for electrical characterization and radiation testing. The first device, referred to as the "dot-ring" structure, shown in Figure 3.7, contains standard MOS capacitor structures with circular contacts of varying sizes (ranging from 62.5 μm to 1 mm diameter) as shown in Figure 3.7. This structure was used primarily for capacitance-voltage (C-V) and current-voltage (I-V) measurements.

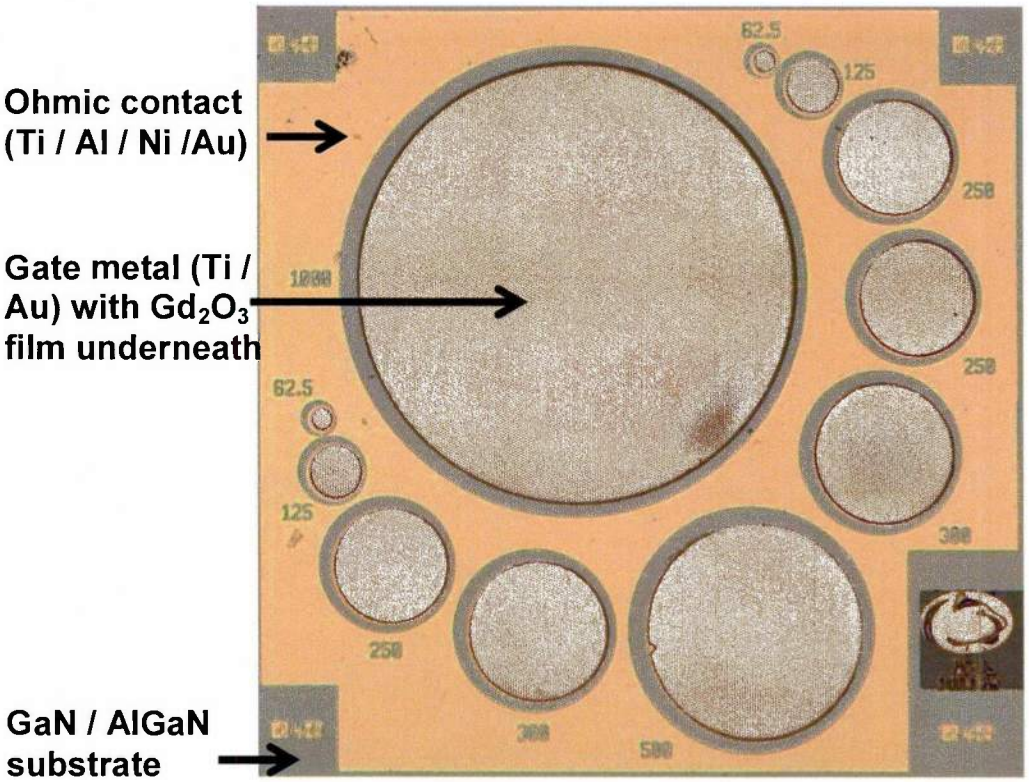

Figure 3.7. Optical microscope image of GaN / AlGaN based "dot-ring" structure with several MOS capacitors with diameters ranging from 62.5 μm to 1 mm.

The second type of device architecture, referred to as "rad sensor", shown in Figure 3.8 contains a number of electrical test structures including the high electron

mobility transistors that were used for radiation detection (HEMTs). Both the MOS capacitor structures and "rad-sensors" were processed using standard lithographic processes. The process steps were the same except different masks were used for the lithography steps to create the different test structures.

The top view of the "rad sensor" is shown in Figure 3.8. The four large areas labeled 1-4 are the high electron mobility transistor (HEMT) devices. The source and drain contacts are labeled "S" and "D" while the gate contact is labeled "G" for each device. The architectures of the transistor devices were designed with interdigitated electrodes of varying geometry so that different device properties such as gate oxide volume, channel width, and gate length could be studied for the optimization of radiation detection. These transistor devices are labeled 1-4. For purposes of repeatability, device 4 was used for measuring the GaN / AlGaN HEMTs properties in this dissertation work. Device 4 has a drain-source spacing of 1 mm and a gate width of 5 μm.

Other device architectures on the chip include two capacitor structures for standard C-V and I-V measurements with a diameter of 150 μm. One of the capacitor structures is coated with Gd_2O_3 while the other is absent of the Gd_2O_3. Transmission Line Measurement (TLM) pads were also present for contact and sheet resistance measurements. The spacing between the various pads was 2.5, 5, 7.5, 10, 15, and 20 μm. Van Der Pauw structures on the chips are used for Hall measurements to determine carrier mobility and concentration. Other structures included an RF field effect transistor, ohmic resistor, and Schottky resistor but were not used in this work.

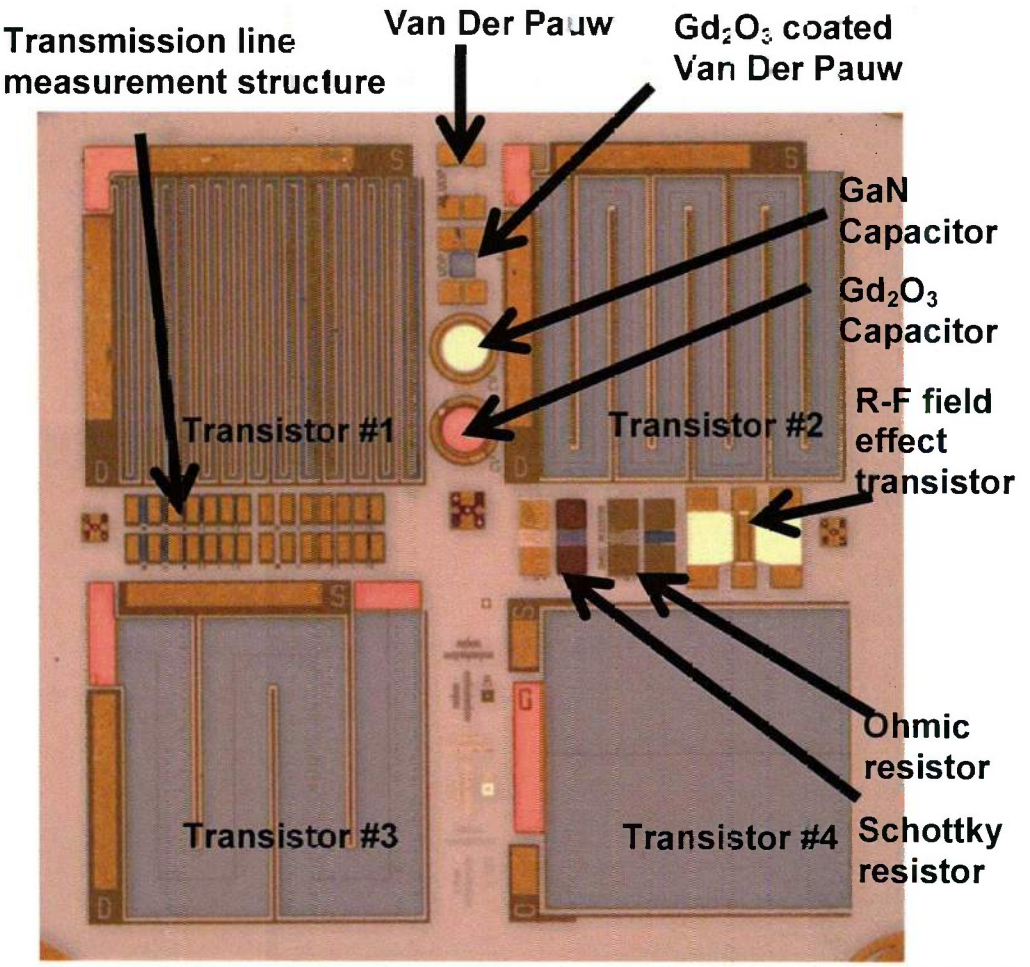

Figure 3.8. Optical microscope image of top surface of GaN / AlGaN based "rad sensor" structures. The device contains a number of electrical test structures including four high electron mobility transistors (HEMTs) with different device geometries, transmission line measurement structures, Van Der Pauw structures, MOS capacitors, an RF-Field effect transistor, an ohmic resistor, and a Schottky resistor. The labels S, D, and G correspond to the source, drain, and gate for each of the four transistor structures.

3.3.3. GaN / AlGaN / Gd_2O_3 / Ti / Au device fabrication

The bare S.C / GaN / AlGaN substrates (CREE Inc.) were first cleaned with isopropanol for 2 minutes, and then rinsed with DI water. Then, they were spin coated with 3012 photo resist at 5000 rpm for 45 seconds and baked at 95 °C for 60 seconds.

The samples were exposed to ultraviolet (UV) light for 7 seconds using a Suss MA/BA6 contact aligner under the "isolation" mask (see Appendix A) to pattern the sample. After UV exposure, the samples were developed in CD-26 for 60 seconds, and then cleaned with IPA and DI water. The samples were then subjected to a chlorine-based reactive ion etch (RIE) to isolate active regions of the GaN/AlGaN structures using a Tegal PM2 etcher. The etch was performed at pressure of 2 mTorr for 104 seconds to reach an approximate thickness of 90 nm. Then, the photoresist was stripped using remover PG and the samples were cleaned in IPA and DI water for 2 minutes each. After isolation level was established, a lift-off technique was used to pattern the ohmic contacts. The samples were spin coated with LOR5A photoresist at 6000 rpm for 45 seconds and baked at 180 °C for 10 min. A second layer of 3012 photoresist was deposited at 6000 rpm for 45 seconds followed by a bake at 95 °C for 60 seconds. The samples were then exposed to ultraviolet (UV) light for 7 seconds under "ohmic" mask (see appendix A) and developed / cleaned as detailed earlier. The ohmic metal stack consisting of Ti / Al / Ni / Au with thicknesses of 15 nm / 100 nm / 50 nm / 50 nm, respectively, were deposited using a Kurt J. Lesker Lab 18 electron beam evaporator. The samples were then dipped in PRS-3000 at 90 °C for 20 minutes to dissolve the remaining photoresist leaving only the metal deposited directly on the GaN/AlGaN substrate. Following the metal deposition, an ohmic anneal was performed at 875°C for 60 seconds in a nitrogen environment using an Alwin 21 AG610 rapid thermal annealing system. At this point, the Gd_2O_3 films were deposited as previously described in section 3.1. Following the film deposition, the films were spin coated using SPR 955 at 3000 rpm for 45 seconds. This was repeated twice to deposit a tri-layer of photoresist. The samples were then patterned using the procedure

listed above according to the dielectric etch mask (see Appendix A). The films were then subject to a chemical etch using a sulfuric acid and water solution at 1:100 ratio. Etching times varied between ten seconds and two minutes depending on the film. The remaining photoresist was removed using PRS3000 as described earlier. Finally, the samples were once again coated with LOR5A and 3012 photoresist as described above. The samples were then patterned under the "Schottky" mask and Ti /Au with thickness 10 nm / 100 nm was deposited using the Lab 18 evaporator. The photoresist was stripped using PRS3000, and the samples were cleaned, leaving the final device architecture. A full detailed process description can be found in Appendix A.

3.4. Electrical characterization techniques

A number of different techniques were used to characterize the Gd_2O_3 films deposited on both Silicon and GaN. Capacitance-Voltage (C-V) measurements were made to measure dielectric constant and loss of the MOS capacitor structures as well as determine the amount of oxide charges present in the structures. Current-Voltage-Temperature (I-V-T) measurements were performed on the MOS capacitors as well to determine the conduction mechanisms within the oxide films.

3.4.1. Capacitance-voltage (C-V) measurements

Capacitance-Voltage measurements were performed on Si(111) and GaN / AlGaN MOS capacitors. The Keithley Model 4200-SCS Semiconductor Characterization System was used to obtain C-V measurements for the MOS capacitors. A 4200-CVU integrated C-V measuring unit was used to extract these measurements. The unit was

calibrated to correct for stray capacitances using open and short calibrations. For the Si / Gd_2O_3 / Ti / Au MOS capacitors, the dielectric constant and loss was measured as a function of frequency from 10kHz to 1 MHz with a 20 mV RMS oscillating signal. Due to the high doping level and degenerative nature of the silicon substrate, depletion was not possible and therefore, standard C-V sweeps were not performed. An example of the measurement setup is shown in Figure 3.9

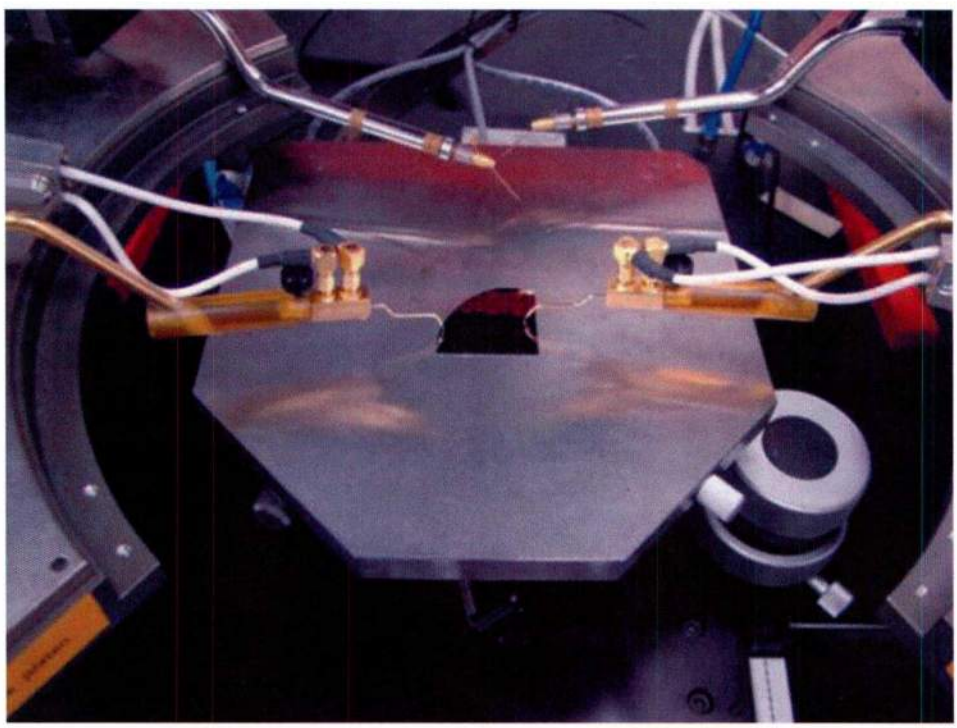

Figure 3.9. Capacitance-voltage (C-V) measurement of Si(111) / Gd_2O_3 / Ti / Au MOS capacitor using a Suss PM5 probe station with probes connected to Keithley 4200 Semiconductor Characterization System.

C-V sweeps were performed on GaN / AlGaN / Gd_2O_3 / Ti / Au MOS capacitors at a frequency of 1 MHz with a 30 mV RMS oscillating signal using the Keithley Model 4200-SCS Semiconductor Characterization System. The gate voltage bias range

depended on the measurement conditions and will be discussed in greater detail in Chapter 7. A pre-soak was also applied for certain measurements. From the C-V measurement, dielectric constant, interface trapped charge, fixed oxide charge, and bulk oxide trapped charge values were extracted.

3.4.2. Current-voltage-temperature (I-V-T) measurements

Current-voltage relationships of the silicon based and GaN / AlGaN based Gd_2O_3 MOS capacitors were measured as a function of temperature in order to determine DC conduction mechanisms within the Gd_2O_3 films. The samples were loaded onto a Cascade Microtech probe station at the Penn State Dielectric Center. An Agilent HP4140B pA meter was used to measure the current. The temperature of the stage was controlled by a Temptronic TP3000A Thermochuck system. The measurements were fully automated and programmed by GADD software developed at Penn State set to run on a Windows personal computer.

The details of the I-V-T measurement were as follows: the samples were swept from -100 V to +100 V at 5 V increments. The samples were held at each voltage for 60 seconds to let the capacitor reach steady-state conditions. Then the current was measured and the sweep continued. Each I-V sweep was performed at 25 °C increments starting from 25 °C to a maximum temperature of 200 °C.

3.4.3. Field effect transistor (FET) measurements

After transistor fabrication was completed on GaN / AlGaN substrates, field effect transistor (FET) measurements were made. The fabricated transistors were depletion

mode devices. For depletion mode devices under standard conditions with no voltage applied, the device is "on", meaning that current is flowing between the source and the drain and the channel is conductive. To turn the device "off", or impede the current flow between the source and the drain, a large enough negative gate voltage (V_G) must be applied between the source and the gate. This is called the threshold voltage, V_T. When the threshold voltage is reached, the device is "off" and the drain current (I_D) is at a minimum.

These measurements were performed using a Keithley Model 4200-SCS Semiconductor Characterization System. The gate voltage was swept from +10 V to –50 V in order to turn "off" the device. The voltage was then swept back to +10 V to assess the stability of the threshold voltage and determine if any hysteresis was present. A constant 10 V bias was applied between the source and drain during the measurement.

3.5. Radiation testing

Radiation induced conductivity (RIC) in Gd_2O_3 films was tested by exposing the devices to gamma and neutron radiation. The irradiations were performed at the Penn State Breazeale Nuclear Reactor in beam port #7. The reactor is a 1 MW TRIGA Mark III reactor. The neutron flux present in the beam is controlled by the reactor's operating power. Due to the nature of reactor, gamma rays are present as well and can contribute to the RIC observed in the Gd_2O_3 devices.

Samples with the best electrical properties were selected for radiation detection. To prepare the samples for radiation detection, they were packaged using Ceramic Dual In-Line Packaging (CERDIP) as shown in Figure 3.10a. To perform this, the samples

were first attached to the CERDIP using silver paste. A small dot of the silver paste was applied to the packaging, and the sample was placed face up over the silver paste. The paste was left for at least 1 hour to let it harden. Next, the corresponding terminals of the desired devices were wirebonded to the CERDIP pins. A Kulicke & Soffa Inc. wirebonder was used for wirebonding. The wirebonding temperature was set to 50 °C and the default power, time, and force settings were used. The wirebonded sample is shown in Figure 3.10b.

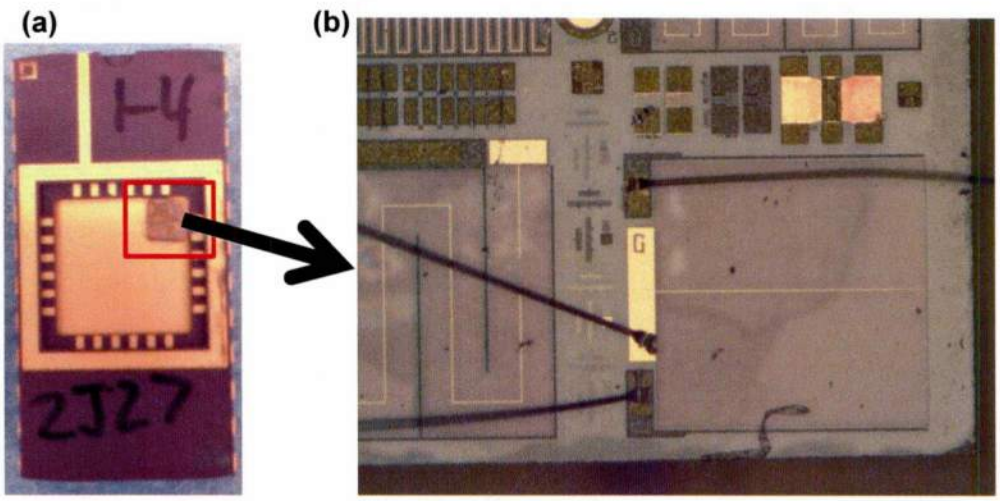

Figure 3.10. (a) Digital image of GaN / AlGaN "rad sensor' device die attached to Cerdip packaging and (b) optical microscope image showing wirebonds to GaN / AlGaN / Gd_2O_3 / Ti / Au MOS-HEMT terminals.

After wirebonding, the samples were taken to the Pennsylvania State University Breazeale Nuclear Reactor for radiation testing. Figure 3.11a shows the beam lab and the pneumatic shutter for beam port #7. The CERDIP devices were placed in a custom built radiation test box with BNC cabling connected to the Keithley Model 4200-SCS Semiconductor Characterization System as shown in Figure 3.11b. The radiation test box

was mounted using a custom built fixture in front of the pneumatic beam port shutter. The table was moved within 6" of the beam hole opening allowing for a precise alignment with the beam path. In order to decrease the signal resulting from unwanted radiation interaction with the other electronic components, a few steps were taken to provide shielding. First, a collimator was inserted into the beam port to bring the effective beam diameter down to 1.5". A lead disc approximately 6" thick with an opening ½" in diameter was placed directly in front of the sample, effectively blocking all electronics aside from the detector itself as shown in Figure 3.11b. This technique allowed for precise and repeatable testing.

The samples were irradiated by thermal neutron beam at powers ranging from 1 kW to 100 kW. A bias was applied to the samples and the shutter was opened to record the change in sample conductivity during irradiation. The shutter was then closed and this process was repeated for a total of 5 times to look at the prolonged effects of exposure. Afterwards, a cadmium foil shield was placed in the beam path in order to stop the thermal neutrons and the experiment was repeated. This allowed for measurement of the gamma only response. Subsequent to radiation testing, the samples were then electrically characterized to see if any degradation in device performance occurred.

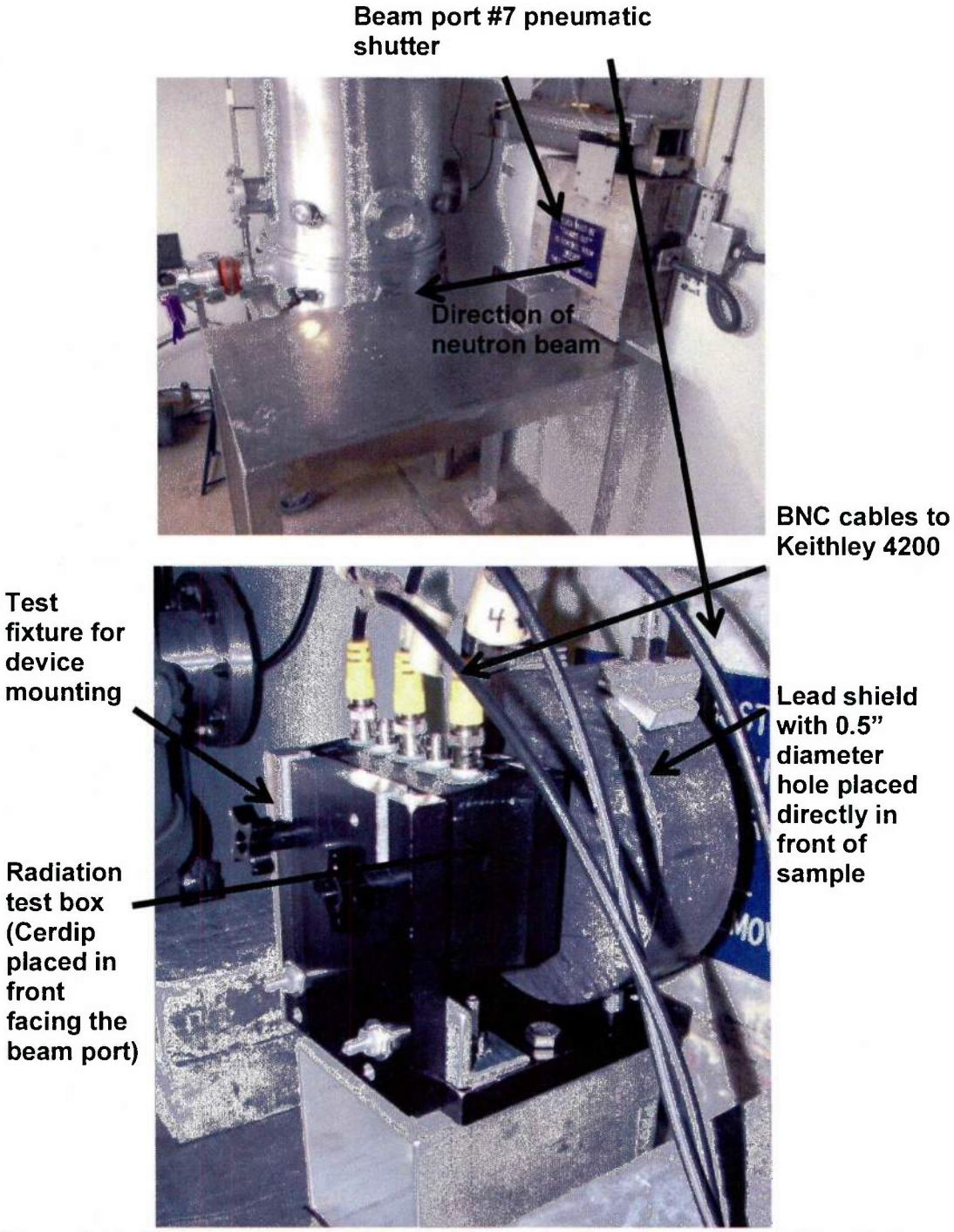

Figure 3.11. Digital images of (a) beam lab housing beam port #7 and (b) radiation detector fixture with lead shield and cable connections to electronics.

3.6. Design of experiments

This section discusses the design of experiments used for the deposition of Gd_2O_3 films. A thorough processing map was established to determine the effects of deposition conditions on the structure and properties of thick Gd_2O_3 films. Initially, films were deposited at ambient temperatures. Films deposited at ambient temperatures underwent cracking and delamination when the film thickness exceeded 4 μm or when subject to annealing temperatures of 200 °C, making device fabrication impossible. Figure 3.12a shows a FIB cross section of a 4 μm thick Gd_2O_3 film deposited at ambient temperature. As can be seen, the cracking originated at the film/substrate interface and extended throughout the film, resulting in widespread surface cracking displayed by the optical microscope image of the top surface of the film in Figure 3.12b

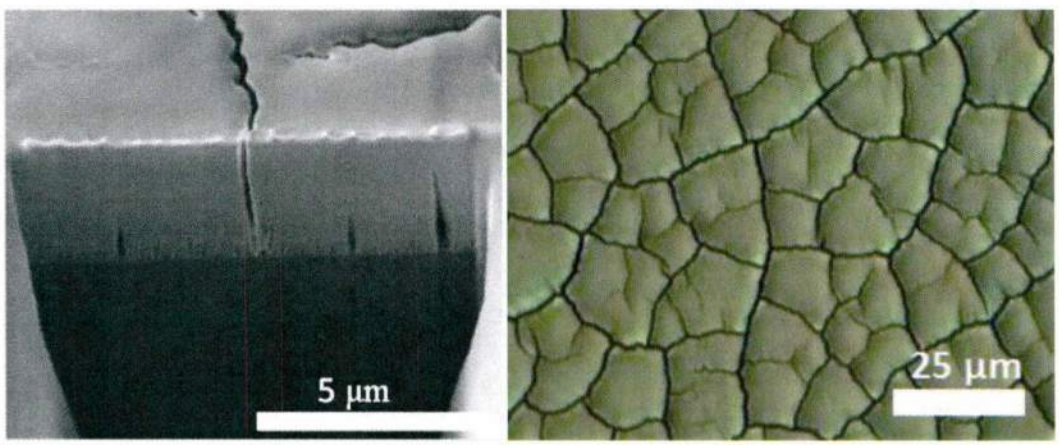

Figure 3.12. (a) SEM image of FIB cross section of thick Gd_2O_3 film deposited at room temperature showing the origin of cracks at the substrate/film interface and extending to the film surface and (b) optical microscopy image of top surface of same Gd_2O_3 film showing widespread surface cracking.

Cracking was observed on silicon, sapphire, quartz, and GaN substrates. Due to the poor structural stability of Gd_2O_3 films deposited at ambient temperatures, the

majority of the work presented in the thesis will focus on films deposited at substrate temperatures of 250 °C to 650 °C.

The effects of substrate temperature, oxygen gas flow, and film thickness were initially investigated systematically in four sets with the experimental details summarized in Table 3.1 Films 1A–D were deposited as a function of varying O_2 flow from 50 to 200 sccm at a deposition temperature of 650 °C. Films 2A–E were deposited as a function of deposition temperature from 250 to 650 °C under a gas flow of 200 sccm.

Table 3.1. Deposition parameters for Gd_2O_3 films deposited via reactive electron beam physical vapor deposition. Set 1 is deposited as a function of oxygen flow at a deposition temperature of 650 °C. Set 2 is deposited as a function of temperature under an oxygen flow of 200 sccm. Set 3 is deposited as a function of thickness at 250 °C and under 200 sccm O_2 flow. Set 4 is deposited as a function of oxygen flow at a deposition temperature of 250 °C.

Film #	Deposition Temperature (°C)	Oxygen flow (sccm)	Film Thickness (μm)	Deposition Rate (Å/s)
1A	650	**50**	2.05	9.75
1B	650	**100**	1.73	9.67
1C	650	**150**	2.03	8.26
1D	650	**200**	2.05	9.75
2A	**250**	200	1.26	6.01
2B	**350**	200	1.23	5.86
2C	**450**	200	2.44	11.60
2D	**550**	200	2.46	11.70
2E	**650**	200	2.05	9.75
3A	250	200	**0.58**	10.75
3B	250	200	**1.11**	8.42
3C	250	200	**2.10**	9.22
3D	250	200	**5.12**	9.93
3E	250	200	**11.01**	12.41
4A	250	**25**	1.36	11.34
4B	250	**50**	1.67	13.93
4C	250	**100**	1.29	10.76
4D	250	**150**	1.39	11.59
4E	250	**200**	0.76	6.34

Films 3A–E were deposited as a function of film thickness from approximately 500 nm to 11 μm at a deposition temperature of 250 °C and 200 sccm O_2 flow. Films 4A–E were deposited as a function of varying O_2 flow at a deposition temperature of 250 °C. In each set, one variable was varied while the rest were kept constant. While independent variables such as temperature and gas flow were easily controlled, slight fluctuations were observed in dependent variables such as deposition rate and pressure. All samples were found to be stable and did not show any signs of film cracking except for sample 3E deposited at 250 °C which had a measured thickness of 11.01 μm. In this work, films as thick as 23μm have been deposited at substrate temperatures of 650 °C without any observed cracking.

Table 3.2 shows the deposition parameters for set 5. These films were deposited as a function of temperature from 250 to 650 °C under a gas flow of 200 sccm using a direct evaporation method where Gd_2O_3 source material was used instead of Gd metal.

Table 3.2. Deposition parameters for set 5. These films were deposited as a function of temperature by direct deposition using Gd_2O_3 as the source material.

Film #	Deposition Temperature (°C)	Oxygen flow (sccm)	Film Thickness (μm)	Deposition Rate (Å/s)
5A	**250**	200	6.08	11.1
5B	**350**	200	5.20	9.6
5C	**450**	200	1.68	3.2
5D	**450**	200	3.67	6.8
5E	**550**	200	6.63	11.9
5F	**550**	200	4.27	7.9
5G	**650**	200	3.34	6.19

Due to the non-fully molten nature of the evaporated source material, the need to use a sweeping beam pattern, and the growth of dendritic structures in the crucible during deposition (as discussed in section 3.1.3), it was extremely difficult to control the

deposition rate and maintain film uniformity over the entire substrate. Films deposited by the direct method were found to have comparatively more defects than those deposited by the reactive method. As a result, the focus of this work will be primarily for films deposited by the reactive method using Gd metal source material.

Due to the requirements for the development of the microelectronic radiation detectors, Gd_2O_3 films with thicknesses of approximately 1 μm were deposited. The effects of temperature and oxygen flow on these films were studied. Table 3.3 displays the deposition parameters for sets 6 and 7 which were deposited as a function of deposition temperature under oxygen flows of 50 and 200 sccm, respectively.

Table 3.3. Deposition parameters for sets 6 and 7 deposited as a function of temperature by reactive EB-PVD with target thickness of 1 μm. Sets 6 and 7 were deposited under (a) 200 sccm and (b) 50 sccm O_2 flow.

Film #	Deposition Temperature (°C)	Oxygen flow (sccm)	Film Thickness (μm)	Deposition Rate (Å/s)
6A	250	200	1.07	7.53
6B	350	200	0.90	7.51
6C	450	200	0.85	6.79
6D	550	200	0.69	6.92
6E	650	200	0.87	8.19
7A	250	50	1.11	9.58
7B	350	50	1.08	15.22
7C	450	50	1.07	8.52
7D	550	50	1.10	11.55
7E	650	50	1.20	9.11

In order to investigate the growth mechanisms at the initial stages of film growth, very thin films less than 50 nm thick were deposited under a number of processing conditions. These films are referred to as films 8A-8E and the deposition parameters are listed in Table 3.4.

Table 3.4. Parameters for set 8 grown by reactive EB-PVD consisting of films less than 50 nm thick deposited under various conditions.

Film #	Deposition Temperature (°C)	Oxygen flow (sccm)	Film Thickness (nm)	Deposition Rate (Å/s)
8A	250	200	47	7.34
8B	250,	25	41	6.84
8C	250	50	-	-
8D	650	50	-	-
8E	650	200	20	3.34

The effects of film thickness on Gd_2O_3 films deposited at a substrate temperature of 250 °C were examined in set 3. The effects of film thickness for films deposited at elevated temperatures were further investigated with the deposition of set 9. Films in set 9 were deposited as a function of film thickness under oxygen flow rate of 200 sccm and deposition temperature of 650 °C.

Table 3.5. Deposition parameters for sets 9 deposited as a function of thickness by reactive EB-PVD at 650 °C under oxygen flow of 200 sccm.

Film #	Deposition Temperature (°C)	Oxygen flow (sccm)	Film Thickness (μm)	Deposition Rate (Å/s)
9A	650	200	0.38	10.4
9B	650	200	0.59	6.83
9C	650	200	1.02	8.23
9D	650	200	2.69	10.9
9E	650	200	5.72	11.5

As will be shown later, decreasing the deposition rate led to the growth of single phase cubic films. Set 10 consists of purely cubic phase films approximately 1 μm thick grown at deposition rates lower than 0.5 Å / s. These films were grown under oxygen flow rate of 50 sccm. Table 3.6 **lists** the deposition conditions for set 10.

Table 3.6. Deposition parameters for set 10. These films were deposited with very low deposition rates (<0.5 A / s) in order to deposit single phase cubic films.

Film #	Deposition Temperature (°C)	Oxygen flow (sccm)	Film Thickness (μm)	Deposition Rate (Å/s)
10A	650	50	0.91	0.44
10B	650	50	1.01	0.48

Deposition parameters for set 11 are shown in Table 3.7. In this set, the effect of ion bombardment on Gd_2O_3 films was examined. The films were grown under similar conditions to set 10 (650 °C, 50 sccm O_2, ~1μm), except with use of the ion source. The voltage was held float at approximately 500V while the IBS current was varied systematically from 0 – 800 mA.

Table 3.7. Deposition parameters for set 11. These films were deposited under low deposition rate (<0.5 A / s) as a function of IBS current. The IBS voltage was held float at approximately 500V and the current varied from 0 to 800 mA.

Film #	Deposition Temperature (°C)	Oxygen flow (sccm)	Film Thickness (μm)	Deposition Rate (Å/s)	IBS Current (mA)
11A	650	50	0.91	0.44	0
11B	650	50	0.70	0.34	200
11C	650	50	0.750	0.38	400
11D	650	50	0.99	0.46	800

There were several other sets of deposition trials, but this dissertation will focus on the deposition sets discussed within chapter 3.

3.7. Heat treatments

Heat treating films can change film phase and structural characteristics as well as improve film electrical properties. Select films were chosen for high temperature anneals in oxygen and nitrogen environments. Films deposited on Si(111) were annealed at

temperatures of 800 °C and 1000 °C for 1 and 3 hours in a Lindberg Blue M tube furnace. Films deposited on GaN could only be annealed for a maximum of 5 minutes at 875 °C in a rapid thermal annealing (RTA) furnace in order to avoid degradation of the ohmic contacts. For future work, it may be helpful to deposit the ohmic contacts after Gd_2O_3 film deposition.

Chapter 4

Results and Discussion: Process-phase relationships in Gd_2O_3 films

This chapter will cover the fundamental relationships between processing and the resulting crystallographic phase, structure, and orientation of Gd_2O_3 films deposited by reactive electron beam-physical vapor deposition (EB-PVD). Confocal Raman spectroscopy and a variety of x-ray diffraction (XRD) techniques were used for film characterization.

Theta-two-theta (θ-2θ) and grazing incidence x-ray diffraction (GIXRD) were used for phase identification and determination of preferred orientation. In addition to phase identification, Rietveld pattern refinement was used to quantitatively calculate phase volume and grain size. Grazing incidence depth profiling analysis was performed on select samples in order to reveal information about structure throughout the film thickness. These techniques are crucial to understanding the evolution of texture during the growth of Gd_2O_3 thick films.

A comprehensive study on the effects of processing parameters will be presented. First, the discussion will cover the effects of deposition temperature on the crystallographic phase and structure of the Gd_2O_3 films, focusing on film set 6 (function of temperature, 200 sccm O_2, ~1 μm). Next, the effect of oxygen flow on the phases of the film will be discussed for both set 1 (650 °C, function of oxygen flow, ~2 μm) and set 4 (250 °C, function of oxygen flow, 1 μm). X-ray diffraction of set 3 (250 °C, 200 sccm O_2, function of thickness) and set 9 (650 °C, 200 sccm O_2, function of thickness) will assist in examining the effect of film thickness on Gd_2O_3 film phase stability at deposition temperatures of 250 °C and 650 °C, respectively. Additionally, the effect of

underlying substrate type on the Gd_2O_3 film crystallographic structure will be discussed. Finally, select samples were subject to heat treatments in order to improve film electrical properties. The effects of these heat treatments on film phase stability and structure will also be presented.

4.1. Effect of deposition temperature on Gd_2O_3 phase stability

Table 4.1 lists the equilibrium peak positions in ° 2θ for high intensity planes of the cubic and monoclinic Gd_2O_3 phases. The listed peak positions for copper K_α radiation were determined from the International Center for Diffraction Data (ICDD) cards[75,76] #0042-1465 and #0043-1014 for the monoclinic and cubic phases, respectively.

Table 4.1. 2θ equilibrium peak positions for high intensity diffraction planes observed in Gd_2O_3 film growth and the corresponding phases for Cu K_α radiation according to ICDD cards #0042-1465 and #0043-1014 (λ= 1.54056 Å).

Cubic Phase		Monoclinic Phase	
Peak (° 2θ)	Phase/Plane	Peak (° 2θ)	Phase/Plane
20.1	C(211)	14.9	M(-201)
28.6	C(222)	28.2	M(111)
30.9	C(321)	30.1	M(-402)
33.1	C(400)	31.0	M(003)
35.2	C(411)	31.5	M(-310)
39.0	C(332)	32.4	M(-112)
47.5	C(440)	51.0	M(020)
52.1	C(611)	60.0	M(421)
56.4	C(440)	60.4	M(-422)
59.2	C(444)	60.9	M(115)

Figure 4.1 shows the θ-2θ XRD patterns for films 6A-E deposited as a function of temperature under 200 sccm O_2 flow at deposition rates greater than 5 Å/s. The monoclinic and cubic peaks are denoted on the patterns with the letters M and C,

respectively, followed by the corresponding Miller indices of the plane in parentheses. Due to the small thickness of these films, the diffraction pattern in Figure 4.1 is shown for Gd_2O_3 films deposited on quartz substrates to remove the overlap of the Si(111) contribution (28.4°) with that of the Gd_2O_3 C(222) peak (28.6°). This allows for quantitative phase volume, texture, and crystallite size analysis. At deposition rates greater than 5 Å /s, diffraction patterns for Gd_2O_3 films were found to be very similar on quartz and silicon substrates.

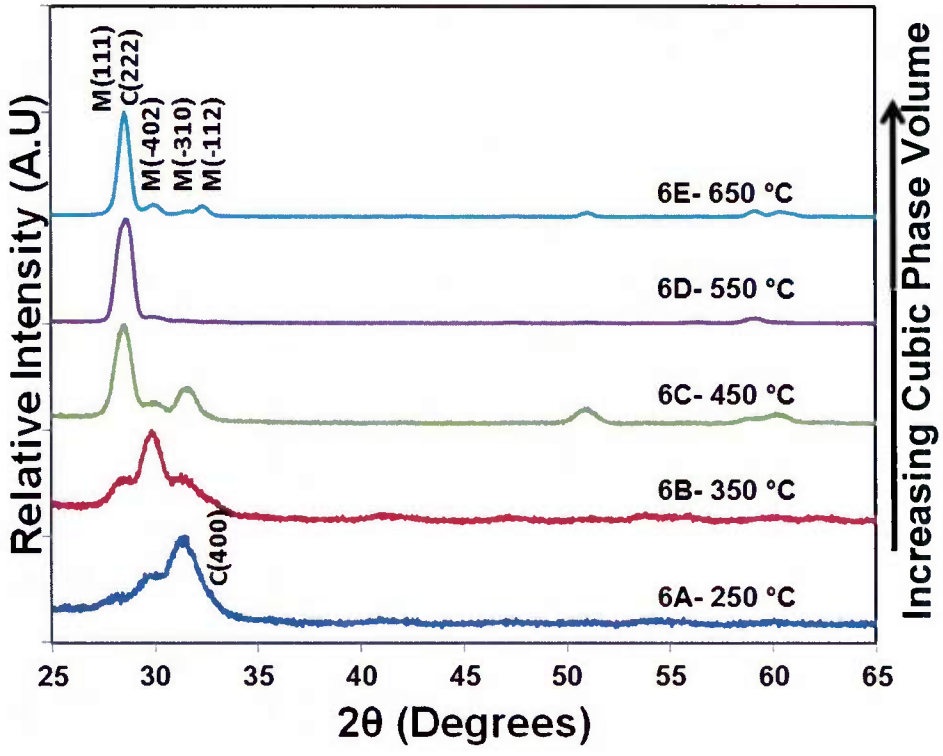

Figure 4.1. θ-2θ X-ray diffraction patterns of Gd_2O_3 films 6A (250 °C), 6B (350 °C), 6C (450 °C), 6D (550 °C), and 6E (650 °C) deposited on quartz as a function of temperature under 200 sccm O_2 flow.

As observed from Figure 4.1, Gd_2O_3 films 6A-6E are polycrystalline and of mixed cubic/monoclinic phase. Film 6A (250 °C, 200 sccm), is primarily monoclinic

with preferred M(-310) orientation, though diffraction from the M(-402) peak is also observed. A low intensity peak is centered at approximately 28.0-28.6° and suggests diffraction from both the M(111) and C(222) planes, resulting in some minor cubic phase contribution. It is important to note that film 6A shows broad diffraction peaks, indicating poor crystallinity as a result of low adatom mobility and limited diffusion at the low deposition temperature of 250 °C. As the deposition temperature is increased to 350 °C (film 6B), the preferred orientation changes to the M(-402) orientation, with additional diffraction observed from the C(222), M(111), M(-112) and M(-310) peaks. The diffraction pattern for film 6B is also characterized by broad peaks indicating poor crystallinity.

The formation of monoclinic phase at low temperatures is initially surprising given the thermodynamic stability of the cubic phase. However, EB-PVD is a non-equilibrium process, and formation of metastable phases may be observed. One potential explanation for the formation of the metastable monoclinic phase in the Gd_2O_3 films is given by Ostwald's empirical "rule of stages",[77] in which intermediate states characterized by metastable polymorphs occur prior to the formation of the stable thermodynamic polymorph. In this case, the metastable monoclinic polymorph is formed in the Gd_2O_3 films, and due to the low adatom mobility, transition to the thermodynamically stable cubic phase cannot occur. Since monoclinic structures possess less symmetry than the cubic phase, the Gd_2O_3 monoclinic phase may be formed more easily and "quenched in" due to the low adatom mobility.

At a deposition temperature of 450 °C (film 6C), a transition to a predominantly cubic phase film is observed with strong out of plane (in the growth direction) C(222)

texturing. A clear shift from a peak position of the M(111) peak at 28.0° to the C(222) peak at 28.6° is observed. Some contribution from the M(-402), M(-310), and M(-112) peaks are present, indicating some monoclinic phase remaining. Similar diffraction patterns are observed for films 6D (550 °C) and 6E (650 °C). The observed trend of increasing cubic phase volume with increasing temperature is in contrast to studies investigating growth of thin polycrystalline Gd_2O_3 film by other deposition methods. Singh et al. deposited 100-300 nm thick polycrystalline Gd_2O_3 films by MOCVD, which resulted in fully cubic highly textured (111) films at a substrate temperature of 525 °C.[49] Upon raising the substrate temperature to 750 °C, monoclinic phase formed. Similar results have been shown for magnetron sputtered Gd_2O_3 films, showing an increase in polycrystalline monoclinic phase volume when the deposition temperature was raised from 470 to 550 °C.[8] The differences between the results shown in this work and those in the literature suggest that deposition method and processing have a significant effect on Gd_2O_3 phase stability.

The presence of the cubic phase at high deposition temperatures can be explained by the large adatom surface mobility which increases the diffusion length required to form the thermodynamically stable cubic phase. It is also important to note that thin film growth for a Zone 2 columnar microstructure (expected at deposition temperatures of 650 °C) is dominated by surface diffusion rather than bulk diffusion. The result is a driving force to minimize the surface energy of the film. It has been shown in bixbyite (Ia3) structured Y_2O_3 films that the (111) planes possess the lowest surface energy.[78] Since the Gd_2O_3 cubic phase shares the same bixbyte (Ia3) crystal structure, this explains the strong

texturing of the C(222) planes observed in the high temperature deposited Gd_2O_3 films 6C-6E.

4.1.1. Quantitative phase volume and crystallite size analysis

In order to gain a better understanding of the phase relationships, quantitative phase volume analysis was employed. No standard method for calculating phase volume for Gd_2O_3 films currently exists. Therefore, three methods were used and compared: 1) Calculation of the ratios of the integrated intensities of the cubic and monoclinic peaks from the θ-2θ XRD patterns, 2) Rietveld refinement of the θ-2θ XRD patterns, and 3) Calculation of the ratios of the peak intensities corresponding to the Raman modes of the cubic and monoclinic phases.

Quantitative phase analysis by XRD is a challenging and often disputed task, especially for textured thin film materials.[79] The first method employed to calculate phase volume relies on the integrated intensities of the main cubic and monoclinic peaks from the θ-2θ XRD data. The patterns were fitted using a Pseudo-Voigt function and the chosen peaks for the analysis were the peaks with the largest integrated intensity as observed in the XRD patterns. The monoclinic phase volume (%M) was calculated using the equation 4.1:

(4.1)

$$\%\, M = \frac{I_{M(111)} + I_{M(-402)} + I_{M(-310)} + I_{M(112)} + I_{M(020)} + I_{M(-422)}}{I_{M(111)} + I_{M(-402)} + I_{M(-310)} + I_{M(112)} + I_{M(020)} + I_{M(-422)} + I_{C(222)} + I_{C(444)}}$$

where I is the integrated intensity of the corresponding diffraction peaks noted in the subscript. The cubic phase volume was calculated as %C = 100 - %M. The calculated phase volumes for films 6A-6E by the integrated intensity, Rietveld, and Raman methods are listed in Table 4.2. As can be seen, substantial increase in the cubic phase volume is observed with increasing deposition temperature for the integrated intensity method. It is important to note that this method does not take into account the effects of preferred orientation or the difference in the intensity of diffraction between the Gd_2O_3 cubic and monoclinic phases, and therefore, should be regarded as semi-quantitative. It is typically expected that a cubic phase will diffract 2-3x stronger than a monoclinic phase due to the increased symmetry of the crystal structure.[80] In order to achieve more accurate results for the calculation of phase volume, Rietveld refinement was utilized.

Table 4.2. Phase volume and crystallite size for films 6A-6E. Phase volume was calculated by the integrated intensity (I-I) method, Rietveld refinement, and Raman spectroscopy. M denotes the monoclinic phase and C denotes the cubic phase. Crystallite size was calculated using Scherrer's equation.

Film	Deposition Temperature (°C)	O_2 flow (sccm)	Phase Volume (%) by I-I Method		Phase Volume (%) by Rietveld		Phase Volume (%) by Raman		Cubic Crystallite Size (nm)	Monoclinic Crystallite Size (nm)
			M	C	M	C	M	C		
6A	250	200	95	5	100	0	100	0	-	12
6B	350	200	83	17	94	6	71	29	19	13
6C	450	200	37	63	34	66	20	80	24	15
6D	550	200	5	95	18	82	10	90	25	14
6E	650	200	12	88	31	69	20	80	45	19

Rietveld refinement was performed using the Whole Pattern Fitting function of JADE MDI software for quantitative determination of phase volume. Since Rietveld refinement is typically meant for randomly oriented samples, a number of considerations

had to be taken into account when performing the refinement for textured thin films. The first and most challenging aspect of refinement of the Gd_2O_3 films was the effect of preferred orientation which causes deviations from the theoretical intensity ratios of the XRD peaks. In the case of the Gd_2O_3 films, strong preferred orientation was often observed from numerous monoclinic and cubic phase reflections. This was accounted for by using either the March-Dollase model[81] or the spherical harmonics model.[82]

Another critical component in Rietveld phase quantification is proper selection of structure data. For the refinement, either crystal structure data or powder diffraction files containing the reference intensity ratio (RIR) are needed. RIR is an instrument independent constant for use in quantitative phase analysis which is measured as the intensity ratio of the diffraction pattern from the selected material relative to the intensity of the diffraction pattern from a corundum standard. For Gd_2O_3, powder diffraction files taken from the ICDD database possess RIR values of 11-14 for cubic Gd_2O_3 and 0.9-3.5 for monoclinic Gd_2O_3. Differences in RIR value can yield significant differences in phase volume. For instance, in calcium aluminum chromium oxide hydrates, a change in RIR from 1.0 to 3.0 was found to affect phase volume calculations by a factor of 3.[83] In order to determine which values were most likely to yield accurate results, a θ-2θ diffraction pattern of single phase cubic powder was taken. The cubic Gd_2O_3 powder was then pressed and heated to 1400 °C and left at temperature to fully transform the cubic Gd_2O_3 to the monoclinic phase. The θ-2θ diffraction patterns for the pure cubic and monoclinic phases are shown in Figure 4.2. The difference in integrated intensity ratio between the cubic and monoclinic Gd_2O_3 phases is approximately 3.5. Based on

this, powder diffraction files (#0042-1465 and #0043-1014) resulting in the closest matching RIR ratio were chosen for Rietveld quantitative analysis listed in Table 4.2.

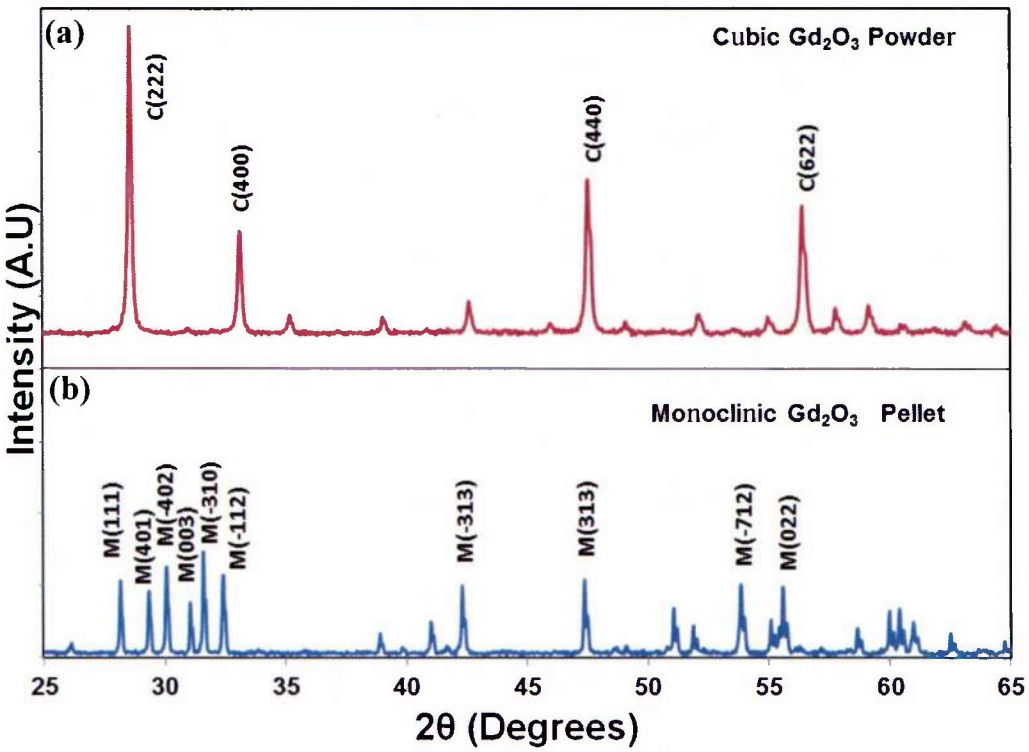

Figure 4.2. θ-2θ X-ray diffraction patterns of (a) fully cubic Gd_2O_3 powder and (b) fully monoclinic Gd_2O_3 pellet after sintering at 1400 °C used to estimate the difference in diffracted intensity between the two phases.

Table 4.2 shows the cubic and monoclinic phase volumes for films 6A-6E quantitatively calculated by the Rietveld refinement. Similar to values computed from using the integrated intensity method, a general trend of increasing cubic phase volume with increasing deposition temperature is observed, with film 6D (550 °C) possessing the greatest cubic phase volume. The greater phase volume in film 6D than film 6E (650 °C) can be explained by the smaller thickness (0.69 μm) of film 6D. The effect of film thickness on phase volume will be discussed in greater detail in section 4.4. Due to the

low RIR of the monoclinic phase, it is apparent that there is still monoclinic phase volume in the high temperature deposited films (6C-6E) even though the peak intensities are relatively small. This suggests that the integrated intensity method presented earlier likely overestimated the cubic phase volume based on the assumption of equal RIR for both phases. In order to verify this conclusion, another characterization technique (Raman) which was not based on x-ray diffraction was needed to correlate the phase volume calculations between the two methods.

Raman spectroscopy is another useful tool for phase identification that can be used to compliment XRD analysis, especially in cases of highly textured thin films. Raman vibrational modes are not directly correlated to the x-ray diffraction peaks and therefore, provide a means to verify the accuracy of the phase volume calculation independent of preferred orientation effects observed in XRD. Table 4.3 lists the Raman band positions and corresponding relative intensities for a cubic Gd_2O_3 powder and single crystal monoclinic Gd_2O_3 taken from the literature.[58]

Raman analysis was performed on set 6 in order to assess the validity of the phase volume calculation by the Rietveld method. Figure 4.3 shows the measured Raman spectra of Gd_2O_3 films 6A-6E on quartz substrates. The broad Raman peaks and low intensity of film 6A (250 °C) confirms the poor crystallinity in the film. As a result, it is difficult to distinguish the peaks due to the poor signal to noise ratio for this film. Film 6B (350 °C) shows predominantly monoclinic bands at 415 cm^{-1} and 389 cm^{-1}, but also displays some cubic contribution from the band at 361 cm^{-1}. For films 6C (450 °C), 6D (550 °C) and 6E (650 °C), a large intensity value is observed from the cubic band located at 361 cm^{-1} suggesting a predominantly cubic film structure. However, intensity of

additional monoclinic bands remains high, suggesting significant presence of the monoclinic phase remains.

Table 4.3. Raman band positions and corresponding relative intensity of cubic Gd_2O_3 powder and single crystal monoclinic Gd_2O_3.

Monoclinic Gd_2O_3 [84]		Cubic Gd_2O_3 [58]	
Band Position (cm^{-1})	Intensity	Band Position (cm^{-1})	Intensity
71	Strong	81	Medium
84	Medium	85	Very Weak
99	Very Strong	95	Strong
108	Medium	108	Very Weak
114	Weak	115	Weak
133	Very Weak	135	Weak
151	Very Weak	145	Weak
175	Medium	198	Weak
219	Medium	235	Weak
233	Weak	299	Very Weak
257	Weak	316	Medium
268	Weak	337	Very Weak
298	Medium	361	Very Strong
385	Strong	401	Weak
415	Medium	413	Very Weak
428	Medium	447	Medium
441	Medium	479	Very Weak
499	Weak	568	Medium

A quantitative Raman phase analysis procedure for Gd_2O_3 films has not been performed in the literature. However, calculation of monoclinic concentration in mixed tetragonal-monoclinic zirconia materials has been performed by a number of authors on the premise that the Raman bands for the two phases are proportional to their concentrations.[85] We employ a similar method to calculate the phase volume of monoclinic and cubic Gd_2O_3 in the films. The peaks from the Raman spectra in Figure 4.3 were fitted using a Gaussian profile and the integrated intensity was calculated for the

two strongest monoclinic and cubic bands located at 361 cm^{-1} and 418 cm^{-1}, respectively. The phase volume was calculated quantitatively using the equation 4.2:

$$\% M = \frac{I_{M(418)}}{I_{M(418)} + I_{C(361)}} \quad (4.2)$$

where $I_{M(418)}$ and $I_{c(361)}$ correspond to the integrated intensities of the monoclinic band located at 418 cm^{-1} and the cubic band located at 361 cm^{-1}, respectively. Though exact agreement in the numerical value is not present, these data suggest good correlation in the trends between the Raman and XRD Rietveld data. As a result, the rest of the quantitative phase analysis that will be presented in this chapter was calculated via the Rietveld refinement technique.

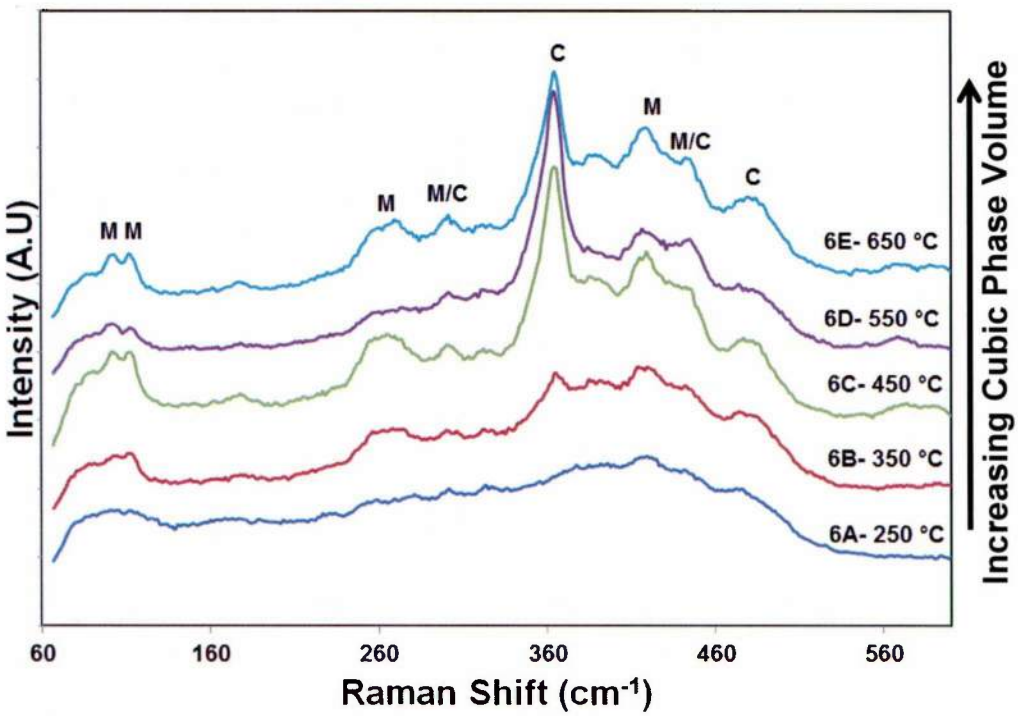

Figure 4.3. Raman spectra of Gd_2O_3 films 6A (250 °C), 6B (350 °C), 6C (450 °C), 6D (550 °C), and 6E (650 °C) deposited on quartz as a function of temperature under 200 sccm O_2 flow. The cubic and monoclinic bands used for quantitative phase volume analysis are marked C and M, respectively.

Another useful physical quantity that can be extracted from XRD analysis is crystallite size. Scherrer's formula was used to determine the XRD crystallite size using equation 4.3 for films 6A-6E shown in Table 4.2:

$$D = \frac{K\lambda}{B\cos\theta} \tag{4.3}$$

where D is the grain size, K is the shape factor, λ is the x-ray wavelength, B is the difference in the instrumental broadening and crystallite size broadening, and θ is the Bragg angle. K was taken to be 0.9 and λ to be 1.54056Å for Cu radiation. The instrument broadening contribution was obtained from a diffraction pattern of a high purity polycrystalline silicon standard that was subtracted from the full width half max (FWHM) of the analyzed peaks. The calculated crystallite sizes for films 6A-6E are listed in Table 4.2, showing a significant increase in crystallite size from 19 nm to 45 nm for the cubic phase with increasing deposition temperature from 250 to 650 °C. The grain size of the monoclinic phase increased slightly from 12 to 19 nm over the same temperature range. These results are explained by the higher adatom mobility and diffusion present at high temperatures which allows for increased grain growth, consistent with the structure zone model. It also highlights the increased growth of the cubic phase with increased deposition temperature.

4.2. Effect of oxygen flow on Gd_2O_3 phase stability

Figure 4.4 shows the θ–2θ XRD patterns of Gd_2O_3 films 4A-4E deposited as a function of O_2 flow rate from 25 - 200 sccm at a substrate temperature of 250 °C under growth rates greater than 5 Å / s. Films 4A-4D (25 - 150 sccm) exhibit a predominantly monoclinic crystal structure with M(-402) preferred orientation. As the oxygen flow

increased from 25-150 sccm, the intensity of the (M-402) peak relative to the M(310) decreased. At an oxygen flow of 150 sccm, a shift in the peak position from 28.0° (4D) to 28.5° (4E) indicated increased reflection from the C(222) plane rather than the M(111) plane, suggesting increased cubic phase volume within the film.

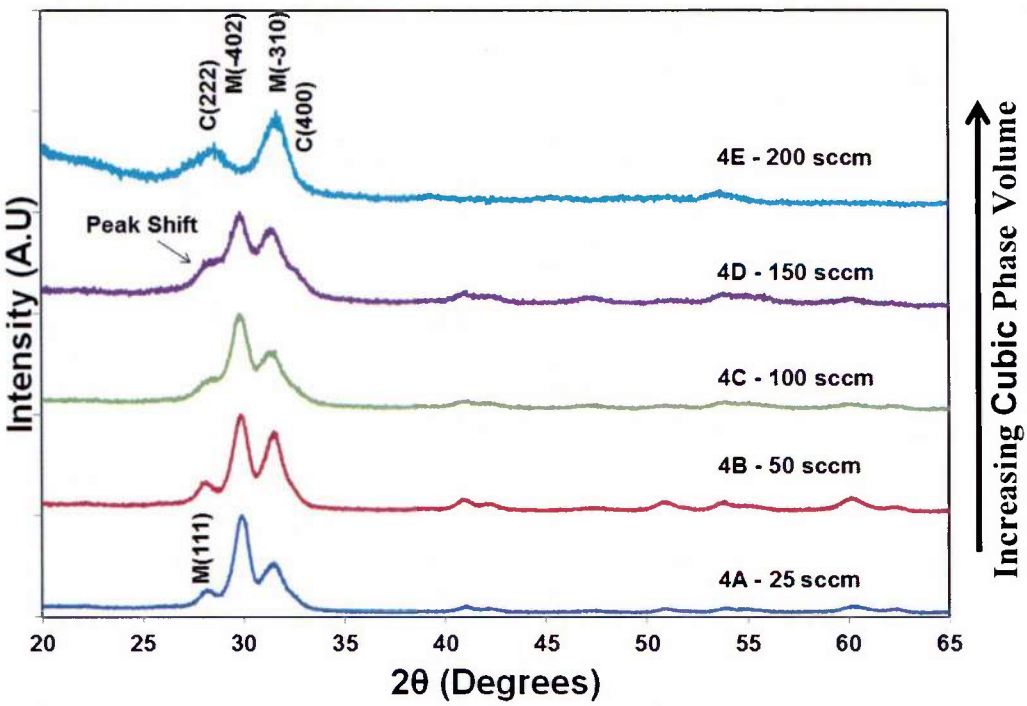

Figure 4.4. θ-2θ X-ray diffraction patterns of Gd_2O_3 films 4A (25 sccm), 4B (50 sccm), 4C (100 sccm), 4D (150 sccm), and 4E (200 sccm) deposited on quartz as a function of oxygen flow at deposition temperature of 250 °C.

Similar results regarding higher concentration of cubic phase volume at greater oxygen partial pressures have been reported for very thin (~20 nm) polycrystalline Gd_2O_3 films.[51] In Y_2O_3 cubic bixbyte structured films, a similar effect has been observed and was attributed to extended defect nucleation as a result of oxygen vacancy aggregates. When one oxygen plane is removed from a pristine bixbyte structure, the resulting cation and anion plane stacking sequence is not allowed from a crystallographic standpoint.

Therefore, planes relax by a small shear which leads to the formation of the monoclinic phase.[86] If this mechanism also occurs in the deposition of Gd_2O_3 films, then, as the oxygen flow is decreased, an increased number of oxygen vacancies are present in the film, resulting in increased formation of the monoclinic phase. This is confirmed by the quantitative phase analysis results presented in Table 4.4.

Table 4.4. Phase volume and crystallite size of Gd_2O_3 films 4A (25 sccm), 4B (50 sccm), 4C (100 sccm), 4D (150 sccm), and 4E (200 sccm) deposited on quartz as a function of oxygen flow at a deposition temperature of 250 °C.

Film	Deposition Temperature (°C)	Oxygen Flow (sccm)	Cubic Phase Volume (%)	Monoclinic Phase Volume (%)	Cubic Crystallite Size (nm)	Monoclinic Crystallite Size (nm)
4A	250	25	0	100	-	20
4B	250	50	0	100	-	19
4C	250	100	2	98	-	18
4D	250	150	20	80	11	14
4E	250	200	80	20	18	-

As observed by the increase in the FWHM of the diffraction peaks in Figure 4.4, the film crystallinity increases slightly with decreasing oxygen flow. One potential reason for this is that excess oxygen incorporation into the films deposited at high oxygen flux results in disruption of the crystal lattice and increased voiding and porosity. Another possible explanation is that the excess oxygen in the chamber during deposition acts to scatter the adsorbing Gd atoms which cause a decrease in adatom surface mobility. This results in poor surface coverage of the adsorbing atoms, resulting in porosity. Additionally, when there is excess oxygen in the chamber, it is more likely that the evaporated Gd atoms will react with the oxygen atoms before reaching the surface. A compound of Gd_2O_3 will have significantly decreased surface mobility as compared to a

lone Gd atom. Indeed, it will be shown in Chapter 6 that films deposited at 250 °C are denser when deposited under lower oxygen flow and that films deposited under higher (200 sccm) O_2 flow possessed porous regions. Quantitative crystallite size calculations are shown in Table 4.4. Increasing oxygen flow resulted in decreasing crystallite size for the monoclinic phase and increased crystallite size for the cubic phase. This may be due to preferential growth of cubic crystallites over monoclinic crystallites due to the greater cubic phase volume.

Figure 4.5 shows the θ–2θ XRD patterns for Gd_2O_3 films 1A-1D deposited as a function of O_2 flow from 50 to 200 sccm at a deposition temperature of 650 °C. Note that these films are all approximately 2 μm thick and showed mixed cubic/monoclinic character. Film 1A (650 °C, 50 sccm O_2, 2.05 μm) is predominantly monoclinic with strong contribution from the C(222) and M(− 402) reflections and minor contributions of the M(-112), M(-422), and M(-310) reflections. According to the quantitative Rietveld analysis, this film possessed 22% cubic phase volume as shown in Table 4.5. For film 1B (650 °C, 100 sccm O_2, 1.73 μm), the intensity of the M(− 402), M(− 112), and M(− 422) peaks decrease, resulting in a predominantly cubic structure (90%) with strong C(222) orientation. The diffraction pattern for film 1C (650 °C, 150 sccm O_2, 2.03 μm) shows the emergence of a strong M(020) orientation. As the oxygen flow is increased to 200 sccm (film 1D), an increase in the cubic phase volume (85%) is observed due to increased intensity from the C(222) peak as well as the emergence of low intensity peaks at 47.5° and 56.4° corresponding to the C(440) and C(622) planes, respectively.

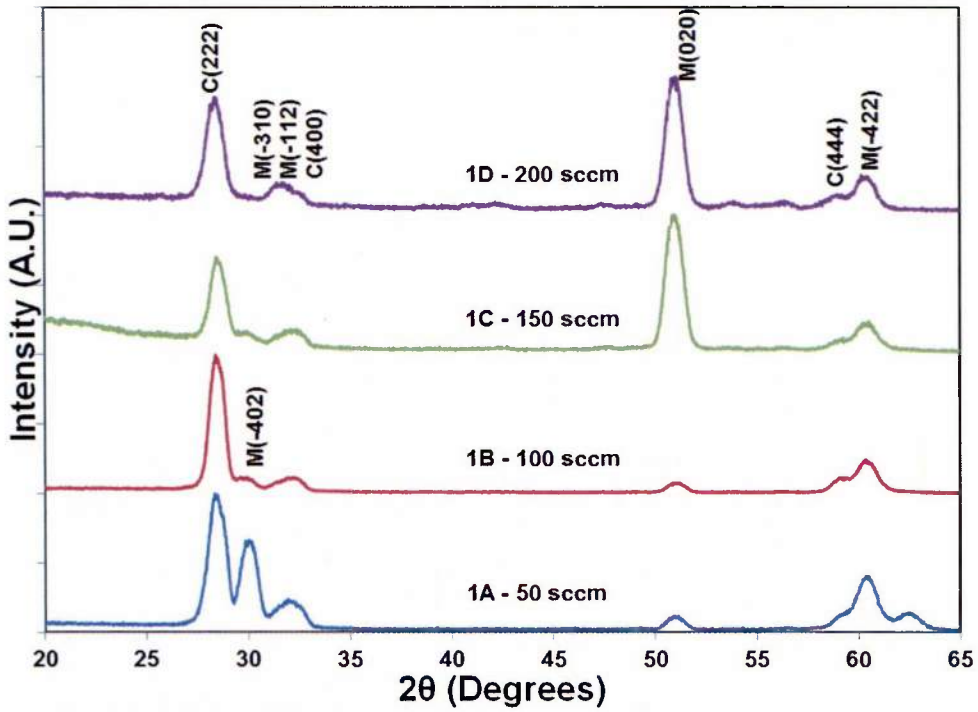

Figure 4.5. θ-2θ X-ray diffraction patterns of Gd_2O_3 films 1A (50 sccm O_2), 1B (100 sccm O_2), 1C (150 sccm O_2), and 1D (200 sccm O_2) deposited on quartz as a function of oxygen flow at a deposition temperature of 650 °C.

The effects of preferred orientation in films 1A-1D can be explained on the following basis. Due to the low oxygen flow present in the deposition chamber for films 1A (650 °C, 50 sccm O_2) and 1B (650 °C, 100 sccm O_2), the atoms were able to diffuse farther and minimize the surface energy of the film. As previously discussed, the C(222) plane has been shown to be the low surface energy plane of the bixbyte Ia3 crystal structure. Unfortunately, the authors are not aware of any studies that have modeled or calculated the surface energies for any materials possessing the C2/m structure. However, the M(-402) plane has been identified as the cleavage plane in single crystal C2/m monoclinic Gd_2O_3.[84] Although not a rule, the cleavage plane for a given crystal structure is typically the lowest surface energy plane. Based on this information and the

results presented in this work, we propose that the M(-402) plane is likely the low surface energy plane in the monoclinic structure. This cannot be verified until the elastic constants of the monoclinic (C2/m) Gd_2O_3 phase are determined. When the oxygen flow was increased to 150 and 200 sccm, increased scattering in the vacuum chamber resulted in decreased adatom mobility. Therefore, the atom diffusion length was not large enough to minimize the surface energy causing the film crystallographic orientation to change to M(020), which is likely a result of strain energy minimization. This will be discussed further in section 4.4, where the effect of film thickness more clearly illustrates the competition between surface energy and strain energy and its effects on film texture and phase.

The crystallite size was calculated for both the cubic and monoclinic phases for films 1A-1D as shown in Table 4.5. Change in oxygen flow resulted in a change in cubic (19 – 27 nm) and monoclinic (15- 29 nm) crystallite size but no clear trend was observed.

It is important to note the difference in the diffraction patterns of Gd_2O_3 films 1D (650 °C, 200 sccm, 2.05 μm, Figure 4.5) and 6E (650 °C, 200 sccm, 0.87 μm, Figure 4.1). Both films were deposited at 650 °C and under 200 sccm O_2 flow at a similar deposition rate, but with different film thicknesses. However, the diffraction patterns are significantly different, with film 1D possessing a higher monoclinic phase content and significant texturing of the M(020) reflection. This suggests that the difference in film thickness between the two films has a significant effect on film phase volume. The effects of film thickness will be discussed in greater detail in sections 4.3 and 4.4.

Table 4.5. Phase volume and crystallite size of Gd_2O_3 films 1A (50 sccm), 1B (100 sccm), 1C (150 sccm), and 1D (200 sccm) deposited on quartz as a function of oxygen flow at deposition temperature of 650 °C.

Film	Deposition Temperature (°C)	Oxygen Flow (sccm)	Cubic Phase Volume (%)	Monoclinic Phase Volume (%)	Cubic Crystallite Size (nm)	Monoclinic Crystallite Size (nm)
1A	650	50	22	78	19	23
1B	650	100	90	10	24	29
1C	650	150	65	35	27	16
1D	650	200	85	15	26	15

4.3. GIXRD depth profiling indicating phase and texture evolution in Gd_2O_3 films

All films discussed up to this point have been either mixed phase (cubic and monoclinic) or fully monoclinic according to the θ-2θ diffraction pattern and associated quantitative analysis. However, the data suggests that the monoclinic and cubic phases may not be distributed evenly throughout the film thickness. In GIXRD, the incident angle is fixed at a constant value throughout the scan. By performing multiple scans with various incident angles, it is possible to vary the x-ray penetration depth into the sample. This allows for depth profiling of film phase and texture.

Figure 4.6 shows the GIXRD patterns taken at various incident angles between 1 and 15 ° for film 6E (650 °C, 200 sccm, 0.87 μm). At high incidence angles (10 and 15°), the patterns are similar to the θ-2θ pattern (Figure 4.1) because the depth of penetration into the film is large. However, a marked difference is observed in the diffraction patterns for incidence angles of 5° and below. A better understanding can be gained from looking at the inset in Figure 4.6. At high incidence angles of 10 and 15°, there is strong diffraction from the C(222) peak, indicating large cubic phase volume. However, at incidence angle of 5°, diffraction is observed from both the C(222) peak at

28.6° 2θ and the M(111) peak at 28.0° 2θ with a large decrease in intensity of the C(222) peak.

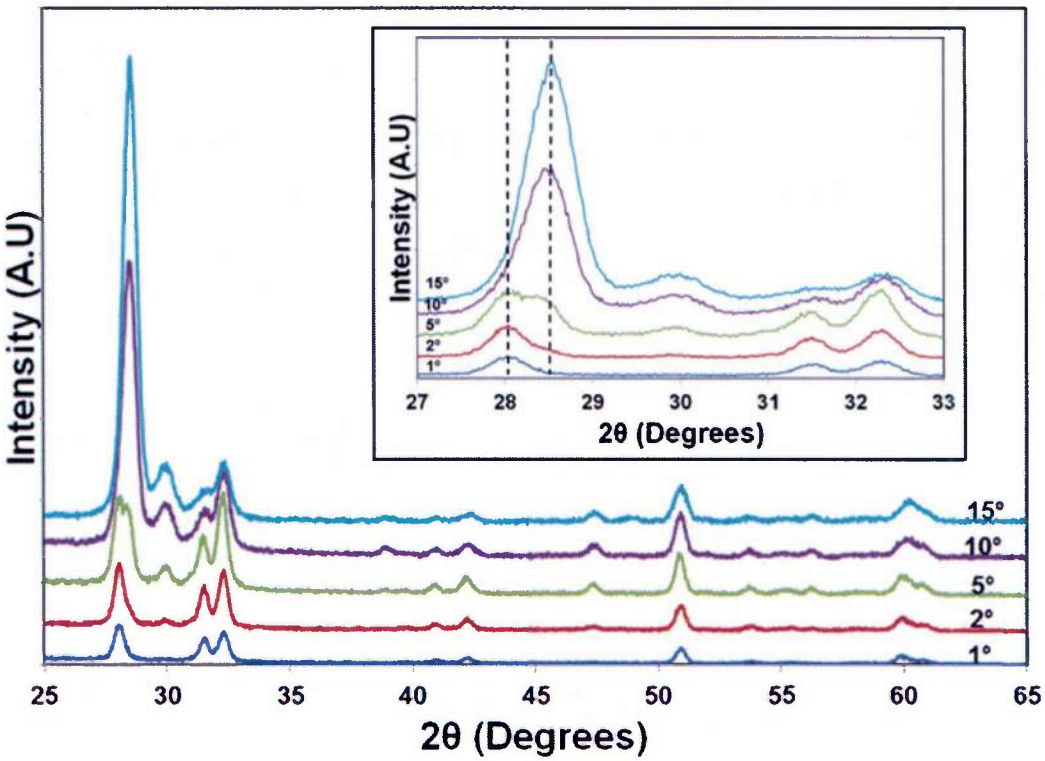

Figure 4.6. Grazing incidence diffraction patterns taken at incident angles of 1, 2, 5, 10, and 15 ° for film 6E (650 °C, 200 sccm O_2, 0.87 μm) deposited on quartz. The inset shows the magnified M(111) and C(222) peaks located at 28.0 and 28.6 °, respectively.

At incidence angles of 1 and 2° which results in very shallow depth of x-ray penetration, diffraction is only observed from the M(111) peak. This disappearance of the C(222) peak at these low incidence angles suggests that there is no cubic phase present in this surface region and that increased monoclinic phase volume formed as the film grew thicker. Additionally, it is important to note that the M(-402) reflection is observed only at large incidence angles (10 and 15°). This further supports the claim that

the M(-402) plane is the low surface energy plane of the monoclinic phase which is present at the initial stages of growth. However, as the film grows thicker, other orientations become more favorable due to strain energy considerations. From this data, it is clear that film thickness plays a role in the texture evolution and phase stability of Gd_2O_3 films deposited by reactive EB-PVD.

4.4. Effect of film thickness on phase of Gd_2O_3 films

In section 4.3, we showed that x-ray depth penetration plays a significant role in the observed phase volume of Gd_2O_3 films as measured by XRD. Therefore, the discussion in this section will focus on deposition sets 3 (250 °C, 200 sccm, function of thickness) and 9 (650 °C, 200 sccm, function of thickness) in order to elucidate the effects of thickness on Gd_2O_3 film phase stability. Figure 4.7 shows the θ-2θ XRD patterns for films 3A-3E deposited at 250 °C under 200 sccm O_2 flow as a function of film thickness from 580 nm to 11.01 μm. Film 3A (580 nm thick) appears to be a mixed cubic and monoclinic phase film. The location of the peak around 28° is broad, suggesting contributions from both the M(111) and C(222) reflections are present. Additionally, reflection from the M(-112) and C(400) convoluted peaks are observed in the diffraction pattern. As the film thickness increases to 1.11 μm (film 1B), the peak position shifted to 28.0° corresponding to the M(111) reflection. No reflections from the cubic phase were observed in this pattern and only monoclinic peaks were observed with the M(-310) peak possessing the largest intensity. As the film thickness increases further (films 3C-3E) up to 11 μm, only monoclinic phase growth is observed and the intensity of the M(-402) reflection increases relative to the other peaks, suggesting slight changes

in preferred orientation. Based on the grain size calculation from the FWHM of the peaks, the crystallite size remains constant at a value of approximately 12 nm as shown in Table 4.6, due to limited grain growth as a result of the low adatom mobility.

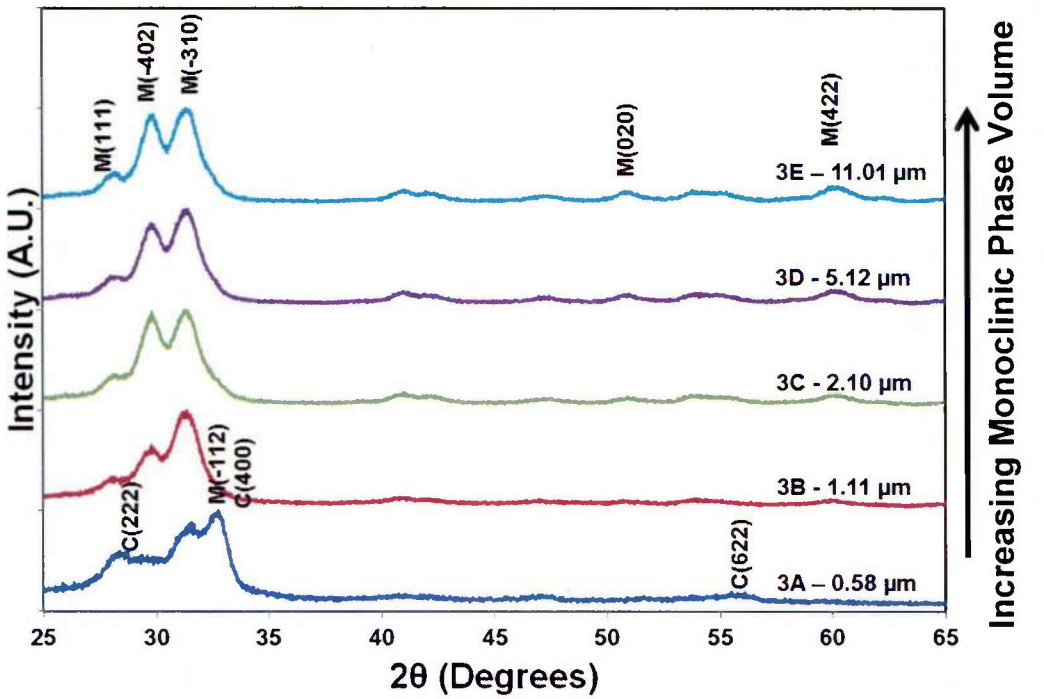

Figure 4.7. θ-2θ X-ray diffraction patterns of Gd_2O_3 films 3A (0.58 μm), 3B (1.11 μm), 3C (2.10 μm), 3D (5.12 μm), and 3E (11.01 μm) deposited on quartz as a function of film thickness at deposition temperature of 250 °C and oxygen flow rate of 200 sccm.

This data suggests that that cubic phase may be present in the initial stages of film growth and monoclinic phase may form as the film thickness increases. Indeed, it will be shown in section 6.1.4 through selected area diffraction (SAD) of a TEM cross sectional sample taken at different points along the film thickness that monoclinic phase gradually forms as the film thickness increases. The reasons for this phase transition are related to strain energy and residual stress state of the film and will be discussed in greater detail in

sections 5.1-5.4. The phase transition from monoclinic to cubic phase with increasing thickness is observed for films deposited at a low deposition temperature of 250 °C. In order to determine if a similar trend occurred at high substrate temperatures, films were deposited as a function of thickness at a deposition temperature of 650 °C (Set 9).

Table 4.6. Phase volume and crystallite size of Gd_2O_3 films 3A (0.58 μm), 3B (1.11 μm), 3C (2.10 μm), 3D (5.12 μm), and 3E (11.01 μm) deposited on quartz as a function of film thickness at deposition temperature of 250 °C and oxygen flow rate of 200 sccm.

Film	Deposition Temperature (°C)	Oxygen Flow (sccm)	Film Thickness (μm)	Cubic Phase Volume (%)	Monoclinic Phase Volume (%)	Cubic Crystallite Size (nm)	Monoclinic Crystallite Size (nm)
3A	250	200	0.58	93	7	12	13
3B	250	200	1.11	0	100	-	13
3C	250	200	2.10	0	100	-	13
3D	250	200	5.12	0	100	-	12
3E	250	200	11.02	0	100	-	12

Figure 4.8 shows the θ-2θ diffraction patterns of Gd_2O_3 films 9A-9E deposited at 650 °C as a function of thickness under 200 sccm O_2 flow and at deposition rates greater than 5 Å / s on quartz substrates. For film 9A (650 °C, 200 sccm O_2, 380 nm), strong preferred orientation of the C(222) plane is observed. Within an intermediate thickness range for films 9B (650 °C, 200 sccm O_2, 580 nm) and 9C (650 °C, 200 sccm O_2, 1.02 μm), increasing the thickness leads to increased intensity of the M(-402) reflection at the expense of the C(222) reflection, and a predominantly monoclinic structure. The M(020) plane becomes strongly oriented for film 9D (2.69 μm), though some reflection is still observed from the C(222) and M(-402) planes. However, once the films reached a critical thickness (between 2.69 and 5.72 μm), the only diffraction peak observed in the patterns is the M(020) peak, resulting in highly textured growth of the monoclinic phase as shown by film 9E (650 °C, 200 sccm, 5.72 μm).

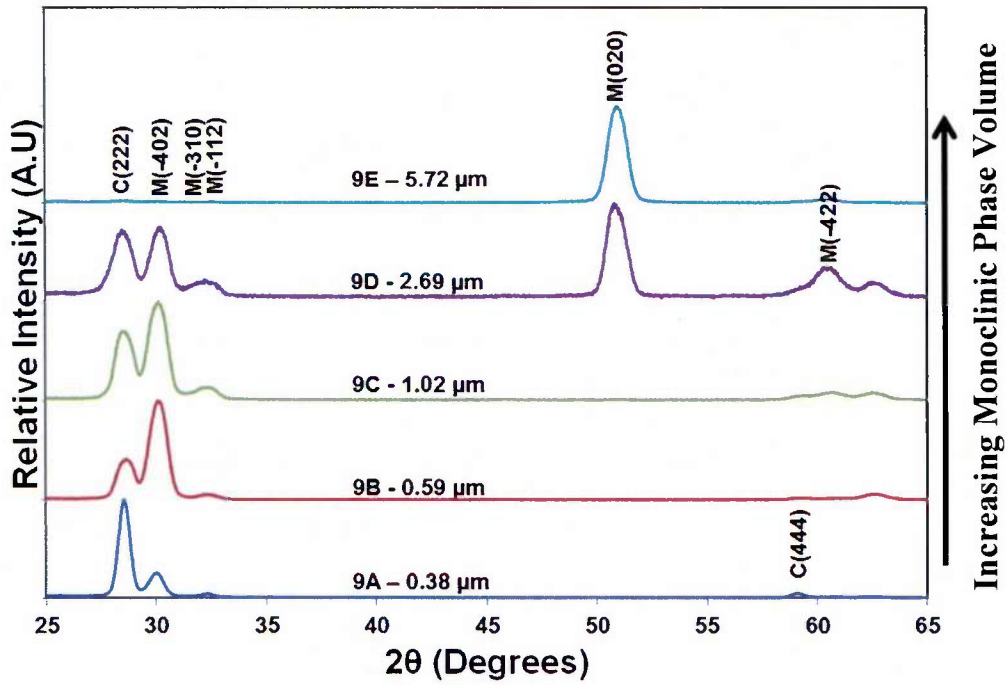

Figure 4.8. θ-2θ X-ray diffraction patterns of Gd_2O_3 films 9A (0.38 µm), 9B (0.59 µm), 9C (1.02 µm), 9D (2.69 µm), and 9E (5.72 µm) deposited on quartz as a function of thickness at deposition temperature of 650 °C and under 200 sccm of O_2 flow.

This growth can be explained on the basis of surface and strain energy minimization. Initial growth of the cubic phase, specifically with C(222) orientation, is preferred due to the low surface energy of the close packed (111) set of planes. Competing growth of the low energy M(-402) planes is also observed. As strain buildup occurs in the film with increasing thickness, there is a driving force to minimize strain energy resulting in transformation to a lower stress state via formation of the monoclinic phase. The growth of the M(020) orientation is observed for all thick films grown by high deposition rates (> 5 Å / s) regardless of oxygen flow. This data suggests that the M(020) plane may be the lowest strain energy plane of the monoclinic structure. It will be shown in Chapter 7, that the growth of the M(020) orientation results in deleterious effects on film morphology and electrical properties. It is important to note, however,

that the x-rays cannot penetrate fully into the Gd_2O_3 film for thickness values greater than 1.2 μm for the C(222) diffraction angle. Therefore, cubic phase may still be present at or near the substrate/film interface. Table 4.7 shows the calculated phase volumes and crystallite sizes for films 9A-9E. The crystallite sizing displayed a decreasing trend with increasing thickness for the cubic phase. This can be explained by the fact that the cubic phase volume decreases with increasing film thickness, resulting in smaller crystallite sizes (51 to 17 nm) calculated from the C(222) reflection. The monoclinic crystallite size increases slightly (19 to 23 nm) over the same range.

Table 4.7. Phase volume and crystallite size of Gd_2O_3 films 9A (0.38 μm), 9B (0.59 μm), 9C (1.02 μm), 9D (2.69 μm), and 9E (5.72 μm) deposited on quartz as a function of thickness at deposition temperature of 650 °C and under 200 sccm of O_2 flow.

Film	Deposition Temperature (°C)	Oxygen Flow (sccm)	Film Thickness (μm)	Cubic Phase Volume (%)	Monoclinic Phase Volume (%)	Cubic Crystallite Size (nm)	Monoclinic Crystallite Size (nm)
9A	650	200	0.38	55	45	51	19
9B	650	200	0.59	12	88	36	19
9C	650	200	1.02	13	87	23	21
9D	650	200	2.69	3	97	17	24
9E	650	200	5.72	0	100	-	23

4.5. Effect of substrate type on crystallographic phase and orientation of Gd_2O_3 films

Figure 4.9 displays typical XRD patterns of Gd_2O_3 films from the same deposition grown on silicon, quartz, sapphire, and GaN substrates. As can be observed from Figure 4.9, the diffraction patterns are very similar, suggesting nearly identical growth on all substrates. During thin film growth, if adatom mobility is high enough and interfacial mismatch is minimized, thin films can grow heteroepitaxially on the underlying substrate in order to minimize strain. However, due to the high rate of

deposition associated with the growth of the Gd_2O_3 films discussed thus far, the substrate was expected to have minor impact on the film growth. When evaporated atoms arrive quickly on the substrate surface, there is not enough time to diffuse along the substrate fully.

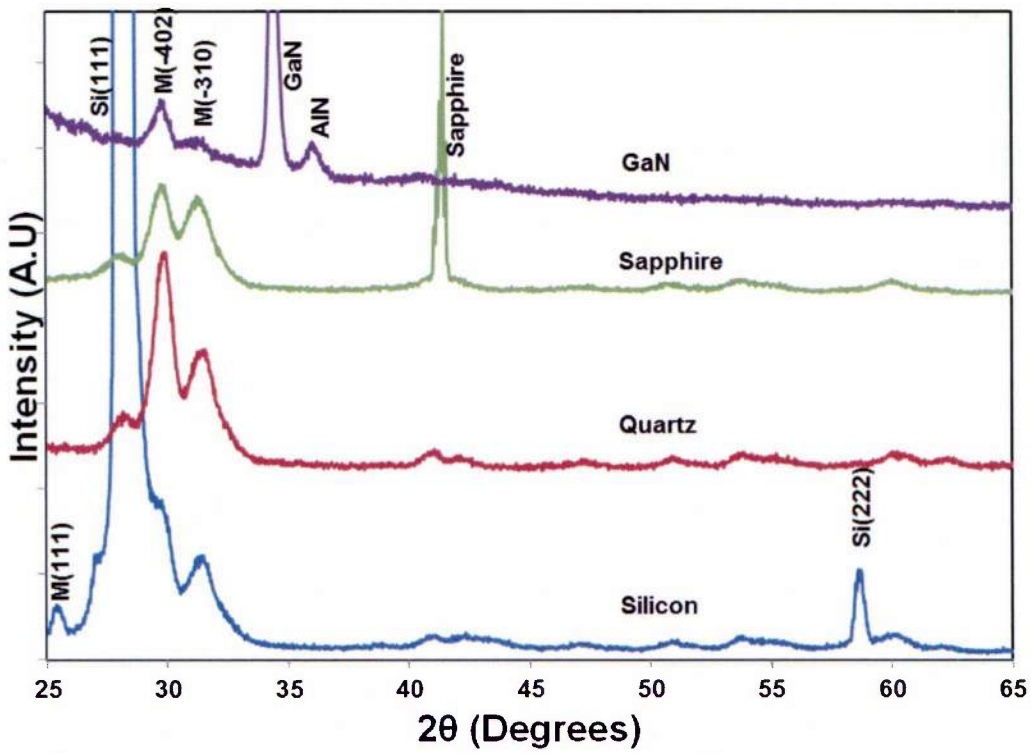

Figure 4.9. θ-2θ X-ray diffraction patterns of Gd_2O_3 film 12C (250 °C, 200 sccm O_2, 0.99 μm) deposited on silicon, quartz, sapphire, and GaN substrates.

4.6. Effect of heat treatments on crystallographic phase and orientation of Gd_2O_3 films

Select Gd_2O_3 films were subjected to heat treatments in an oxygen atmosphere in order to improve their electrical properties. X-ray diffraction was completed on these samples in order to determine the effects of high temperature heat treatments on the phase stability and structure of the Gd_2O_3 films. Figure 4.10 displays the theta-two-theta x-ray

diffraction pattern for film 12B (650 C, 200 sccm O_2, 1.1 μm) deposited with growth rate of > 5 Å / s.

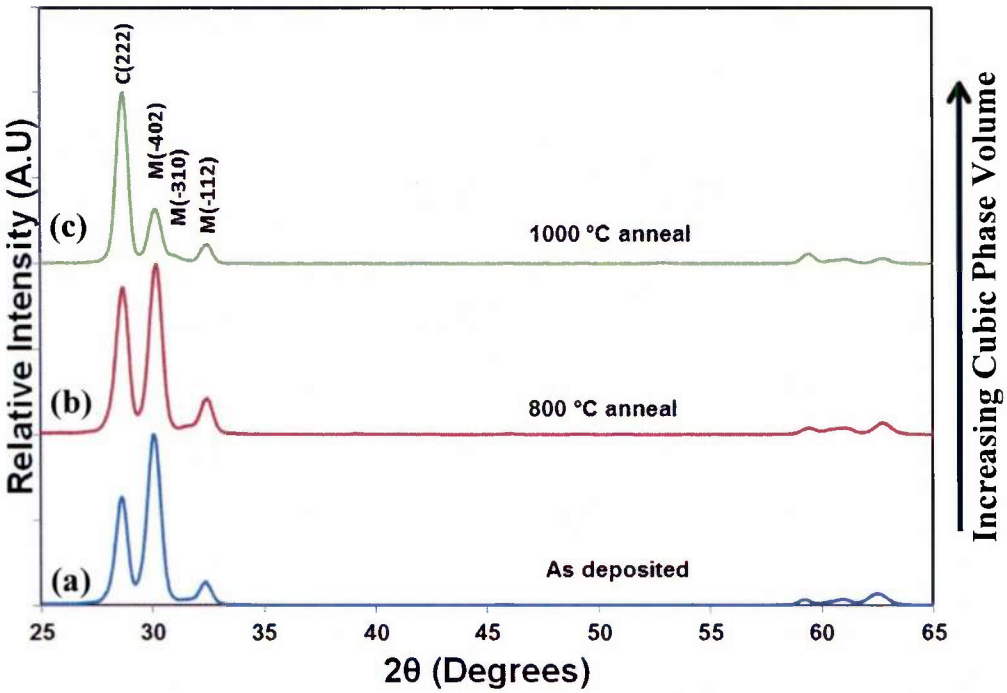

Figure 4.10. θ-2θ X-ray diffraction patterns of Gd_2O_3 film 12B (650 °C, 200 sccm O_2, 1.1 μm): (a) as deposited, (b) after1 hour anneal in oxygen at 800 °C and (c) after1 hour anneal in oxygen at 1000 °C

From the diffraction pattern of the as deposited sample shown in Figure 4.10 and the quantitative Rietveld analysis in Table 4.8, it can be seen that the film is majority monoclinic phase (cubic phase volume of 16%) with preferred M(-402) orientation. After annealing at 800 °C in an oxygen environment for 1 hour, the peak intensity ratio of C(222) / M(-402) increases, accompanied by an increase in the cubic phase volume of the film to 20% as measured by Rietveld refinement. After annealing at 1000 °C for 1 hour, the cubic phase volume increases to 49%. Two factors are primarily responsible for this increase in monoclinic to cubic phase transition. First, it is likely that increasing the

temperature provides the added diffusion necessary to allow the structure to form the thermodynamically stable cubic phase. Secondly, if the films were oxygen deficient, increased oxygen incorporation into the film may help stabilize the cubic phase. This further reinforces the possibility that oxygen deficiency plays a contributing role in the formation of the monoclinic phase as discussed in section 4.2. Table 4.8 also lists the calculated crystallite size for film 1B. There is a slight increase in crystallite size from 26 nm to 37 nm for the cubic phase after annealing at 800 °C. Increasing the annealing temperature to 1000 °C results in a significant increase in crystallite size for the cubic phase to a value of 61 nm. Interestingly, the crystallite size of the monoclinic phase increases with annealing temperature despite the increasing cubic phase volume.

Table 4.8. Phase volume and crystallite size for film 12B (650 °C, 200 sccm O_2, 1.1 μm) subjected to heat treatments in oxygen atmosphere.

Film	Cubic Phase Volume (%)	Monoclinic Phase Volume (%)	Cubic Crystallite Size (nm)	Monoclinic Crystallite Size (nm)
As deposited	16	84	26	22
800 °C anneal	20	80	37	33
1000 °C anneal	49	51	61	40

4.7. Conclusions

The effects of processing Gd_2O_3 film phase stability was studied via XRD and Raman spectroscopy. Quantitative phase volume analysis was performed via a Rietveld refinement technique. Gd_2O_3 films deposited at high rates (> 5 Å / s) were polycrystalline and of mixed cubic/monoclinic phase. The qualitative trends are summarized in Table 4.9. For ~1 μm thick films deposited as a function of temperature at constant 200 sccm O_2 flow (set 6), increasing the deposition temperature from 250 °C to 650 °C was found to increase the cubic phase volume in the film, improve the crystallinity, and increase the

crystallite size. The observed increase in cubic phase volume with increasing deposition temperature appears to be unique to Gd_2O_3 films deposited by EB-PVD, as greater monoclinic content is typically observed with increasing temperature for films prepared by other deposition methods.[49,8]

Table 4.9. Summary of process-phase trends describing the effects of temperature, oxygen flow, and thickness on the phase of Gd_2O_3 films deposited at high rates greater than 5 Å / s. The bolded letters indicate the varied deposition parameters for each set.

Set	Temperature (°C)	Oxygen flow (sccm)	Thickness (μm)	Trend
6	**Function of temperature (250 – 650 °C)**	200	~1	Increasing cubic phase volume with increasing temperature
1	650 °C	**Function of O_2 flow (50 -200)**	~2	No trend
4	250 °C	**Function of O_2 flow (25 -200)**	~1	Increasing cubic phase volume with increasing oxygen flow
3	250 °C	200 sccm	**Function of thickness (0.5 – 11)**	Increasing monoclinic phase volume with increasing film thickness
9	650 °C	200 sccm	**Function of thickness (0.4 – 6)**	Increasing monoclinic phase volume with increasing film thickness

For films deposited as a function of oxygen flow at low deposition temperature of 250 °C (Set 4), increasing the oxygen flow from 25 to 200 sccm was found to increase the cubic phase volume in the material, consistent with other reports found in the literature. At high deposition temperatures of 650 °C, the O_2 flow affected the preferred orientation of the film, and showed an increase in cubic phase content from 50 to 100 sccm, but decreased for higher oxygen flow (150, 200 sccm O_2). The effects of processing on the phase of Gd_2O_3 films deposited at rates greater than 5 Å / s is

summarized in Figure 4.11 which shows the effects of temperature, oxygen flow, and thickness on Gd_2O_3 phase content.

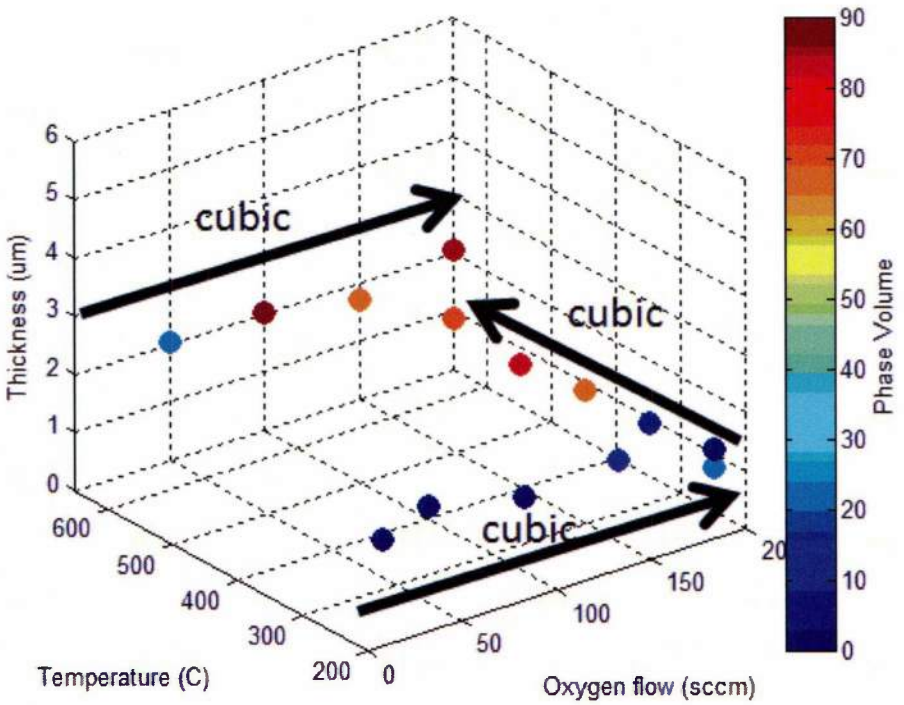

Figure 4.11. Process-phase summary map displaying the effects of temperature, oxygen flow, and thickness on the phase of Gd_2O_3 films deposited at high rates (greater than 5 Å / s) by reactive electron beam physical vapor deposition (EB-PVD).

GIXRD depth profiling analysis showed that cubic phase was detected at large incidence angles, but only monoclinic phase was observed at low incidence angles. This suggested that cubic phase grew near the film/substrate interface and monoclinic phase formed as the film grew thicker. This was supported by the θ-2θ diffraction patterns of sets 3 (250 °C, 200 sccm O_2, function of thickness) and 9 (650 °C, 200 sccm O_2, function of thickness) which both showed increasing monoclinic phase volume with increasing film thickness. At high deposition rates (> 5 Å / s), films were shown to grow similarly

on silicon, quartz, sapphire, and GaN substrates suggesting that the large flux of arriving atoms at the film surface dominates the growth over any interfacial effects. High temperature heat treatments in an oxygen atmosphere resulted in phase transition from the metastable monoclinic phase to the thermodynamically stable cubic phase with no film cracking, which was attributed to increased diffusion and oxygen incorporation into the film.

Chapter 5

Results and Discussion: Deposition of single phase cubic films and stress induced phase transformation

In chapter 4, it was shown that all films deposited at high rates (>5 Å / s) by reactive electron-beam physical vapor deposition (EB-PVD) possessed either fully monoclinic or mixed cubic and monoclinic phase character. For the mixed phase films, cubic phase was present near the substrate/film interface, and monoclinic phase volume increased as the film thickness increased. In order to understand the development of phase formation for thick Gd_2O_3 films, it is necessary to examine the growth processes at the initial stages of film growth. Therefore, analysis of Gd_2O_3 films less than 50 nm thick will be presented (set 8, variable temperature, variable O_2 flow, < 50 nm thick). In addition, this data will form the basis for discussion of the cubic to monoclinic phase transition.

Links between the deposition parameters and residual stress state of the Gd_2O_3 films and their resulting effects on film phase stability will be discussed. By decreasing the deposition rate to less than 1 Å/s for films grown at temperatures of 650 °C (set 10, 650 °C, 50 sccm, <0.5 Å/s), films up to 1 μm thick were grown in the pure cubic C (Ia3) phase. The growth of the thermodynamically stable cubic phase under these conditions is attributed to both higher surface mobility of the adatoms during growth leading to longer diffusion distances and to increased tensile stresses within the film. To differentiate between these two contributions, ion beam assisted deposition (IBAD) using ~500 eV oxygen ions was performed to introduce compressive stress into the Gd_2O_3 films (set 11, 650 °C, 50 sccm O_2, 0.5 A/s, function of ion beam current) to form the monoclinic phase.

Wafer curvature measurements, X-ray diffraction, and confocal Raman spectroscopy were utilized to characterize the films and present evidence for the existence of a stress-induced phase transition in the Gd_2O_3 films. Additionally, x-ray pole figure analysis was performed in order to determine in-plane texture of the Gd_2O_3 films on various substrates.

5.1. Deposition of thin (< 50 nm) single phase Gd_2O_3 films at low temperature

Based on the results presented in section 4.4 which showed increasing monoclinic phase volume with increasing film thickness, it was predicted that a very thin layer of Gd_2O_3 may grow in the cubic phase for a small film thickness. Therefore, thin (< 50 nm) films were deposited under a variety of conditions (films 8A-8E) and analyzed via x-ray diffraction. The grazing incidence x-ray diffraction (GIXRD) pattern for Gd_2O_3 film 8A (250 °C, 200 sccm O_2, 47 nm) is shown in Figure 5.1

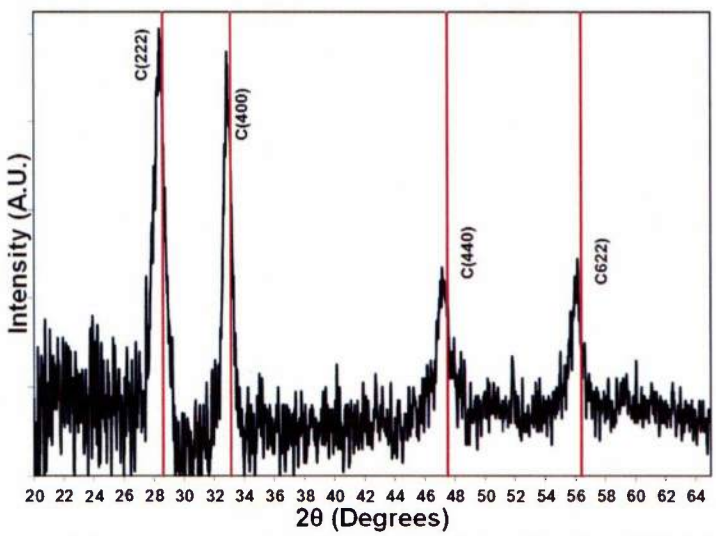

Figure 5.1. Grazing incidence pattern of fully cubic Gd_2O_3 film 8A (250 °C, 200 sccm O_2, 47 nm thick). Red lines show equilibrium peak position given by ICDD card #0042-1014.

As can be seen from the pattern, the only visible peaks are the C(222), C(400), C(440), and C(622) peaks, indicating that the film is indeed fully cubic and randomly oriented. It is important to note that the positions of the diffraction peaks of the thin film grown at 250 °C shown in Figure 5.1 are shifted to lower angles 2θ by approximately 0.1-0.5 degrees 2θ from the equilibrium positions evaluated by ICDD diffraction card #00-043-1014.[76] This is similarly observed in the θ-2θ scan, suggesting a large amount of tensile strain in the out-of-plane direction, which corresponds to compressive stress in the plane of the film for a biaxial stress state.

The out-of-plane strain may be calculated by the following equation:

$$\varepsilon_z = \frac{d - d_e}{d_e} \tag{5.1}$$

where d is the measured interplanar spacing and d_e is the equilibrium interplanar spacing absent of stress. Using equation 5.1, the strain was calculated from the θ-2θ XRD pattern of film 8A for the C(222), C(400), C(440), and C(622) planes. The values for d_e were evaluated from the cubic ICDD card for Gd_2O_3 #0043-1014. The calculated strain is approximately 0.6-0.7% as shown in Table 5.1

Table 5.1. Calculated strain for film 8A (250 °C, 200 sccm, 47 nm) based on equation 5.1

Plane	Equilibrium d spacing from ICDD # 0042-1014 (Å)	Measured d spacing (Å)	% Strain
(222)	3.121	3.142	0.7
(400)	2.703	2.721	0.7
(440)	1.912	1.925	0.7
(622)	1.630	1.640	0.6

Under the assumption of isotropic elasticity, the strain can be related to the stress using Hooke's law (equation 5.2):

$$\varepsilon_z = \{\sigma_z - \nu(\sigma_x + \sigma_y)\}/E \quad (5.2)$$

where E is Young's modulus, v is Poisson's ratio, and σ_x, σ_y are the in-plane stresses. Assuming a biaxial stress state where $\sigma_x = \sigma_y$, the equation can be reduced to equation 5.3 and the residual stress can be calculated:

$$\sigma_x = -\frac{E}{2\nu}\varepsilon_z \quad (5.3)$$

Based on the lattice spacings for the various planes measured in Table 5.1, the resulting residual stress given by equation 5.3 is approximately between -1.5 and -1.7 GPa. The negative sign indicates compressive stress acting within the plane of the film.

To further investigate the degree of residual stress in the films, XRD $\sin^2\psi$ residual stress analysis was performed. The XRD $\sin^2\psi$ technique[87] works by measuring the lattice spacing at various tilt angles from the surface normal, and extracting the residual stress from these strain measurements. Calculation of the residual stress is given by equation 5.4:

$$\frac{d_\psi - d_0}{d_0} = \frac{1+\nu}{E}\sigma \sin^2\psi \quad (5.4)$$

where ψ is the angle of sample tilt from the surface normal, E is Young's modulus, v is Poisson's ratio, σ is the in-plane-stress, d_0 is the lattice spacing at $\psi = 0$, and d_ψ is the lattice spacing at every tilt angle ψ. For a particular set of planes, the stress can be determined from the slope of the plot of the strain versus $\sin^2\psi$. The $\sin^2\psi$ technique was performed on the C(222) planes of film 8A (250 °C, 200 sccm O_2, 47 nm) and the resulting plot is shown in Figure 5.2. Since the elastic constants for Gd_2O_3 are unknown, the specific values for Young's modulus of the (222) plane could not be used in the calculation. Therefore, the bulk Young's modulus (148 GPa) and Poisson's ratio (0.29)

were taken from the NIST database.[88] From Figure 5.2, the measured slope corresponds to a stress value of -1.7x ± 0.1 GPa (where $x = \frac{(\frac{E}{1+\nu})_{222}}{(\frac{E}{1+\nu})_{bulk}}$), similar to the values previously calculated.

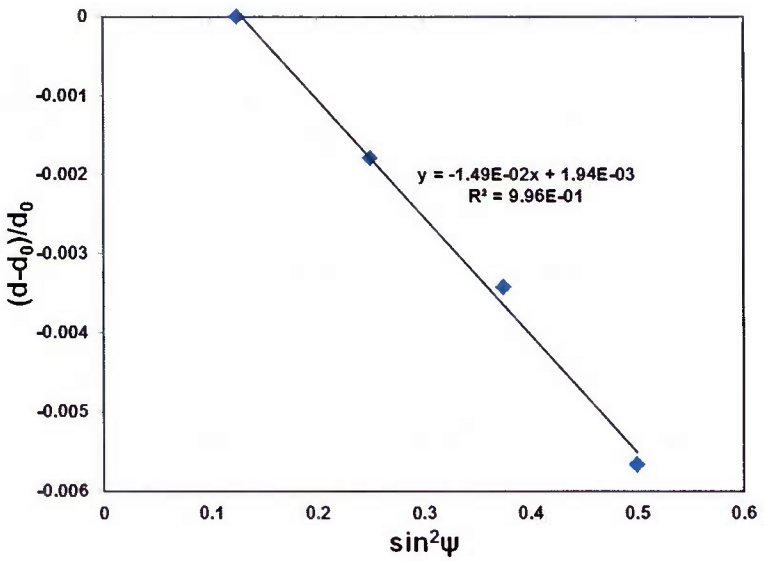

Figure 5.2. $Sin^2\psi$ versus strain plot for film Gd_2O_3 film 8A (250 °C, 200 sccm O_2, 47 nm). From the slope, a compressive stress of -1.7x ± 0.1 GPa (where x the ratio between Young's modulus for the C(222) plane and the bulk) was calculated.

The magnitude of the calculated compressive stress (-1.7 GPa) is very large for a film that is only 47 nm thick. It is unclear where the source of this residual stress originates. The low deposition temperature of 250 ° C should result in small amounts of tensile extrinsic stresses due to coefficient of thermal expansion (CTE) mismatch. Therefore, it is suggested that the large compressive stress generated is due to intrinsic growth stresses. Due to the nature of electron beam evaporation, the kinetic energy imparted to the substrate via the evaporated atoms is extremely low, eliminating "atomic

peening"[89] as a source of compressive stress. Possible explanations may come from surface stresses due to island formation before coalescence[90] or adatom injection into the grain boundaries.[91] Nevertheless, this large compressive stress may be the driving force for the formation of the monoclinic phase as the film grows thicker. The large compressive stress results in increased strain energy within the film. Once the strain energy reaches a certain critical limit, transformation from the cubic phase to the metastable monoclinic phase occurs in order to minimize the strain energy.

5.2. Effects of residual stress on Gd_2O_3 thin films

A trend of increasing monoclinic phase content with increasing film thickness was observed for set 3 (250 °C, 200 sccm O_2, function of thickness) and set 9 (650 °C, 200 sccm O_2, function of thickness). For intermediate film thicknesses (500 nm to 3 μm), the cubic phase volume is larger for films from set 9 (650 °C) than those from set 3 (250 °C). One explanation for this behavior is that the surface mobility of the adatoms is increased at these elevated temperatures, resulting in larger diffusion lengths which allow for atomic rearrangements into the more thermodynamically stable cubic structure and preferred C(222) low surface energy orientation. It is interesting to note though, that in the case of low temperature deposition, films are initially fully cubic at very small thicknesses (Figure 5.1). This suggests that adatom mobility is not the only mechanism for phase transformation. Another explanation is offered relating to the residual stress state of the films, where increased compressive stresses may result in formation of the monoclinic phase.

The extrinsic stress in the film due to coefficient of thermal expansion (CTE) mismatch is given by equation 5.5:

$$\sigma_{CTE} = \frac{E_c}{1-\nu_c}(\alpha_s - \alpha_c)(T_f - T_d) \qquad (5.5)$$

where $\frac{E_c}{1-\nu_c}$ is the biaxial modulus of the Gd_2O_3 film, α_s and α_c are the coefficients of thermal expansion of the substrate and film, respectively, and T_f and T_d are the final and deposition temperatures, respectively. It is not possible to calculate the absolute value of thermal stress in these films because of their mixed cubic and monoclinic phase nature. The CTE of monoclinic Gd_2O_3 has been reported to be significantly higher (9-15 x 10^{-6} / °C depending on orientation) than that of cubic Gd_2O_3 (7.95 x 10^{-6} / °C).[92] However, the coefficient of thermal expansion in both cases is higher in the film than in the silicon substrate (2.55 x 10^{-6} / °C),[93] and therefore, increasing the deposition temperature will result in increased tensile residual stresses within the film upon cooling.

Due to the unknown elastic constants of Gd_2O_3 as well as the mixed phase nature and heavy degree of texture in the thicker Gd_2O_3 films, the XRD $\sin^2\psi$ technique for measurement of the residual stress was determined to possess significant amount of error for some samples. Therefore, the wafer curvature technique in conjunction with Stoney's equation was employed to measure the residual stress of the thicker films. Since the calculation of residual stress by this method is based entirely on the curvature of the wafer and the material properties of the substrate, the film material properties are not needed. This allows for simple calculation of the residual stress in multi-phase films.

The expected trend of increased tensile residual stress with increasing deposition temperature is reflected in Figure 5.3a which shows the total residual stress measured by

the wafer curvature technique for Gd_2O_3 films 7A-7E (function of temperature, 50 sccm O_2 flow, ~1 μm) grown on silicon.

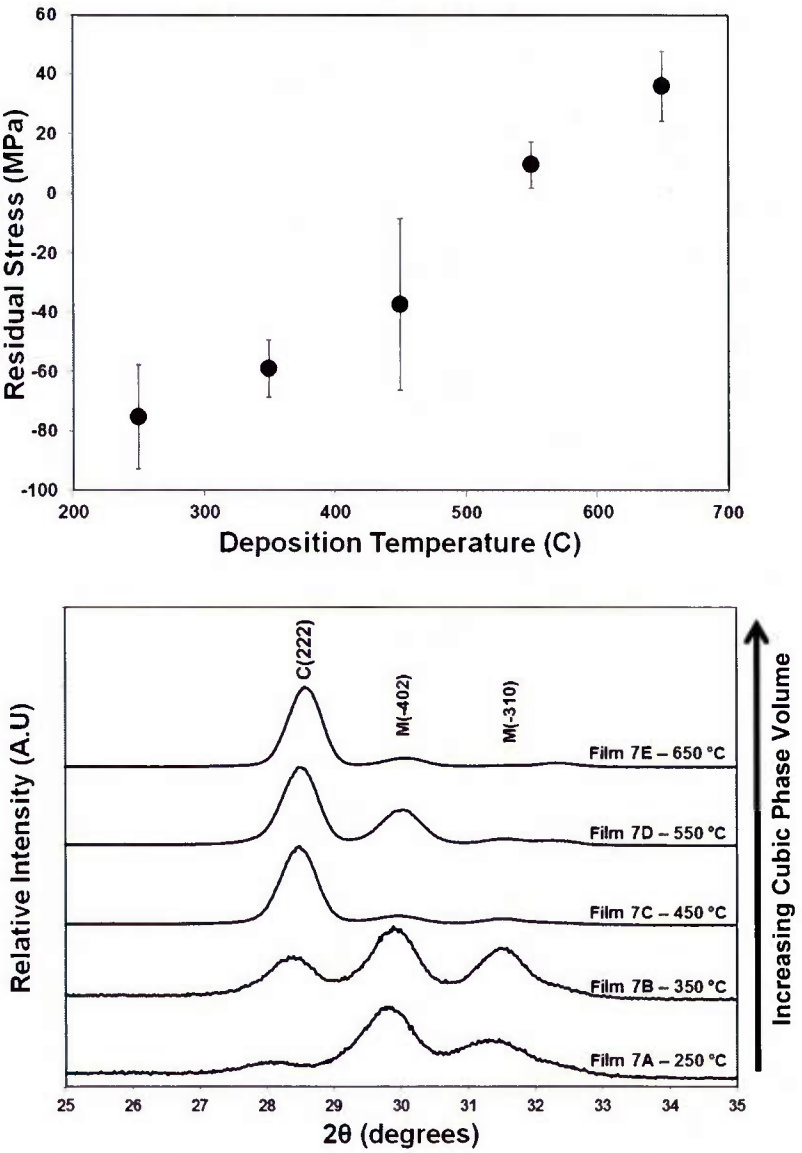

Figure 5.3. (a) Measured residual stress via wafer curvature technique for ~1 μm thick films 7A (250 °C), 7B (350 °C), 7C (450 °C), 7D (550 °C), and 7E (650 °C) deposited as a function of temperature on Si(111) under 50 sccm O_2 flow and (b) corresponding θ-2θ diffraction patterns deposited on quartz substrates showing increasing cubic phase volume with increasing temperature.

Figure 5.3b displays the corresponding θ-2θ diffraction patterns for films 7A-7E grown on quartz which clearly show increasing cubic phase content with increasing deposition temperature. The increased tensile stresses for films deposited at higher temperatures may therefore stabilize a greater amount of cubic phase within the film. It is important to note, however, that the total residual stress includes both the extrinsic and intrinsic components of the residual stress, which is a complex combination of variables during the growth process and cannot be fully explained by the CTE mismatch alone.

5.3. Deposition of thick single phase cubic Gd_2O_3 films

Until this point, the discussion has focused on films with high growth rates, > 5 Angstroms / s, which has resulted in mixed cubic/monoclinic phase growth for films greater than 50 nm thick regardless of deposition temperature. It was proposed that the relatively fast deposition rates were not allowing adequate time for the adatoms to diffuse resulting in a "quenched in" monoclinic structure. Therefore, the deposition temperature was set at 650 °C and the rate was lowered to approximately 0.5 Å / s to determine if these conditions would allow for formation of the pure cubic phase for a thick gadolinium oxide film. Figure 5.4 displays the θ-2θ diffraction pattern for film 10B (650 °C, 50 sccm O_2, 910 nm, 0.5 Å / s) on silicon, sapphire, quartz, and GaN substrates. Aside from the Al_2O_3, GaN, and AlGaN substrate peaks, all observed peaks in the diffraction pattern correspond to cubic reflections of Gd_2O_3. However, it is important to note that the preferred orientation in the Gd_2O_3 film differs depending on the substrate type, in contrast to films deposited under high rates of deposition (> 5 Å/s), where there was no change in preferred orientation. This will be discussed in greater detail in sections 5.5 and 5.6.

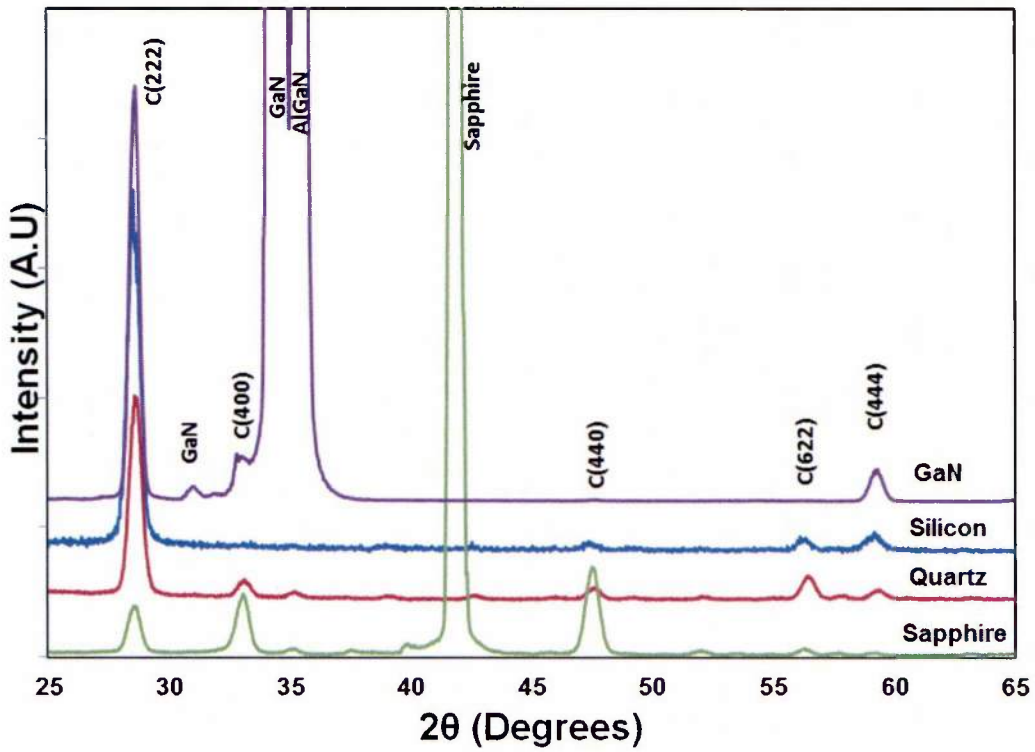

Figure 5.4. θ-2θ X-ray diffraction patterns of fully cubic Gd_2O_3 film 10B (650 °C, 50 sccm O_2, 910 nm, 0.5 Å/s) deposited on sapphire, quartz, silicon, and GaN.

The measured tensile residual stresses by the wafer curvature method for the cubic phase film 10B (650 °C, 50 sccm O_2, 910 nm, 0.5 Å/s) deposited at 650 °C on silicon was 166 ± 38 MPa. The measured residual stress of the pure cubic film deposited on the sapphire substrate was 45 ± 19 MPa. The increased compressive stress in this film compared to the one grown on silicon can be attributed to the smaller CTE mismatch between the sapphire substrate (7.30 x 10^{-6} / °C) and the film (7.07 - 15 x 10^{-6} / °C depending on phase and orientation) as compared to the silicon substrate (2.55 x 10^{-6} / °C). This increase in compressive stress is also reflected in the peak shift within the diffraction pattern to lower angles two-theta.

It is important to note that the measured residual stress of cubic phase film 10B was significantly larger (166 ± 38 MPa) than for the mixed phase film 7E (650 °C, 50 sccm O_2, 1.2 μm, 9.1 Å / s, Figure 5.3b) deposited on silicon at the same temperature (35 ± 11 MPa), suggesting that larger tensile stresses may play a role in assisting formation of the cubic phase. Indeed, all single phase cubic films deposited at 650 °C possessed higher tensile stress than mixed phase films deposited at the same temperature. As evidenced by lowering the deposition rate, the growth of the pure cubic phase under these conditions can once again be related to the effect of surface diffusion lengths and residual stress state. In this case, it is difficult to determine whether the cubic phase formation was caused by the increased adatom mobility due to the lower deposition rate, or rather a result of the increased tensile stress, or a mixed combination.

5.4. Stress induced phase transformation by ion beam assisted deposition (IBAD)

In order to differentiate between these two possible mechanisms, an experiment was designed using ion beam assisted deposition (IBAD) to induce compressive stress during Gd_2O_3 film growth on sapphire substrates. Sapphire substrates were chosen to avoid significant interfacial layer formation as in the case of the silicon substrates. Additionally, increased compressive stress due to the CTE mismatch between the sapphire substrate and Gd_2O_3 film was predicted to help in driving the phase transition. Ion bombardment during film growth using an O_2 plasma at a floating voltage of approximately 500V was performed for films 11B (650 °C, 50 sccm O_2, 200 mA), 11C (650 °C, 50 sccm O_2, 400 mA), and 11D (650 °C, 50 sccm O_2, 800 mA). The deposition rate was kept at < 0.5 Å / s for all the films. Due to the low deposition rate and the

increased energy (i.e. current density) from the ion beam, it was possible to alter the stress state of the films while keeping surface energy and atom diffusion lengths large. This allowed for structural rearrangement of atoms and isolation of the effects of diffusion length vs. residual stress on the phase stability of the Gd_2O_3 films.

The θ-2θ diffraction patterns for films 11A-11D deposited as a function of ion beam power are shown in Figure 5.5. Table 5.2 displays the cubic and monoclinic phase volumes calculated from the Rietveld refinement of the pattern as well as the measured residual stress values determined by the wafer curvature method.

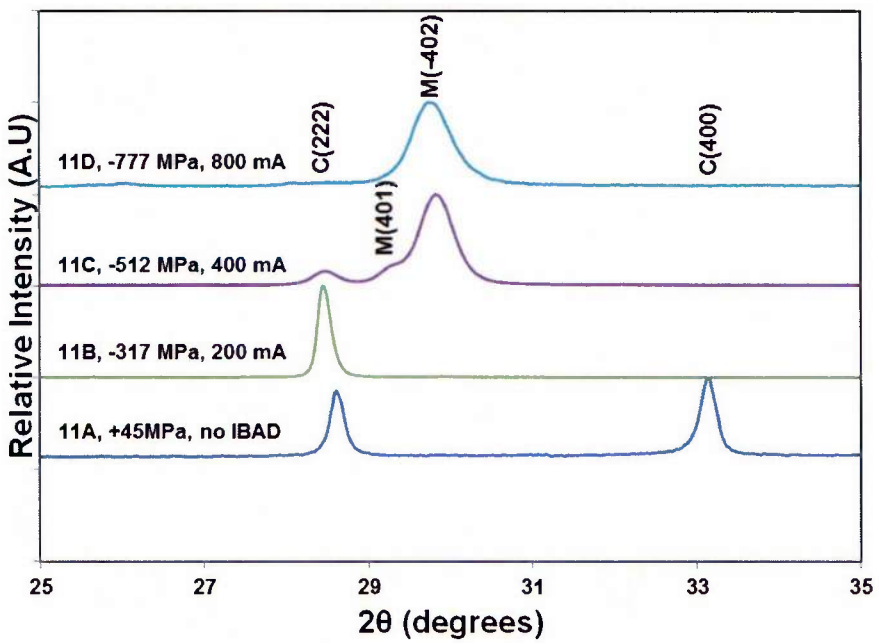

Figure 5.5. θ–2θ XRD patterns of Gd_2O_3 films 11A (0 mA), 11B (200 mA), 11C (400 mA), and 11D (800 mA) grown on sapphire at 650 °C and 50 sccm O_2 under low growth rate of ~0.5 Å / s as a function of ion beam source current.

Film 11A (0 mA) deposited without any IBAD assistance under a low deposition rate possessed a tensile stress of approximately 45 MPa and is fully cubic in nature.

Applying 200 mA (film 11B) of current during deposition resulted in 317 MPa of compressive stress in the film. From Figure 5.5, film 1B is still predominantly of the cubic phase with a small amount of monoclinic phase formation. The increase in the energy at the film surface also promoted the growth of a strong preferred C(222) orientation under heavy strain. This is reflected in the shift of the C(222) peak in the XRD pattern from approximately 28.6 to 28.4 degrees two-theta and a measured residual stress of -317 MPa. This stress was enough to induce a small amount of monoclinic phase formation in the film.

Table 5.2. Phase volume and crystallite size for Gd_2O_3 films 11A (0 mA), 11B (200 mA), 11C (400 mA), and 11D (800 mA) grown on sapphire at 650 °C and 50 sccm O_2 under low growth rate of ~0.5 Å / s as a function of ion beam source current.

Film	Ion Beam Current (mA)	Cubic Phase Volume (%)	Monoclinic Phase Volume (%)	Measured Residual Stress (MPa)	Cubic crystallite size (nm)	Monoclinic crystallite size (nm)
11A	0	100	0	45 ± 19	45	-
11B	200	98	2	-317 ± 76	54	13
11C	400	5	85	-517 ± 44	28	18
11D	800	0	100	-777 ± 77	-	16

Increasing the ion beam current further for film 1C (400 mA) resulted in a compressive stress state of -512 MPa. The XRD pattern (Figure 5.5) shows that this film is predominantly monoclinic phase. This suggests that a significant amount of the cubic phase was converted to monoclinic phase with an applied stress between -317 and -517 MPa. Further increasing the ion beam current for film 11D (800 mA) resulted in a pure monoclinic Gd_2O_3 film with a compressive residual stress of -777 MPa. No evidence of the cubic phase was observed.

The crystallite sizes for films 11A – 11D are also listed in Table 5.2. An increase in cubic crystallite size (45 nm to 54 nm) was observed with an increase in ion beam

current from 0 mA to 200 mA. This is explained by the extra energy supplied by the highly mobile ions to overcome the nucleation barrier and begin growth. Further increasing the ion beam current to 400 mA results in a decrease of cubic crystallite size (54 to 28 nm) and an increase in monoclinic crystallite size (13 to 18 nm) as a result of the phase transition in which more monoclinic crystallites grow at the expense of cubic crystallites.

Raman spectroscopy was performed on films 11A-11D deposited as a function of IBS current to further validate the film phases as shown in Figure 5.6. The locations of the Raman bands for each sample were indexed to determine the phase content. For baseline comparison, a Raman scan of cubic Gd_2O_3 powder was included. The primary band corresponding to the cubic phase is shown at approximately 365 cm^{-1}. The primary band of the monoclinic phase is located at approximately 420 cm^{-1}.

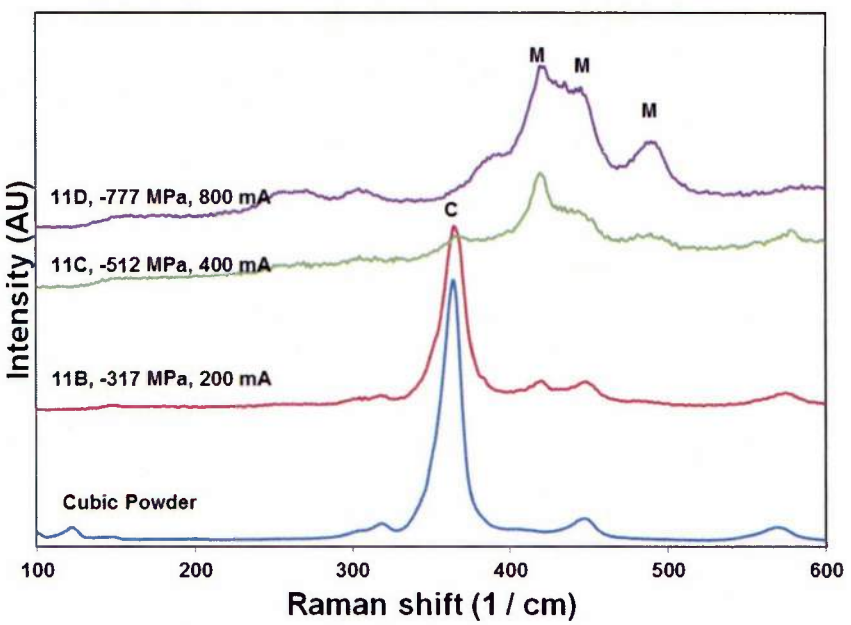

Figure 5.6. Raman spectra of cubic Gd_2O_3 powder and Gd_2O_3 films 11B (200 mA), 11C (400 mA), and 11D (800 mA) grown on sapphire at 650 °C and 50 sccm O_2 under low growth rate of ~0.5 Å / s as a function of ion source current.

The Raman results correspond closely to the results shown from the x-ray diffraction patterns. There is a clear increase in the monoclinic phase content with increasing ion source amperage and increasing residual stress, again with the majority of the transformation occurring between films 11B (-317 MPa) and 11C (-512 MPa). Film 11D (-777 MPa) also displayed no evidence of the cubic phase by Raman spectroscopy suggesting that a cubic to monoclinic phase change in Gd_2O_3 can occur by introducing compressive stress into the lattice. Indeed, based on these results, it is likely that compressive stress is the primary reason for the phase transition observed with increasing film thickness.

These results may be analogous to pressure induced phase transformations observed in diamond anvil cell experiments of bulk Gd_2O_3 in which high pressure was found to transform Gd_2O_3 from the cubic structure to higher density structures.[39] In these experiments, it has been shown that under hydrostatic pressure conditions, approximately 7-15 GPa of pressure is necessary to stabilize the phase change which is significantly higher than the measured residual compressive stress (300 – 500 MPa) in the Gd_2O_3 films. Due to large surface to volume ratio, nanocrystalline materials may have vastly different properties than bulk materials. Therefore, it may be possible to intitiate phase transitions that are not possible in the bulk under the same conditions. It has been shown in Zr_3N_4 that even though the overall stress in a thin film is low, high local stress regions can lead to the nucleation of a metastable phase.[94] For instance, in ZrO_2 thin films, a stress-induced phase transition from the tetragonal to monoclinic phase was driven with only 300 MPa of compressive stress.[95]

There are numerous recent studies detailing phase transformations of Y_2O_3[96,97], Er_2O_3[98], Dy_2O_3[98], and Gd_2O_3[99,100] films and bulk materials using large ion energies (200 keV+) to drive the phase transformation. The phase transitions have been attributed to a number of factors including: 1) large damage cascade followed by recrystallization due to a thermal spike and 2) damage accumulation resulting in clustering of defects and an increase in the Gibb's Free energy above the phase boundary limit.[98] The first explanation is unlikely due to the low energy of the impinging ions in our experiments (400-500eV) vs (200keV+) in the other experiments. The second explanation may possibly explain the source of the residual stress. More specifically, the accumulation of defects due to the bombarding ions disrupting the crystal structure results in increased film stresses and eventually leads to the monoclinic phase formation. Finally, loss of oxygen during ion irradiation has been suggested as a contributing factor to the phase transition in other oxide materials under irradiation.[99] However, in this experiment, the film was bombarded with oxygen ions and the surface mobility was large allowing us to discount oxygen deficiency as a reason for the phase transition.

5.5. Texture evolution in single phase cubic films deposited at low rates

Figure 5.4 showed the θ-2θ XRD patterns for film 10B (650 °C, 50 sccm O_2, 910 nm, 0.5 Å/s) deposited on silicon, quartz, sapphire, and GaN being 100% cubic phase regardless of the underlying substrate composition and structure. However, differences in the preferred orientation and residual stress state of the films were observed. The relative intensities of the C(222), C(400), C(440), and C(622) peaks for film 10B are listed in

Table 5.3 and compared to the expected intensity from the ICDD powder diffraction file #0042-1014.

Table 5.3. Relative intensities of main cubic peaks for Gd_2O_3 film 10B (650 C, 50 sccm O_2, 910 nm.

Sample	C(222) Relative Intensity (%)	C(400) Relative Intensity (%)	C(440) Relative Intensity (%)	C(622) Relative Intensity (%)
10B / Silicon	100	0	2	3
10B / Quartz	100	10	7	17
10B / Sapphire	31	44	100	5
10B / GaN	100	7	3	0
ICDD #0042-1014	100	32	35	13

Due to the small lattice mismatch of Gd_2O_3 C(222) interplanar spacing (3.121 Å) with that of Si(111) (3.136 Å), there is a strong degree of C(222) preferred orientation observed in the film grown on silicon, with minimal contribution from the other Gd_2O_3 peaks. The film grown on quartz also possessed some preferred C(222) orientation, but is more random in growth as compared to the silicon. This can be accounted for by the fact that the C(222) planes are the low surface energy planes of the cubic bixbyte Ia3 structure. The C(222) planes have also been shown to nucleate even on amorphous substrates despite there not being a template for its growth.[49] The film grown on sapphire exhibited C(440) preferred orientation despite being a higher surface energy plane. This is attributed to the smaller lattice mismatch of the sapphire (006) basal plane interplanar spacing (2.164 Å) with the spacing of the Gd_2O_3 C(440) plane (1.911 Å). The film grown on GaN grows with strong C(222) preferred orientation despite the large lattice mismatch (20%) between GaN and Gd_2O_3 and large difference in the basal plane spacing of GaN (2.59 Å) and the Gd_2O_3 C(222) interplanar spacing (3.12 Å). This is partly due to the close symmetry that the (111) planes in the bixbyite structure share with the (0001)

GaN basal plane. For very thin Gd_2O_3 films (<70 nm) deposited by MOCVD, Gd_2O_3 was shown to grow epitaxially on GaN with significant dislocation density.[55]

In order to learn more about the texture evolution in the Gd_2O_3 films deposited at low rates, grazing incidence x-ray diffraction (GIXRD) depth profiling was employed. GIXRD scans were taken for film 10B (650 °C, 50 sccm O_2, 910 nm, 0.5 Å/s) deposited on quartz at incidence angles of 1, 2, 5, 10, and 15 degrees as shown in Figure 5.7.

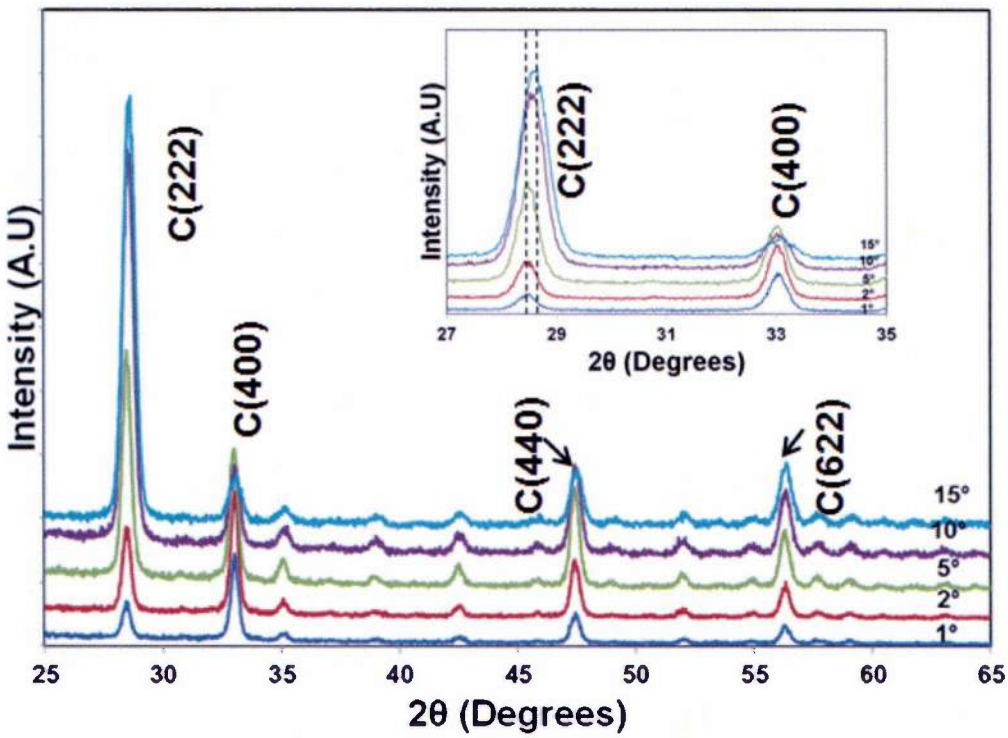

Figure 5.7. Grazing incidence diffraction patterns taken at incidence angles of 1, 2, 5, 10, and 15 degrees for film 10B (650 °C, 50 sccm O_2, 910 nm, 0.5 Å/s) deposited on quartz. The inset shows the magnified C(222) and C(400) peaks.

At a large incidence angle of 15°, the depth of penetration into the film is large and the GIXRD pattern appears to be similar to the θ-2θ pattern, suggesting that the film deposited on quartz is mostly randomly oriented. The inset in Figure 5.7 displays the

magnification of the C(222) and C(400) peaks. It is important to note that as the penetration depth increases, the intensity ratio of the C(222) to C(400) peak increases. This suggests that even for a fully cubic phase film, the C(222) planes are not stable at large film thicknesses. This is further supported by the shift in the C(222) peak position from approximately 28.6 ° to 28.4 ° as the penetration depth increases.

5.6. Pole figure analysis for determination of preferred orientation

Pole figures are stereographic projections of the crystallographic directions present in a material. More specifically, pole figures describe the statistical average distribution of the pole density for a certain-plane. In a randomly oriented material, the pole density is uniform. When the pole density is concentrated in the stereographic projection, this suggests the presence of preferred orientation. While θ-2θ XRD scans provide information about out-of-plane texture in thin films, pole figures can reveal information about in-plane texture as well. Fiber texture refers to films where preferred orientation exists in the out-of-plane orientation, but the films are randomly oriented in-plane. Biaxial texture occurs when the in-plane orientation becomes locked with respect to the substrate. In this section, pole figure analysis will be used to determine the degree of in-and-out-of-plane texture for 1) mixed phase films deposited at high rates, 2) single phase films deposited at low rates, and 3) films deposited at low rates using ion beam assisted deposition. These samples will specifically show the effects of increasing surface energy and adatom mobility on the texture in thick Gd_2O_3 films. The samples used for pole figure analysis to illustrate a wide range of texture are listed in Table 5.4.

Table 5.4. Films used in pole figure analysis and corresponding in-and-out-of-plane textures.

Film	Temperature (°C)	O_2 flow (sccm)	IBS Current (mA)	Deposition Rate (Å / s)	Substrate	Out-of-plane texture	In-plane texture
6A	250	200	0	7.5	Quartz	Weak M(-310)	Random
6E	650	200	0	8.2	Quartz	Strong C(222)	Random
10B	650	50	0	0.48	Quartz	Strong C(222)	Random
10B	650	50	0	0.48	Sapphire	Strong C(440)	Medium C(440)
10B	650	50	0	0.48	GaN	Strong C(222)	Strong C(222)
11B	650	50	200	0.34	Quartz	Strong C(222)	Strong C(222)
11B	650	50	200	0.34	Sapphire	Very Strong C(222)	Very Strong C(222)

5.6.1. Mixed phase films deposited at high rates

Figure 5.8 shows the C(222) and M(-402) pole figures for mixed phase film 6A (250 °C, 200 sccm O_2, 7.5 Å/s) deposited on quartz. As observed from the C(222) pole figure, the distribution of the contour lines and their wide spacing suggests random orientation of the (222) grains distributed throughout the film. There is some weak out-of-plane texture of the M(-402) planes shown by the low intensity (~1000 counts) and widely spaced contour lines. Other pole figures (not shown here) display that there is no in-plane orientation for this film, but rather random orientation of crystallites dispersed throughout the film. This is expected due to the low deposition temperature (250 °C) and deposition rates which results in a low adatom mobility and an inability for the films to develop any in-plane orientation with respect to the substrate.

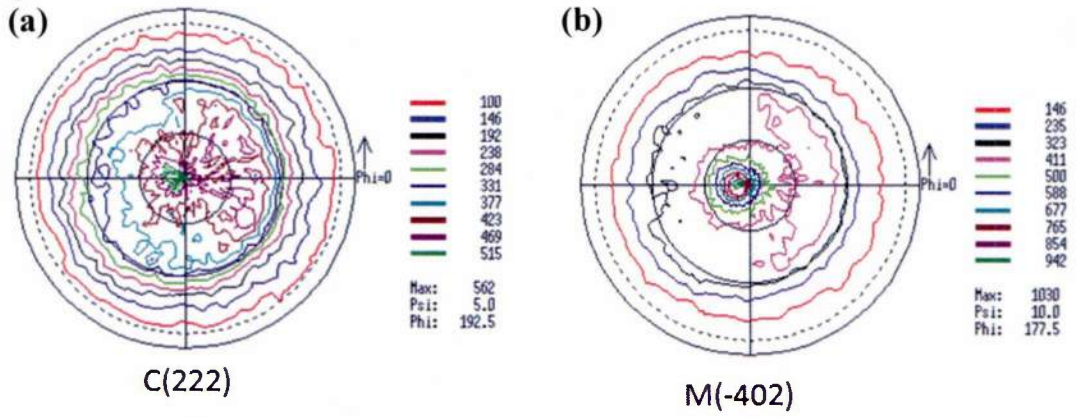

Figure 5.8. (a) C(222) and (b) M(-402) pole figures of film 6A (250 °C, 200 sccm O_2, 7.5 Å / s) deposited on quartz showing weak out-of-plane texture and random in-plane texture.

Figure 5.9 displays the C(222) and M(-402) pole figures for film 6E (650 °C, 200 sccm O_2, 8.2 Å /s) deposited on quartz. This film shows strong fiber texture of the C(222) planes with tightly packed contour lines and high intensity (~9000 counts). Weak out-of-plane texture of the M(-402) plane is also observed. This film is only strongly oriented in the out-of-plane direction, with random in-plane orientation. Despite the high deposition temperature, the fast arrival of metal flux at the film surface as well as the amorphous substrate does not allow for in-plane alignment of the Gd_2O_3 film.

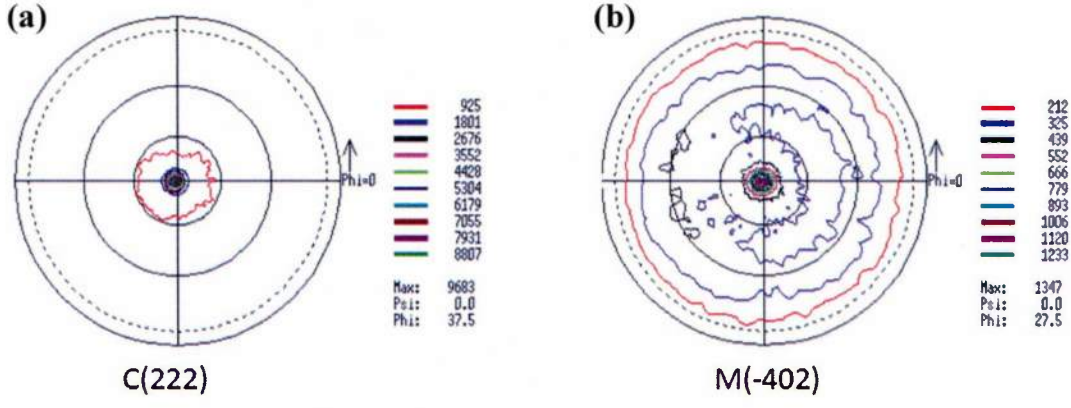

Figure 5.9. (a) C(222) and (b) M(-402) pole figures of film 6E (650 °C, 200 sccm O_2, 8.2 Å / s) deposited on quartz showing strong fiber texture and random in-plane texture.

5.6.2. Single phase cubic films deposited at low rates on different substrate materials

Figure 5.10 displays the pole figures for single phase cubic film 10B (650 °C, 50 sccm O_2, 0.5 Å / s) deposited on quartz. There is a strong out-of-plane texture for the C(222) planes with maximum intensity located at ψ angle of 0°. There is some weak texturing of the C(400) planes which are offset slightly from the center with a maximum intensity at approximately 15 degrees from the surface normal.

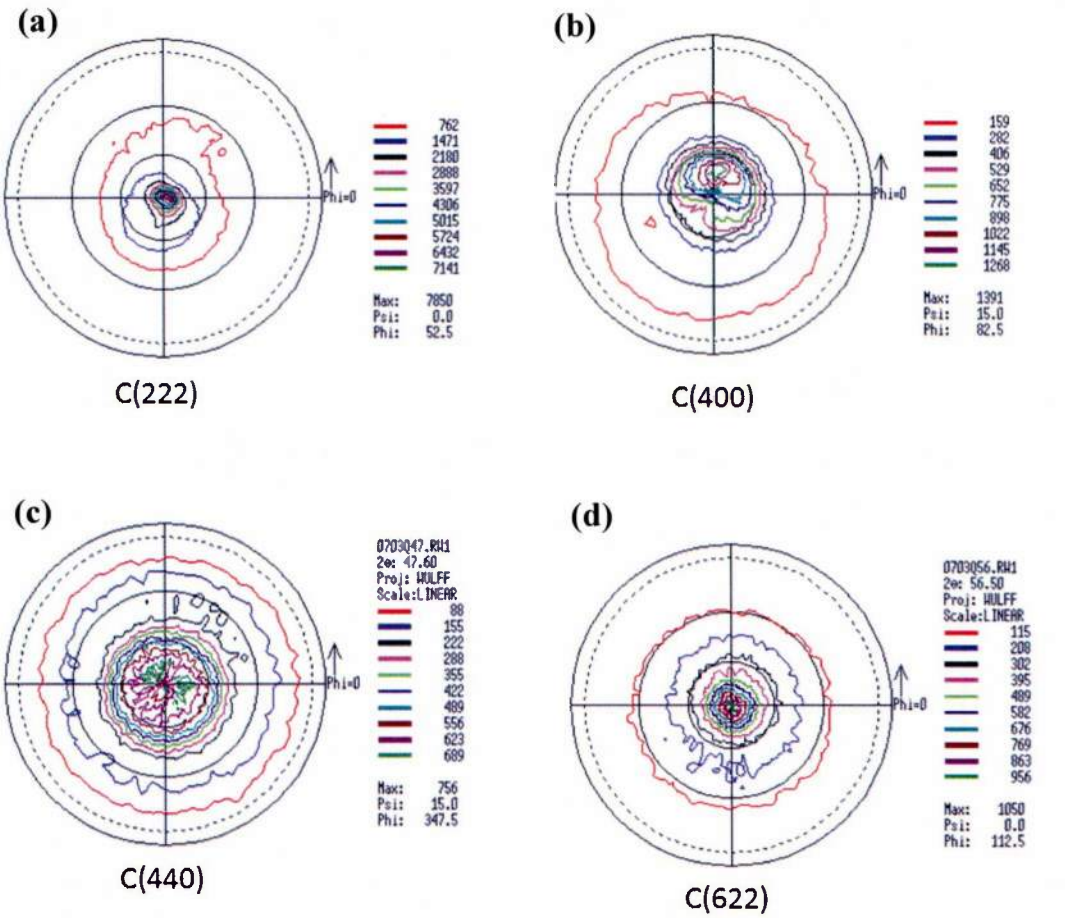

Figure 5.10. Pole figures of (a) C(222), (b) C(400), (c) C(440), and (d) C(622) planes for film 10B (650 °C, 50 sccm O_2, 0.5 A / s) deposited on quartz showing strong fiber texture and random in-plane texture.

The C(440) planes are randomly oriented throughout the sample and the C(622) planes show a weak fiber texture. Despite the low deposition rate and fully cubic nature of the film, no in-plane orientation is observed for film 10B deposited on quartz. This is likely due to the amorphous nature of the quartz substrate which does not provide an adequate template for epitaxy.

The pole figures for film 10B (650 °C, 50 sccm O_2, 0.5 Å / s) deposited on sapphire are shown in Figure 5.11. In agreement with the θ-2θ XRD pattern, there is a strong C(440) out-of-plane texture (Figure 5.11c). Weak out-of-plane texturing of the C(222), C(400) and C(622) planes are observed as shown in Figures 5.11a, 5.11b, and 511.d, respectively. The C(222) pole figure possesses a maximum intensity for six poles located at approximately 35° from the surface normal. The theoretical angle between the C(440) and C(222) planes in a cubic crystal is 35.2°, suggesting that an in-plane orientation of the C(440) crystallites exists in this film. This is likely due to the low growth rate and small difference in the sapphire (006) basal plane interplanar spacing (2.164 Å) with the spacing of the Gd_2O_3 C(440) plane (1.911 Å). However, the spread of the contour lines is very large, scattering over approximately 20-25 degrees suggesting that the in-plane orientation is weak.

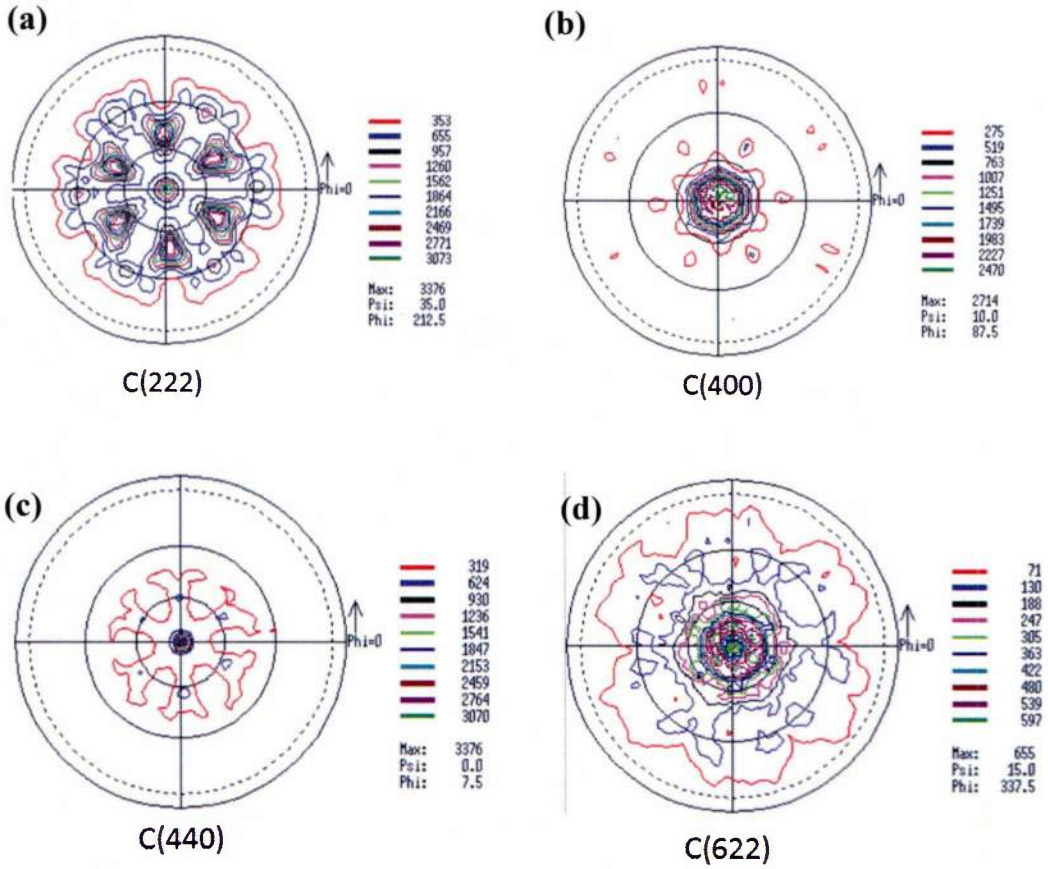

Figure 5.11. Pole figures of (a) C(222), (b) C(400), (c) C(440), and (d) C(622) planes for film 10B (650 °C, 50 sccm O_2, 0.5 Å / s) deposited on sapphire showing strong out-of-plane texture and medium in-plane texture.

The pole figures for film 10B (650 °C, 50 sccm O_2, 0.5 Å / s) deposited on GaN are shown in Figure 5.12. The C(222) pole (Figure 5.12a) shows extremely strong out-of-plane texture. A strong contribution from the C(400) planes (Figure 5.12b) is observed as well. Interestingly, the C(440) pole figure shows six poles located at 35° from the surface normal. This angle agrees well with the theoretical angle between the C(222) and C(440) planes, suggesting very strong in-plane orientation of the C(111) crystallites. This is further supported by the six C(622) poles (Figure 5.11d) which show a maximum

intensity at 30 ° ψ, close to the theoretical angle of 29.5° between the C(622) and C(222) planes. Additionally, the spread of the contour lines is scattered over only a few degrees, suggesting very good in-plane orientation. This is likely a result of the close symmetry the C(111) bixbyite plane shares with the GaN (0002) basal plane.

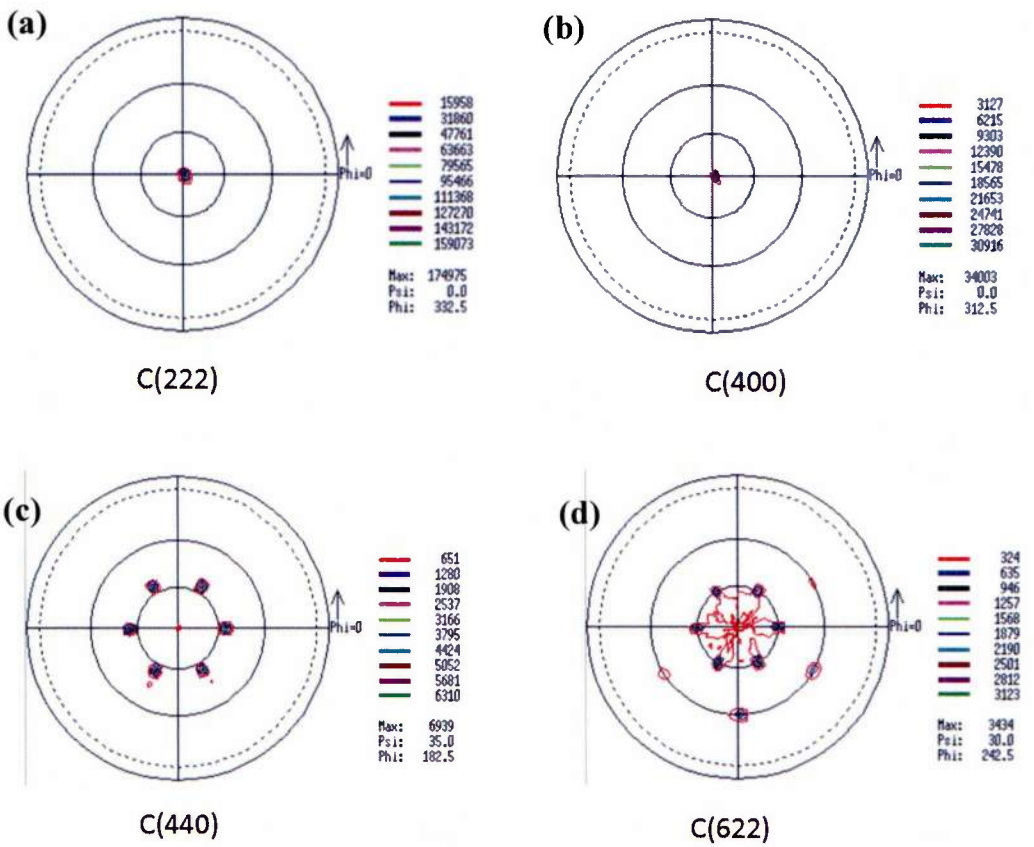

Figure 5.12. Pole figures of (a) C(222), (b) C(400), (c) C(440), and (d) C(622) planes for film 10B (650 °C, 50 sccm O_2, 0.5 Å / s) deposited on GaN showing strong in and out-of-plane texture.

Interestingly, sixfold symmetry was observed for the C(111) planes instead of the expected threefold symmetry. Similar sixfold symmetry was also present for bixbyite Sc_2O_3 grown epitaxially on GaN via molecular beam epitaxy and was attributed to a 180

° rotational twin.[101] Twinning of the C(111) plane has been used to explain sixfold orientation in other cubic bixbyite oxides grown on GaN.[102] For film 10B, as the film thickness increases, the large lattice mismatch (~20%) between GaN and Gd_2O_3 causes formation of defects within the film, which initiate polycrystalline growth as observed by the formation of the C(400) planes. Nevertheless, the excellent sixfold in-plane alignment of the C(111) crystallites suggests the possibility of epitaxy for a smaller Gd_2O_3 film thickness.

Figure 5.13 displays the pole figures for film 11B (650 °C, 50 sccm O_2, 200 mA) deposited on quartz using ion beam assisted deposition. As observed from the C(222) pole (Figure 5.13a), a very strong out-of-plane C(222) texture (94,000 counts) exists. The C(400) pole figure (Figure 5.13b) shows threefold symmetry of the C(111) poles at an angle of 55° from the surface normal, consistent with the theoretical angular difference (54.7°) between the C(222) and C(400) planes. The C(440) and C(622) poles also reveal the presence of in-plane orientation (Figure 5.13c and 5.14d, respectively), confirming that the film is heavily textured both in-and-out-of-plane. The spread of the contour lines is shown over approximately 5-10 degrees, showing strong in-plane orientation. The formation of biaxial texture on an amorphous substrate such as quartz shows the capability of using ion beam assisted deposition to tailor the orientation of the films.

Figure 5.14 displays the pole figures for film 11B (650 C, 50 sccm O_2, 200 mA) deposited on sapphire using ion beam assisted deposition. Note that the intensities are lower due to use of an iron filter to protect the diffractometer detector from damage due to high intensity. The iron filter decreases the measured intensity by approximately an order of magnitude.

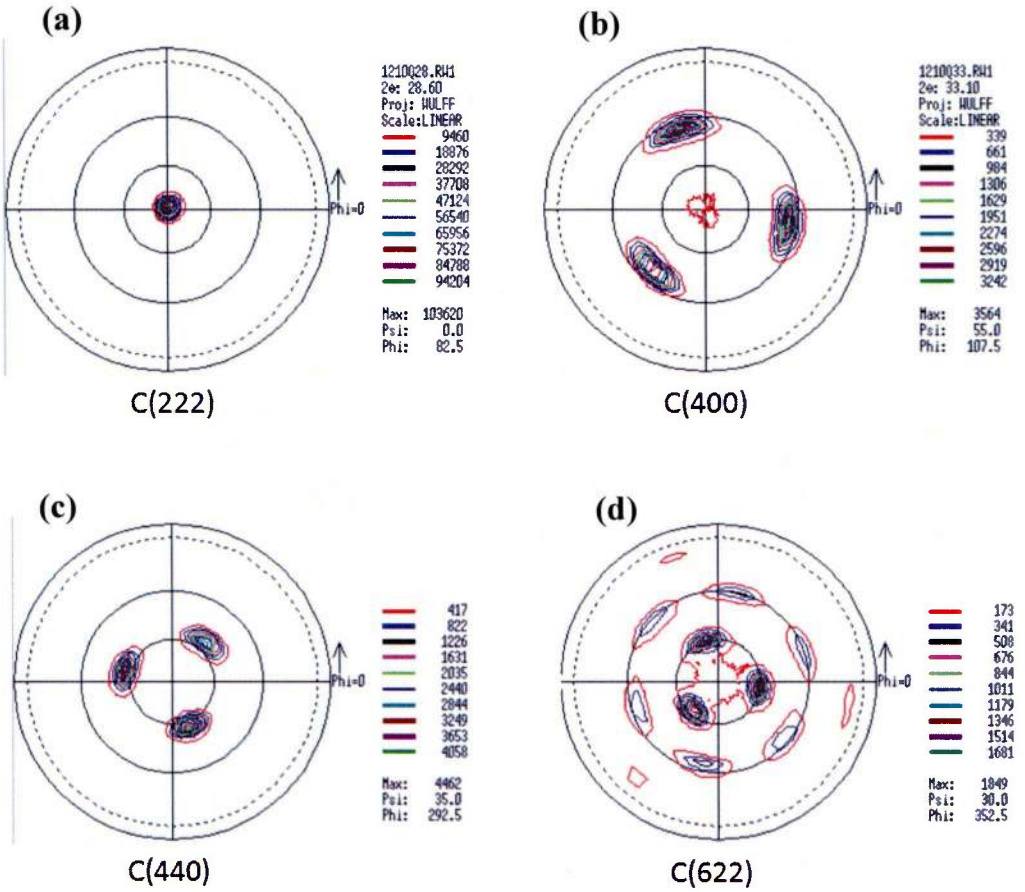

Figure 5.13. Pole figures of (a) C(222), (b) C(400), (c) C(440), and (d) C(622) planes for film 11B (650 °C, 50 sccm O_2, 0.5 Å / s, 200 mA) deposited on quartz using ion beam assisted deposition (IBAD) showing strong in and out-of-plane texture.

The pole figures for film 11B deposited on sapphire are similar to that of film 11B deposited on quartz. However, the spread in the contour lines is extremely small, suggesting excellent in-plane texture. This is likely due to the ability for the Gd and O atoms to order themselves along a single crystalline template as opposed to an amorphous substrate such as quartz. Despite the formation of a small amount of monoclinic phase (2%), the films are nearly epitaxial. This suggests that perhaps by slightly lowering the

ion beam energy, IBAD can facilitate the growth of thick epitaxial C(111) oriented Gd_2O_3 films.

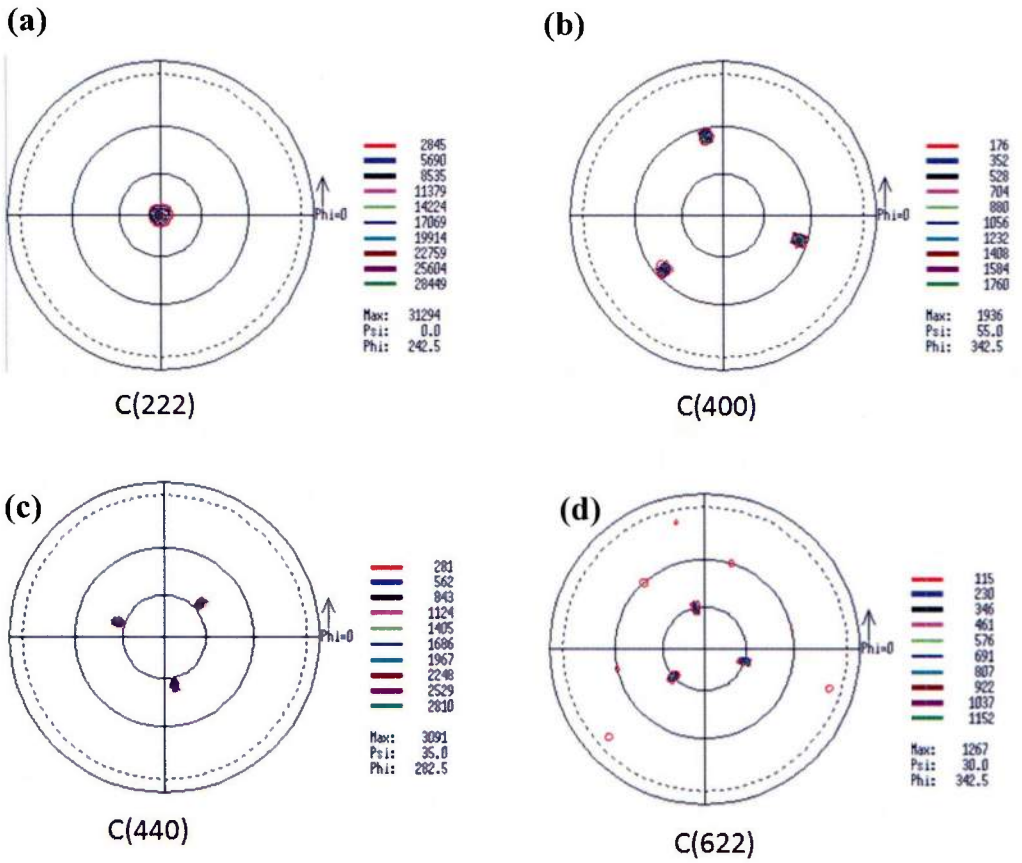

Figure 5.14. Pole figures of (a) C(222), (b) C(400), (c) C(440), and (d) C(622) planes for film 11B (650 °C, 50 sccm O_2, 0.5 Å / s, 200 mA) deposited on sapphire using ion beam assisted deposition (IBAD) showing very strong in and out-of-plane texture.

5.7. Conclusions

Single phase cubic films were deposited under select conditions at a deposition temperature of 250 °C for very thin films (< 50 nm). It was shown through XRD residual stress measurements that cubic phase films deposited under these conditions were under significant compressive stress. This compressive stress was hypothesized to be the driving force for the cubic to monoclinic phase transition. In order to determine

whether or not compressive stress could drive the phase transition, wafer curvature technique was used to determine the total residual stress in the Gd_2O_3 films deposited under different conditions. It was found that increasing the deposition temperature resulted in increased tensile stresses in the Gd_2O_3 films. The accompanying increase in cubic phase volume was attributed to both increased tensile stresses in the film and increased adatom mobility allowing for the formation of the cubic phase. The deposition rate was then lowered to < 1 Å / s at a deposition temperature of 650 °C which allowed for the deposition of 1 μm thick cubic phase films. Wafer curvature measurements showed that the cubic phase films possessed tensile stress approximately 100 MPa greater than the mixed phase films deposited at the same temperature with high deposition rate. In order to separate the effects of adatom mobility and residual stress on the phase stability, an experiment was designed using ion beam assisted deposition (IBAD) which allowed for the introduction of compressive stress in the film while keeping the adatom diffusion length on the film surface large. The experimental results confirmed the hypothesis of stress dependent phase stability. Increasing the amount of compressive stress in the Gd_2O_3 films through ion bombardment during growth as shown in Figure 5.15 resulted in driving the cubic to monoclinic phase transition. The bulk of the phase change occurs between 317 and 517 MPa of applied compressive stress for the experimental conditions studied.

The texture evolution of the Gd_2O_3 films was further investigated using θ-2θ, GIXRD depth profiling and pole figure analysis. θ-2θ analysis showed that the out-of-plane texture differed significantly based on the substrate type. GIXRD analysis showed that for pure cubic phase films deposited under low rates at 650 °C, the C(222) planes are

heavily textured near the substrate/film interface and that with increasing film thickness, other orientations begin to be favored. This is attributed to increased strain with increasing film thickness.

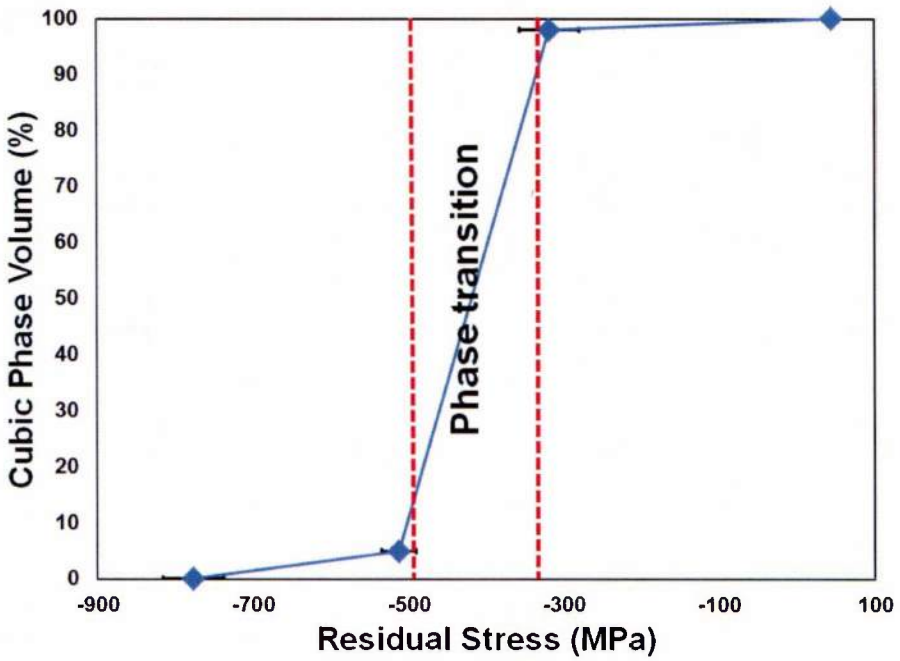

Figure 5.15. Relationship between residual stress and phase volume for films 11A (0 mA), 11B (200 mA), 11C (400 mA), and 11D (800 mA) grown on sapphire at 650 °C and 50 sccm O_2 under low growth rate of ~0.5 Å / s as a function of ion source current. The bulk of the phase transition occurs when the compressive residual stress is between 317 MPa and 517 MPa.

Pole figure analysis was employed to look at the in-plane texture of the Gd_2O_3 films. It was shown that mixed phase films deposited at low temperatures possess weak out-of-plane texture / random texture. Mixed phase films deposited at high temperatures possess a fiber texture, but lack the necessary adatom mobility to develop in-plane texture. For single phase cubic films grown under low rates of deposition, out-of-plane texture is observed on quartz substrates. However, weak and strong in-plane textures are

observed for sapphire and GaN substrates, respectively, and will be related to the film structure in Chapter 6. The use of ion bombardment resulted in the formation of moderate biaxial texture for films grown on quartz. For films grown on sapphire, a very strong biaxial texture is achieved with ion bombardment which adds additional energy to the system.

Chapter 6

Results and Discussion: Microstructure, composition, and interfacial phenomena of Gd_2O_3 films.

In this chapter, the effects of processing on film morphology, interfacial chemistry and composition will be discussed. Analysis of film morphology was primarily carried out by scanning electron microscopy (SEM), transmission electron microscopy (TEM), and atomic force microscopy (AFM). SEM was used to image the top surface of the films and examine grain size and surface porosity. TEM was used in conjunction with electron diffraction to investigate the cross sections of the Gd_2O_3 films, with specific emphasis on porosity, crystallinity, phase, orientation, and interfacial phenomenon. AFM was used to measure the surface roughness of the films. X-ray photoelectron spectroscopy (XPS) and energy dispersive x-ray spectroscopy (EDS) were performed on select films for compositional investigation.

Throughout this chapter, film processing and crystallographic structure will be linked to the film microstructure. The chapter will begin with characterization of set 8, composed of very thin Gd_2O_3 films (variable temperature, variable O_2 flow, < 50 nm thick), in order to understand the growth processes at the first stages of film growth. Then, discussion will move to the effect of deposition temperature on thick (> 1 μm) Gd_2O_3 film structure with emphasis on sets 2 (function of temperature, 200 sccm O_2 flow, ~1 – 2 μm) and 6 (function of temperature, 200 sccm O_2 flow, ~1 μm thick). The effect of oxygen flow will be discussed, with emphasis on sets 1(650 °C, function of oxygen flow, ~2 μm) and 4 (250 °C, function of oxygen flow, ~1 μm). Characterization of sets 3 (250 °C, 200 sccm O_2, function of film thickness) and 9 (650 °C, 200 sccm O_2, function

of film thickness) will cover the effect of film thickness on Gd_2O_3 films. The effects of low deposition rate and substrate type on film structure will be examined with characterization of films from set 10. Furthermore, the effects of ion bombardment on the microstructure of the films will be discussed in set 11 (650 °C, 50 sccm O_2, 0.5 A/s, function of ion beam current). Lastly, characterization of select films subject to heat treatments will be presented and discussed.

6.1. The effects of processing on Gd_2O_3 film structure and interface

6.1.1. The structure of thin (< 50 nm) Gd_2O_3 films deposited on silicon (111)

To gain a better understanding of the growth mechanisms present in the thick (> 1 μm) Gd_2O_3 films, it is important to look at the initial stages of film growth. Therefore, the structure and morphology of Gd_2O_3 thin films from set 8 (< 50 nm thick Gd_2O_3 films) were examined. Figure 6.1a – 6.1c displays the top surface SEM images of films 8A (250 °C, 200 sccm O_2, 47 nm thick), 8B (250 °C, 25 sccm O_2, 41 nm thick), and 8E (650 °C, 200 sccm O_2, 20 nm thick), respectively. As shown from x-ray diffraction measurements in section 5.1, film 8A deposited at 250 °C and under 200 sccm O_2 flow, was fully cubic and possessed random orientation. The film surface as shown in Figure 6.1a is characterized by clusters of small grains separated by voids. Figure 6.1b displays the top surface SEM image of mixed phase film 8B deposited at 250 °C under 25 sccm O_2 flow. This film shows a denser surface morphology with more surface continuity. The presence of voiding between the grains is not as apparent. This is due to less oxygen being present in the chamber resulting in greater Gd adatom diffusion length and better surface coverage leading to less entrapped oxygen within the film. This will be discussed further in section 6.1.3. Film 8c displays the top surface SEM image of mixed phase film 8E

deposited at 650 °C under 200 sccm O_2 flow. This film has a very dense surface morphology and possesses a larger grain diameter than the film deposited at 250 °C as a result of the greater adatom mobility supplied by elevated temperature (650 °C) which allows for densification and grain growth consistent with the structure zone model.[15]

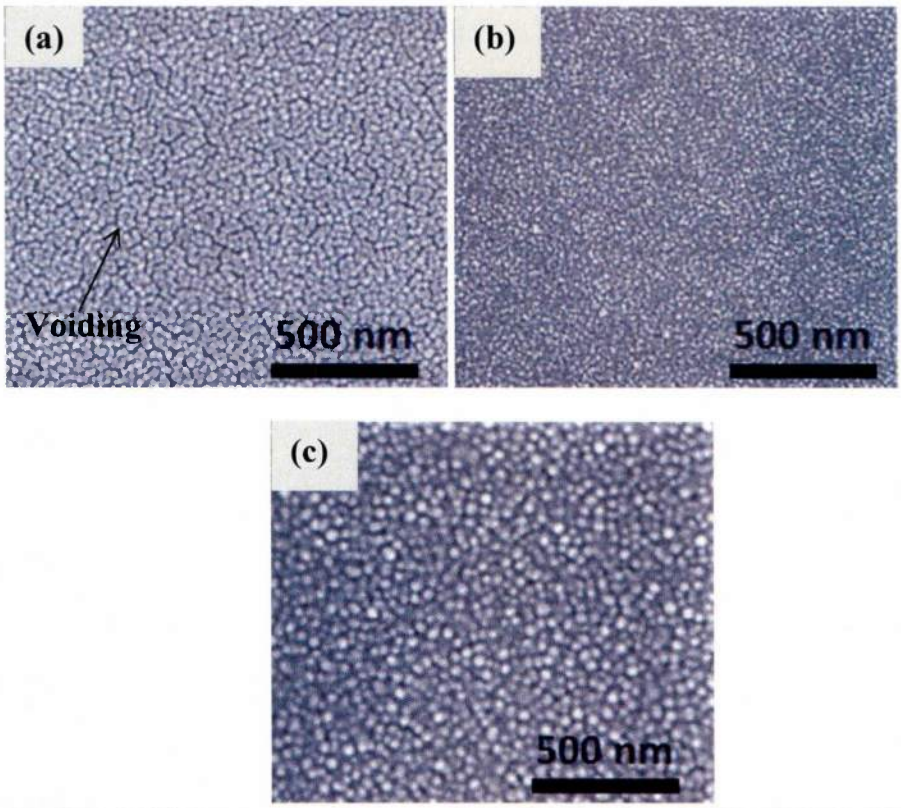

Figure 6.1. Select SEM top surface images of thin Gd_2O_3 films (a) 8A (250 °C, 200 sccm O_2, 47 nm), (b) 8B (250 °C, 25 sccm O_2, 41 nm), and (c) 8E (650 °C, 200 sccm O_2, 20 nm) deposited on silicon.

For further analysis of the structure and phase, TEM analysis of the film cross sections was employed. Figure 6.2 shows the low-magnification bright-field TEM images of thin Gd_2O_3 films 8A and 8E grown at (a) 250 °C and (b) 650 °C under 200 sccm O_2 flow, collected along the Si <110> zone axis under multibeam diffraction

conditions. As shown in Figure 6.2a, the surface of the film grown at 250 °C appears to be rough, while the surface of the film grown at 650 °C is relatively smooth (Figure 6.2b).

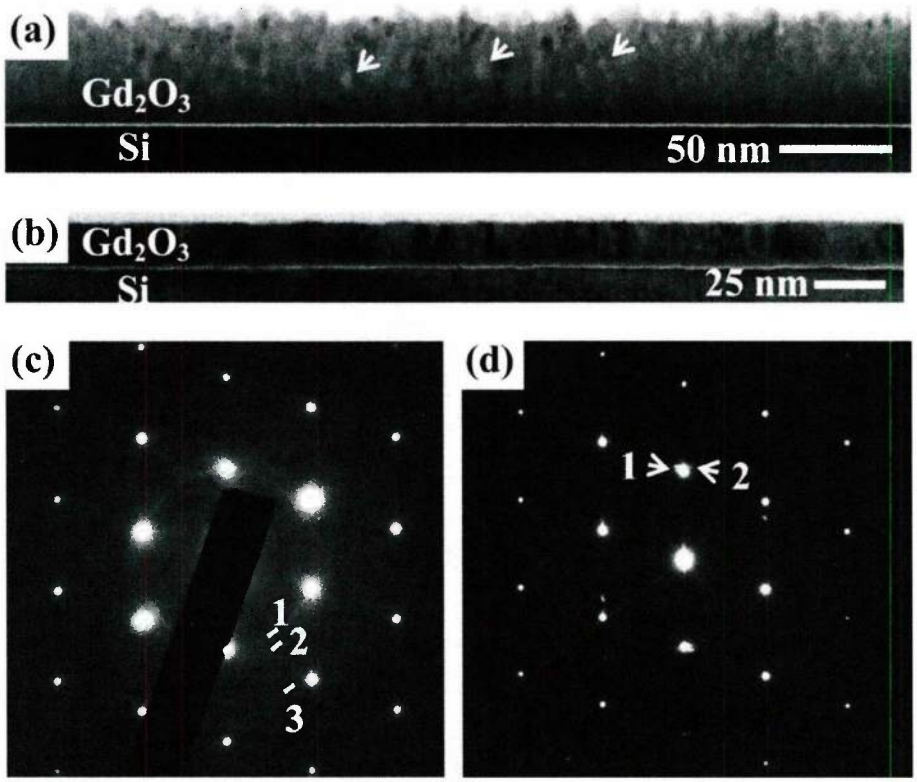

Figure 6.2. Low-magnification bright-field TEM images of thin Gd_2O_3 films (a) 8A (250 °C, 200 sccm O_2, 47 nm) and (b) 8E (650 °C, 200 sccm O_2, 20 nm). The arrows denote porous regions. The corresponding SAD patterns are shown in (c) and (d), respectively.

For both heterostructures, a thin layer with a bright contrast exists at the film/substrate interface. Nanometer-size pore-like features with a relatively brighter contrast than the rest of the film were also observed in the 250 °C grown film, as indicated by the arrows in Figure 6.2a. High-resolution TEM indicated that those features were disordered domains surrounded by the crystallites. The relatively brighter contrast of these pore-like features suggests that these features are probably more oxygen-rich than the Gd_2O_3 crystallites. In comparison to 8A (250 °C), the thin film 8E grown at

650 °C appears to be dense without pore-like features, in similar fashion to the surface images shown in Figure 6.1c.

It is important to note that film 8E (20 nm) is thinner than film 8A (47 nm), making direct comparison of the two films difficult. However, film 8E clearly has a larger grain size than 8A even though 8E film thickness is approximately half that of 8A. Generally, surface roughness and grain size increase with film thickness. However, as will be shown later in section 6.2, thick Gd_2O_3 films (>1 μm) deposited at 650 °C remain dense throughout the nucleation region which is approximately 200 nm thick before the onset of columnar growth. Therefore, we believe that a similar structure to film 8E will be observed even for films 50 nm thick. Instead, the difference in the structure between 8A and 8E can be explained by the greater surface diffusion present for samples deposited at higher substrate temperatures. For film 8A, the deposition temperature of 250 °C results in a structure with small crystallites separated by voids which cannot be filled due to the low surface mobility of the adatoms. The increased temperature of 650 °C allows the adatoms to diffuse further resulting in improved surface coverage and higher density.

Figures 6.2c and 6.2d are SAD patterns corresponding to the brightfield TEM images shown in Figures 6.2a and 6.2b, respectively. Each SAD pattern was collected from a region containing both the Si substrate and the Gd_2O_3 film, in which the strong spots are from the single crystalline Si substrate while the reflections from the film are rather weak due to the low film thickness. As shown in the SAD patterns, the reflections from 8A (250 °C) and 8E (650 °C) are different, indicating that the films have different phases and microstructure. For 8A, the thin film grown at 250 °C, the reflections

observed in Figure 6.2c can be described as nearly continuous rings, indicating that the film consists of small crystallites with random orientations. Indexing the SAD pattern (Figure 6.2c) of 8A (250 °C) suggests that it is predominantly cubic with the three rings 1, 2, and 3 corresponding to the C(222), C(400), and C(440) reflections of cubic Gd_2O_3, respectively. In comparison, the reflections shown in Figure 6.2d have a short arc/spot appearance, indicating a textured structure for the 650 °C grown film (8E). The two short arcs 1 and 2 in the diffraction pattern shown in Figure 6.2d, correspond to the C(222) reflection of cubic Gd_2O_3 and the M(-402) reflection of monoclinic Gd_2O_3, respectively. This confirms that the 650 °C film (8E) consists of both cubic and monoclinic Gd_2O_3 phases (mixed phase).

In Figure 6.2a, several regions appear to be disordered besides the pore-like region indicated by the arrows. While some of those regions may be amorphous, we believe that the majority of them are crystalline as indicated by the SAD pattern. The disordered appearance of those regions in the high-resolution TEM image is most likely related to the crystallographic orientations of the crystallites. The crystallites were likely oriented in such directions that the *d*-spacings of the crystal planes parallel to the incident electron beam are beyond the resolution of the TEM, which led to the disordered appearance. Further analysis in the FEI Titan 3 microscope may assist in resolving the disordered appearance.

To further support the SAD pattern results, high resolution TEM images were obtained for films 8A and 8E as shown in Figure 6.3.

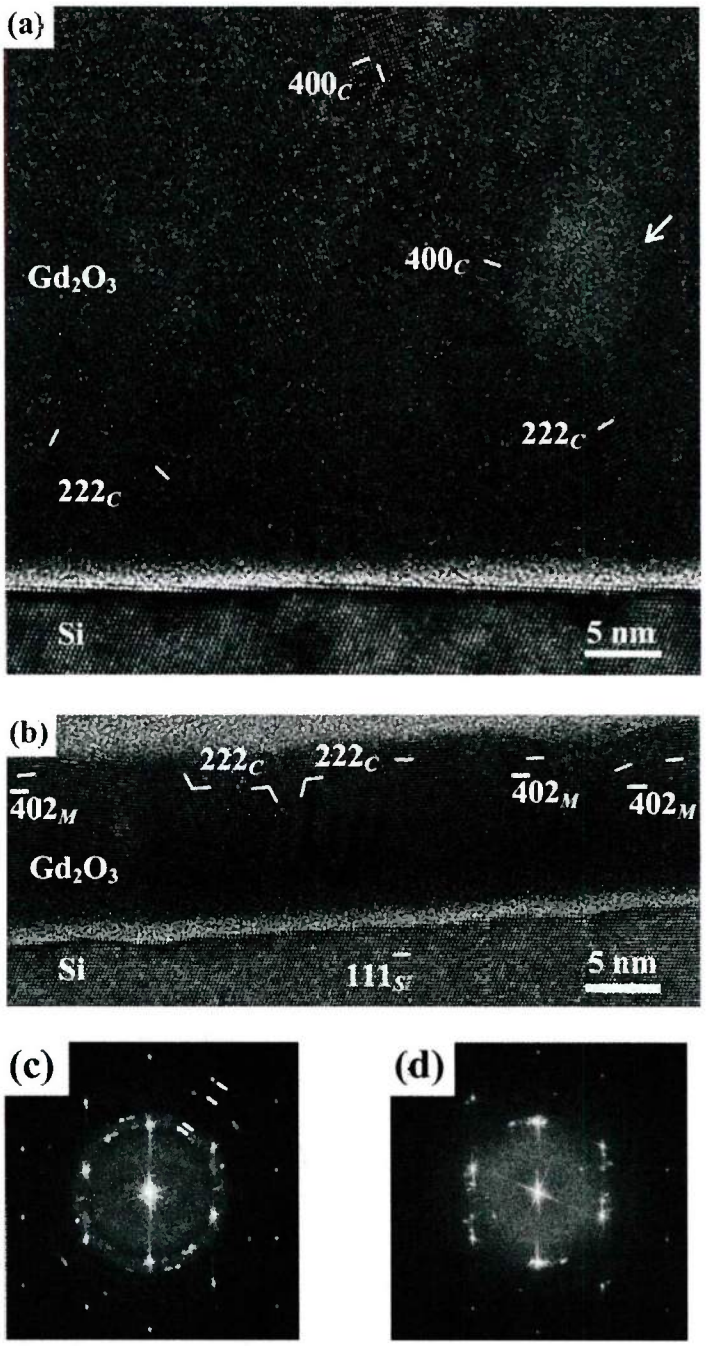

Figure 6.3. High-resolution TEM images of thin Gd_2O_3 films (a) 8A (250 °C, 200 sccm O_2, 47 nm) and (b) 8E (650 °C, 200 sccm O_2, 20 nm). A few crystallographic planes were indicated by short white lines and labeled. FFT patterns of (c) 8A and (d) 8E. Four spotty rings are marked by short white lines in (c).

A high-resolution TEM image of the 250 °C grown Gd_2O_3 film (8A) is shown in Figure 6.3a, which reveals crystallites with different orientations and sizes on the order of ~10 nm. The Fast Fourier Transform (FFT) pattern of the image is shown in Figure 6.3c, in which four spotty rings are apparent. The spacings of these 4 spotty rings correspond to the *d*-spacings of the cubic C(222), C(400), C(440), and C(622) planes, thus indicating that the 250 °C film is cubic.

Figure 6.3b is a typical high-resolution TEM image of the 650 °C grown Gd_2O_3 film (8E), with the corresponding FFT pattern shown in Figure 6.3d. The film consists of domains with sizes on the order of ~10 – 20 nm. Both cubic and monoclinic domains were observed, with the C(222) and M(-402) planes nearly parallel to the (111) plane of the Si substrate. High-resolution TEM images collected from the interface regions of 8A (250 °C, Figure 6.3a) and 8E (650 °C, Figure 6.3b), indicate a bright layer that is disordered with a thickness of ~2 nm. These disordered layers are SiO_x-rich, similar to the interface layers between electron-beam evaporation deposited thin polycrystalline Gd_2O_3 films on Si substrates reported in the literature.[60,103,104]

The effects of temperature clearly had a substantial impact on film phase, growth and morphology of the thin films from set 8. The initial growth characteristics set the template for the resulting growth of the thick Gd_2O_3 films. In the next sections, the effects of increasing deposition temperature, oxygen flow, and film thickness will be discussed for micron thick Gd_2O_3 films.

6.1.2. Effects of temperature on Gd_2O_3 film morphology deposited on Si(111)

Figures 6.4a – 6.4e show SEM top surface images for thick (~1-2 μm) Gd_2O_3 films 2A-2E deposited as a function of temperature under 200 sccm O_2 flow.

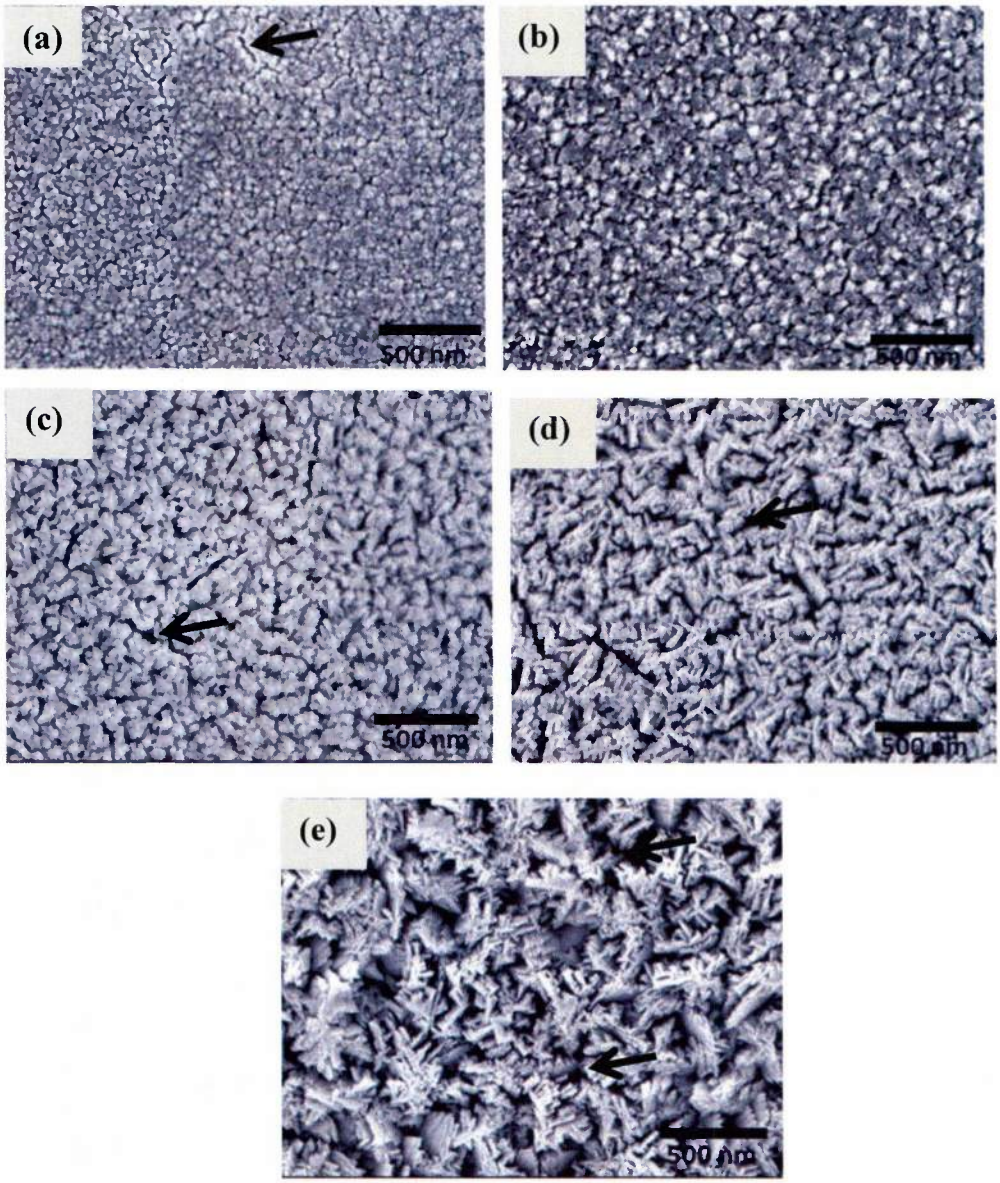

Figure 6.4. SEM top surface images of Gd_2O_3 films (a) 2A (250 °C), (b) 2B (350 °C), (c) 2C (450 °C), (d) 2D (550 °C), and (e) 2E (650 °C) deposited as a function of temperature under 200 sccm O_2 flow at high rates (> 5 Å / s). Arrows denote voiding.

As observed in Figure 6.4a, film 2A deposited at 250 °C shows film growth leading to a slightly porous surface morphology with small grain sizes of approximately 50 nm separated by voids.

As the deposition temperature is increased to 350 °C (film 2B), the surface becomes more textured with voiding still being observed as shown in Figure 6.4b. Further increasing the deposition temperature to 450 °C (Film 2C, Figure 6.4c) results in significant grain growth and a marked increase in the surface porosity/voiding. At deposition temperatures of 550 °C (film 2D) and 650 °C (film 2E), this effect becomes more pronounced as shown in Figures 6.4d and 6.4e, respectively. The top surface image of sample 2E deposited at 650 °C shows an extremely complex, rough, and porous surface morphology. Image analysis was attempted in order to obtain grain size for the high temperature grown films, but the rough, irregular surface made it difficult to obtain accurate values. However, the increase in grain size does correlate with increase in crystallite size as calculated using Scherrer's formula from the x-ray diffraction measurements in section 4.2

As previously discussed in section 2.4.3, coatings deposited by vapor techniques at high substrate temperatures typically exhibit a dense columnar or equiaxed grain structure due to the high adatom mobility which allows for structural rearrangement and densification according to the structure zone model presented by Thornton[43] and Messier.[15] However, due to the relatively high rate of evaporation for films 2A-2E, it is possible that the metal flux is arriving so quickly that the surface mobility is limited. This results in an effect called shadowing, in which high points on the growing film surface receive more metal flux than the valleys resulting in increased void formation.[105] Due to the high rates of deposition, the adatom mobility is not sufficiently high for the atoms to provide full surface coverage so the atoms coalesce in the high flux regions. When this occurs, voids begin to form between the columns. Due to geometrical

constraints, the shadowing effectively screens the flux of arriving metal atoms and the low mobility prevents the voids from being filled. However, this may not solely explain the observed surface morphology as a function of temperature observed in Figure 6.4.

Based on the fact that higher temperature results in greater surface mobility, it would be expected that the effect of shadowing would be more pronounced in low temperature films and would lead to increased porosity. Indeed, in section 6.1.1, it was shown that this is the case for very thin (< 50 nm) Gd_2O_3 films, where film 8E deposited at 650 °C was significantly denser than film 8A deposited at 250 °C. However, this appears to be different in the case of thicker films (> 1 μm), where film 2E deposited at 650 °C appears to be more porous than film 2A deposited at 250 °C (Figure 6.4). This discrepancy is explained by the combined effects of temperature and shadowing during Gd_2O_3 film growth. At low deposition temperatures, there is insufficient mobility for significant grain growth or preferential texturing. This leads to a high density of nuclei and a low grain coalescence rate. As the film grows thicker, the low surface mobility results in the formation of small voids between the crystallites. When the deposition temperature is increased, more surface energy is provided resulting in preferential growth of large columnar grains at a deposition temperature of 650 °C. While the columns themselves are dense, they may grow at different rates or in various orientations leading to non-uniform grain growth. These protruding columns act to block the incoming vapor flux. The atoms coalesce at the column tips, resulting in porosity between the columns. As the columns grow larger with increasing film thickness, the voiding between them increases, resulting in a porous top surface as shown in Figure 6.4e. An additional reason as to the complex Gd_2O_3 surface morphology can be explained by the increase in

monoclinic phase content with increasing film thickness. This will be discussed in greater detail in section 6.1.4

Grain size measurements were performed on the SEM surface images at magnification of 50,000 × for Gd_2O_3 films deposited at 250 °C. Figures 6.5a and 6.5b display an SEM surface image and the Clemex analytical software technique for grain size measurement of sample 2A deposited at 250 °C under 200 sccm O_2 flow. The colored areas in Figure 6.5b correspond to the individual grains.

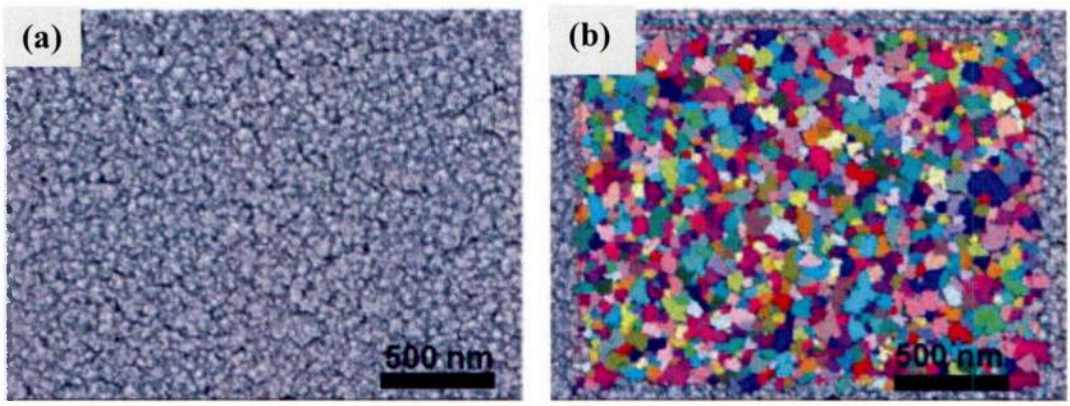

Figure 6.5. (a) SEM surface image of film 2A (250 °C, 200 sccm O_2, 1.26 μm) and (b) the corresponding grain size measurement technique. The measured grain size was 51.2 ±1.6 nm for film 2A deposited at 250 °C under 200 sccm O_2 flow.

Ten SEM images were obtained from various locations on the surface of each film and subsequently measured by the Clemex analytical software grain size characterization technique. Only the grain size of films deposited at 250 °C was quantitatively measured. Films deposited at elevated temperatures displayed a large amount of surface texturing resulting in the previously discussed irregular grain structure and therefore, grain size could not be quantitatively measured for those samples accurately.

TEM cross sectional samples were prepared in order to further investigate the effect of temperature on Gd_2O_3 film microstructure. Film 6A (250 °C, 200 sccm O_2,

1.07 μm), deposited under similar conditions as 2A, was used for analysis. Figure 6.6 shows (a) low-magnification and (b) higher magnification bright-field TEM images of Gd_2O_3 film 6A grown at 250 °C under 200 sccm O_2 flow, collected along the Si<112> zone axis.

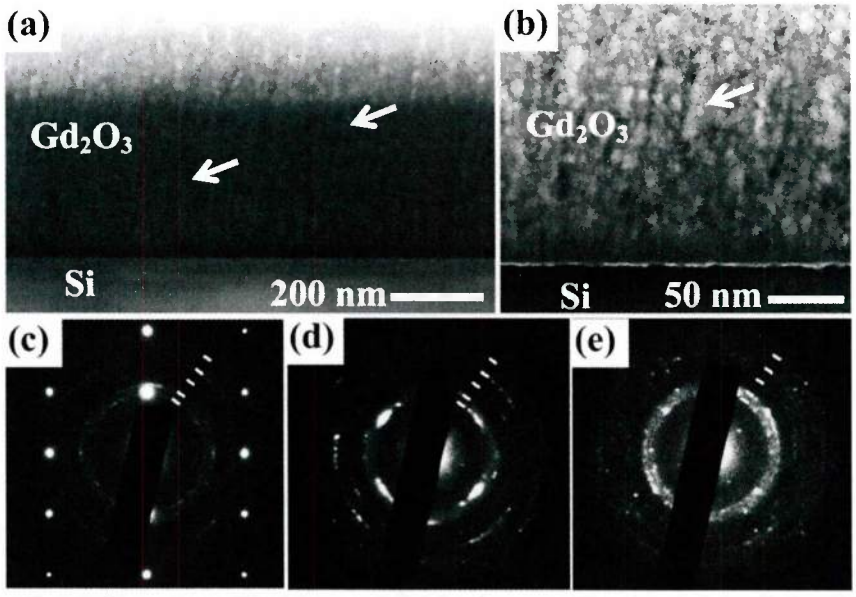

Figure 6.6. (a) Low-magnification and (b) high-magnification bright-field TEM images of thick Gd_2O_3 film 6A (250 °C, 200 sccm O_2, 1.07 μm). The arrows denote porous regions. SAD patterns were collected from the (c) interfacial region, (d) the middle section, and (e) the top section of the film, respectively. Five primary diffraction rings are marked by short white lines in each diffraction pattern for identifying crystal planes and phases present.

Film 6A consists of a high density of porous regions as shown by the arrows in Figure 6.6a-b. In addition, a disordered layer with a relatively brighter contrast is also present at the film/substrate interface (Figure 6.6b). Such a layer is not apparent in the lower magnification image (Figure 6.6a), presumably due to the small thickness of the layer and the overall dark contrast of the interface region caused by the large TEM specimen thickness. Figures 6.6c–e show SAD patterns collected from the interfacial

region consisting of both the bottom section of the film and the Si substrate, the middle section, and the top section of the film, respectively.

The diffraction rings in the SAD patterns suggest that thick film 6A contains randomly oriented grains with small sizes, similar to the thin 250 °C grown film (8A) discussed in section 6.1.1. In Figure 6.6c, the five diffraction rings (with increasing radii) correspond to the C(222), C(400), C(422), C(440), and C(622) reflections of cubic Gd_2O_3, respectively. Therefore, the bottom section of the film is predominantly cubic, consistent with the observation from the thin 250 °C grown film (8A). The diffraction patterns from the middle and the sections of the film shown respectively in Figures 6.6d and 6.6e also appear to be dominated by five diffraction rings of cubic Gd_2O_3. However, extra reflections from another phase are also visible. In particular, additional reflections are not present between the strong C(222) and C(400) rings in the bottom section of the film (Figure 6.6c), yet weak reflections are discernible between these two rings in SAD patterns collected from the middle (Figure 6.6d) and top (Figure 6.6e) sections of the film as shown in Figures 6.6d and 6.6e. Considering that the high intensity reflections of monoclinic Gd_2O_3, M(111), M(401), M(-402), M(003), M(310), and M(-112), lie near or in between the cubic C(222) and C(400) rings, the SAD results indicate the formation of a small amount of monoclinic phase in the middle and top sections of the film. Therefore, the monoclinic phase gradually formed as the thickness of film 6A increased. This confirms the earlier prediction of the occurrence of a phase transition with increasing Gd_2O_3 film thickness, which was based on the x-ray diffraction results presented in section 4.4. Additionally, high-intensity arcs are observed in Figure 6.6d, indicating the presence of regional texture in the middle section of the film.

It is worth noting that a diffuse ring overlaps with the first two diffraction rings (C(222) and C(400)) of the crystalline Gd_2O_3 in Figures 6.6d and 6.6e. The diffuse ring arose due to the increased volume of amorphous porous regions for the film in the growth direction. In comparison, the diffraction pattern collected from the interface region (Figure 6.6c), consists of sharp diffraction rings from crystalline Gd_2O_3. Similarly, in the diffraction pattern of the 250 °C heterostructure with the thin Gd_2O_3 film 8A shown in Figure 6.2c, the Gd_2O_3 reflections were dominated by sharp rings 1, 2, and 3. Diffuse rings associated with amorphous Gd_2O_3 were not observed in either Figure 6.2c or Figure 6.6c, which strongly suggests that the thin film (8A) and the bottom part of the thick film (2A) are primary crystalline. This indicates that amorphous like regions formed as the film thickness grew larger, possibly a result of the cubic to monoclinic phase transition.

Figure 6.7 shows (a) low-magnification and (b) higher magnification bright-field TEM images of Gd_2O_3 film 6E (650 °C, 200 sccm O_2, 0.87 μm) grown at 650 °C, collected along the Si<112> zone axis. The film, especially the top section, possesses a columnar structure with large grains elongating in the growth direction. The film was dense near the film/substrate interface, consistent with the structure of the 20 nm thin film (8E) deposited at 650 °C. Pores formed between the columnar grains as the growth proceeded as denoted by the arrows in Figure 6.7(a). This is due to the effects of columnar grain growth, shadowing, and increasing monoclinic phase content previously discussed. As a result of the increased porosity near the top of the film, the surface becomes very rough.

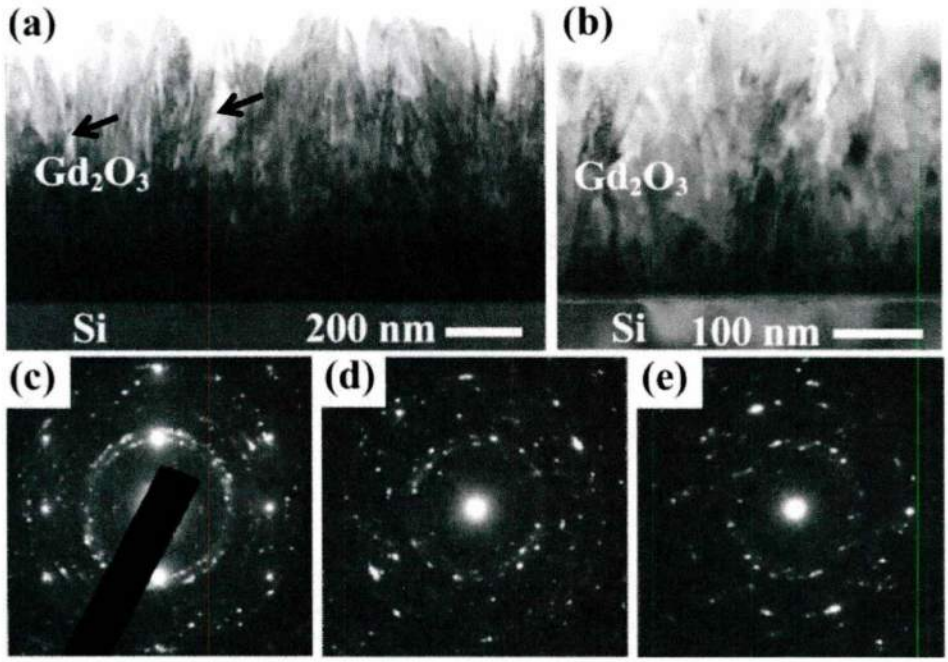

Figure 6.7. (a) Low-magnification and (b) high-magnification bright-field TEM images of thick Gd_2O_3 film 6E (650 °C, 200 sccm O_2, 0.87 μm). The arrows denote porous regions. SAD patterns collected from the (c) interfacial region, (d) the middle section, and (e) the top section of the film, respectively.

The SAD patterns collected from the interfacial region, the middle section, and the top section of film 6E (650 °C, 200 sccm O_2, 0.87 μm) are shown in Figures 6.7c – 6.7e, respectively. As revealed in Figure 6.7c, the diffraction rings from the bottom section of the 650 °C film appear to be relatively continuous. Therefore, the grains near the film/substrate interface have a small size, similar to those in the thin 650 °C film 8E. The Gd_2O_3 diffraction rings appear to be less continuous in SAD patterns collected from the middle and the top sections of the film as a result of increasing grain size suggesting greater crystallinity in the film growth direction. Diffraction consists of both monoclinic and cubic Gd_2O_3 reflections, with monoclinic rings dominating as the film grows thicker (Figure 6.7c).

The change in surface morphology as a function of deposition temperature was further investigated by AFM surface topography. Figure 6.8a shows a fairly smooth and uniform surface for sample 2A deposited at 250 °C under 200 sccm O_2 flow. AFM topography of film 2E deposited at 650 °C (Figure 6.8b) shows a much rougher and textured film supported by the TEM cross section shown in Figure 6.7

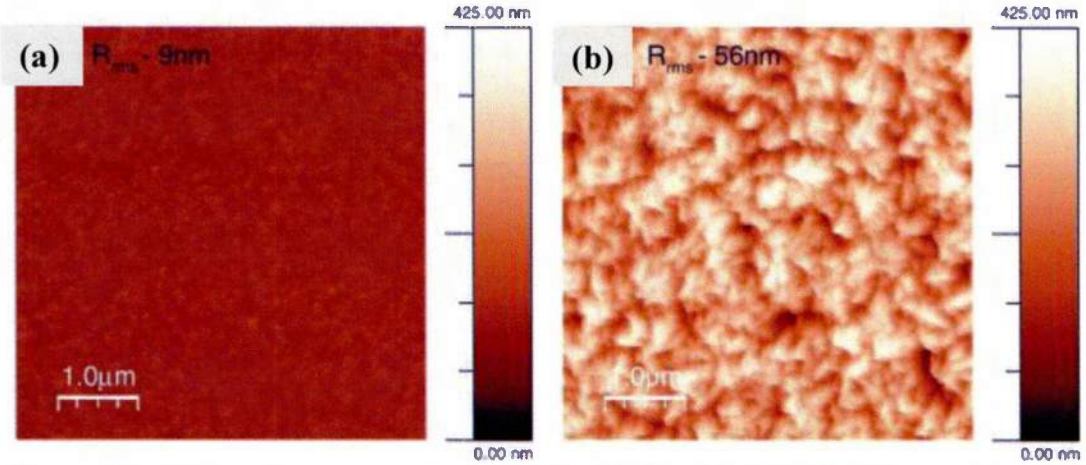

Figure 6.8. AFM surface topography of Gd_2O_3 (a) film 2A (250 °C, 200 sccm O_2, 1.26 µm) and (b) film 2E (650 °C, 200 sccm O_2, 2.05 µm).

RMS surface roughness measurements were made for each sample by calculating an average value from three topography scans taken over 1 μm^2 and 5 μm^2 areas. An increase in surface roughness from 8.6 ± 0.5 nm to 56.6 ± 1.2 nm is observed with increasing deposition temperature from 250 °C to 650 °C. A peak to valley roughness of approximately 400 nm is observed in Gd_2O_3 film 2E deposited at 650 °C, suggesting that the porosity observed between the columns in the cross sectional TEM image is significant. This could have deleterious effects on electrical fabrication and properties resulting in poor contact uniformity, increased leakage currents, and reduced dielectric constant.

6.1.3. Effect of oxygen flow on the Gd_2O_3 film morphology of s deposited on Si(111)

The effects of O_2 flow on the microstructure of the thick Gd_2O_3 films from set 1 (650 °C, function of O_2, ~2 μm) and set 4 (250 °C, function of O_2, ~1 μm) were examined via TEM, SEM, and AFM. The O_2 flow not only affects the film phases, but also impacts the film porosity and the film/substrate interfacial reaction region. As discussed in section 6.1, for thin films (< 50 nm, set 8), lowering the oxygen flow from 200 sccm (film 8A) to 25 sccm (film 8b) for films deposited at 250 °C resulted in a denser surface morphology with less voiding which was attributed to adatom mobility during growth. A similar trend is observed for thick Gd_2O_3 films deposited at 250 °C (set 4).

Figure 6.9 shows the SEM top surface images for set 4 (250 C, function of O_2 flow, ~1 μm). The surface of film 4A (Figure 6.9a) deposited under 25 sccm O_2 flow shows a very dense and textured surface morphology. The grains are well defined with sharp edges. As the O_2 flow is increased to 50 sccm, low voiding between the grains is observed, though the general structure is preserved. As the oxygen flow is increased to 100 sccm (film 4C, Figure 6.9c) and 150 sccm (film 4D, Figure 6.9d), the surface becomes increasingly less textured and more porous. Finally, for film 4E (Figure 6.9e) deposited under 200 sccm O_2 flow, a significant amount of surface porosity is observed. The grains also possess a more spherical geometry than the films deposited at lower oxygen flow (25 – 150 scm) which possessed pyramidal geometry. These observations are supported by the diffraction patterns displayed in section 4.4 which showed improved crystallinity and reduced FWHM for films deposited at low oxygen flow. Additionally, the cubic phase volume fraction (Table 4.4) increased with increasing oxygen flow which may be related to the observed structure.

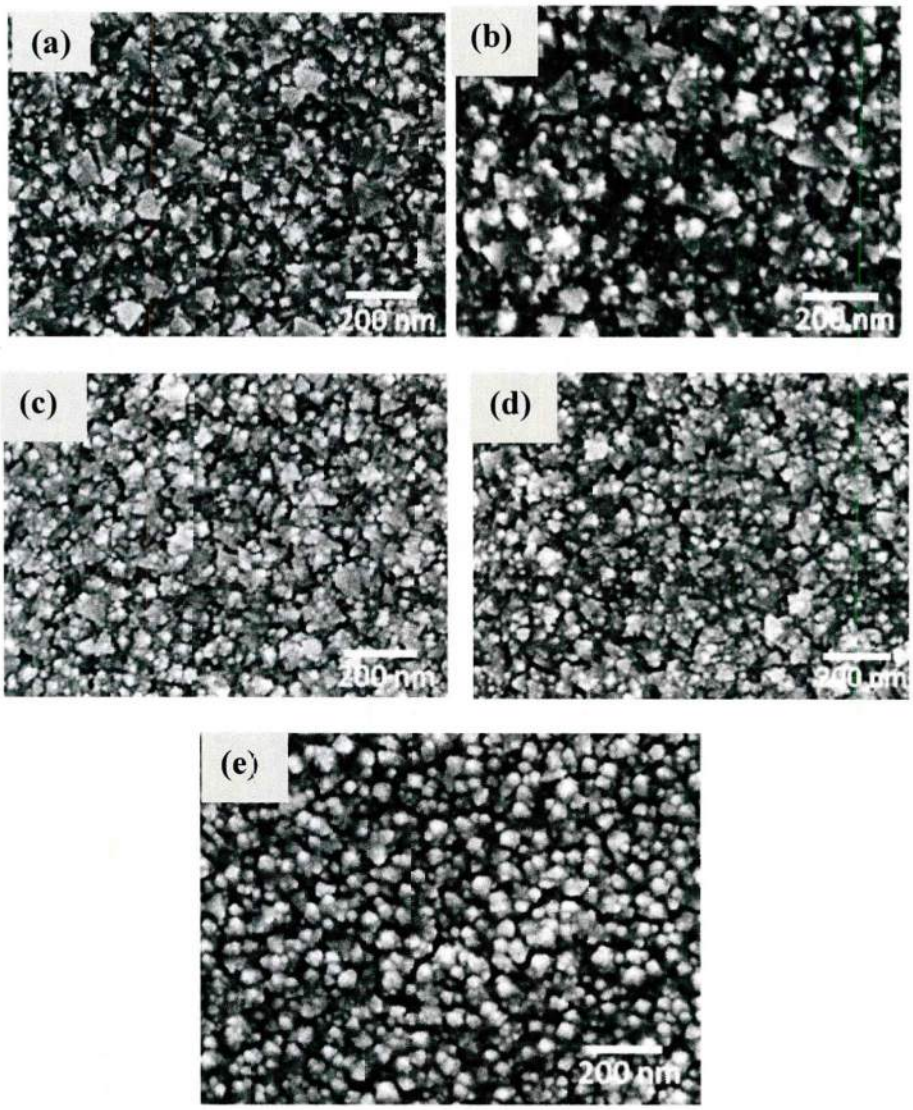

Figure 6.9. SEM top surface images of Gd_2O_3 films (a) 4A (25 sccm O_2), (b) 4B (50 sccm O_2), (c) 4C (100 sccm O_2), (d) 4D (150 sccm O_2), and (e) 4E (200 sccm O_2) deposited as a function of oxygen flow at 250 °C at high rates (> 5 Å / s).

The increased porosity observed in the higher O_2 flow films can be described by the effects of adatom mobility similar to the case of the thin (<50nm) films discussed in section 6.1. Increasing the amount of oxygen in the chamber reduces the Gd adatom diffusion length and results in poor surface coverage. Due to shadowing of the incoming

Gd flux, the effects of poor adatom mobility are compounded as the film grows thicker resulting in a more pronounced porosity between the grains for thicker films.

For further understanding of oxygen flow effects on the thick Gd_2O_3 films deposited at 250 °C, TEM analysis was performed. Figure 6.10 shows (a) low-magnification and (b) high-magnification bright-field TEM images of 1.11 μm thick Gd_2O_3 film 7A grown at 250 °C using an oxygen flow of 50 sccm, collected along the Si<112> zone axis. TEM analysis suggests that film 7A (250 °C, 50 sccm O_2, 1.1 μm) also consists of small crystallites surrounded by a few porous regions, similar to film 6A (250 °C, 200 sccm O_2, 1.07 μm Figure 6.6). In addition, a thin interface layer with a relatively brighter contrast is present. Figures 6.10c – 6.10e show SAD patterns collected from the interfacial region consisting of both the bottom section of the film and the Si substrate, the middle section, and the top section of the film, respectively.

The diffraction rings in the SAD patterns suggest that the film contains randomly oriented grains with small sizes, similar to the 250 °C film (6A) grown under 200 sccm O_2. The SAD pattern from the bottom section of the film shown in Figure 6.10c is similar to that of 6A (Figure 6.2c), indicating that the bottom part of film 7A grown under 50 sccm is also predominantly cubic. However, some weak spots did exist between the strong C(222) and C(400) rings in Figure 6.10c, suggesting that a small amount of monoclinic phase formed near the film/substrate interface with lower O_2 flow (50 sccm). Furthermore, as shown in Figures 6.10d and 6.10e, many diffraction rings from monoclinic Gd_2O_3 were perceived in the SAD patterns from the middle and the top sections of the film. These results suggest qualitatively that more monoclinic Gd_2O_3

formed during the growth under 50 sccm O_2 (7A) than under 200 sccm O_2 (6A), consistent with the x-ray diffraction results presented in section 4.4.

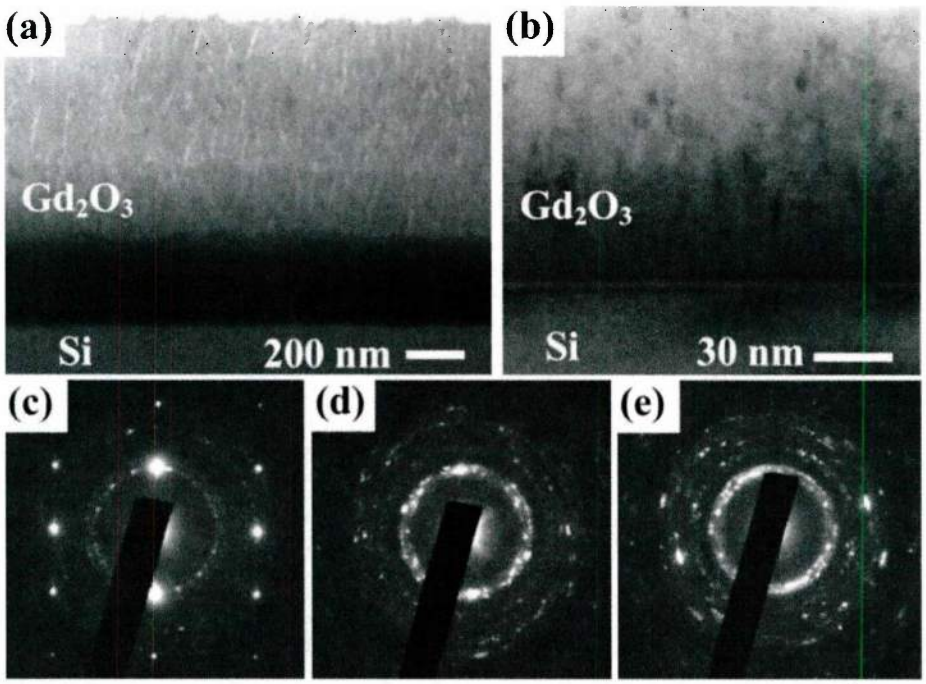

Figure 6.10. (a) Low-magnification and (b) high-magnification bright-field TEM images of thick Gd_2O_3 film 7A (250 °C, 50 sccm O_2, 1.11 μm). SAD patterns collected from the (c) interfacial region, (d) the middle section, and (e) the top section of the film, respectively.

A careful comparison of the TEM images from the thick 250 °C films grown using different O_2 flows revealed differences in the microstructure. As demonstrated in Figures 6.2a, 6.2b, 6.10a, and 6.10b, a lower O_2 flow of 50 sccm led to reduced film porosity and a more homogeneous thin interfacial disordered SiO_x layer as compared to the films deposited at higher O_2 flow (200 sccm). These differences in the microstructure may be explained qualitatively in terms of the O_2 flow reducing Gd adatom mobility. The lower O_2 flow allowed more time for the Gd atoms to diffuse on the surface before reacting with oxygen, which leads to a more complete surface coverage of Gd_2O_3. In

comparison, the high O_2 flow reduced the Gd diffusion length on the surface, thus leading to the formation of Gd_2O_3 nanocrystallites and porous regions in between.

Figure 6.11 shows the top surface images for films from set 1 deposited as a function of oxygen flow at a deposition temperature of 650 °C. For film 1A (Figure 6.11a) deposited under 50 sccm O_2 flow, an irregular and complex surface morphology is observed. Distinct platelets arranged in a ridge-like formation are present. The surface image of film 1B (Figure 6.11b) deposited under 100 sccm O_2 flow has a similar surface to that of film 1A with distinct platelets. As the oxygen flow is increased to 150 and 200 sccm for films 1C and 1D, the distribution of these platelets appears to be more sporadic and the surface is generally less ordered as shown in Figures 6.11c-d. Additionally, film 1A deposited under 50 sccm O_2 flow appears to have the densest surface, though substantial surface porosity is observed in all the films. These results may be explained by the increased adatom mobility provided from lower oxygen content in the chamber which may reduce some of the shadowing effects. Indeed, for set 4 deposited as a function of O_2 flow at 250 °C, the oxygen content played a large role in the film structure and morphology. However, at higher temperatures, adatom mobility is dominated by the energy supplied by the increased temperature which allows the atoms to diffuse far greater distances than in the case of the 250 °C films. The relative effect of oxygen flow at this high deposition temperature is likely minimal compared to the effects of temperature.

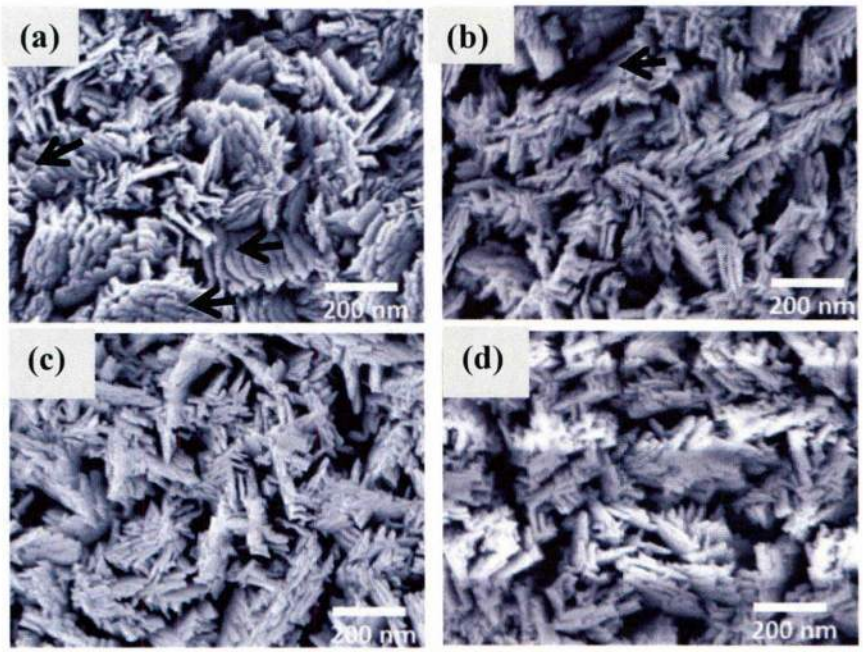

Figure 6.11. SEM top surface images of Gd_2O_3 films (a) 1A (50 sccm O_2), (b) 1B (100 sccm O_2), (c) 1C (150 sccm O_2), and (d) 1D (200 sccm O_2) deposited on silicon as a function of oxygen flow at 650 °C at high rates (> 5 Å / s). Arrows denote ridge-like growth.

Another explanation for the slight differences in film morphology may be offered in terms of the relative phase content and preferred orientation. From section 4.2, it was observed that the diffraction patterns from film 1A and 1B had strong preferred orientation of the C(222) and M(-402) reflections with very slight diffraction from the M(020) plane. In comparison, the diffraction patterns of films 1C and 1D, deposited under 150 sccm and 200 sccm of oxygen flow, respectively, showed substantial contribution from the M(020) orientation. The appearance of disorder and irregular grain growth appears to be linked to the formation of the M(020) grain orientation. The origin and effects of this surface morphology will be discussed in further detail in section 6.4 for films deposited as a function of thickness, as growth of the M(020) orientation occurs only in thick films grown at high temperatures.

For further investigation of the thick Gd_2O_3 film structure deposited under low O_2 flow, TEM analysis was performed. Figure 6.12 shows (a) low-magnification and (b) higher magnification bright-field TEM images of thick (~1.2 μm) Gd_2O_3 film 7E grown at 650 °C under 50 sccm O_2, collected along the Si<112> zone axis. Similar to the thick 650 °C film grown under 200 sccm O_2, this film also possesses a columnar structure with large grains elongating in the growth direction. Furthermore, it was dense near the film/substrate interface but elongated pores formed between grains as the growth proceeded. The SAD patterns collected from the interface region containing both Si and the bottom section of the film, the middle section, and the top section of the film are shown in Figures 6.12c – 6.12e, respectively. The SAD patterns from the bottom of the film show diffraction from both cubic and monoclinic grains. The short/arc appearance suggests that texture is present at the bottom of the film. The SAD patterns from the middle and top sections of the film contain spotty rings from large monoclinic Gd_2O_3 grains, similar to the case in the thick 650 °C film grown under 200 sccm O_2, suggesting transition to monoclinic phase with increasing film thickness, consistent with X-ray diffraction results. Comparison of Figures 6.12a (film 7E) and 6.7a (film 6E) reveals that film 7E deposited at lower O_2 flow (50 sccm) appears to possess less intercolumnar porosity than film 6E grown under 200 sccm O_2 flow, consistent with surface images shown in Figure 6.11. Additionally, film 7E deposited under lower O_2 flow appeared to have a slightly smoother surface due to the more uniform columnar growth and reduced voiding.

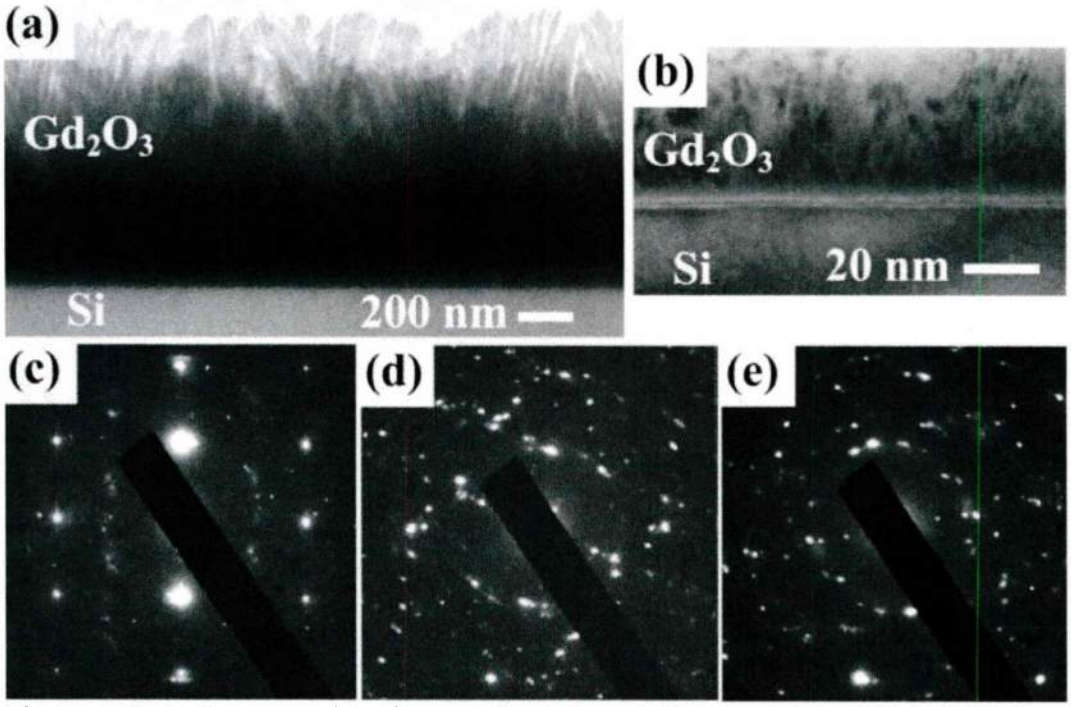

Figure 6.12. (a) Low-magnification and (b) high-magnification bright-field TEM images of thick Gd_2O_3 film 7E (650 °C, 50 sccm O_2, 1.2 μm). SAD patterns collected from the (c) interfacial region, (d) the middle section, and (e) the top section of the film, respectively.

Grain size measurements obtained by the Clemex method are shown in Figure 6.13 for films 4A – 4E (250 °C, function of oxygen flow, ~ 1 μm). For films deposited at 250 °C, the oxygen flow had little effect on the measured grain size for films deposited between 25 and 150 sccm O_2. At oxygen flow of 200 sccm, the grain size decreases slightly as supported by the X-ray diffraction results presented in section 4.2. Figure 6.13 also shows AFM surface roughness measurements for both sets 4 (250 °C) and 1 (650 °C) deposited as a function of oxygen flow. The surface roughness for films deposited at 250 °C is also not significantly affected by oxygen flow. As will be shown in section 6.1.4, at this low deposition temperature, the surface roughness scales with the film thickness. For films deposited at 650 °C, the surface roughness was found to be

relatively independent of oxygen flow between 50-150 sccm, but increased substantially at an oxygen flow rate of 200 sccm. This increase in surface roughness was supported by the large intercolumnar porosity and high peak to valley distances observed in the TEM brightfield images shown earlier.

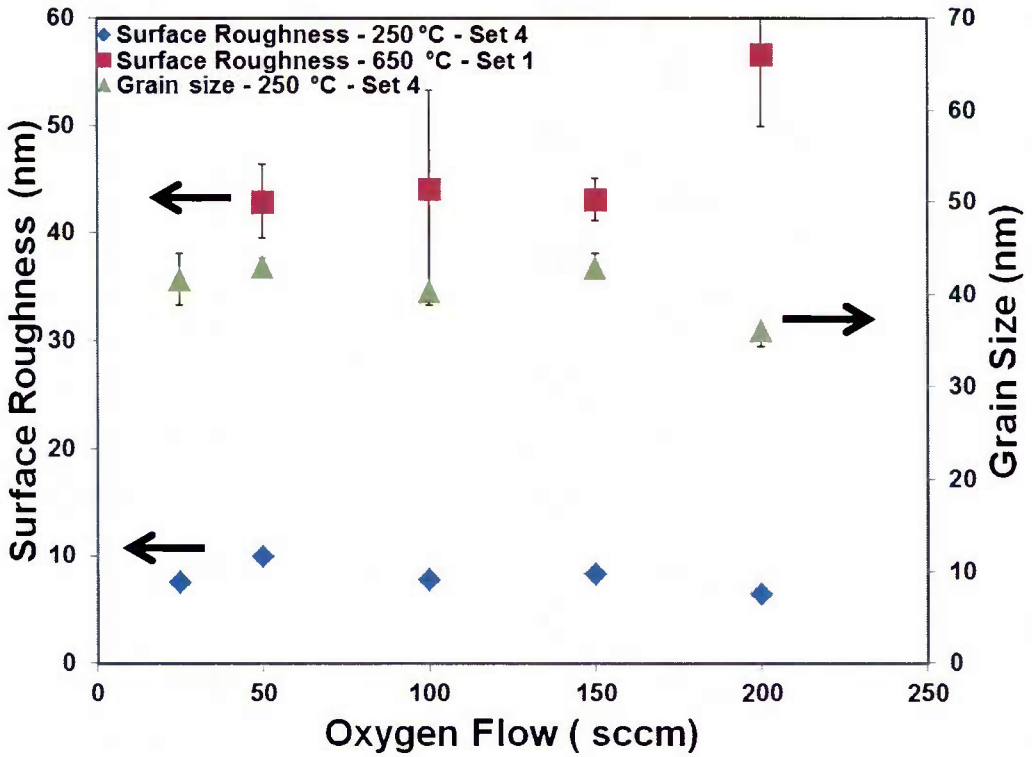

Figure 6.13. AFM RMS surface roughness and grain size for set 4 (250 °C, function of oxygen flow, ~1 μm) and set 1 (650 °C, function of oxygen flow, ~2 μm).

6.1.4. Effect of film thickness on Gd_2O film morphology deposited on Si(111)

Based on the differences observed between the crystalline phases, orientation, and morphology of the very thin films (set 8) discussed in section 6.1 and the thick films from various sets shown in sections 6.2 and 6.3, further examination of the effect of film thickness was performed systematically for the Gd_2O_3 films. Therefore, sets 3 and 9, deposited as a function of film thickness at 250 °C and 650 °C, respectively, were

characterized in more detail. Figure 6.14 displays surface images from film 3A, 580 nm thick and film 3D, 5.2 microns thick. For films deposited at 250 °C (set 3), aside from the increased grain size, there is no substantial change in the surface morphology or film porosity. This suggests that after the initial dense crystalline region shown in the TEM micrograph (Figure 6.6a), the films develop porosity and grow uniformly as the thickness increases. This is due to the fact that the low substrate temperature does not provide enough surface mobility for the films to undergo significant grain growth, resulting in a Zone 1 type microstructure with small grains, separated by voids. There is slight grain growth (28 nm – 50 nm) as the film grows thicker as evidenced by the surface images.

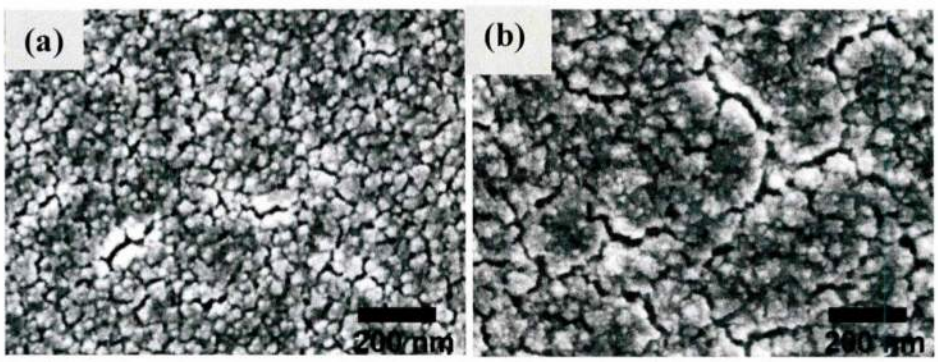

Figure 6.14. SEM surface images of film (a) 3A (580 nm) and (b) 3D (5.2 μm) deposited on silicon at 250 °C under 200 sccm O_2 flow at high rates (> 5 Å / s).

Figure 6.15 shows the surface morphologies of Gd_2O_3 films from set 9 deposited on silicon as a function of thickness at a temperature of 650 °C and under an O_2 flow of 200 sccm at high growth rates of ~1 nm / s. Figure 6.15a displays the surface morphology of film 9A (380 nm). The image is characterized by a dense underlayer with various features partially covering the surface which is linked to the dense nucleation

zone observed in the TEM images before columnar growth. The various observed features can be attributed to the mixed phase nature of the film. More specifically, the inset in Figure 6.15a shows a large triangular C(222) facet, surrounded by smaller crystallites, likely representative of M(-402) grains. The difference in the grain size of the cubic and monoclinic crystallites is consistent with crystallite size calculated with Scherrer's equation in Table 4.7.

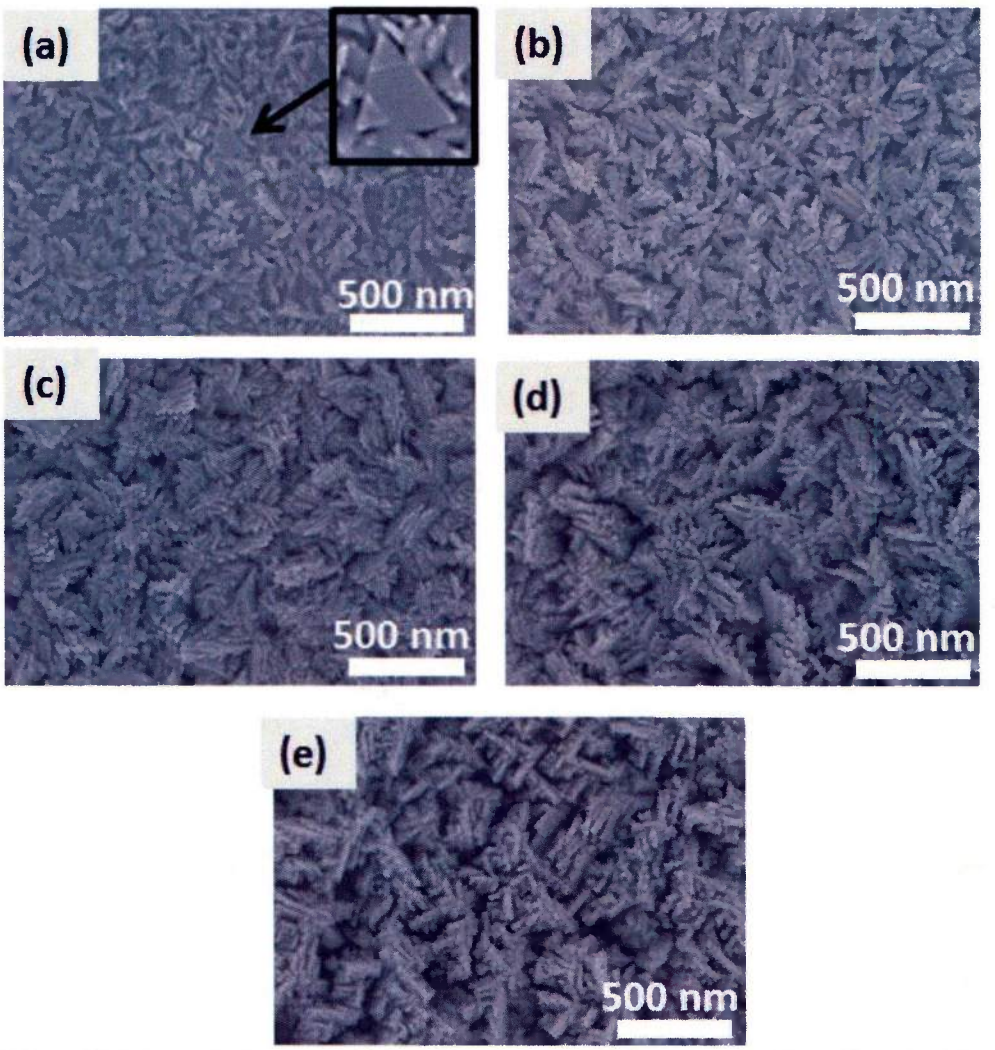

Figure 6.15. SEM morphology of Gd_2O_3 films (a) 9A (0.38 μm), (b) 9B (0.59 μm), (c) 9C (1.02 μm), and (d) 9D (2.69 μm), and (e) 9E (5.72 μm) deposited on Si(111) at 650 °C under 200 sccm O_2 flow at high rates (> 5 Å / s). The inset in Figure 6.15a shows a C(222) triangular facet.

With increasing film thickness (from 380 to 590 nm), significantly enhanced surface coverage is observed for film 9B (Figure 6.15b) as a result of the onset of columnar growth. The surface image of film 9C (1.02 μm thick) shown in Figure 6.15c reveals a denser surface morphology with significant grain growth. As the film grows thicker, there is a substantial change in surface morphology observed for film 9D (2.69 μm thick) displayed in Figure 6.15d. This surface is characterized by an increase in the surface porosity and irregular growth of varying surface orientations. For film 9E (5.72 um thick, Figure 6.15e), this surface porosity appears to be even more pronounced.

Two mechanisms can be attributed to the onset of the rough and highly porous surface morphology with increasing thickness at high deposition temperatures (650 °C). The first is linked to the effect of shadowing discussed in section 6.1.2. As the columnar grains grow larger, more metal flux arrives at the column tips. Due to the high rate of incoming metal atoms, the adatoms cannot diffuse quickly enough to fill the voids between the columns. While this can explain the slight surface porosity observed in films 9A-9C, it cannot fully account for the evolution of the structure as evidenced by the substantial increase in surface porosity for films 9D and 9E. Another possibility is linked to the formation of the monoclinic phase and preferred orientation of the M(020) plane. The diffraction pattern for film 9A-9C possessed primarily diffraction from the C(222) and M(-402) planes (Figure 4.8). The diffraction pattern for film 9D, however, had strong intensity from the M(020) peak which coincides with the onset of the surface porosity observed in Figure 6.15d. Film 9E showed diffraction only from the M(020) orientation which correlates with the highly porous structure observed in Figure 6.15e. As the columns grow in the M(020) orientation, the less symmetrical monoclinic

structure leads to poor packing density in the film. The growth of this grain orientation combined with shadowing effects led to the highly irregular and porous surface morphology.

Figure 6.16 shows the effect of film thickness on the measured grain size via the Clemex analytical technique and the AFM surface roughness of films 3A-3E deposited at 250 °C under 200 sccm. The measured grain size increased from a value of 36.2 ± 0.7 nm for film 3A with thickness 580 nm to 52.1 ± 1.2 nm for film 3E with thickness 11.01 μm. The surface roughness of these films increased from approximately 5.8 nm to 13.9 nm.

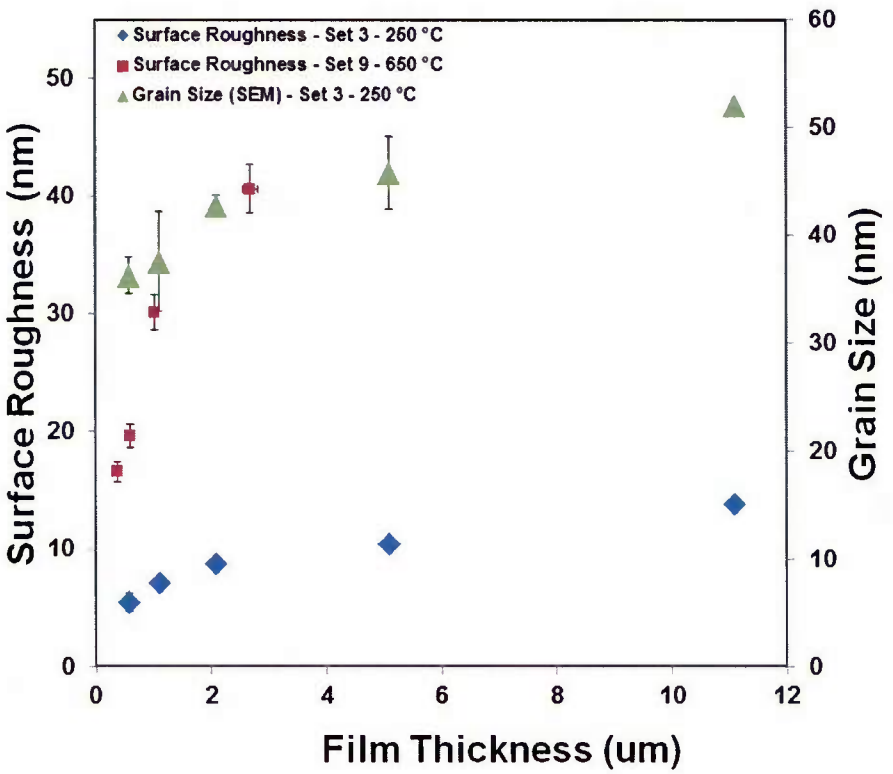

Figure 6.16. SEM grain size and AFM surface roughness of Gd_2O_3 films from set 3 (250 °C, 200 sccm O_2, function of thickness) and set 9 (650 °C, 200 sccm O_2, function of thickness).

Figure 6.16 also displays the measured AFM surface roughness for films 9A - 9D (650 °C, 200 sccm O_2, function of thickness). There is a significant increase in the surface roughness of the films with increasing film thickness for films deposited at 650 °C from approximately 17 nm RMS for film 9A with thickness 380 nm to 40 nm RMS for film 9D with a thickness of 2.69 μm. This has important implications for the fabrication of microelectronic devices. Indeed, the peak to valley distances for films 9A-9D range from 115 nm to 327 nm. This large surface porosity may result in poor contact uniformity, decreased dielectric constant, and increased dielectric losses.

6.1.5. Interfacial structure and composition of Gd_2O_3/Si(111) films

The interfacial structure and chemistry of select Gd_2O_3 films deposited on silicon (111) under various conditions shown in Table 6.1 were studied by TEM, EDS, and EELS. The various deposition conditions such as temperature, oxygen flow rate, film thickness, and deposition time are found to have a significant effect on interfacial size, structure, and composition.

Table 6.1. Deposition conditions and interfacial layer structure for select Gd_2O_3 films.

Film	Deposition Temperature (°C)	Oxygen Flow (sccm)	Thickness (μm)	Interfacial Layer Size (nm)	Interfacial Composition and Structure
6A	250	200	1.07	5	Gd-Si-O diffusive, indulating
8A	250	200	0.047	2	Flat, sharp SiO_x-rich
6E	650	200	0.87	10	Gd-Si-O diffusive
8E	650	200	0.020	2	Flat, diffusive SiO_x-rich
7A	250	50	1.11	3	Gd-Si-O diffusive
7E	650	50	1.20	6	Gd-Si-O diffusive

Figure 6.17a is a high-resolution TEM image collected from the interface region of film 6A. As indicated by the arrows, select Si / interfacial regions possess a slightly brighter contrast than the rest of the Si substrate. The formation of such interfacial regions is an indication that further interfacial reaction via oxygen diffusion into the Si substrate occurred during the extended growth period of 6A as compared to the homogenous interfacial layer observed in film 8A (Figure 6.3a) deposited under the same conditions, but shorter deposition time (~20x reduction). It is also worth noting that the interfacial layer appears to be undulating, which suggests that interdiffusion of Si and Gd had also occurred. The thickness of the interfacial layer for 6A is approximately 5 nm.

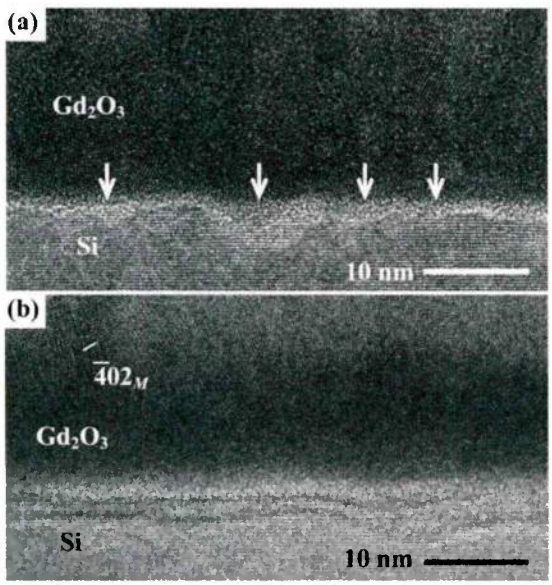

Figure 6.17. High-resolution TEM images collected from the interfacial regions of Gd_2O_3 films (a) 6A (250 °C, 200 sccm O_2, 1.07 μm) and (b) 6E (650 °C, 200 sccm O_2, 0.87 μm) deposited on silicon under 200 sccm O_2 at high rates (> 5 Å / s).

The interfacial layer between Gd_2O_3 film 6E (650 °C, 200 sccm O_2, 0.87 μm) and the Si substrate (Figure 6.17b) also appears to be different than that of 8E (650 °C, 200 sccm O_2, 0.20 μm, Figure 6.3b). It is larger in size (~10 nm), suggesting further

interfacial reaction occurred during the extended growth at 650 °C. This is explained by the greater diffusion length of the atoms due to the increased deposition time. A comparison of the interfacial layers of films 6A and 6E (Figure 6.17) suggests that increasing the deposition temperature from 250 to 650 °C results in increased diffusion and a 2x increase in interfacial layer size (5nm to 10 nm).

Figure 6.18a is a high-resolution TEM image collected from the interfacial region of the Gd_2O_3 film 7A (250 °C, 50 sccm O_2, 1.11 μm). The lower O_2 flow, along with the higher film density, results in a decrease in the amount of oxygen diffusing into the Si surface during Gd_2O_3 deposition, thus reducing SiO_x thickness at the interface. A thin disordered interfacial layer with a uniform thickness of ~2 nm is apparent (Figure 6.18a).

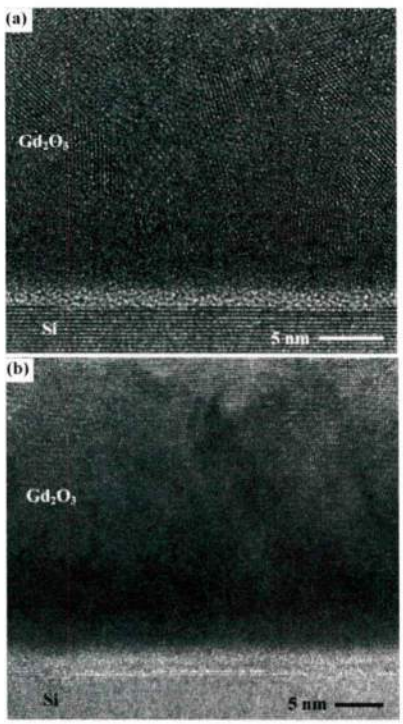

Figure 6.18. High-resolution TEM images collected from the interfacial regions of Gd_2O_3 films (a) 7A (250 °C, 50 sccm O_2, 1.11 μm) and (b) 7E (650 °C, 50 sccm O_2, 1.20 μm) deposited on silicon under 50 sccm O_2 at high rates (> 5 Å / s).

Figure 6.18b is a high-resolution TEM image of the interface region of Gd_2O_3 film 7E (650 °C, 50 sccm O_2, 1.20 μm). An undulating layer is also observed for film 7E, however, it is narrower in comparison with that in film 6E (650 °C, 200 sccm O_2, Figure 6.17b). Thus, lower O_2 flow has also resulted in a reduced interfacial reaction for films grown at 650 °C.

Chemical analysis, with a focus on the interfacial chemistry, was carried out using a combination of high-angle annular-dark-field scanning transmission electron microscopy (HAADF STEM), XEDS, and EELS. In HAADF STEM images, the intensity is nearly proportional to Z^n, where Z is the atomic number of the material and the value of the power n ranges from ~1.6 to 1.9. Thus, Z-contrast STEM images provide compositional information of the materials. Figures 6.19a and 6.19b show representative HAADF STEM images of thin Gd_2O_3 films 8A (250 °C, 200 sccm O_2, 47 nm) and 8E (650 °C, 200 sccm O_2, 20 nm).

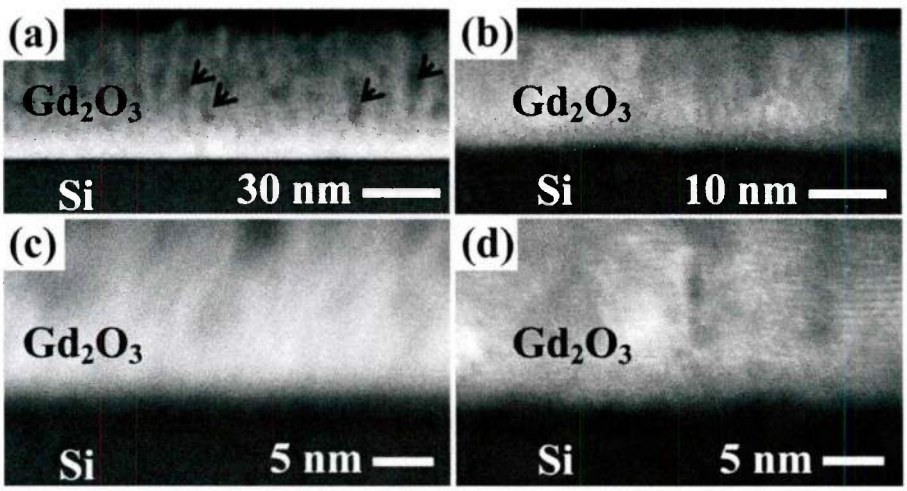

Figure 6.19. Low-magnification HAADF STEM images of thin Gd_2O_3 films (a) 8A (250 °C, 200 sccm O_2, 47 nm) and (b) 8E (650 °C, 200 sccm O_2, 20 nm) grown under 200 sccm oxygen flow. Higher magnification images collected near the interface regions of the (c) 8A and (d) 8E heterostructures, respectively.

In each heterostructure, the interfacial layer possesses an overall relatively darker contrast than the film and the Si substrate. This indicates that it has a relatively lower average Z and is thus most likely SiO_x-rich. Figure 6.20 shows XEDS spectra collected from the interfacial layers in the two heterostructures, which also reveal the SiO_x-rich nature of the interface. The presence of the C and Mo peaks in the spectra is attributed to atmospheric carbon contamination and the Mo TEM grid, respectively.

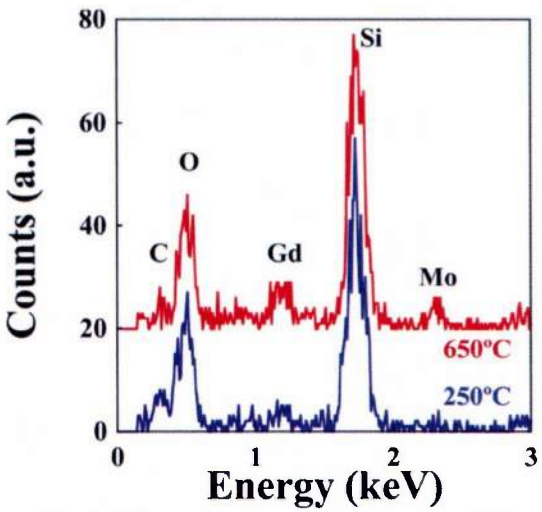

Figure 6.20. EDS spectra collected from the interfacial layers of the films 8A (250 °C, 200 sccm O_2, 47 nm) and 8E (650 °C, 200 sccm O_2, 20 nm) heterostructures. The C peak is from atmospheric carbon contamination and Mo peak is related to the Mo TEM grid.

In the literature, formation of similar SiO_x-rich interface layers has been attributed to high oxygen partial pressure in the growth chamber for Gd_2O_3/Si(100) heterostructures grown by electron beam evaporation.[104] Such interfacial layers were eliminated in heterostructures grown by MBE, in which the oxygen partial pressure was significantly lower.[6,106] In our case, while a HF-dip was applied to remove the native surface oxide layer immediately before the Si substrates were loaded into the growth chamber, thermal deoxidation of the substrate surface was not performed. Furthermore, the base pressure of

the chamber was relatively high ($<6 \times 10^{-6}$ Torr) and O_2 was introduced into the chamber ~15 s before the Gd flux. Thus, a thin layer of amorphous SiO_x might be present on the Si surface prior to the start of Gd_2O_3 film deposition. As the growths continued, O_2 might diffuse through the polycrystalline Gd_2O_3 film and react with Si to form extra SiO_x. Such a process was also observed in another study which detailed the post-growth thermal annealing of Gd_2O_3/Si(100) in an oxygen atmosphere.[60,103]

The interfacial layer in a heterostructure with a thick Gd_2O_3 film (films 6A and 6E) was thicker than that in a heterostructures with a thin film (films 8A and 8E) grown at the same temperature and O_2 flow as shown in Table 6.1. This supports the fact that deposition time and temperature results in greater diffusion and larger interfacial thicknesses. Furthermore, heterostructures grown with a lower O_2 flow possessed thinner interfacial layers than those grown with a higher O_2 flow (Table 6.1). This supports the finding that extra SiO_x formed as the deposition process proceeded via the diffusion of oxygen into the interfacia region and the subsequent reaction with Si. The thin amorphous interface layer could prevent the possible heteroepitaxial growth of Gd_2O_3 films on Si(111), thus affecting the crystal quality, film stress, and electronic properties. It would be of great interest for future studies to investigate how a SiO_x free Si surface affects the growth, interfacial structure, interfacial chemistry, microstructure, stress, and surface morphology of the Gd_2O_3 films.

For film 8A (Figure 6.19a), the pore-like features (indicated by the arrows) possess a relatively darker contrast (darkfield) than the rest of the film. Thus, the pore-like features may be relatively less Gd-rich than stoichiometric Gd_2O_3, which led to a lower average *Z* and darker contrast. Another possible reason for the dark contrast of the

pore-like features is that they may possess a relatively lower density than the rest of the Gd_2O_3 film. This makes these features virtually "thinner" in the imaging direction, which consequently resulted in the lower intensity in the HAADF STEM image. Pore-like features were not observed in film 8E due to the dense structure resulting from higher adatom mobility. The slight lateral contrast variation of film 8E (Figure 6.19b) is mainly due to the different orientations of the grains, which resulted in differences in the amounts of electrons diffracted into the STEM detector from individual grains.

TEM images of the interfacial layers for films 8A and 8E (Figure 6.3a and 6.3b) appeared to be similar. However, further investigation using the *Z*-contrast HAADF STEM images (Figure 6.19a and 6.19b) revealed that these interface layers were indeed different. The interface layer of 8A appears to be sharp with a uniform thickness while the interface of 8E has a relatively diffusive contrast. This may be seen more clearly in Figures 6.19c and 6.19d, higher magnification STEM images of the 8A and 8E, respectively. The interface layer of 8E possesses a nonuniform thickness and a lateral contrast variation. Such a diffusive appearance indicates that interfacial interdiffusion of Gd and Si occurred during the high temperature deposition. More specifically, Si outward diffusion may have occurred forming the Gd-Si-O layer. This is supported by the small Gd peak in the XEDS spectrum from this SiO_x-rich layer in 8E (Figure 6.20)

Increased interfacial reaction occurred between the thick (~1 μm) Gd_2O_3 films and the Si substrates due to the extended growth periods (~20 min) for films 6A and 6E. Figure 6.21 shows HAADF STEM images collected from the interfacial regions of films 6A and 6E. The top and bottom dashed lines indicate the approximate positions of the Gd_2O_3/interfacial layer and interface layer/Si boundaries, respectively. As shown in

Figure 6.21a, the interfacial layer between film 6A and the Si substrate possesses a diffusive contrast that appears to be undulating. The total thickness of the intermixing layer at the interface is ~5 nm, as estimated based on the contrast variation in the STEM image. The interfacial layer thickness increased to >10 nm for Gd_2O_3 film 6E (Figure 6.21b), due to the high deposition temperature resulting in increased diffusion at the interface.

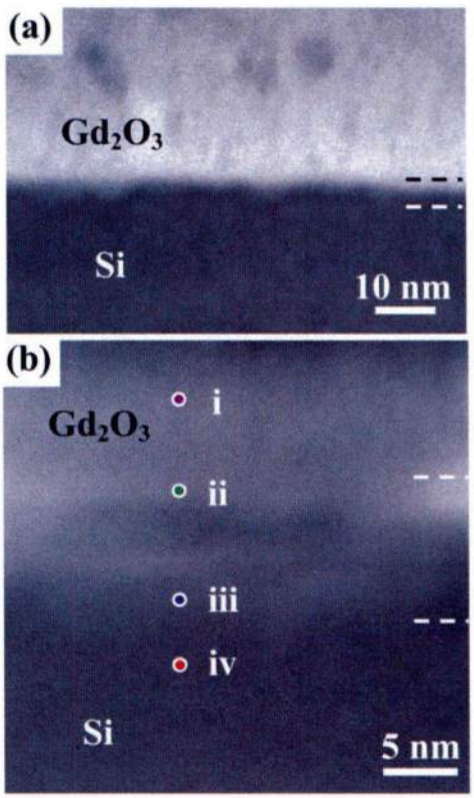

Figure 6.21. HAADF STEM images collected from the interface region of the thick Gd_2O_3 films (a) 6A (250 °C, 200 sccm O_2, 1.07 μm) and (b) 6E (650 °C, 200 sccm O_2, 0.87 μm) grown under 200 sccm O_2 flow. The top and bottom dashed lines indicate the approximate positions of the Gd_2O_3/interfacial layer and interface layer/Si boundaries, respectively.

Figure 6.22a shows EEL spectra collected from positions *i* to *iv* indicated in Figure 6.21b. All the spectra were collected under the STEM mode using an electron probe with a nominal size of 0.5 nm, which provided a spatial resolution <1 nm. As indicated by the arrows, a weak Si edge (green arrow) and a weak Gd edge (blue arrow) were present in the spectra from near the top (position *ii*) and the bottom (position *iii*) of the interface layer, respectively. Therefore, the results indicate that the composition of the layers can be described as follows: *i*) Gd2O3, *ii*) Gd rich – O – Si, *iii*) Gd-O-Si rich, and *iv*) Si.

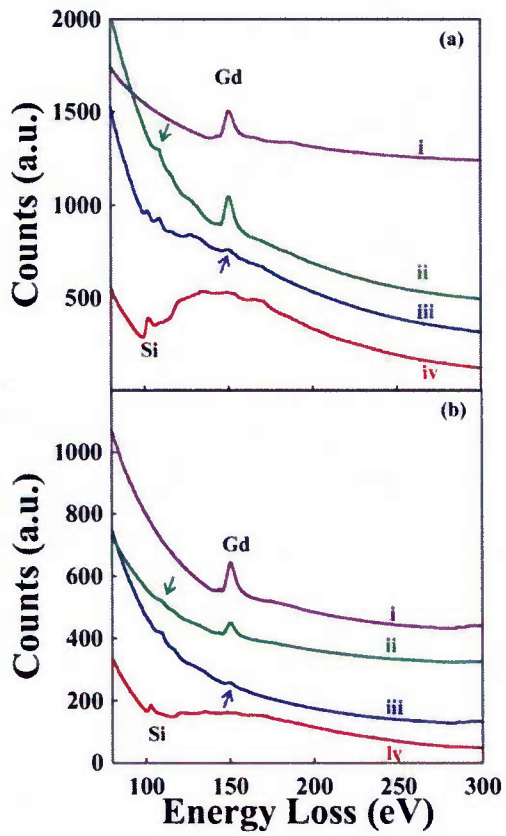

Figure 6.22. EEL spectra collected from positions *i* to *iv* as indicated in (a) 6E (Figure 6.21b) and (b) 7E (Figure 6.23b). The upper arrow (green) indicates a weak Si edge while the lower arrow (blue) indicates a weak Gd edge.

To further investigate the interfacial properties of Gd_2O_3 grown on Si at low oxygen flow, HAADF STEM images (Figure 6.23) were collected from the interfacial regions of films 7A (250 °C) and 7E (650 °C) grown under 50 sccm O_2 flow.

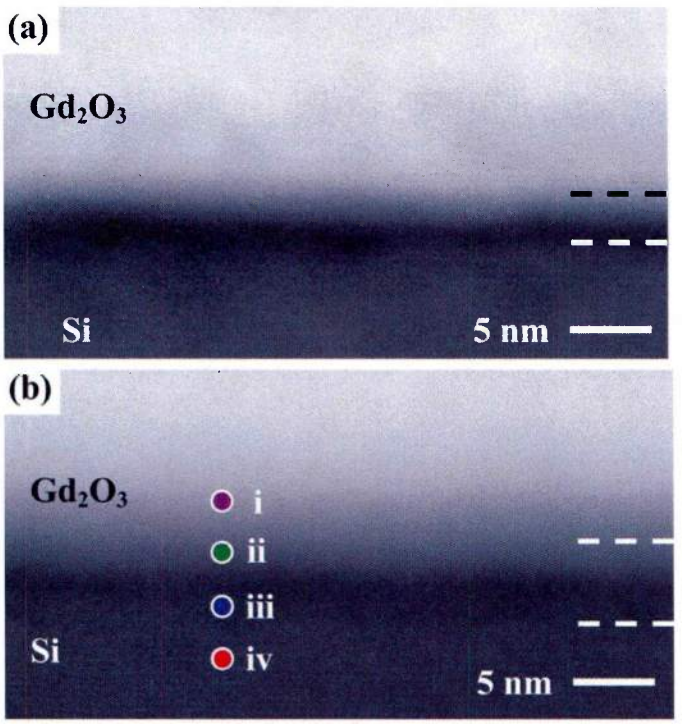

Figure 6.23. HAADF STEM images collected from the interfacial region of the thick Gd_2O_3 films at (a) 7A (250 °C, 50 sccm O_2, 1.11 μm) and (b) 7E (650 °C, 50 sccm O_2, 1.20 μm) grown under 50 sccm oxygen. The top and bottom dashed lines indicate the approximate positions of the Gd_2O_3/interfacial layer and interfacial layer/Si boundaries, respectively.

The total thicknesses of the interface layers estimated based on the STEM image contrast variation and EELS measurements were ~3 and 6 nm for 7A and 7E, respectively, smaller than in films 6A (5 nm) and 6E (10 nm) grown under 200 sccm O_2 flow. However, the same trend of increasing interfacial layer size with increasing deposition temperature was observed. EELS examinations indicated that these interface layers were also mixed Gd-Si-O layers. Figure 6.22b shows EEL spectra collected from

positions *i* to *iv* indicated in Figure 6.23b. Again, a compositional transition from Si to Gd-Si-O to Gd_2O_3 in the growth direction was observed.

Similar Gd-Si-O interfacial layers were also observed in a few earlier reports on the thermal stability of very thin Gd_2O_3 films (< ~15 nm) grown on Si(100) substrates by electron-beam evaporation.[60,103,104] In those studies, a thin (1.5 nm) SiO_x interfacial layer was observed between the 500 °C deposited film and the substrate. Rapid thermal annealing (RTA) in O_2 at higher temperatures resulted in the formation of an intermixed 3 nm thick Gd-Si-O layer between the Gd_2O_3 film and the SiO_x layer.[104] Furthermore, an increase in the thickness of the SiO_x layer between the Gd-Si-O layer and the Si substrate was observed after RTA, which was attributed to the further reaction between oxygen and Si due to oxygen diffusion through the Gd_2O_3 film. Such an increase in the SiO_x layer size during deposition was not observed in our heterostructures with thick films. We believe that is due to the significantly reduced amount of oxygen diffusing to the Si surface as the thickness of the Gd_2O_3 films increased. As a result, the entire SiO_x layer intermixed with Gd_2O_3 to form the interfacial Gd-Si-O layer as the growth proceeded. In an earlier study on RTA of a ~10 nm Gd_2O_3/ SiO_x /Si(100) structure, N_2 was used instead of O_2 as the annealing atmosphere.[107] Since oxygen was absent in the atmosphere, the thickness of the SiO_x layer was found to be reduced due to its intermixing with the Gd_2O_3 film to form Gd-Si-O. Gd_2O_3 was theoretically predicted to be thermodynamically stable in contact with Si at a temperature of 1000 K.[108] Indeed, Gd_2O_3/Si heterostructures without Gd-Si-O interfacial layers were obtained using MBE growth under ultrahigh vacuum.[6,106] Based on analysis of the interface chemistry and the results reported in the literature, we conclude that oxygen plays a crucial role in the interfacial reaction between

Gd_2O_3 and Si. At generally used growth temperatures (<1000 K), the Gd_2O_3/Si interfacial reaction and the formation of the Gd-Si-O interfacial layer occur only when excess oxygen reaches the interface. The excess oxygen reacts with Si to form SiO_x, which will then intermix with Gd_2O_3, leading to the formation of the Gd-Si-O interface layer.

6.1.6. Effect of deposition rate and substrate material on Gd_2O_3 film morphology

It was previously shown in section 4.5 that the XRD patterns of the mixed phase Gd_2O_3 films deposited under high rates of deposition on silicon and other substrates are very similar in terms of phase and preferred orientation. As a result, it was expected that the surface morphologies would be similar regardless of underlying substrate. Figure 6.24 shows the surface morphologies of film 12E (650 °C, 200 sccm O_2, 1.03 μm) deposited on silicon(111), sapphire, GaN, and quartz substrates at a deposition rate of 10 Å / s.

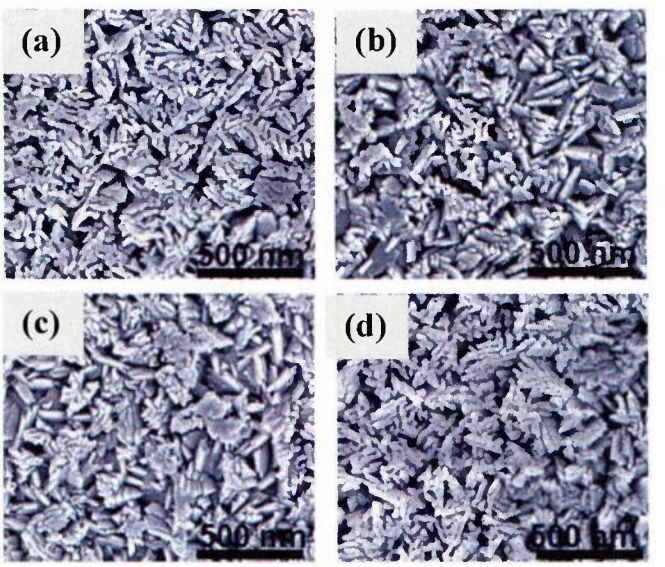

Figure 6.24. SEM surface images of film 12E (650 °C, 200 sccm O_2, 1.2 μm, 10 Å / s) deposited on (a) silicon (111), (b) sapphire, (c) GaN, and (d) quartz.

As expected, the surface morphologies are relatively similar despite being grown on the various substrates. Due to the high rate of growth, structural rearrangement at the substrate/film interface is impeded by the constant flux of arriving Gd atoms at the surface resulting in lower mobility of the adatoms. Therefore, all the films grow in a similar fashion resulting in the observed ridge-like morphology which is attributed to both shadowing and formation of irregular monoclinic phase facets.

Lowering the deposition rate below 0.5 Å / s at a deposition temperature of 650 °C and O_2 flow of 50 sccm resulted in formation of single phase cubic Gd_2O_3 films for films as thick as 1 μm. Figure 6.25a – 6.25d display the SEM surface morphologies of Gd_2O_3 film 10A (650 °C, 50 sccm O_2, 1.01 μm, 0.5Å / s) deposited on silicon, GaN, quartz, and sapphire, respectively. A comparison of all four samples reveals that these films deposited with a very low growth rate (0.5 Å / s) have significantly denser surface morphology than mixed phase films deposited at higher rates of deposition (5 Å / s). This is primarily due to the elimination of shadowing as a result of the enhanced adatom mobility. Since less flux is arriving due to the low evaporation rate, the Gd metal atoms are able to diffuse much further without interruption, resulting in less porosity between the growing columns. Additionally, the presence of only one phase allows for higher packing density within the film and lower strain energy barriers that compete with growth corresponding to mixed phases.

Significant differences were observed in the preferred orientation and crystallite sizes depending on the underlying substrate type for films grown at low deposition rates as demonstrated by XRD analysis in section 5.3. The increased mobility of the adatoms allows the atoms to rearrange themselves on the surface to minimize the free energy.

Based on this knowledge, significant variation in the film microstructures grown on different substrates was expected. The surface morphology of film 10A grown on silicon (Figure 6.25a) is primarily composed of the large triangular facets (~170 nm) of the C(222) planes, supported by the strong preferred orientation observed in the XRD pattern. The film grown on GaN (Figure 6.25b) shows a similar surface morphology with large grain size (~160 nm) and significant faceting of the C(222) planes. Some of the C(222) facets appear to be disrupted by the presence of other grains. The large grain size observed for the films deposited on GaN and silicon can be explained by the strong C(222) in and out-of-plane orientation as well as highly coherent growth at the interface as will be shown by the TEM analysis.

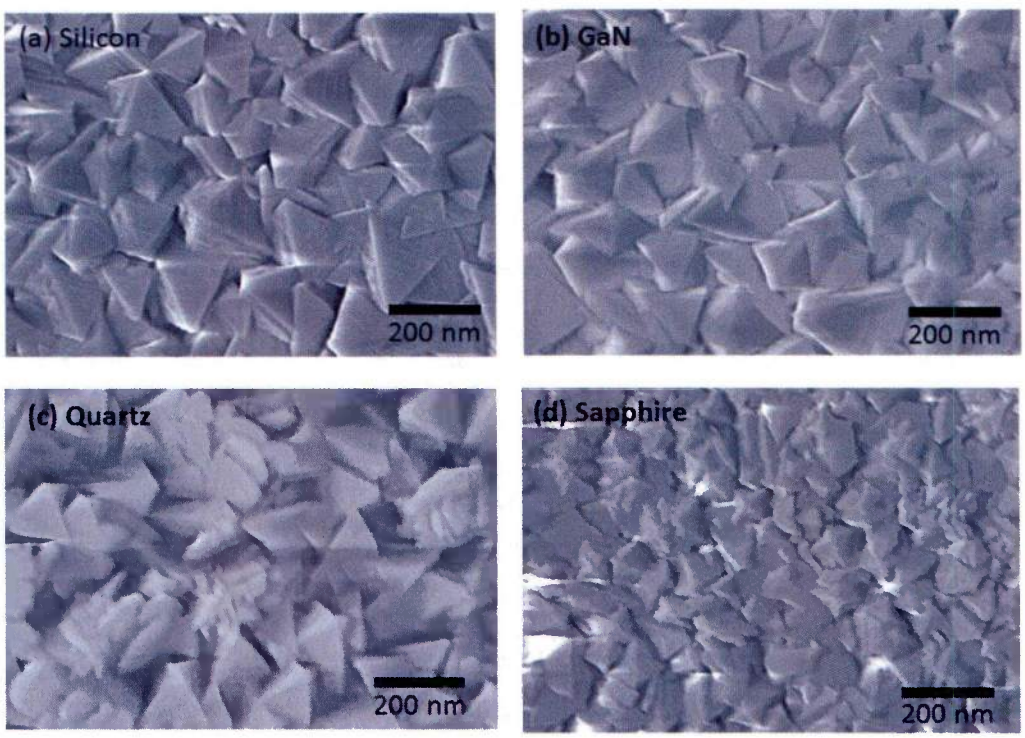

Figure 6.25. SEM surface images of Gd_2O_3 film 10A (650 °C, 50 sccm O_2, 1.01 μm, 0.5 Å / s) on (a) silicon(111), (b) GaN, (c) quartz, and (d) sapphire substrates.

For film 10A grown on quartz (Figure 6.25c), slight faceting of the C(222) planes is observed with the formation of smaller polycrystalline material between them. The Gd_2O_3 grain size on quartz was slightly smaller (~110 nm) than that of the GaN and silicon samples. This can be explained by the fact that on an amorphous template, there is no interface energy anisotropy for grain rotation. Since the interface energy is uniform, no preferred in-plane orientation will exist as confirmed by the pole figure analysis shown in section 5.6. Therefore, only an out of plane fiber texture will exist based on the competition between surface and strain energy. As a result, the Gd_2O_3 film 10A grown on quartz is mostly (111) oriented in efforts to minimize surface energy, but nucleation and growth of other grains occurs to minimize strain energy which results in the additional smaller grain size material observed in Figure 6.25c.

For Gd_2O_3 film 10A grown on sapphire (Figure 6.25d), a polycrystalline surface morphology with much smaller grain size (85 nm) is observed. The decrease in grain size is likely a result of compressive stress in the film. When the stress is increased, and the lattice expands in the out of plane direction, this causes an increase in the lattice energy. Due to the increase in lattice energy, the driving force for growth is lessened, and other grains are nucleated.[109] Additionally, a small amount of monoclinic phase formed for this film as a result of the increased compressive stress acting to further reduce the grain size.

TEM analysis was performed to further investigate the nature of the growth of film 10A on the various substrates. Figure 6.26a shows a low-magnification bright-field TEM image of single phase cubic Gd_2O_3 film 10A (650 °C, 50 sccm O_2, 1.01 μm, 0.5 Å/s) deposited on Si(111) and grown at 650 °C, collected along the Si<112> zone.

Similar to those films deposited at 650°C under high rates of deposition (~5 Å/s), a columnar morphology is observed. However, the grain growth is more uniform with column widths spanning ~ 100 nm. The film appears to be significantly denser without significant porosity observed between the grains. This is a result of the single phase cubic growth combined with increased surface adatom mobility due to the lower evaporated Gd flux.

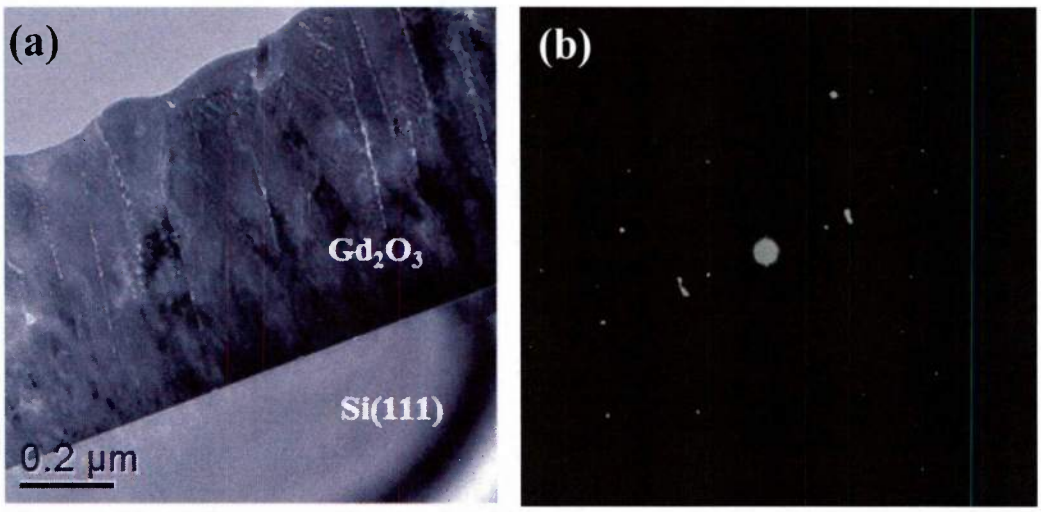

Figure 6.26. (a) Low-magnification bright-field image of thick Gd_2O_3 film (650 °C, 50 sccm O_2, 1.01 μm, 0.5 Å / s) deposited on silicon (111) and (b) corresponding SAD pattern collected from the film.

Figure 6.26b shows a diffraction pattern taken from the middle section of Gd_2O_3 film 10A deposited on silicon. The bright arcs suggests heavy texturing of the C(222) planes as expected from the XRD pattern (Figure 5.4) and SEM top surface image (Figure 6.25a). Indexing the additional arcs/spots shows that all the rings are cubic, confirming the results shown by XRD. The strong preferred growth of the Gd_2O_3 C(222) planes can be attributed to the low surface energy of the (111) planes in the Ia3 structure.[97] The low surface energy results in little competition for nucleation of grains

oriented in other directions besides the most energetically favorable (222) orientation, allowing for larger and more uniform growth of the C(222) grains. However, based on this information, we would expect strong preferred orientation of the C(222) planes regardless of the underlying substrate, unless the strain energy is high enough to disrupt crystal growth. Differences in preferred orientation were observed for films grown on quartz and sapphire substrates. One explanation for the increased C(222) preferred orientation on the silicon substrate may result from the fact that the mismatch in interplanar spacing between the Si(111) planes (3.136 Å) and Gd_2O_3 C(222) planes (3.121 Å) is small, which promotes epitaxial growth. However, it was shown that for mixed phase Gd_2O_3 films deposited on Si(111), that an Gd-Si-O amorphous layer was present between the film and substrate, which prevents epitaxial growth.

High resolution TEM analysis was employed to investigate the interfacial region of film 10A grown on silicon. Figure 6.27 shows high magnification bright-field TEM images of the interfacial region of film 10A grown on silicon. Figure 6.27a shows a region denoted by dashed arrows where there is a clear amorphous interfacial layer approximately 5 nm thick separating the Gd_2O_3 film and silicon substrate. In this region, growth of Gd_2O_3 cubic grains with various orientations is observed.

Figure 6.27b shows a region denoted by dashed arrows where the interfacial layer appears to be primarily crystalline. In this region, the growth consists primarily of C(222) planes parallel to the substrate. This is due to the close lattice match of Si(111) and C(222) which promotes an epitaxial relationship.

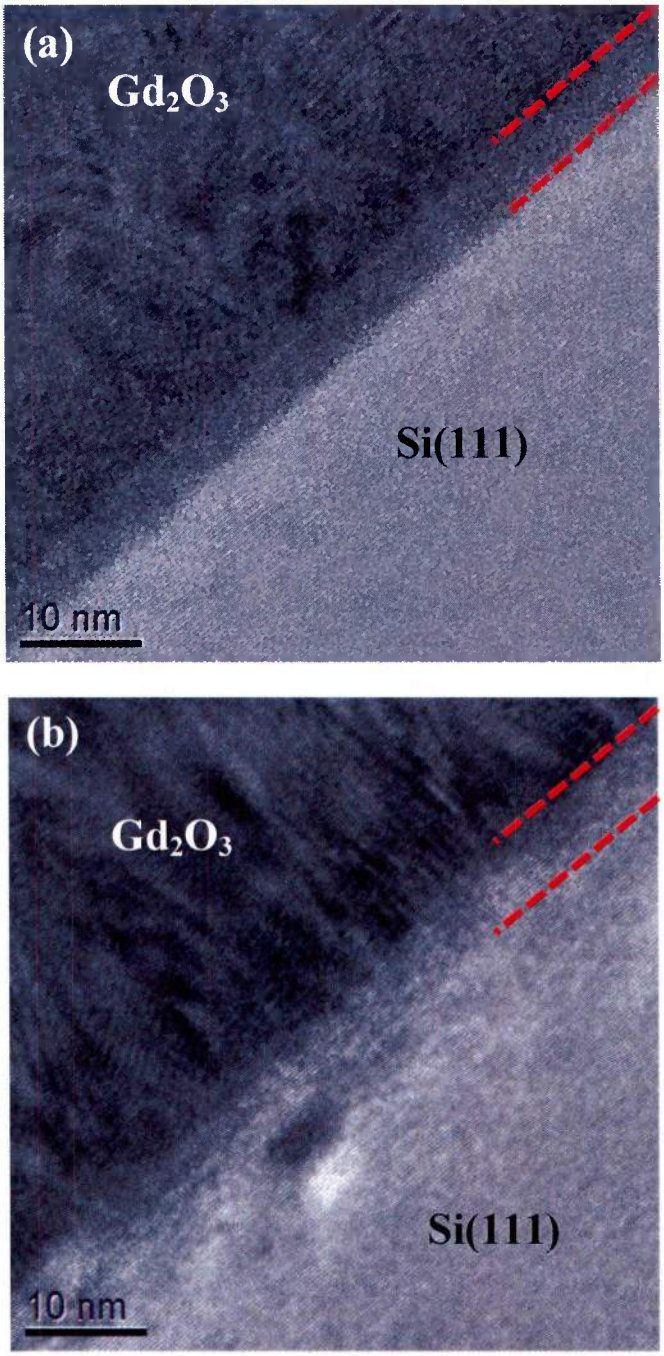

Figure 6.27. High-resolution TEM images collected from the interfacial region of the Gd_2O_3 film 10A (650 °C, 50 sccm O_2, 1.01 μm, 0.5 Å/ s) deposited on silicon showing (a) amorphous and (b) crystalline character. The dashed lines denote the interfacial region.

The existence of different interfacial regions within the same Si/Gd_2O_3 heterostructure is surprising. This may be explained by partial regrowth of SiO_x on the silicon surface during the time the silicon substrate is etched and the chamber is evacuated (approximately 5-10 min) or complex stress/strain relationships during the initial nucleation and growth mechanisms with different grain orientations.

Figure 6.28a shows a low magnification bright field TEM image of Gd_2O_3 film 10A (650 °C, 50 sccm O_2, 1.01 μm, 0.5 Å/s) on a GaN / AlGaN substrate. Uniform growth of feather-like C(222) facets as observed. The top of the columns possess a small amount of porosity, due to the strong faceting of the (222) planes. The widths of the columns appear to span approximately 150 - 250 nm at the thickest points, suggesting very large grain growth.

Figure 6.28b displays a selected area diffraction pattern using a circular aperture with a diameter of 500 nm from the top section of film 10A grown on GaN. A single crystal-like diffraction pattern is observed suggesting the growth of a very large C(222) grain in this region. Additional rings suggest the presence of other polycrystalline cubic material. Figures 6.28c, 6.28d, and 6.28e display SAD patterns taken using a smaller 150 nm diameter aperture from the bottom, middle, and top section of the film, respectively, along one columnar grain. Diffraction from the bottom part of the film indicates the growth of a single cubic Gd_2O_3 grain in the C(222) orientation within the region defined by the 150 nm diameter. This is indicated by the spacing between the diffracted spots and the absence of diffraction rings which indicate polycrystalline growth. Figure 6.28d shows diffraction from the middle of the film at same lateral coordinates and it can be observed that the diffraction pattern still corresponds to a single

C(222) grain. Near the top film surface, Figure 6.28e shows that there is development of additional diffraction spots and diffraction rings, besides the C(222). This is due to the fact that the width of the columns is smaller at the top of the film, resulting in diffraction from adjacent grains. However, it is important to note that the C(222) diffraction spots are still relatively bright. This diffraction data suggests that columns with widths of approximately 200 nm are able to grow with epitaxial relationship to the GaN substrates.

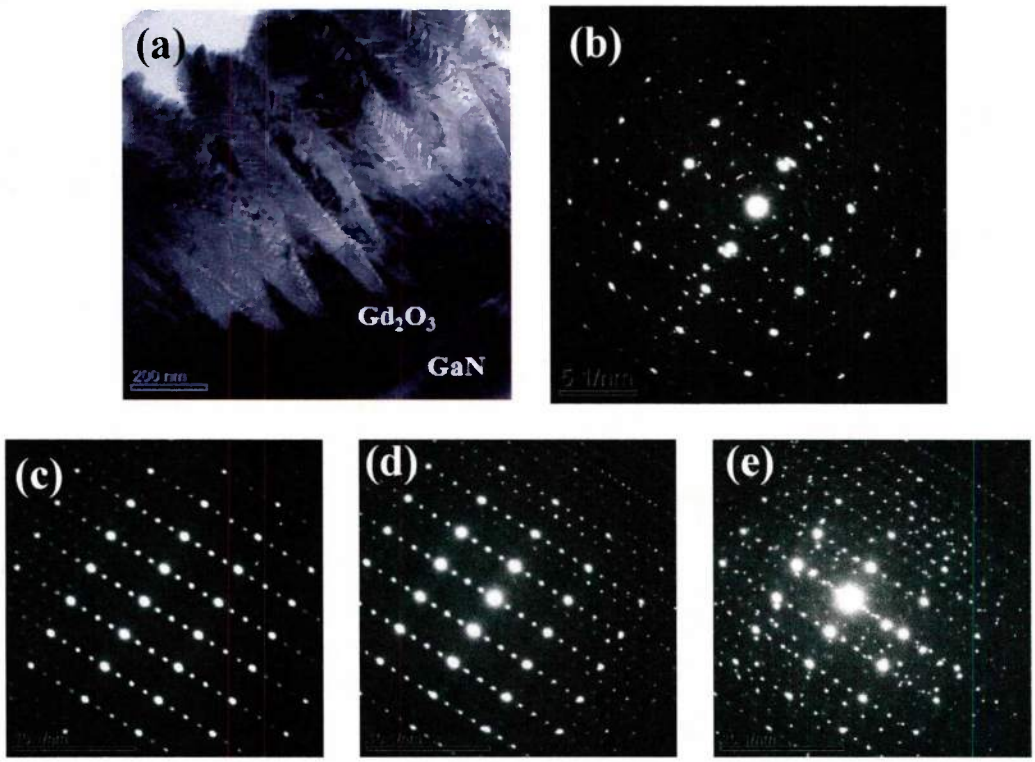

Figure 6.28. (a) Low-magnification bright-field TEM images of Gd_2O_3 film 10A (650 °C, 50 sccm O_2, 1.01 μm, 0.5 Å / s) deposited on GaN. SAD patterns collected from (b) the whole film with a 500 nm diameter circular aperture. SAD patterns collected from (c) interfacial region, (d) middle, and (e) top sections of the Gd_2O_3 film using a 150 nm diameter circular aperture, respectively.

Figure 6.29 displays a high resolution TEM image the interfacial region of the Gd_2O_3 / GaN interface for film 10A. The interface is entirely crystalline and the Gd_2O_3

film grows directly on the GaN basal plane without the formation of an amorphous interfacial layer. The absence of an amorphous interfacial layer could result in significant measured differences in the electrical properties of the Gd_2O_3 films deposited on GaN as compared to silicon.

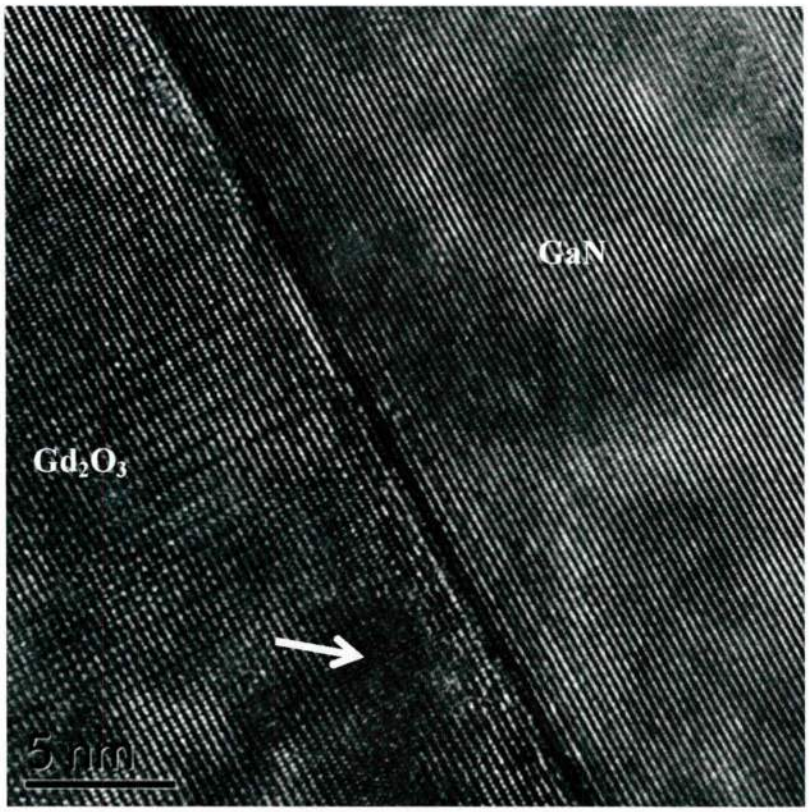

Figure 6.29. (a) High-resolution TEM image collected from the interfacial region of Gd_2O_3 film 10A (650 °C, 50 sccm O_2, 1.01 μm, 0.5 Å / s) deposited on GaN. The arrow denotes a defect region.

The potential for single crystal growth is highlighted in Figure 6.29. There is uniform growth of a single set of Gd_2O_3 C(222) lattice planes consistent with the electron diffraction patterns. The formation of a defect is visible near the interfacial region. This is likely a misfit dislocation formed in order to relieve the strain as a result of the large lattice mismatch (20%) between the GaN(0001) basal plane and Gd_2O_3 (111) plane.[97] The

continued formation of these defects will disrupt the lattice structure and result in growth of other grain orientations which explains the polycrystalline nature of the film. Nevertheless, these results are promising and suggest the possibility of single crystal growth of $C(222)_{Gd2O3} \parallel H(0001)_{GaN}$, at least in the early stages of coating growth. As the film grows, stresses resulting from the lattice mismatch, coefficient of thermal expansion mismatch, and intrinsic growth stresses are likely to result in the formation of defects which could result in the formation of other grain orientations and potentially secondary monoclinic phase. Single crystal films have potential for significantly enhanced charge carrier transport which is beneficial for radiation detection purposes.

For comparison, Figure 6.30a shows a low magnification bright field TEM image of film 10A (650 °C, 50 sccm O_2, 1.01 μm, 0.5Å/s) deposited on a sapphire substrate. Deposition on the sapphire substrate resulted in growth of significantly thinner columns (~30 nm) as compared to the growth on Si(111) and GaN with porosity forming near the top of the film. The increased compressive stresses may impede adatom mobility across the surface. Furthermore, the lattice energy is increased which decreases the driving force for grain growth. As a result there is competition for nucleation of grains exhibiting a number of different orientations which leads to growth of multiple grains with smaller sizes. High resolution TEM taken at the interface of Gd_2O_3 film 10A grown on sapphire is shown in Figure 6.30b. A small (2 nm thick) interfacial layer is observed with bright contrast. This layer appears to be primarily crystalline. Unfortunately, EDS or EELS data is not available for this interface layer so the composition is unknown.

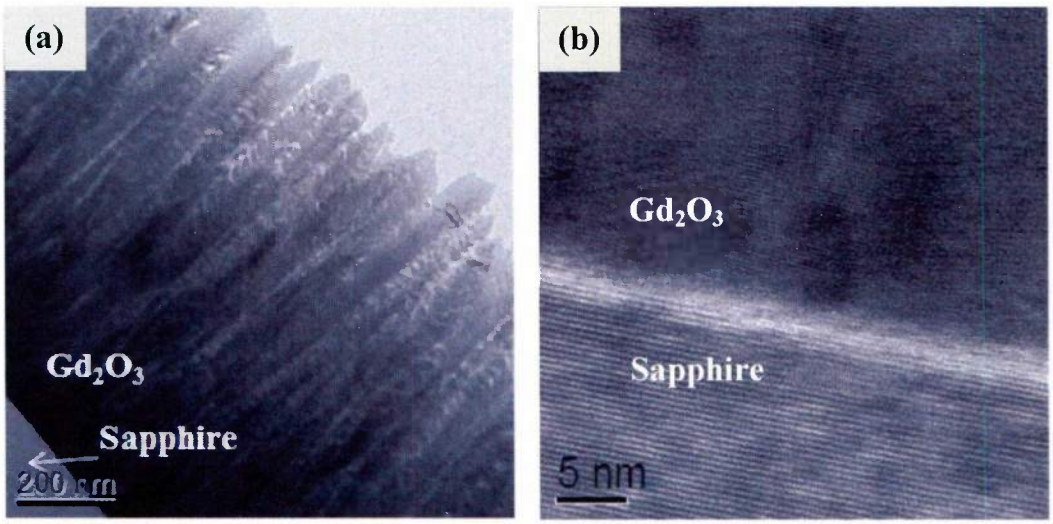

Figure 6.30. (a) Low-magnification and (b) high-magnification bright-field TEM images of Gd_2O_3 film 10A (650 °C, 50 sccm O_2, 1.01 μm, 0.5 Å / s) deposited on sapphire.

6.1.7. Effect of ion bombardment on the morphology of Gd_2O_3 films deposited on sapphire

Surface images of the films from set 11 deposited as a function of ion source current on sapphire are shown in Figure 6.31. For a baseline film, Figure 6.31a, shows that the surface morphology of Gd_2O_3 film 11A (650 °C, 50 sccm O_2, 0.4 Å/s, 0 mA) deposited without ion beam assist (0 mA) exhibits a fairly uniform distribution of small faceted grains across the surface. As the IBS energy is introduced and increased from 0 to 200 mA (film 11B, Figure 6.31b, 200 mA), there appears to be increased grain growth as shown in Figure 6.31b. This can be correlated to the increased energy from the ion source which quickly allows atoms to overcome the activation barrier for nucleation, leading to longer diffusion lengths, and therefore, increased grain growth. The surface appears to be more dense with fewer C(222) facets observed.

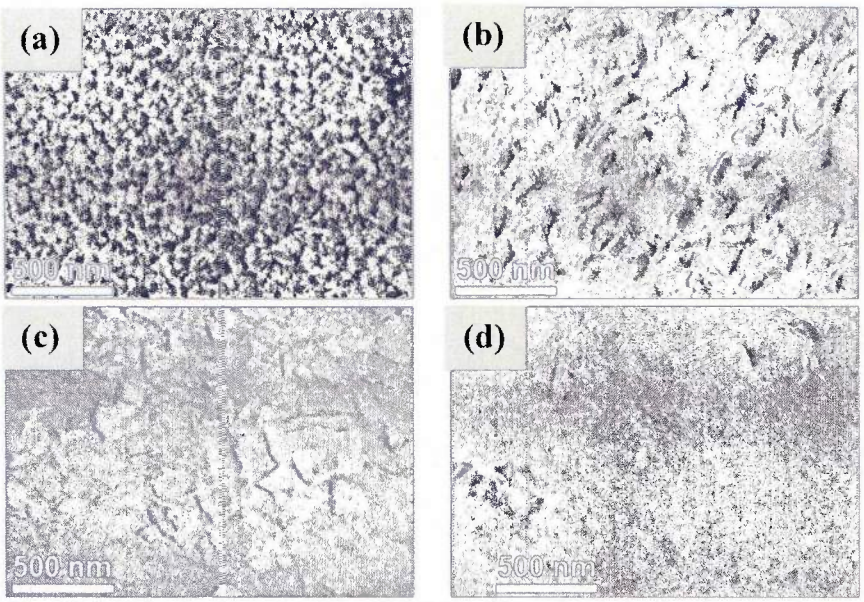

Figure 6.31. SEM top surface images of Gd_2O_3 films deposited using ion beam assisted deposition with currents of (a) 11A (0 mA), (b) 11B (200 mA), (c) 11C (400 mA), and (d) 11D (800 mA) deposited on sapphire as a function of IBS current at 650 °C, 50 sccm O_2, and with growth rate of ~ 0.5 Å / s.

As the ion beam current is increased to 400 mA for film 11C (Figure 6.31c), the surface becomes more dense due to the higher adatom mobility along with a transition in phase volume to 95% monoclinic phase. Figure 6.31d shows the surface morphology of fully monoclinic film 11D (Figure 6.31d) deposited with 800 mA IBS current in which the surface is very smooth and dense. It is clear from Figure 6.31 that the surface morphology becomes smoother as result of film densification and increased diffusion distance with increasing ion beam current (energy).

Figure 6.32a shows a low magnification bright field TEM image of single phase monoclinic film 11D (650 °C, 50 sccm O_2 flow, 0.5 Å/s, 800 mA) deposited on a sapphire substrate. As shown in section 5.4, the large compressive stress resulting from the ion bombardment resulted in a phase transition to the monoclinic phase. Unlike the films deposited without IBS, a columnar morphology is not observed. Instead, the film

possesses a significantly denser structure with no apparent voiding, consistent with the SEM top surface images.

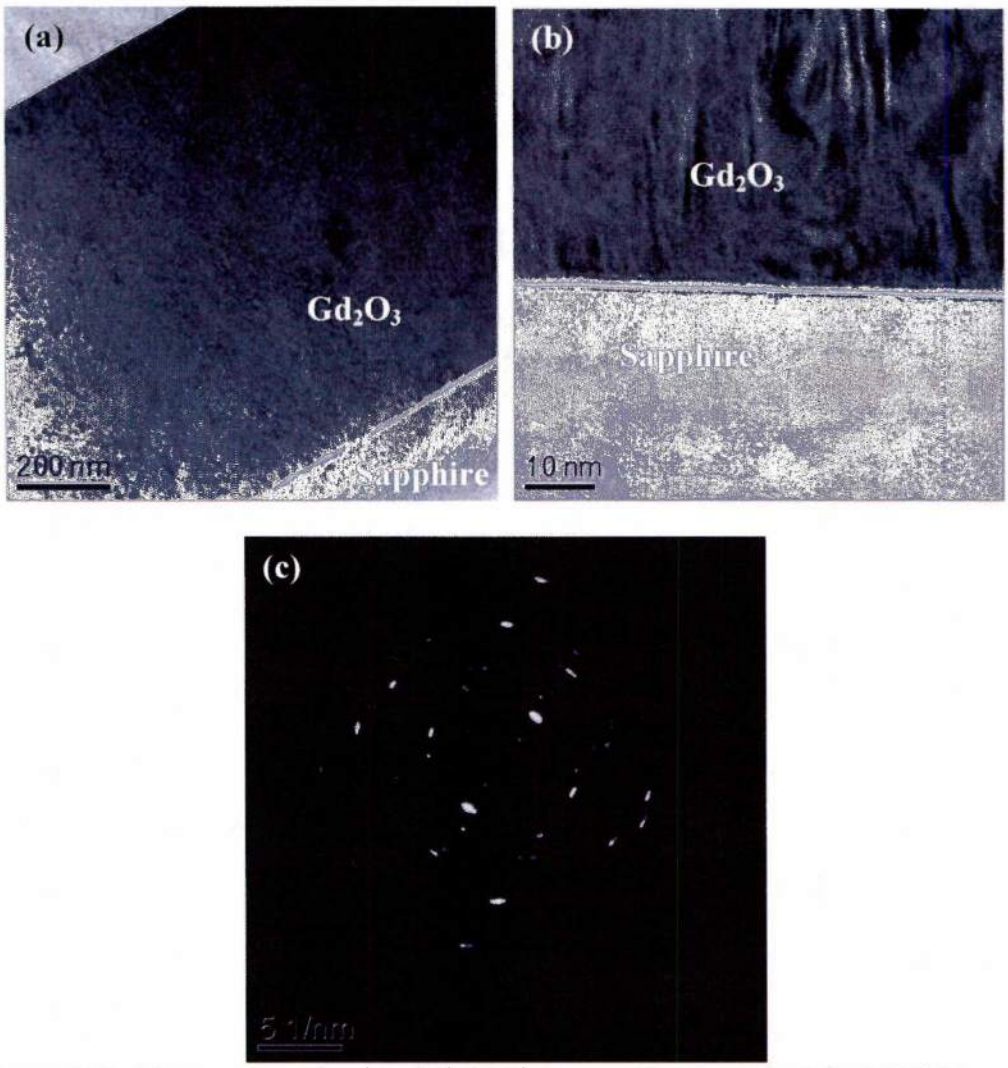

Figure 6.32. (a) Low-magnification and (b) high-magnification bright-field TEM images of thick Gd_2O_3 film 11D (650 °C, 50 sccm O_2, 0.5 Å / s) deposited on sapphire under 800 mA of IBS current, and (c) SAD pattern collected from the middle section of the film.

A high magnification TEM image shown in Figure 6.32b shows that the M(-402) oriented grains grow parallel to the substrate surface. This is further reflected in the SAD pattern shown in Figure 6.32c, which is characterized by bright arcs showing significant

texturing of the M(-402) plane. The highly ordered growth is due to the increased energy from the ion beam which allows the structure to retain the low surface energy orientation. Additionally, all the additional diffraction rings correspond to monoclinic planes, suggesting that the film fully transformed to the monoclinic phase as shown by Raman and XRD in section 5.4. These results highlight the capability of using IBS to synthesize single phase films with smooth surfaces and dense microstructures, which can result in significantly improved film electrical properties.

6.1.8. Effect of heat treatments on Gd_2O_3 film morphology deposited on Si(111)

Heat treatments were performed on the Gd_2O_3 films in order to improve the film electrical properties. Figures 6.33a and 6.33b show top surface SEM images of mixed phase film 12E (650 °C, 200 sccm O_2 flow, 1.2 μm, ~5 Å/s) in the as deposited state and after anneal in oxygen at 1000 °C for 1 hour, respectively. Significant grain growth is observed in the top surface, but is also accompanied by an increase in surface porosity. As the grains grow larger and coalesce, porosity begins to form between the columns.

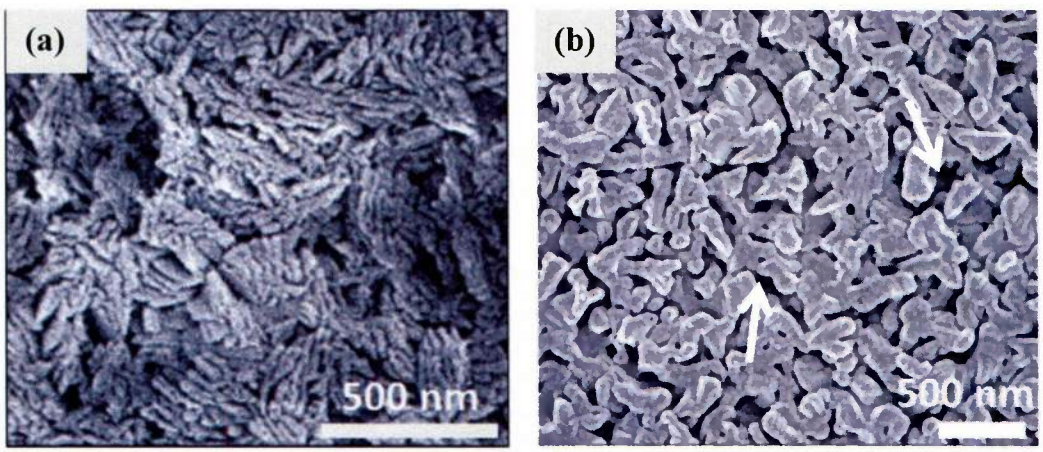

Figure 6.33. SEM top surface images of mixed phase film 12E (650 °C, 200 sccm O_2, 1.2 μm) in the following conditions: (a) as deposited and (b) heat treated at 1000 °C in O_2 environment for 1 hour. Arrows denote porous regions.

The effect of heat treatments on single phase cubic films was also investigated. Cubic film 10A (650 °C, 50 sccm O_2 flow, 1.01 μm, 0.5 Å/s) deposited on silicon was subject to a heat treatment in oxygen for 1 hour at 1000 °C as shown in Figure 6.34. As observed by this low-magnification bright-field TEM image of the heat treated Gd_2O_3 film, collected along the Si<112> zone axis, significant grain coarsening and surface roughening occurred. Additionally, formation of voids (features showing bright contrast) between the grains is observed, slightly increasing the porosity within the film. However, the porosity is significantly reduced as compared to the heat treated mixed phase films.

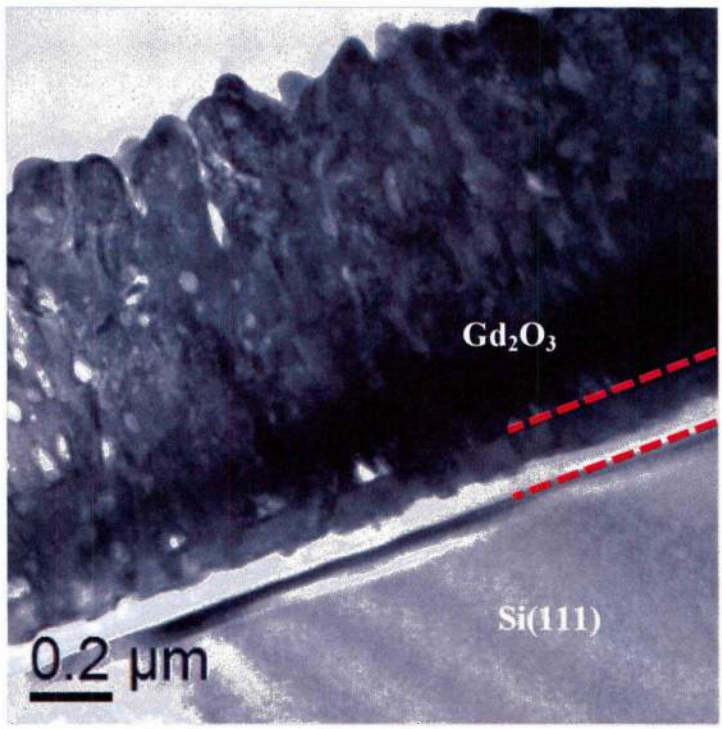

Figure 6.34. Low-magnification bright-field TEM image of cubic Gd_2O_3 film 10A (650 °C, 50 sccm O_2, 1.01 μm, 0.5 Å/ s) after heat treatment at 1000 °C in O_2 environment for 1 hour.

Figure 6.35 shows the interfacial region of cubic film 10A deposited on silicon after heat treatment at 1000 °C in O_2 environment. The interface appears to phase separate into two distinct regions. Note that there is debris covering the layers which is likely resputtered material from the ion beam cleaning during TEM sample preparation. From EDS data (not pictured), the first interface region at the substrate is an approximately 85 nm thick SiOx layer with no Gd detected. Selected area diffraction (not shown here) suggests this layer is amorphous.

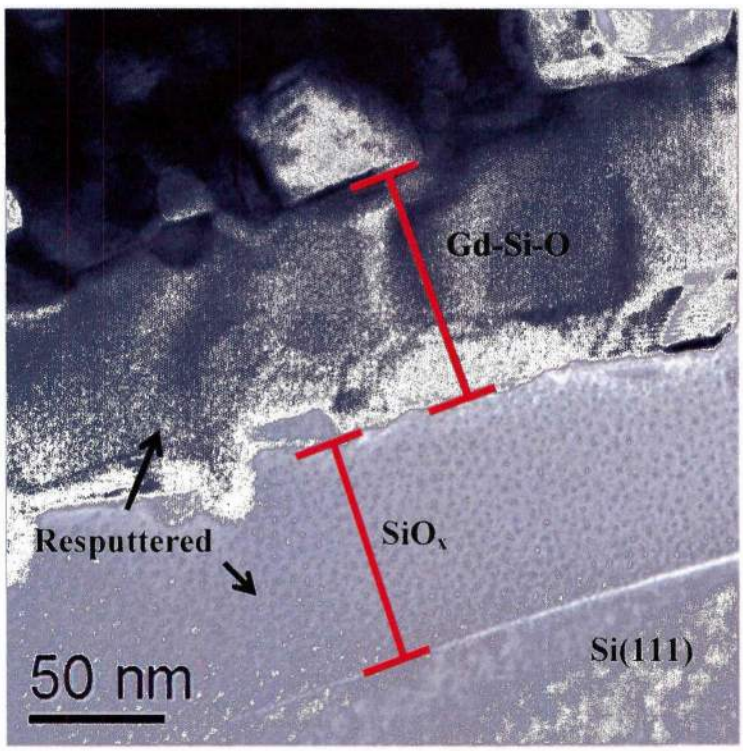

Figure 6.35. High-magnification bright-field TEM image of the interface of cubic Gd_2O_3 film 10A (650 °C, 50 sccm O_2, 1.01 μm, 0.5 Å / s) after heat treatment at 1000 °C in O_2 environment for 1 hour. Arrow denotes resputtered material.

The second region is a Gd-Si-O layer which is approximately 88 nm thick. This layer is crystalline as can be observed from the lattice fringes in the regions where the resputtered material is absent. Above this layer, the Gd_2O_3 film is apparent. Obviously,

annealing at 1000 °C in O_2 atmosphere leads to substantial diffusion and interfacial layer growth.

6.2. Compositional analysis

6.2.1. X-Ray photoelectron spectroscopy

X-ray photoelectron spectroscopy (XPS) was used to further characterize the chemical state and film composition of select films 2A (250 °C, 200 sccm O_2, 1.26 μm) and 2E (650 °C, 200 sccm O_2, 2.05 μm). Sputter depth profiling was performed to investigate the chemistry and composition of the Gd_2O_3 films as a function of depth. Figures 6.36a and 6.36b show the core level spectra measured at various depths ranging from the middle of the film through the interface for film 2E.

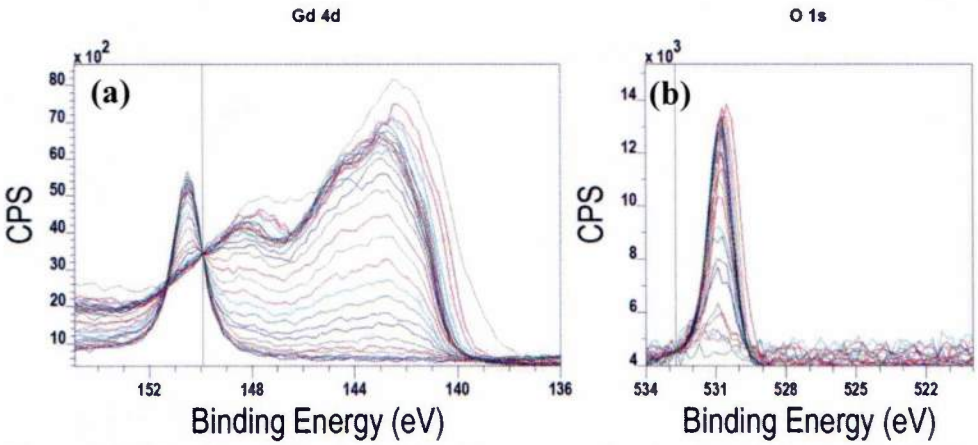

Figure 6.36. Depth profile of XPS binding energy levels of (a) Gd 4d and (b) O1s of film 2E (650 °C, 200 sccm O_2, 2.05 μm).

The Gd 4d level shown in Figure 6.36a for film 2E is characterized by multiplet splitting of the Gd 4d hole with the 4f7 valance electrons to form 9D and 7D ionic states with binding energy of 149 and 143 eV, respectively.[110] The Si 2s peak located at 151 eV begins to rise as the penetration depth increases through the interfacial layer and the

substrate. The O 1s peak shown in Figure 6.37b has a single uniform peak that decreases as the depth penetration increases. This suggests that Gd-O bond for film 2E is heterogeneous throughout the oxide volume.

Figures 6.37a-b show the core level spectra measured at various depths ranging from the middle of the film through the interface for film 2A (250°C, 200 sccm O_2, 1.26 μm). The peaks of the Gd 4d core level spectra shown in Figure 6.37a displays a shift in binding energy with increasing penetration depth of approximately 4eV.

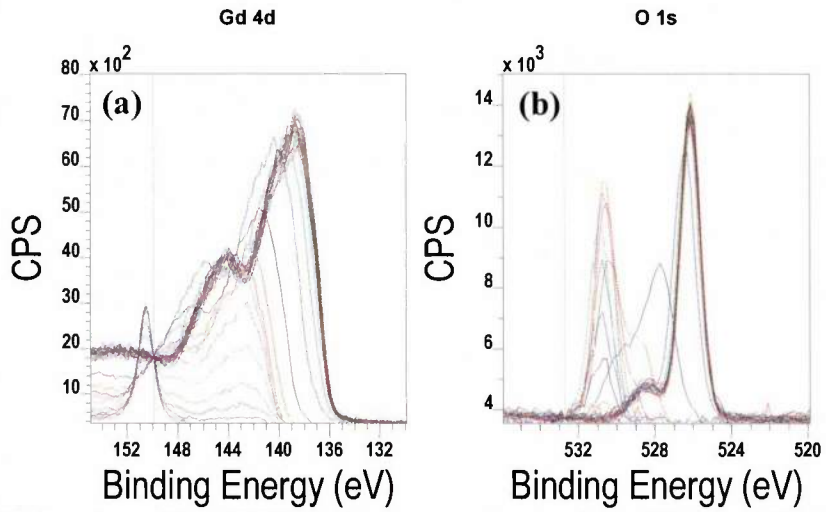

Figure 6.37. Depth profile of XPS binding energy levels of (a) Gd 4d and (b) O1s of film 2A (250 °C, 200 sccm O_2, 1.26 μm).

The observed shift is likely due to surface charging. Insulating materials such as Gd_2O_3 result in positive charge buildup on the sample surface. As a result, the kinetic energy of the photoelectrons decreases resulting in a shift in the spectra to higher binding energies. Additionally, since the information depth of XPS (~10 nm) is approximately equal to the RMS surface roughness of Gd_2O_3 film 2A, differential surface charging may occur in which the insulating properties of the film are not equal throughout the

thickness. The peak shape remains unchanged during the shift, which further supports that this is simply a shift due to charging rather than chemical state.

The O 1s spectra shown in Figure 6.37b also displays a peak shift of approximately 4eV. However, there is an intermediate state where the peak shape is distorted, suggesting a possibility of a change in chemical state. If a change in the chemical state is present, it may be related to the O rich pore like regions observed in the TEM images. Unfortunately, it is impossible to definitively determine whether or not the shift is related to a change in the chemistry of the oxygen bonding state or surface charging.

XPS analysis was further used to measure the O : Gd ratio of the films. Evident from the compositional profile shown in Figure 6.38a, deposition of Gd_2O_3 at 250°C for film 2A results in an oxygen rich film, with a measured O : Gd ratio of 1.86:1. However, when the deposition temperature is increased to 650°C for film 2E (Figure 6.38b), the O : Gd ratio is very close to the 1.5:1 ratio of stoichiometric Gd_2O_3. It is important to note that without extreme care and use of a verified external standard, XPS should be regarded as a semi-quantitative technique. Nevertheless, the higher degree of oxygen content in film 2A is consistent with TEM results presented in section 6.1 which showed the presence of oxygen rich regions for films deposited at 250 °C.

In addition, evaluation of Figure 6.38 indicates diffusion of Si, Gd, and O resulting in formation of a ternary interface layer. According to the compositional profile, the ternary interface layer at 250°C is approximately 50 nm, while at 650°C the interface layer is nearly 150 nm, suggesting that enhanced reactivity occurs for samples at higher temperature. However, the interfacial layer for these samples as observed by TEM

was approximately 3 nm and 10 nm, respectively. The discrepancy in these results could be attributed to the different sputtering rates of Gd, O, and Si. This error is compounded by the fact that the etch depth in Figure 6.38 was calculated by taking the etch time to reach the silicon substrate and diving by the film thickness under the assumption of a linear etch rate. Additionally, the high surface roughness of the films and small information depth of XPS may further disrupt the accuracy of depth profiling.

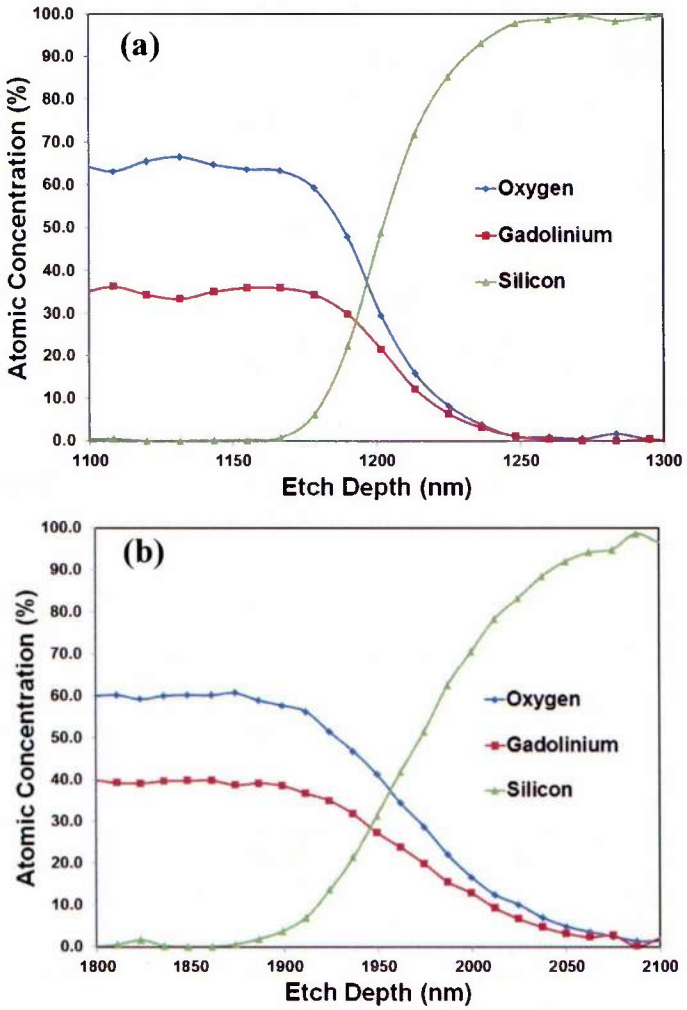

Figure 6.38. Atomic composition of Gd_2O_3 films (a) 2A (250°C, 200 sccm O_2, 1.26 μm) and (b) 2E (650°C, 200 sccm O_2, 2.05 μm) as a function of etch depth.

6.2.2. Energy dispersive x-ray spectroscopy

Energy dispersive x-ray spectroscopy (EDS) was performed on the Gd_2O_3 films in order to learn more information about the compositions. These measurements are semi-quantitative and may not provide accurate results with regards to the exact stoichiometry of the Gd_2O_3 films. However, EDS provides a means to compare the relative O : Gd ratios in the Gd_2O_3 films.

Figure 6.40a displays the EDS data for set 2 (function of temperature, 200 sccm O_2, 1-2 μm) deposited as a function of temperature under 200 sccm O_2 flow. As the deposition temperature is increased, the oxygen to gadolinium ratio decreases from approximately 1.52 to 1.16 from 250 °C to 650 °C. This corresponds to a percentage decrease of 23.6%. The percentage decrease from the XPS measurements for the same samples was 22.7%. The similarity between these measurements suggests good agreement and that EDS may be used to estimate the O : Gd ratio for qualitative trends. The EDS confirms the XPS data suggesting that films deposited at low temperatures are oxygen rich. This is supported by the entrapped oxygen pockets observed in the low temperature deposited films (Figure 6.6) by TEM in section 6.1. Additionally, increased temperature adds energy to the system, which allows greater diffusion lengths, and therefore, films that are more likely to be closer to stoichiometry, as excess oxygen would diffuse out of the film.

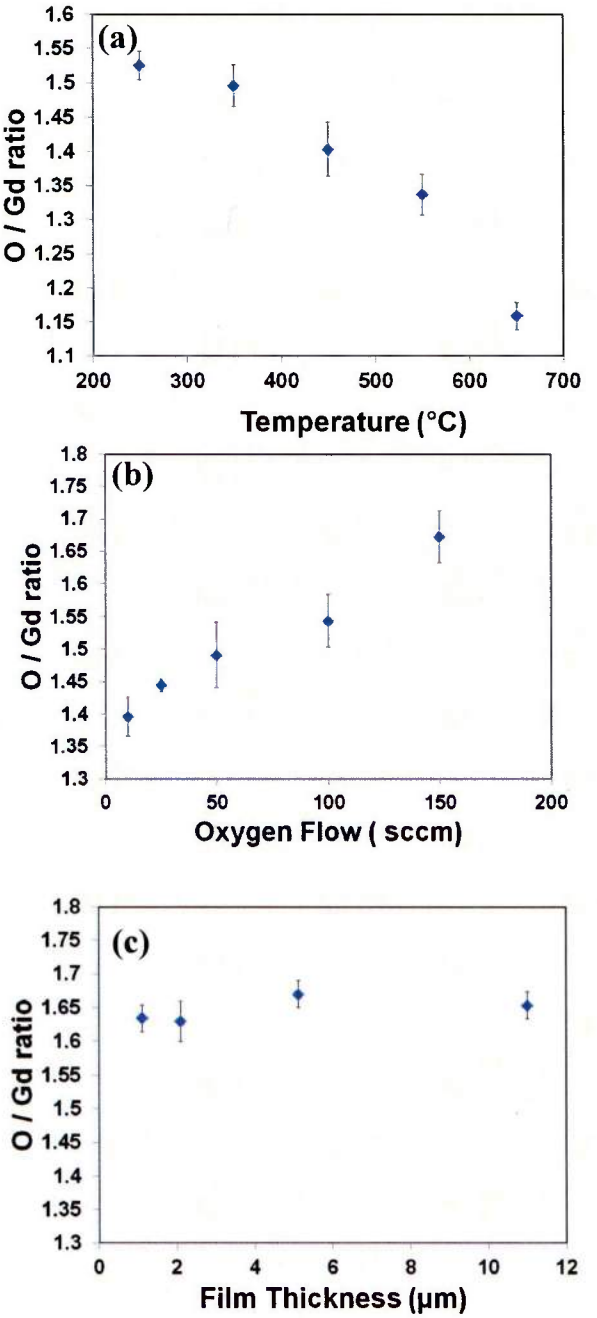

Figure 6.39. O : Gd ratio calculated from EDS measurements for (a) set 2 (function of temperature, 200 sccm O_2, 1-2 µm), (b) set 4 (250 °C, function of oxygen flow, ~1 µm), and (c) set 3 (250 °C, 200 sccm O_2, function of thickness), respectively.

EDS data for films 4A-4E (250 °C, function of oxygen flow, ~1 μm) are shown in Figure 6.40b. Not surprisingly, the oxygen concentration in the films increases with increased O_2 flow during the deposition process. The effect of oxygen flow appears to have a much larger effect on O : Gd of the films deposited at low temperatures (250 °C) than those deposited at high temperatures (650 °C). This is likely due to the reduced surface mobility at low temperature, and the effective trapping of oxygen within the film structure as previously discussed. It is unknown whether the excess oxygen is located in the bulk of the film, at the grain boundaries, or at the film/substrate interface. The presence of excess oxygen can be correlated with the greater porosity of the films deposited at lower temperatures and higher oxygen flows as supported by the TEM and SEM results.

Films deposited as a function of thickness at a low deposition temperature of 250 °C are shown in Figure 6.40c. Interestingly, there is not a substantial difference in the O : Gd ratio over a thickness of range of approximately 1 micron to 11 microns. This suggests that as the growth of the film proceeds, the O : Gd ratio is fairly uniform suggesting robust processing and stability.

6.3. Conclusions

In this chapter, the effects of processing on the structure, composition, and interfacial chemistry of Gd_2O_3 films were investigated by a variety of characterization techniques. The chapter began with a review of the structure and morphology of very thin Gd_2O_3 films (< 50 nm) that were deposited under various conditions. Fully cubic film 8A (250 °C, 200 sccm O_2, 47 nm) was shown to be characterized by small clusters of crystalline grains separated by voids. Nanometer-size pore-like features were

observed and determined to be disordered domains surrounded by crystallites. Decreasing the oxygen flow to 25 sccm was found to decrease the film porosity and improve film crystallinity. Increasing the deposition temperature to 650 °C was found to further densify the film.

Next, the effects of processing on the phase, structure, and morphology of ~1 μm thick Gd_2O_3 films deposited on Si(111) were investigated. Selected area diffraction confirmed the existence of a phase transition from cubic to monoclinic phase along the film thickness for both films deposited at 250 °C and 650 °C. Table 6.2 summarizes the effects of processing on the morphology of the Gd_2O_3 films grown at high deposition rates greater than 5 Å / s. For ~1 μm thick films deposited as a function of temperature at constant 200 sccm O_2 flow (set 6), increasing temperature resulted in a change from a porous fibrous morphology to a structure with a dense nucleation zone followed by columnar growth. Voids formed between the columns due to shadowing effects and mixed phase growth, resulting in increased surface porosity and roughness. For films deposited as a function of oxygen flow at a deposition temperature of 650 °C (set 1), no significant changes were observed in the film structure. For films deposited as a function of oxygen flow at deposition temperature of 250 °C (set 4), increasing the oxygen flow was found to result in increased porosity in the film due to the lower adatom mobility resulting from excess oxygen in the chamber. Increasing the film thickness at a deposition temperature of 250 C (set 3) resulted to an increase in grain size, but no substantial change in surface morphology. For films grown at 650 C (set 9), film growth was initially characterized by large (~50 nm) cubic (222) facets surrounded by smaller monoclinic grains. As the film thickness increased, the monoclinic grains dominated the

surface morphology. A resulting complex surface morphology with ridge-like features was observed for thick films and attributed to both shadowing effects and highly oriented growth of M(020) grains.

Table 6.2. Summary of process-phase trends describing the effects of temperature, oxygen flow, and thickness on the morphology of Gd_2O_3 films deposited at high rates greater than 5 Å / s. The bolded letters indicate the varied deposition parameters for each set.

Set	Temperature (°C)	Oxygen flow (sccm)	Thickness (μm)	Trend
6	**Function of temperature (250 - 650 °C)**	200	~1	Increasing temperature results in columnar structure with increased grain size, roughness and surface porosity.
1	650 °C	**Function of O_2 flow (50 -200)**	~2	No substantial effects observed. Temperature dominates surface characteristics.
4	250 °C	**Function of O_2 flow (25 - 200)**	~1	Increasing oxygen flow leads to smaller grain size and increased porosity.
3	250 °C	200 sccm	**Function of thickness (0.5 - 11)**	Increasing thickness leads to increased grain size, but similar morphology
9	650 °C	200 sccm	**Function of thickness (0.4 - 6)**	Thin films show large C(222) grains mixed with small monoclinic phase crystallites. Surface porosity increases with increasing thickness.

The effects of processing on the interfacial structure of select Gd_2O_3 films deposited at high rates (> 5 Å / s) on silicon were studied. The results were summarized in Table 6.1. Very thin films (<50 nm) deposited at 650 and 250 C possessed thin (2 nm) SiO_x rich interfacial layers. Due to longer deposition times which resulted in increased diffusion, thick films possessed mixed Gd-Si-O interfacial layers. The size and structure of the interfacial layer was dependent upon the deposition conditions.

Generally, higher oxygen flow and higher deposition temperature led to larger interfacial layer size and a more undulating interface. The interfacial reaction was determined to proceed as a result of intermixing of the SiO_x layer with the Gd_2O_3 layer to form the Gd-Si-O interface during deposition.

Films deposited at high rates (> 5 Å / s) resulted in similar morphologies regardless of the underlying substrate. However, when the deposition rate was lowered to < 0.5 Å / s. significant differences were observed in the structure of the Gd_2O_3 films due to the increased adatom mobility on the film surface. Table 6.3 summarizes the effects of substrate material on the structure of film 10A grown at low rate. Gd_2O_3 films grown on silicon (111) possessed large grain size and strong C(222) faceting. Interestingly, the interfacial structure for film 10A grown on silicon was not uniform with some interfacial regions for film 10A being primarily crystalline while others possessed amorphous character. In the regions with a crystalline interface, highly ordered growth of the C(222) planes were observed, while regions with amorphous interfacial layer showed polycrystalline character. Gd_2O_3 films grown on GaN exhibit a completely crystalline interfacial layer. As a result of this and the close symmetry of the (222) planes with the GaN basal plane, regions of near epitaxy are observed during film growth. The film consists of large columns (~200 nm) in direct epitaxial with the substrate. Due to the large lattice mismatch, however, dislocations form and polycrystalline grain growth occurs in some regions as the film thickness increases. Films grown on quartz possess slightly smaller grain size as a result of the formation of multiple grains with various orientations. This is due to the amorphous nature of the substrate which does not provide a template for preferred in-plane orientation. Films grown on sapphire exhibited

significantly smaller grain size and column width. This was attributed to increase in lattice energy due to increased compressive stresses as well as formation of small amount of monoclinic phase.

Table 6.3. Effect of substrate material on morphology of Gd_2O_3 film 10A (650 °C, 50 sccm O_2, 1.01 μm, 0.5 Å / s).

Substrate	Top Surface Grain Size (nm)	Column Width (nm)	Description
Si(111)	170	100-200	Surface composed entirely of C(222) facets with large grain size. Uniform columnar grain growth
Quartz	110	-	Surface composed of C(222) facets with formation of smaller polycrystalline material
Sapphire	85	30-50	Surface composed of various different facets showing clear polycrystalline growth. Small grain size and column width attributed to increased compressive stress
GaN	160	100-250	Surface composed mainly of C(222) facets with large grain size. Regions of near epitaxial growth observed. No interfacial layer

The effects of ion bombardment on Gd_2O_3 film structure were examined. Increasing ion beam current resulted in increased film densification and smoother surface morphology. These results show that ion beam assisted deposition can be used to deposit smooth, dense single phase thick Gd_2O_3 films. Next, the effects of heat treatments on Gd_2O_3 film morphology were studied. It was found that heat treatments in oxygen at 1000 °C led to increased film porosity and substantial increase in interfacial layer size. The interface phase separated into two distinct regions, an amorphous SiOx region and a crystalline Gd-Si-O region. Lastly, XPS and EDS were used to investigate the O : Gd ratio in the films. Films deposited at low temperatures were found to be oxygen rich,

consistent with the TEM results which showed porous oxygen-rich regions. As the deposition temperature increased, the O : Gd ratio decreased. Increasing the oxygen flow for films deposited at 250 °C (set 4) resulted in substantial change in the O : Gd ratio while there was minimal effect at 650 °C (set 1). Lastly, the O : Gd ratio was similar for films deposited as a function of thickness, suggesting uniformity in the O : Gd ratio through the film thickness. As shown by the results in this chapter, it is clear that the deposition conditions have substantial effect on film structure and morphology, which will be shown to have significant effects on film electrical properties in chapter 7.

Chapter 7

Results and Discussion: Electrical properties and neutron detection response of thick film Si(111) / Gd_2O_3 / Ti / Au MOS capacitors and GaN / AlGaN / Gd_2O_3 / Ti / Au HEMTs

7.1. Introduction

In this chapter, the effects of processing on the electrical properties, device performance, and neutron response of Si(111) / Gd_2O_3 / Ti / Au metal-oxide-semiconductor (MOS) capacitors, GaN / AlGaN / Gd_2O_3 / Ti / Au MOS capacitors, and high electron mobility transistors (HEMTs) will be discussed.

Frequency dispersion of the dielectric properties over a range of 10kHz – 1MHz was examined for the Si(111) / Gd_2O_3 / Ti / Au MOS capacitors. From these measurements, the effects of processing, structure, and phase on Gd_2O_3 dielectric constant were obtained. Capacitance-voltage (C-V) and conductance-voltage (G-V) measurements were performed on the GaN / AlGaN / Gd_2O_3 / Ti / Au MOS capacitors to extract values of bulk trapped charge and interface trapped charge in the devices. Furthermore, a charge trapping effect and non-volatile memory window were investigated via C-V methods.

For the Si(111) / Gd_2O_3 / Ti / Au MOS capacitors, DC current-voltage (I-V) measurements were performed to determine leakage currents of the Gd_2O_3 films. The effects of deposition temperature, film thickness, oxygen flow, and deposition rate on the DC I-V properties were determined and related to the film structure. Additionally, I-V measurements as a function of temperature (I-V-T) were performed to determine the

conduction mechanisms present in the Gd_2O_3 films and determine trap levels. I-V-T measurements were also performed on GaN / AlGaN / Gd_2O_3 / Ti / Au capacitors.

The operation of GaN / AlGaN / Gd_2O_3 / Ti / Au MOS-HEMTs was examined with a focus on the necessary device performance for radiation detection. The effect of film processing on the switching characteristics and leakage currents was examined. Finally, the performance of the MOS-HEMTs under thermal neutron irradiation was studied.

7.2. Dielectric properties

The frequency dispersion of the real dielectric constant, imaginary dielectric constant, and dielectric loss in the range of 1kHz – 1MHz was studied for the Gd_2O_3 films. As observed from the dielectric dispersion measurement of a typical Gd_2O_3 film shown in Figure 7.1, there is a significant reduction in dielectric constant with increasing measurement frequency for the as-deposited sample. This was originally thought to be caused by space charges which can respond at low frequencies but cannot become polarized quickly enough to respond at high frequencies. However, films were then heat treated in air at 100 °C, allowed to cool to room temperature and then, immediately re-measured. After heat treatment, the films possessed excellent frequency dispersion over a frequency range of 1 kHz to 1 MHz, with very minor reduction in the dielectric constant. This is explained by the outgassing of trapped moisture within the Gd_2O_3 film. The entrapped water causes a strong dipolar orientation response and inflates the measured dielectric constant due to the high permittivity value of water (ε = 80).[111] Indeed, it is well known that rare earth oxides can be highly hygroscopic.[112] The

frequency dispersion of the dielectric constant measured after heat treatment shows that there is minimal contribution from space charge polarization within the Gd_2O_3 film. Additionally, the loss factor is significantly reduced after the heat treatment.

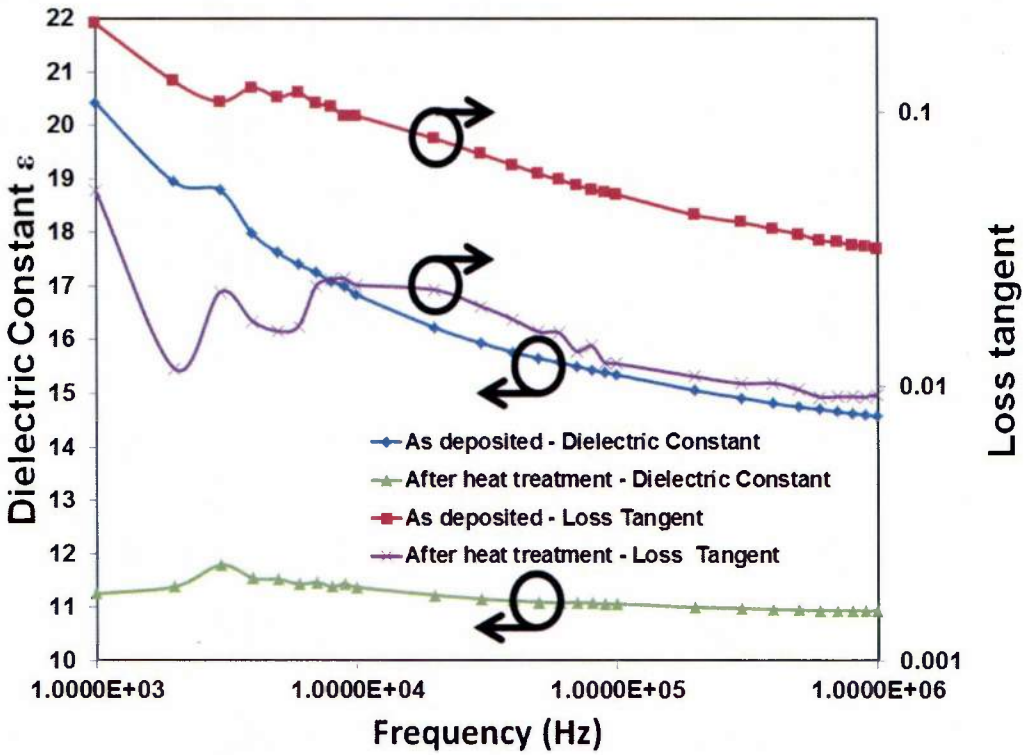

Figure 7.1. Dispersion of the dielectric constant and loss tangent of a Gd_2O_3 film as a function of frequency (a) as deposited and (b) after heat treatment at 100 °C. Arrows denote corresponding y axis.

7.2.1. Effects of processing on the dielectric constant

The effects of processing, structure, and crystallographic phase on the dielectric constants of the Gd_2O_3 films were further examined. Table 7.1 displays the dielectric constants for select Gd_2O_3 films measured at a frequency of 1MHz. All films were

measured at room temperature directly after heat treatment at 100 °C to ensure accurate determination of the dielectric constant.

Table 7.1. Dielectric constants for select Gd_2O_3 films measured at 1 MHz.

Film	Temperature (°C)	O_2 flow (sccm)	Thickness (μm)	Dielectric Constant
1A	650	**50**	2.05	13.4
1B	650	**100**	2.03	13.9
1C	650	**150**	1.73	14.0
1D	650	**200**	2.05	13.6
3A	250	200	**0.58**	12.0
3B	250	200	**1.11**	10.9
3C	250	200	**2.10**	10.9
3D	250	200	**5.12**	10.9
3E	250	200	**11.01**	-
4A	250	**25**	1.36	17.7
4B	250	**50**	1.67	17.7
4C	250	**100**	1.29	14.4
4D	250	**150**	1.39	13.2
4E	250	**200**	0.76	11.4
6A	**250**	200	1.07	11.7
6B	**350**	200	0.90	15.6
6C	**450**	200	0.85	15.8
6D	**550**	200	0.69	16.9
6E	**650**	200	0.89	17.2
9A	650	200	**0.38**	22.0
9B	650	200	**0.59**	22.7
9C	650	200	**1.02**	-
9D	650	200	**2.69**	14.3
9E	650	200	**5.72**	13.9

For films 6A-6E (function of temperature, 200 sccm O_2, ~1 μm), a general trend of increasing dielectric constant with increasing temperature was observed from a value of 11.7 for film 6A (250 °C) to a value of 17.2 for film 6E (650 °C) as observed in Figure 7.2a. A number of possibilities for this observed dielectric behavior are proposed. The first is explained by the increase in crystallinity in the Gd_2O_3 film with increasing deposition temperature as previously shown by XRD analysis in section 4.1.

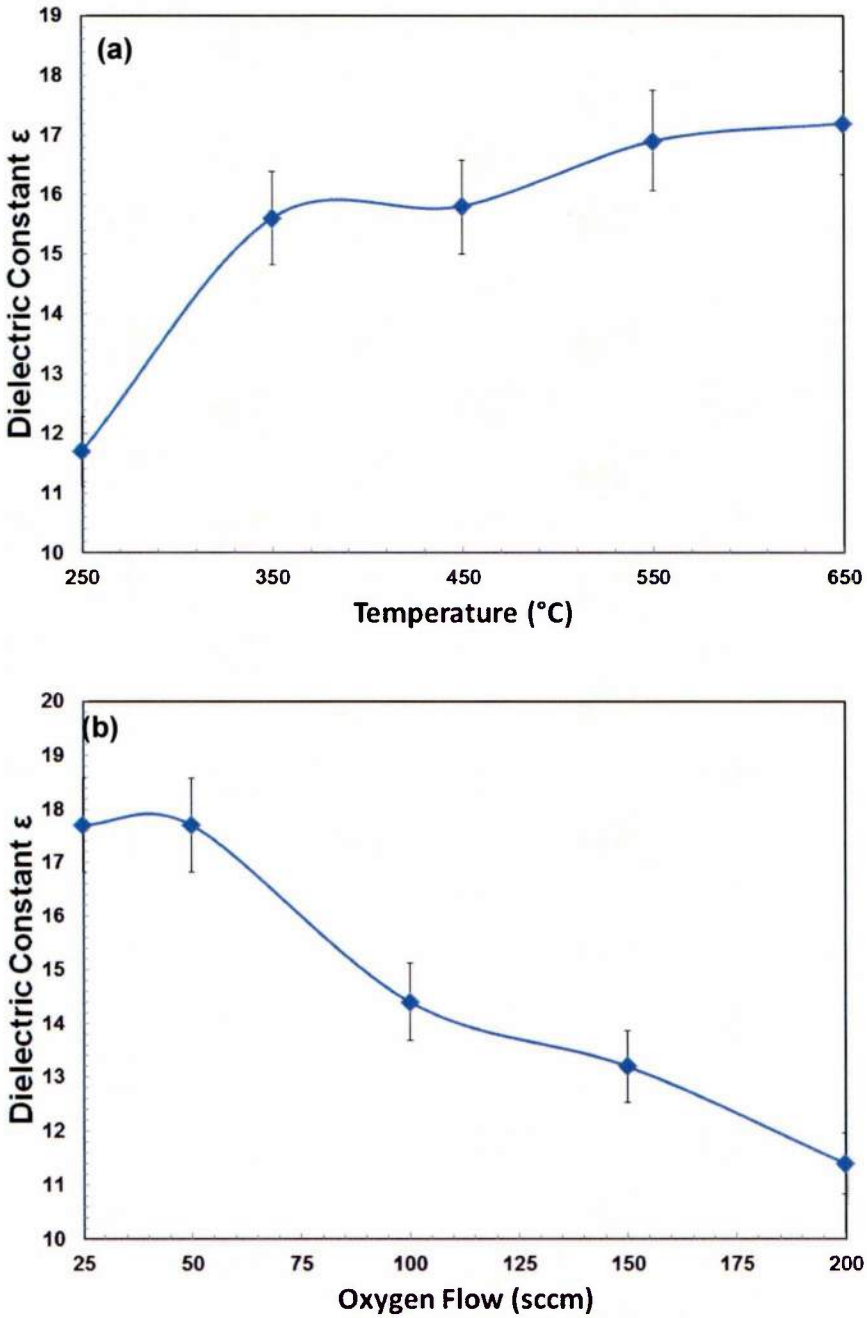

Figure 7.2. Gd_2O_3 permittivity measured at a frequency of 1 MHz as a function of (a) temperature of films 6A-6E (function of temperature, 200 sccm O_2, ~1 μm) and (b) oxygen flow rate for films 4A-4E (250 °C, function of O_2 flow, ~1 μm).

Indeed, it was shown in section 6.2 through transmission electron microscopy (TEM) that films deposited at low temperature possessed regions of porosity which would effectively lower the dielectric constant since permittivity of air is equal to a value of one. Therefore, the increase in film density coupled with the higher dielectric constant from crystalline Gd_2O_3 explains the observed behavior.

A significant change is not observed in the film dielectric constant value (13-14) for films 1A-1D (650 °C, function of O_2 flow, ~2 μm) deposited as a function of O_2 flow at 650 °C as observed from Table 7.1. This is consistent with diffraction data and microscopy results which showed that there is minimal effect of oxygen flow on phase volume, microstructure, and O : Gd ratio at a deposition temperature of 650 °C. Therefore, it can be concluded that the film dielectric constant is highly correlated with film phase, structure, and composition.

As shown in Figure 7.2b, a significant decrease in the dielectric constant from a value of 17.7 to a value of 11.7 is observed for films 4A-4E (250 °C, function of O_2 flow, ~1 μm) with increasing oxygen flow at a deposition temperature of 250 °C. A number of possibilities exist for the decrease in dielectric constant in the material. The first is related to the density of the film. Films deposited at lower oxygen flow rates were significantly denser than films deposited at higher oxygen flow rates due to reduced atomic collisions (scattering) during deposition. The porosity that formed due to the higher oxygen flow rate and thus, lower surface adatom mobility, effectively reduces the dielectric constant. Additionally, the grain size and crystallinity decreased with increasing O_2 flow. However, this alone may not be sufficient to explain such a drastic decrease in film dielectric constant. Therefore, it is also necessary to consider phase volume analysis.

As displayed in Table 4.4, decreasing the amount of oxygen flow resulted in an increase in the amount of the monoclinic phase from 100% (Film 4A, 25 sccm O_2) to roughly 20% (Film 4A, 200 sccm O_2). The increase in dielectric constant with increased monoclinic phase is in contrast to the studies investigating magnetron sputtering deposition of polycrystalline Gd_2O_3 films[51,8] in which an increase in the monoclinic phase resulted in a decrease or no change of the dielectric constant. However, another study has shown that epitaxial deposition of Gd_2O_3 films by MBE[56] has resulted in a higher dielectric constant for single phase monoclinic films ($\kappa = 17$) as compared to single phase cubic films ($\kappa = 14$).

To further investigate the effects of phase volume on the Gd_2O_3 film dielectric constant, we employ the Clausius-Mossoti relation. The Clausius–Mossotti relation[113] provides a link between the physical structure of a material and the dielectric constant κ:

$$\kappa = \frac{1+\frac{8\pi\alpha_m}{3V_m}}{1-\frac{4\pi\alpha_m}{3V_m}} \qquad \text{Eq. 7.1}$$

where α_m is the microscopic polarizability and V_m is the molar volume. Since the molar volume of the Gd_2O_3 monoclinic unit cell[75] (43.67 mol / cm^3) is smaller than the molar volume of the cubic unit cell[76] (47.58 mol / cm^3), one would expect to observe a higher dielectric constant for Gd_2O_3 films of the monoclinic phase assuming a constant microscopic polarizability. Therefore, it is expected that for a mixed phase polycrystalline film, an increase in monoclinic phase volume will be accompanied by a higher dielectric constant if the microscopic polarizability remains constant. Using a value of 9.23 for the Gd_2O_3 microscopic polarizability[57] yields expected dielectric constant values of κ = 14.0 and κ = 24.2 for the cubic and monoclinic phases

respectively. To assess the validity of the relation, the dielectric constant of pure highly crystalline cubic phase film 11A and pure monoclinic phase film 11D were measured and found to be $\kappa = 13.6$ and $\kappa = 23.5$, respectively. The Claussius-Mossoti relation suggests excellent agreement for the monoclinic and cubic phase films.

Table 7.1 displays the effects of film thickness on the dielectric constant for films 9A-9E (650 °C, 200 sccm O_2, function of thickness). Increase in the film thickness from 380 nm (film 9A) to 590 nm (film 9B) resulted in an increase of dielectric constant value from 20 to 24. This is explained by the increased monoclinic phase volume observed for film 9B as compared to 9A, and the retention of high film density before the onset of columnar growth. With increasing thickness for films 9C-9E, the dielectric constant decreases to values of 19, 16, and 14, respectively, despite the fact that the monoclinic phase grew exclusively as the film grew thicker. This is correlated directly with the increase in film porosity observed due to voiding between the growing columns as shown in Chapter 6.4.

The effect of film thickness on the dielectric constant for films 3A-3E (250 °C, 200 sccm O_2, function of thickness) are shown in Table 7.1. The dielectric constant for these samples is low due to the poor crystallinity and porosity characterized by low temperature deposition and high oxygen flow. Additionally, the calculated dielectric constant was very similar between the samples due to the similarity in phase volume.

7.2.2. Bulk and interface charges

C-V measurements can yield information about fixed oxide charge, interface trapped charge, oxide trapped charge, and mobile oxide charge within oxide thin films.

A typical C-V curve for a MOS capacitor will have three distinct regions corresponding to accumulation, depletion, and inversion. However, the degenerative silicon substrates used in this work possess high doping ($N = 10^{19}\ cm^{-3}$) and low resistivity (0.002 - 0.008 ohm - cm) which prevents substantial penetration of the electric field into the substrate. As a result, significant depletion of the carriers in the silicon substrate does not occur and the measured capacitance (C_m) is quite low resulting in a ratio of C_m/C_{ox} of close to 1, where C_{ox} is the oxide capacitance in accumulation. Indeed, for thicker films (> 1 μm), the capacitance remained constant even when sweeping the voltage from a value of -30 V to +30 V (largest allowed by the instrument). A substrate with low resistivity was necessary for radiation detection studies to ensure that the electric field stayed confined to the film and that charge collection due to gamma radiation generated in the substrate was minimized. Since significant depletion is not observed, it is difficult to extract information about the trapped charge density in the oxide films. Therefore, capacitance-voltage characterization was performed for GaN / AlGaN / Gd_2O_3 / Ti /Au MOS capacitors.

Figure 7.3 displays the C-V data for GaN / AlGaN / Gd_2O_3 / Ti / Au MOS capacitors 7A (250 °C, 50 sccm O_2, 1.1 μm), 7E (650 °C, 50 sccm O_2, 1.20 μm), and 10A (650 °C, 50 sccm O_2, 1.01 μm, 0.5Å/s). For comparison, C-V data for a GaN / AlGaN / Ti / Au Schottky gate MS capacitor (without oxide layer) is also plotted. All samples were swept from -20 V to 0 V to -20 V to drive the capacitor from inversion to accumulation and back to inversion.

As observed from Figure 7.3, the threshold voltage (V_{TH}) of the MS control sample is approximately -2.9 V with sharp transitions between accumulation, depletion,

and inversion. Additionally, no hysteresis is observed in the C-V curve. The C-V curves for the Gd_2O_3 devices retained this sharp transition, without any "smearing out" characteristics suggesting good interface quality between the Gd_2O_3 film and GaN substrate.[114] Deposition of the Gd_2O_3 film, however, results in significant shift of the threshold voltage (ΔV_{TH}) towards more negative values. The leftward shift of the C-V curve is attributed to positive fixed oxide charge present within the Gd_2O_3 film. In oxide materials, positive fixed charge have typically been linked to oxygen vacancies and broken bonds.[115] ΔV_{TH} values for select samples are listed in Table 7.2.

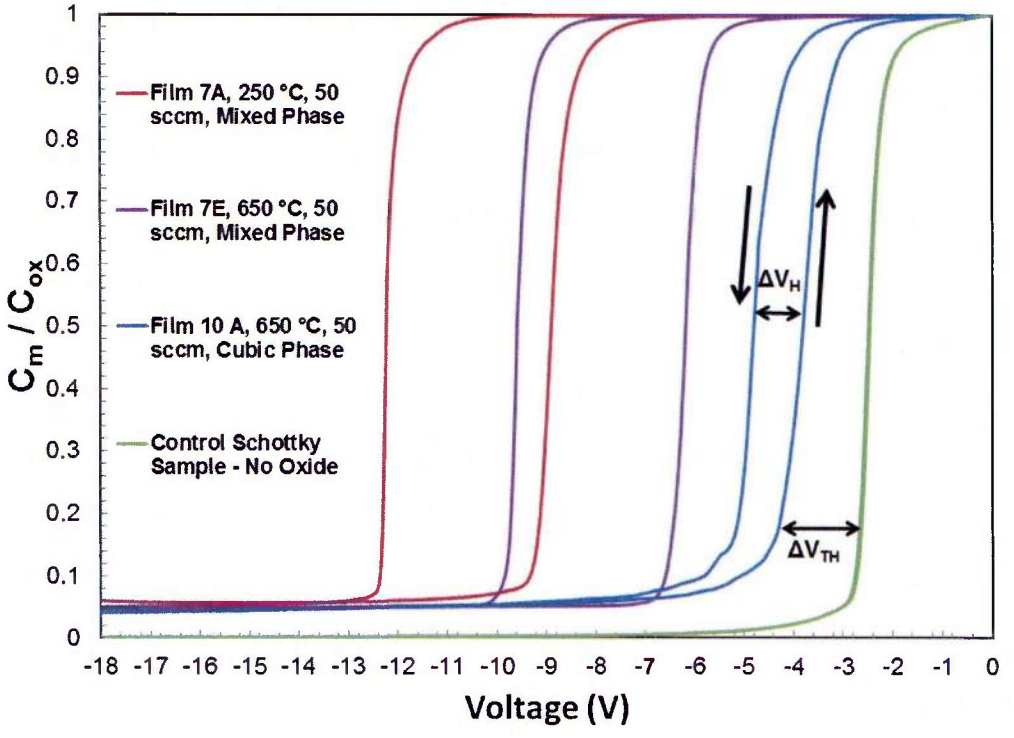

Figure 7.3. Capacitance-Voltage curves taken at 1 MHz for GaN / AlGaN / Gd_2O_3 / Ti / Au MOS capacitors 7A (250 °C, 50 sccm O_2, 1.1 µm), 7E (650 °C, 50 sccm O_2, 1.20 µm), 10A (650 °C, 50 sccm O_2, 1.01 µm, 0.5Å/s) and GaN / AlGaN / Ti / Au Schottky control sample.

The largest ΔV_{TH} values of 8.35 V and 6.52 V are observed for films 6A (250 °C, 200 sccm O_2, 1.07 μm) and 7A (250 °C, 50 sccm O_2, 1.10 μm), respectively. Increasing the deposition temperature resulted in smaller ΔV_{TH} values of 6.08 V and 4.81 V for films 6E (650 °C, 200 sccm O_2, 0.87 μm) and 7E (650 °C, 50 sccm O_2, 1.1 μm). From these values, it is clear that decreasing deposition temperature and increasing oxygen flow result in increased fixed positive oxide charge. We have shown in Chapter 6.2 through EDS and XPS compositional analysis results that oxygen content decreases with increasing deposition temperature and with decreasing oxygen flow. However, TEM analysis in Chapter 6.1.2 has shown that films deposited at 250 °C possess oxygen rich disordered regions and are less homogenous and dense than films grown at 650 °C. Therefore, despite the greater concentration of oxygen in films deposited at 250 °C, the increased crystallinity and greater homogeneity of the films deposited at 650 °C results in significantly reduced fixed oxide charge. Indeed, this is further supported by the small ΔV_{TH} value (1.85 V) of single phase cubic film 10A (650 °C, 50 sccm O_2, 1.01 μm, 0.5Å/s) which possessed excellent crystallinity and homogeneity.

Table 7.2. Threshold voltage shift (ΔV_{TH}), hysteresis (ΔV_H), bulk trapped charge (N_{it}), and interface state density (D_{it}) for select Gd_2O_3 films.

Sample	Dep. Temp (° C)	O_2 Flow (sccm)	Film t (μm)	Dep. Rate (Å/s)	ΔV_{TH} (V)	ΔV_H (V)	N_{it} (cm^{-2})	D_{it} (eV^{-1}-cm^{-2})
6A	250	200	1.07	7.53	8.35	3.07	6.9×10^{11}	1.56×10^{11}
6E	650	200	0.87	8.19	6.08	3.48	3.2×10^{11}	1.27×10^{11}
7A	250	50	1.10	9.58	6.52	3.35	3.0×10^{11}	4.01×10^{11}
7E	650	50	1.20	9.11	4.81	3.41	2.7×10^{11}	4.61×10^{11}
10A	650	50	1.00	0.48	1.85	0.89	6.9×10^{10}	1.05×10^{11}

The interface trap density D_{it} was calculated from the C-V and G-V curves using the Cole-Hillman method[116] shown in equation 7.2:

$$D_{it} = \frac{2}{qA}\frac{G_{max}}{\omega}\left[\left(\frac{G_{max}}{\omega C_{ox}}\right)^2 + \left(1 - \frac{C_m}{C_{ox}}\right)^2\right]^{-1} \quad (eV^{-1}\text{-}cm^{-2}) \quad \text{Eq 7.2}$$

where D_{it} is the interface state density, q is the electronic charge, A is the capacitor area, C_{ox} is the capacitance in accumulation, G_{max} is the peak value of the conductance from the G-V curve, ω is the angular frequency, and C_m is the measured capacitance at G_{max}. The extraction of D_{it} from the C-V and G-V curves is shown in Figure 7.4.

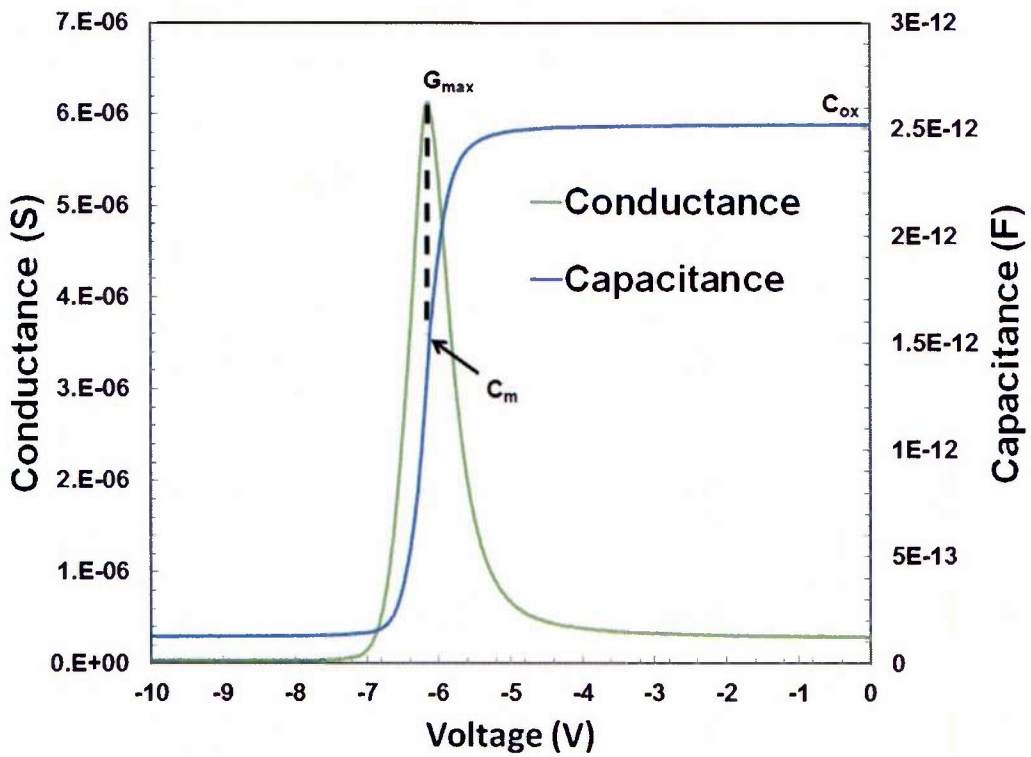

Figure 7.4. Example of G-V and C-V curve used for extracting the density of interface states (D_{it}) for sample 7E (650 °C, 50 sccm O_2, 1.1 μm).

The calculated values for D_{it} are shown in Table 7.2. For films 6A, 6E, 7A, and 7E deposited at high rates, raising the oxygen flow from 50 sccm to 200 sccm by a factor of 4 reduces the interface state density by a factor of 4 from ~4 x 10^{11} to ~1 x 10^{11} eV^{-1}-cm^{-2}. Indeed, this data suggests that oxygen flow plays a more important role than temperature in determining the D_{it}. One possibility is that for films deposited at 50 sccm O_2 under high rates, not enough oxygen is present to passivate the surface states. Single phase cubic film 10A deposited at low rates possessed the lowest D_{it} (1 x 10^{11} eV^{-1}-cm^{-2}) of all measured samples. This is unsurprising given the near-epitaxial growth observed in the TEM analysis shown in Chapter 6.1.6.

All the GaN / AlGaN / Gd_2O_3 / Ti / Au MOS capacitors showed significant amount of hysteresis, ΔV_H, as shown in Figure 7.3. Hysteresis is indicative of the presence of trapping of slow charge carriers. The hysteresis possessing counter-clockwise character is a result of electron trapping within the bulk oxide film and/or at the semiconductor / film interface. Since the measured D_{it} was fairly low and similar for all samples deposited at high rates, it is likely that the ΔV_H is mainly a result of bulk oxide trapping. ΔV_H is significantly reduced for single phase film 10A deposited at low rates. From the hysteresis it is possible to calculate the trapped charge using equation 7.3[117]:

$$N_{it} = \frac{\Delta V_H C_{ox}}{qA} \qquad (cm^{-2}) \qquad \text{Eq 7.3}$$

where N_{it} is the concentration of trapped charge, ΔV_H is the hysteresis, C_{ox} is the capacitance in accumulation, q is the electronic charge, and A is the area of the capacitor. The measured values for N_{it} are listed in Table 7.2.

Recent work by Chang et al. has shown that crystalline Gd_2O_3 can act as a charge trapping layer with a nonvolatile memory effect.[118] While this is desirable for charge memory storage devices, a memory effect would lead to instability and suboptimal device performance for the HEMTs during neutron detection. Chang et al. have proposed that this effect occurs in crystalline Gd_2O_3 films deposited on GaN/AlGaN structures, but is absent in amorphous Gd_2O_3-based devices. To test this phenomenon, C-V characteristics of GaN / AlGaN / Gd_2O_3 / Ti / Au MOS capacitors 6A (250 °C, 200 sccm O_2, 1.07 μm) and 10A (650 °C, 50 sccm O_2, 1.01 μm, 0.5Å/s) were investigated. 6A and 10A were chosen due to their poor and excellent crystallinity, respectively.

Figure 7.5a shows the C-V curve of Gd_2O_3 film 6A. For the first measurement, the gate bias was swept from 0 V to -20V at 1MHz frequency (curve 1). The C-V curve shows clear accumulation, depletion, and inversion regions with a threshold voltage of approximately -14V. The C-V measurement was then repeated multiple times (curves 2 and 3), with an applied soak before the sweep to test the threshold voltage stability and charge trapping effect. As observed from Figure 7.5, the C-V curve shifted to the right, with application of ~2 and 3 V positive voltage soaks suggesting charge trapping was occurring. To determine if the charge trapping effect was reversible, the device was then biased in depletion at a voltage of -30 V. The sweep was repeated and it was observed that the threshold voltage could shift back leftward, suggesting that the charge trapping effect is indeed reversible for film 6A.

Figure 7.5b shows the C-V curve for Gd_2O_3 film 10A. For the first measurement, the gate bias was swept from 0 V to -20V at 1MHz frequency (curve 1). The sample was

then soaked at +10 V and the C-V sweep was re-measured (curve 2). A slight 2 V positive shift is observed in the C-V curve.

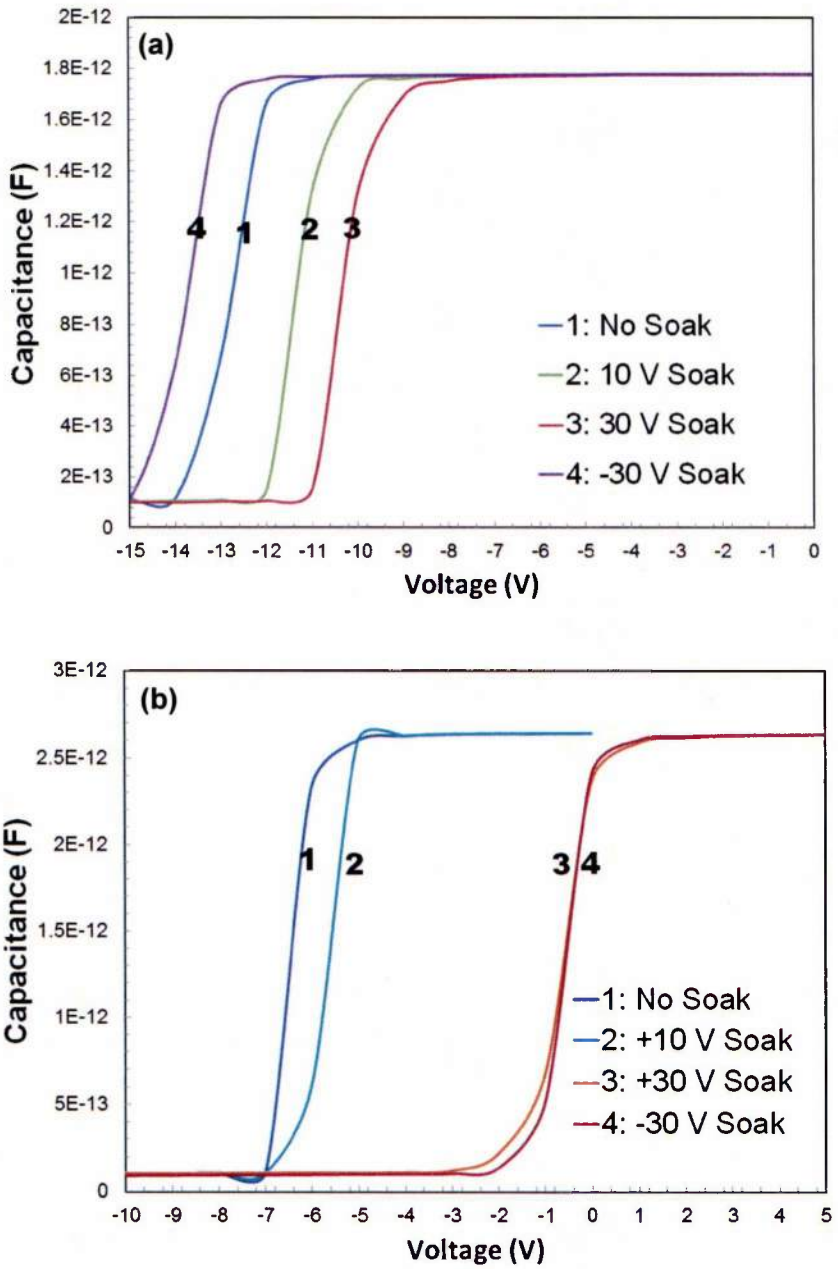

Figure 7.5. C-V curves for GaN / AlGaN / Gd_2O_3 / Ti / Au MOS capacitors (a) 6A (250 °C, 200 sccm O_2, 1.07 μm) and (b) 10A (650 °C, 50 sccm O_2, 1.01 μm, 0.5Å/s).

After applying a +30 V soak and re-sweeping (curve 3), a significant shift in the threshold voltage (5 V) was observed. A -30 V bias was then applied to deplete the capacitor, and the sweep was re-run (curve 4). However, no return to the original state was observed and the threshold remained fixed. Therefore, a nonvolatile memory effect is observed in the highly crystalline Gd_2O_3 devices deposited at 650 °C, but not in the poorly crystalline devices deposited at 250 °C. In comparison, Chang et al. found that the nonvolatile memory effect was present in their crystalline samples, but not their amorphous samples.[118] Furthermore, they suggested that recovery is only achievable through time dependent natural charge loss. These trapped charges could have significant effect on device operation, the effects of which will be discussed in more depth in the following sections.

7.3. DC conduction in Si(111) / Gd_2O_3 / Ti / Au MOS capacitors

DC conduction in Gd_2O_3 films was investigated through current-voltage-temperature (I-V-T) measurements. These measurements are used to determine the conduction mechanisms which dominate charger carrier transport within the oxide. Due to the costs and time associated with the measurements, select samples were chosen for evaluation. For the I-V-T measurements, the applied voltage ranged from 0 to 100V in both positive bias (substrate injection) and negative bias (gate injection). Due to the low penetration depth of the electric field into the degeneratively doped silicon substrate, it is possible to analyze conduction mechanisms in both positive and negative bias without significant effects from substrate conduction. The magnitude of the electric field range studied depended on the oxide film thickness. Figure 7.6 displays the I-V-T data

for Si / Gd_2O_3 / Ti / Au MOS capacitor 9D (650 °C, 200 sccm O_2, 2.69 μm) measured at temperatures from 25 °C to 200 °C. For purposes of film thickness and device area normalization, we plot the results in terms of current density J (A / cm^2) and electric field E (V/m).

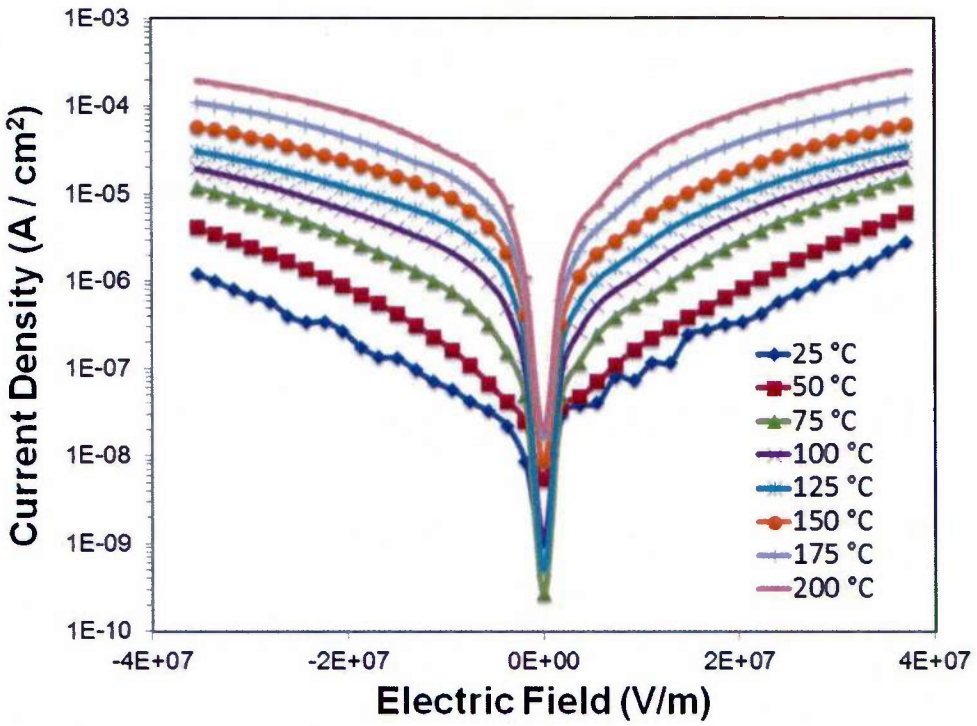

Figure 7.6. J-E characteristics for Si / Gd_2O_3 / Ti / Au film 9D (650 °C, 200 sccm O_2, 2.69 μm) measured under temperature range of 25 - 250 °C.

Current in an ohmic conduction regime is expressed in equation 7.4:

$$J = \frac{qn_0\mu E}{d} \qquad (A / cm^2) \qquad \text{Eq.7.4}$$

where J is the current density, n_0 is the density of free carriers, μ is the carrier mobility, V is the voltage, and d is the film thickness. Log I vs Log V is plotted for film 9D under negative bias in the low field region ($1x10^6$ V / m – $1x10^7$ V / m) for measurement

temperatures of 25 – 200 °C as shown in Figure 7.7. The dots are the measured data points and the solid line is the fit to the data.

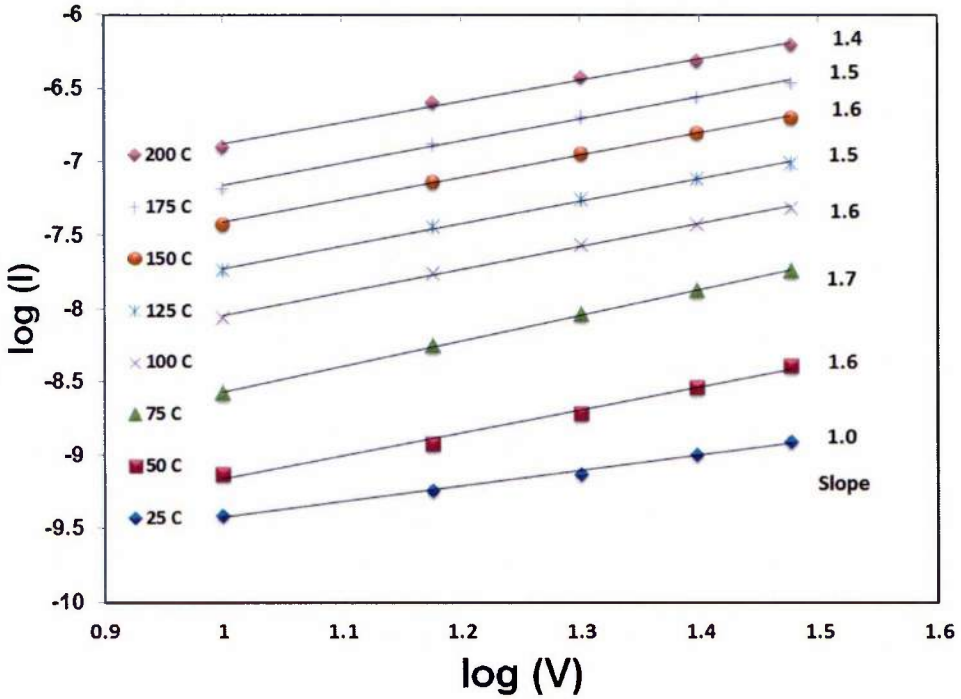

Figure 7.7. Log I vs Log V under gate injection for Gd_2O_3 film 9D (650 °C, 200 sccm O_2, 2.69 μm) measured between 25 – 250 °C under low electric field of $1x10^6$ V / m – $1x10^7$ V / m.

At room temperature (25 °C), the slope is equal to 1 indicating that the I-V relationship is linear and therefore dominated by ohmic conduction. At higher measurement temperatures under gate injection, the slope increases to a value of 1.4 – 1.7 which cannot be attributed to ohmic conduction. Under substrate injection, a good fit to ohmic conduction is not observed (not plotted). This is possibly due to contribution from the interfacial layer at the Si / Gd_2O_3 interface which results in a combination of bulk and interfacial conduction. A comprehensive study of conduction mechanisms for Gd_2O_3

films with different interfacial layer size and composition could help reveal the effects of the interface on conduction.

Since ohmic conduction was not observed except at room temperature under gate injection, various non-linear conduction mechanisms were investigated to explain the observed behavior. The conduction mechanisms are grouped into two categories; electrode limited conduction where contacts or interfacial effects dominate conduction and bulk limited conduction where conduction is limited by the oxide itself. The first investigated mechanism was the electrode limited Schottky emission mechanism. The expression for Schottky emission is given by equation 7.5[119]:

$$J = A^* T^2 exp\left[\frac{-q(\phi - \sqrt{qE_{ox}/4\pi\varepsilon_r\varepsilon_0}}{k_B T}\right] \qquad (A / cm^2) \qquad \text{Eq. 7.5}$$

where J is the current density, A* is the Richardson constant, T is the measurement temperature, q is the electronic charge, ϕ is the Schottky barrier height, E_{ox} is the electric field across the oxide, k_B is Boltzmann's constant, ε_r is the oxide dielectric constant, and ε_0 is the permittivity of free space. Therefore, if Schottky conduction is a dominating mechanism, $\ln(J/T^2)$ vs $\sqrt{E_{ox}}$ should yield a linear plot. The fit to Schottky emission is plotted for both positive and negative bias in Figures 7.8a and 7.8b, respectively.

The data in Figure 7.8 displays a good linear fit to the Schottky conduction under both gate and substrate injection. However, in order to confirm that Schottky mechanism is dominating conduction in this range, the permittivity calculated from the slope of the plot based on equation 7.5 must be in good agreement with the measured permittivity of the material.

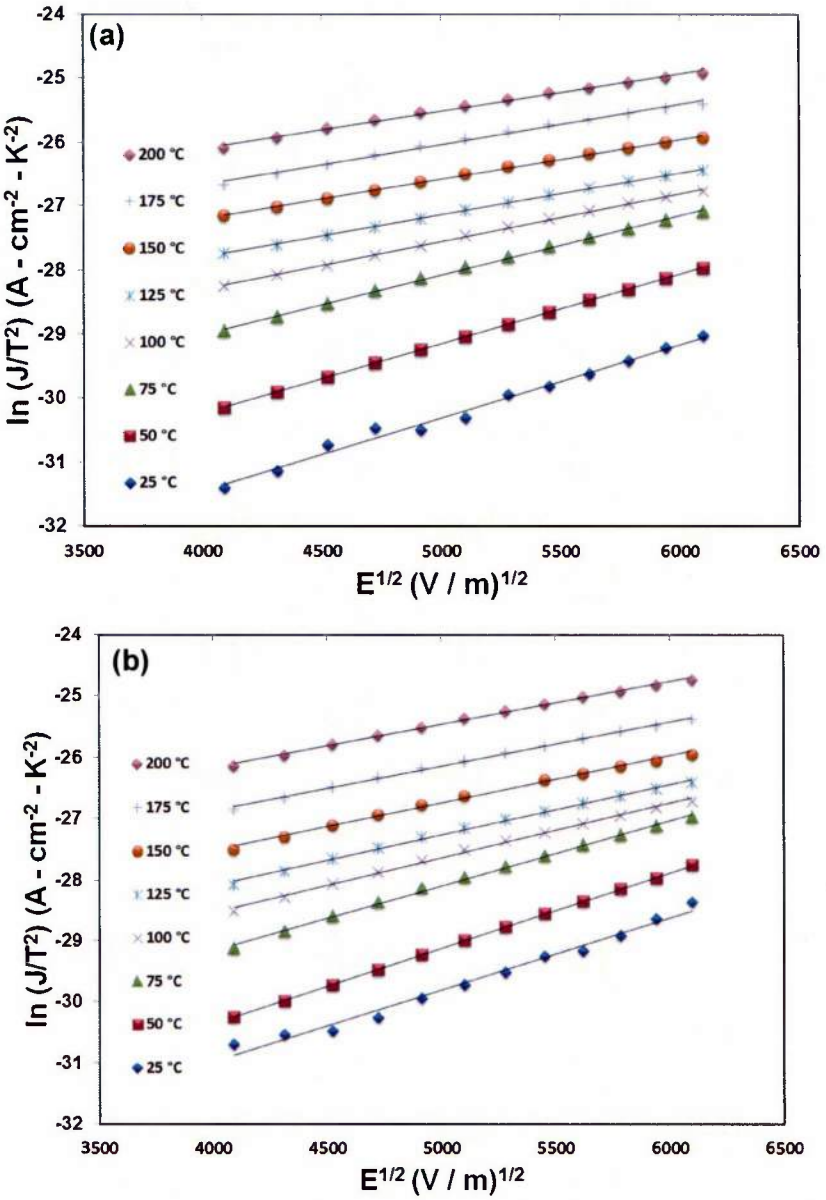

Figure 7.8. Schottky emission plots (ln (J/T^2) vs $E^{1/2}$) under (a) gate injection and (b) substrate injection for Gd_2O_3 film 9D (650 °C, 200 sccm O_2, 2.69 μm).

Table 7.3 displays the calculated dielectric constants from the Schottky plots which are found to be between 1.4 and 2.9 for the temperature range of 25 – 200 °C. This is significantly lower than the measured static permittivity of the Gd_2O_3 films (10-24). However, it has been proposed that the optical permittivity should be used when

the charge carriers possess high velocity since it only induces the electronic component of polarization. In comparison, if the carriers are slow, then the static permittivity should be used.[120] For Gd_2O_3 films, optical permittivity[121] has been used in the literature. The optical permittivity of the Gd_2O_3 films in this work was extracted from the measured refractive index using the ellipsometry technique. The refractive index was found to range from 1.4 - 2.1 depending on the deposition conditions (see appendix B). Using the relation, $n^2 = \varepsilon_o$, this yields an optical dielectric constant of 1.95 – 4.4. These values match quite well with the calculated dielectric constants extracted from the Schottky plots for temperatures of 75 – 200 °C under gate injection and 100 – 200 °C under substrate injection, suggesting Schottky emission is dominant in this regime.

Table 7.3. Calculated dielectric constant from Schottky and Poole-Frenkel plots for Si / Gd_2O_3 / Ti / Au device 9D (650 °C, 200 sccm O_2, 2.69 μm).

	Negative bias (gate injection)		Positive bias (substrate injection)	
Measurement Temperature (°C)	Calculated dielectric constant – Schottky	Calculated dielectric constant – Poole Frenkel	Calculated dielectric constant – Schottky	Calculated dielectric constant – Poole Frenkel
25	1.4	17.3	1.3	10.0
50	1.6	15.8	1.3	9.6
75	2.0	22.7	1.6	16.0
100	2.5	47.0	2.0	27.2
125	2.9	66.0	2.1	32.6
150	2.8	76.3	2.2	28.9
175	2.7	71.6	2.1	38.1
200	2.9	155.7	2.2	47.8

The reduced Schottky barrier height is obtained from the slope of the $\ln(J/T^2)$ vs 1/T plot shown in Figure 7.9a for various voltages. The reduced barrier height decreases linearly with $V^{1/2}$. By extrapolating to V = 0, the effective Schottky barrier height can be

determined as shown in Figure 7.9b. From the plot, a Gd_2O_3 / Au barrier height of 0.54 eV is extracted. This is significantly smaller than the ~3 eV barrier height we can expect based on the work function of the Au electrode[122] (5.1 eV) and the electron affinity of Gd_2O_3 (~2 eV).[123] However, this barrier height is similar to the value reported in the literature of 0.33 and 0.51 eV by two different methods for a 70 nm thin film Si / Gd_2O_3 / Au structure.[124] A few possibilities can explain the low value of the barrier height compared to the theoretical value. The first is related to Fermi level pinning, where a large density of surface states "pins" the Fermi level at a surface state energy. Indeed, while absent in single crystal Gd_2O_3, Fermi level pinning has been shown to exist in amorphous and polycrystalline Gd_2O_3.[125]

Another possibility is related to bulk trap states which modulate the barrier value. A recent report which found a barrier height of 0.6 eV for a thin epitaxial Si / Gd_2O_3 / Pt structure suggested the lower extracted barrier height is a result of a defect-related energy band in the oxide.[123] Additionally, for the substrate injection case, a barrier height of 0.56 eV (not plotted) was extracted for the Si / Gd_2O_3 interface, very similar to that of the Gd_2O_3 / Ti / Au interface. This suggests that the Si / Gd_2O_3 interface does not contribute significantly to Schottky emission, and further supports that the cause of reduced barrier height is related to the existence of a bulk trap state rather than an interface state.

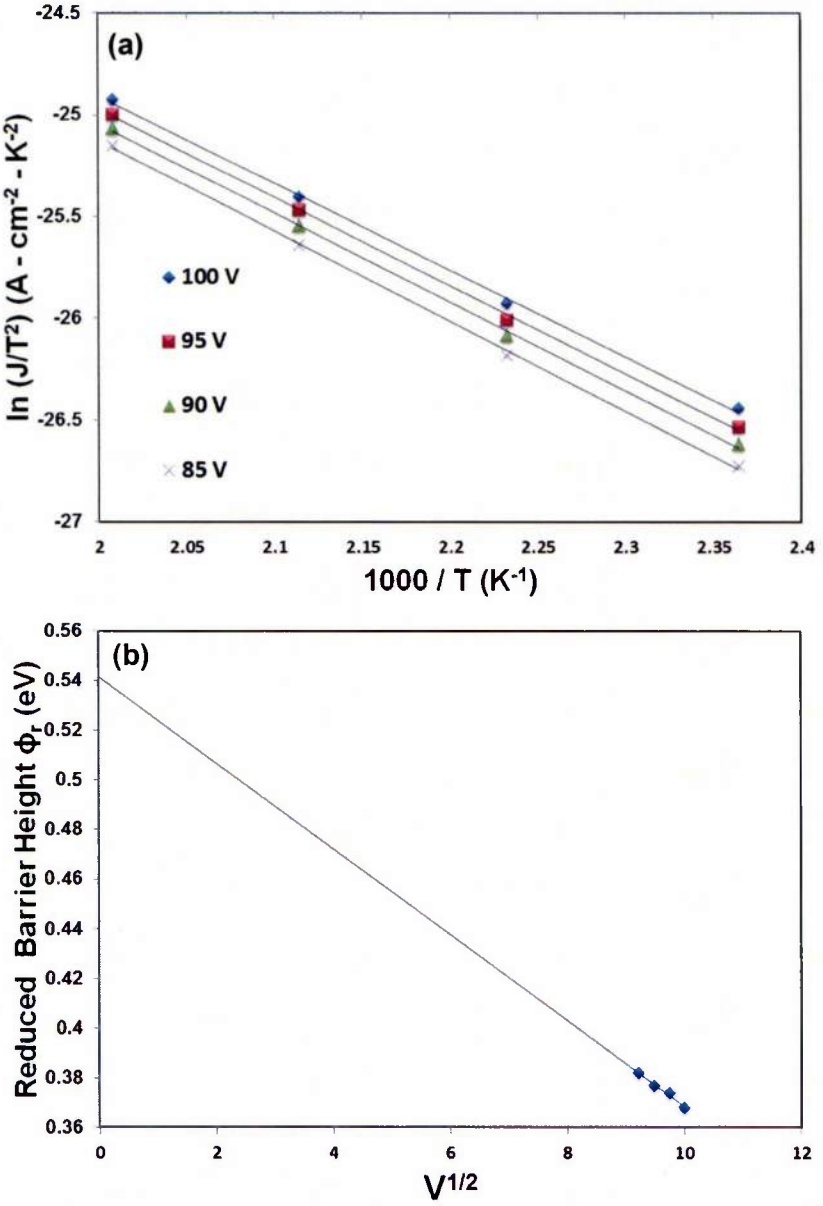

Figure 7.9. (a) Arrhenius $\ln(J/T^2)$ vs 1/T plots used to extract reduced Schottky barrier height for various voltages (85, 90, 95, 100) and (b) extraction of effective Schottky barrier height by extrapolation of reduced barrier height vs $V^{1/2}$ to V=0 under gate injection for film 9D (650 °C, 200 sccm O_2, 2.69 μm).

As shown in Table 7.3, despite the good linear fits at temperatures of 25 °C and 50 °C, the extracted dielectric constant is too low to indicate that the Schottky conduction

mechanism is dominant and suggests another conduction mechanism may be possible. Therefore, bulk-limited Poole-Frenkel conduction was investigated in the Gd_2O_3 films. Poole-Frenkel is very similar to Schottky conduction except that the electrons are injected from bulk traps within the oxide conduction band rather than from an electrode. For Poole-Frenkel conduction[119], the current density is given by equation 7.6:

$$J = (qN_C\mu)E_{ox}\left[\frac{-q(\phi-\sqrt{qE_{ox}/\pi\varepsilon_r\varepsilon_0}}{k_BT}\right] \quad (A/cm^2) \qquad \text{Eq 7.6}$$

where J is the current density, q is the electronic charge, N_c is the density of states in the conduction band, μ is the electronic drift mobility, E_{ox} is the electric field across the oxide, ϕ is the trap energy level, ε_r is the oxide dielectric constant, ε_0 is the permittivity of free space, k_B is Boltzmann's constant, and T is the measurement temperature. From equation 7.6, ln (J/E) vs $V^{1/2}$ should give a linear relationship for this conduction mechanism. The Poole-Frenkel plots are shown for gate and substrate injection in Figure 7.10a and 7.10b, respectively, showing good fitting characteristics. The permittivities were obtained from the slope using equation 7.6 and are listed in Table 7.3. For gate injection, at temperatures between 25 – 75 °C, the extracted permittivities (15-22) agree well with the static permittivities measured from the C-V measurements in section 7.2.2.

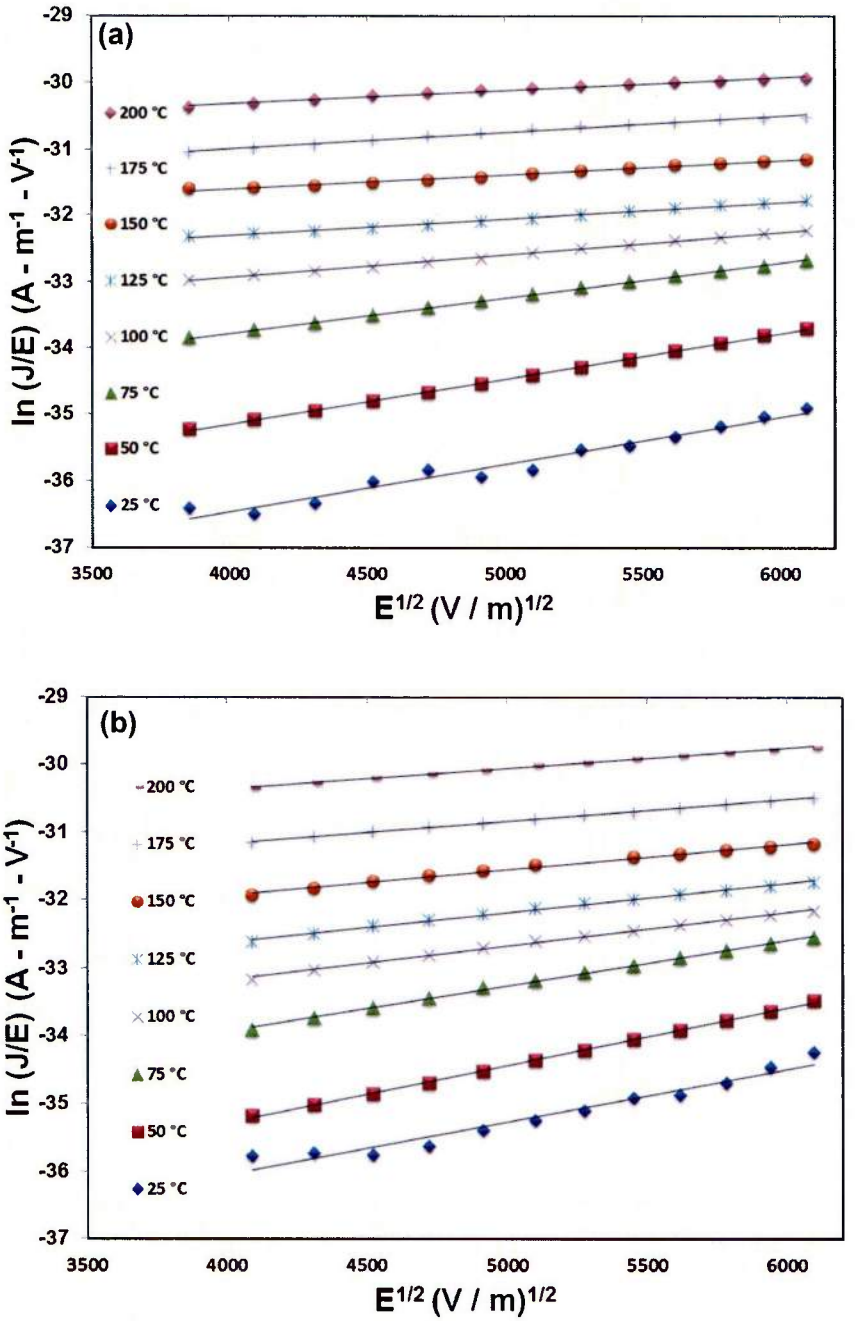

Figure 7.10. Poole-Frenkel plots (ln (J/E) vs $E^{1/2}$) under (a) gate injection and (b) substrate injection for Gd_2O_3 film 9D (650 °C, 200 sccm O_2, 2.69 μm).

In addition, the trap activation energies (E_t) at a given voltage may be calculated from the slope of ln (J/E) vs 1/T plot using equation 7.6. For the gate injection case, this plot is shown in Figure 7.11a.

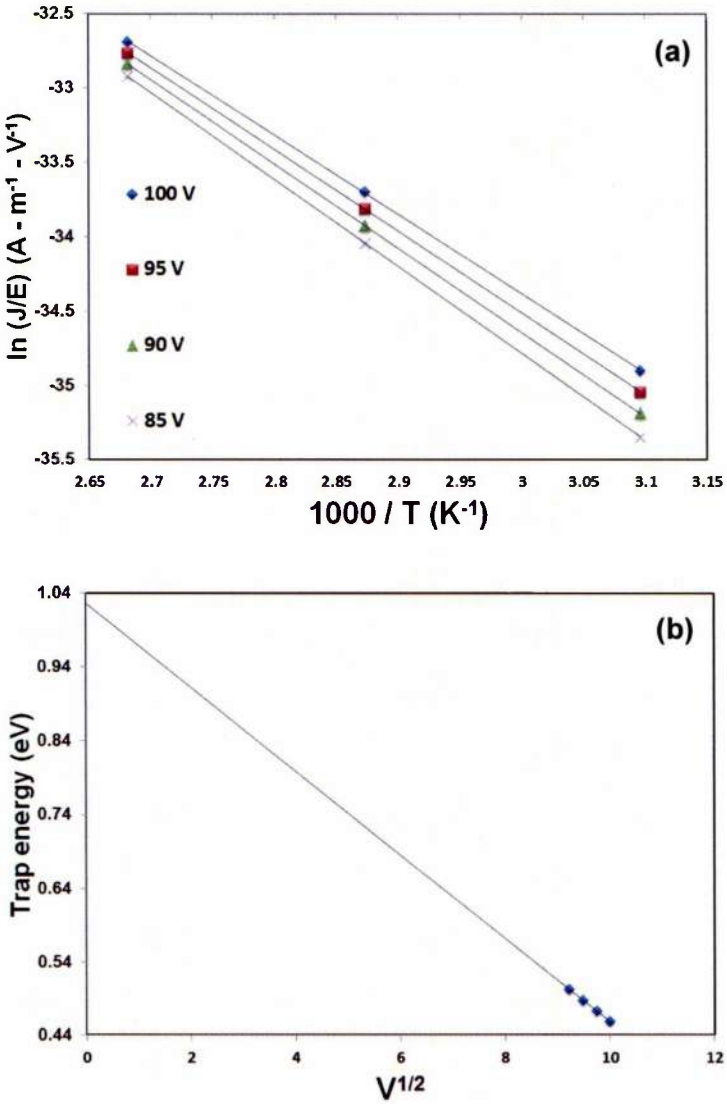

Figure 7.11. (a) Arrhenius ln(J/E) vs 1/T plots to extract trap energy levels for various electric field strengths and (b) extraction of zero field trap ionization energy by extrapolation of trap energy vs $V^{1/2}$ to V=0 under gate injection for Gd_2O_3 film 9D (650 °C, 200 sccm O_2, 2.69 μm).

The zero-field ionization energy was extracted by extrapolating the E_t vs. $V^{1/2}$ plot to yield the zero field trap ionization energy (ϕ_t) as shown in Figure 7.11b. From these plots we extract trap energy levels of 1.03 eV and 1.25 eV for gate and substrate injection, respectively. These trap levels match well with previously reported trap level of 1.2 eV under gate injection for epitaxial 6 nm thick Gd_2O_3 deposited on p-type Si.[121]

Due to the large thickness (2.69 μm) of film 9D (650 °C, 200 sccm O_2, 2.69 μm) and the maximum applied voltage of 100V, a large electric field could not be placed across the device. Therefore, conduction mechanisms of film 9A (650 °C, 200 sccm O_2, 0.38 μm) were studied in order to determine the dominant mechanism in the high electric field region. Film 9A was deposited under similar conditions as film 9D, but with smaller film thickness. Space charge limited current conduction (SCLC) mechanism is given by equation 7.7 for a single discrete trap level:

$$J = \frac{9}{8}\mu\varepsilon_r\varepsilon_0\frac{V^2}{d^3} \qquad (A / cm^2) \qquad \text{Eq. 7.7}$$

where J is the current density, μ is the carrier mobility, ε_r is the oxide dielectric constant, ε_0 is the permittivity of free space, V is the applied voltage, and d is the film thickness. According to equation 7.7, for SCLC conduction mechanism, a log I versus log V should yield a linear fit with a slope of 2. Figure 7.12 shows the log I versus log V plots and the fits to the SCLC conduction mechanism.

Under gate injection, in the temperature range of 150 – 200 °C, the data fits well to the SCLC mechanism with a single discrete trap level. In the temperature range of 75 – 125 °C, the data fits the SCLC conduction mechanism but the slope (2.4) was higher than 2. This indicates that the trap states may be exponentially distributed in the energy

gap.[126] Under substrate injection, a good fit to the SCLC conduction mechanism was not found.

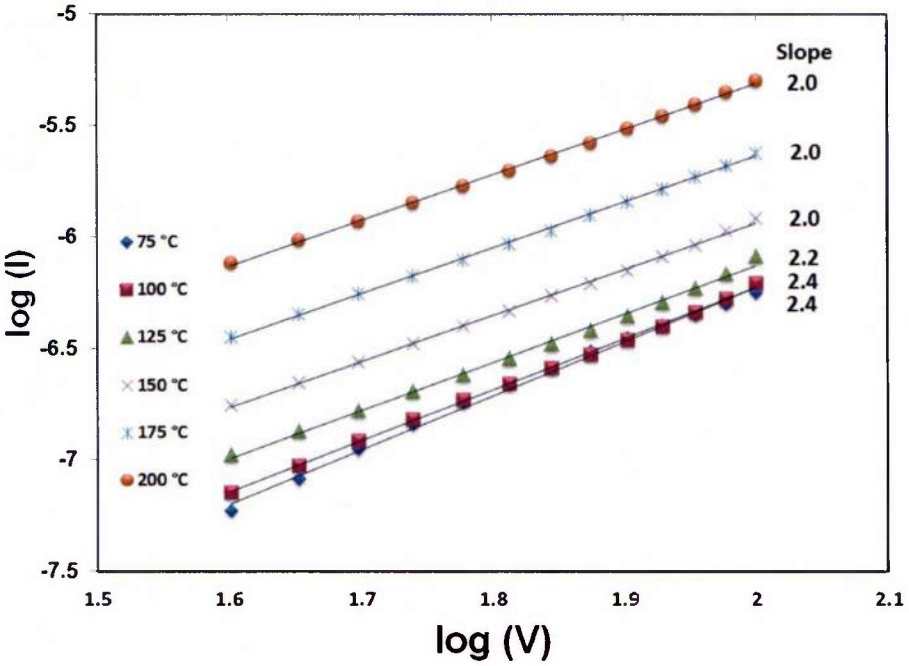

Figure 7.12. Log I versus Log V showing space charge limited conduction under high electric fields for Gd_2O_3 film 9A (650 °C, 200 sccm O_2, 0.38 μm).

Unfortunately, due to the high required electric field to induce the SCLC mechanism and the maximum 100 V bias of the measurement apparatus, we are unable to confirm the thickness dependence of the SCLC mechanism based on equation 7.7 for thicker Gd_2O_3 films since the SCLC mechanism appears only for electric field values greater than $1x10^8$ V / m. However, it is important to note that increased film thickness resulted in significant changes in film phase and structure. Therefore, conduction through the films may not be equivalent for the same applied electric field in different films. It is strongly suggested that further work investigate the effects of processing, film structure, and phase on Gd_2O_3 conduction mechanisms. Clearly, conduction in thick Gd_2O_3 films is

governed by a number of different conduction mechanisms across a wide temperature and electric field range.

7.4. Conduction mechanisms in GaN / AlGaN / Gd_2O_3 / Ti / Au MOS capacitors

The I-V-T characteristics for fully cubic Gd_2O_3 film 10A (650 °C, 50 sccm O_2, 1.01 μm, 0.5Å/s) deposited on GaN /AlGaN is shown in Figure 7.13. As observed, the curve is highly asymmetric, with the forward bias current being approximately 2 orders of magnitude higher than the reverse bias current. For the GaN / AlGaN / Gd_2O_3 / Ti / Au MOS capacitor devices, we studied the conduction mechanisms in the positive bias region (substrate injection) under accumulation to ensure that the electric field drops only across the oxide and that no significant contributions from substrate conduction are observed.

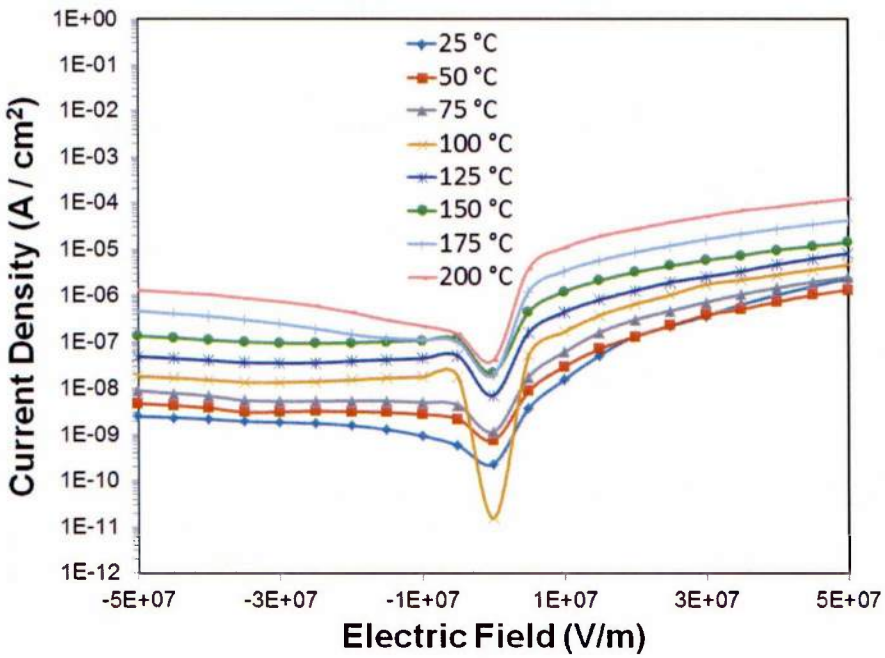

Figure 7.13. J-E characteristics for GaN / AlGaN / Gd_2O_3 / Ti / Au film 10A (650 °C, 50 sccm O_2, 1.01 μm, 0.5Å/s) measured under temperature range of 25 - 250 °C.

Between 25 – 100 °C, the experimental data in the positive bias regions was fitted to the Poole-Frenkel model using equation 7.6. Dielectric constants of 12-23 were extracted using the slope of the linear ln (J/E) vs $E^{1/2}$ plots. These values are in good agreement with the static permittivity measured by C-V measurements. From the temperature dependence, a trap height of 0.46 eV was calculated. As the temperature is increased between 125 and 200 °C, the Poole-Frenkel model no longer holds. Instead, transition to Schottky mechanism is observed. Schottky plots of ln (J/T^2) vs $E^{1/2}$ yielded dielectric constants of 2-2.5, a good match to the optical dielectric constants measured through ellipsometry. A Schottky barrier height of 0.79 eV was calculated from the data.

7.4. Integration of Gd_2O_3 into GaN / AlGaN HEMTs

After transistor fabrication was completed on GaN / AlGaN substrates, field effect transistor (FET) measurements were made to determine the quality of the devices. The fabricated transistors were depletion mode devices. For depletion mode devices under standard conditions with no voltage applied, the device is "on", meaning that current is flowing between the source and the drain and the channel is conductive. To turn the device "off", or impede the current flow between the source and the drain, a large enough negative gate voltage (V_G) must be applied between the source and the gate. This is called the threshold voltage, V_T. Two figures of merit for these devices are the on/off ratio and the subthreshold swing (SS). The on/off ratio refers to the ratio of the maximum measured current in the on state to the minimum measured current in the off state in the drain. Due to the small generated currents from neutron absorption in Gd_2O_3,

a low leakage current in the drain in the off state is necessary (< 1 nA) for radiation detection and therefore, a high on/off ratio is desired. The subthreshold swing is an indicator of how quickly a transistor can switch on and off and a lower number indicates faster switching.

The transfer characteristics for GaN / AlGaN / Gd_2O_3 / Ti / Au MOS-HEMT 10A (650 °C, 50 sccm O_2, 1.01 μm, 0.5Å/s), a GaN / AlGaN / SiO_2 / Ti / Au MOS-HEMT, and a control GaN / AlGaN / Ti / Au MS-HEMT without a gate oxide are shown in Figure 7.14. For the control sample, the threshold voltage is approximately -4 V. The on/off ratio for this device is only 45 and the subthreshold swing is 585 mV/ decade. The properties of the control device are quite poor likely due to significant leakage from the gate. Insertion of the SiO_2 oxide layer improves the on/off ratio to approximately 10^6. The threshold voltage is shifted towards a negative value by only ~1 V, suggesting small amount of fixed oxide positive charge. Insertion of the Gd_2O_3 oxide layer significantly improves the transistor properties. The measured on/off current ratio of ~5 x 10^9 for the device with Gd_2O_3 film 10A is among the highest values for GaN / AlGaN MOS-HEMTs reported in the literature.[127] Additionally, the subthreshold swing is greatly improved over the control device, being reduced to 88 mV / decade. However, it is important to note that a significant amount of hysteresis is observed in the transfer curves of the Gd_2O_3 device that is not present in the control device or in the SiO_2 device. This is likely related to the effects of charge trapping shown previously through C-V measurements. Additionally, repeated gate voltage sweeps resulted in shifting of the threshold voltage. This threshold voltage instability is detrimental for device operation and more work is needed to determine how to mitigate this issue.

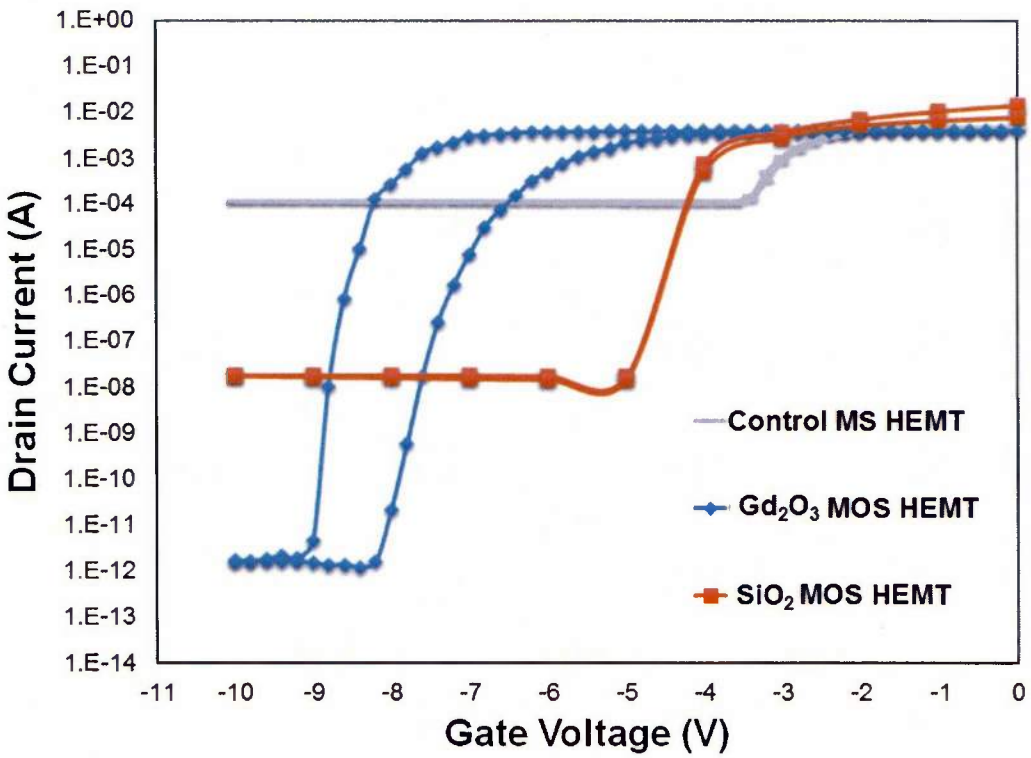

Figure 7.14. Transfer characteristics of Gd_2O_3 MOS HEMT, SiO_2 MOS HEMT, and a control MS HEMT without oxide layer.

The high on/off ratio corresponds to low leakage current in the drain in the off state (< 10 pA). Low drain leakage currents in the off state allow for measurement of radiation induced phenomenon within the devices which based on our results require leakage currents of <1 nA. The in-situ radiation testing was performed at a value of V_g right below V_t to ensure that off state drain currents are low. It is critical, however, that the leakage current through the gate oxide must be low enough in the off state so that it is possible to simultaneously measure the current increases in the gate as a result of the radiation. For the Gd_2O_3 devices, even at values of V_g as high as -50V, the gate current remains <100pA. Therefore, the Gd_2O_3 devices were adequately resistive for use in radiation testing. It is also important to note that only devices where the Gd_2O_3 film was deposited at 650 °C showed good transfer characteristics adequate for neutron detection.

Gd_2O_3 HEMTs incorporating films deposited at 250 °C suffered from poor on/off ratios (~10^6) and extremely large (~30 V) threshold voltage shifts.

7.5. Thermal neutron and gamma response of GaN / AlGaN MOS HEMTs

After transistor characterization and packaging, select samples were taken to the Breazeale nuclear reactor for thermal neutron irradiation in the beam lab. Results from three GaN / AlGaN / Gd_2O_3 / Ti /Au HEMTs are presented: a ~1 μm thick cubic phase film (Film 10A, 650 °C, 50 sccm O_2, 1.01 μm, 0.5Å/s), a ~1 μm thick mixed phase film (Film 12F, 650 °C, 50 sccm O_2, 1.03 μm, 7.4Å/s), and a ~10 μm thick mixed phase film (Film 12G, 650 °C, 50 sccm O_2, 10.2 μm, 7.6Å/s). Additionally, a ~1 μm thick SiO_2 control sample was fabricated in order to isolate the gamma ray contribution since SiO_2 is not sensitive to neutrons.

The gate bias was set 1 V below the threshold voltage to ensure the device remained in the off state during irradiation. Since the threshold voltage varied between samples, the necessary voltage required to turn the device off resulted in differences in electric field applied across the oxide for different devices. The threshold voltage for Gd_2O_3 devics was significantly higher (Δ = ~3 V) than that of SiO_2 as was shown in Figure 7.14, resulting in a larger electric field needed across the oxide. Unfortunately, a larger gate bias could not be placed across the SiO_2 device to ensure the same electric field across all devices due to the high gate leakage within the SiO_2 which was unsuitable for neutron detection. The drain voltage was set to a default value of 10 V unless the drain currents were exceedingly high in which case the drain voltage was lowered to ensure drain currents <500 pA.

Once the samples were biased below the threshold voltage, the neutron beam shutter was opened and the in-situ current response was measured in both the drain and the gate as shown in Figure 7.15. Due to the negative bias applied on the gate, the current is negative in sign, and the current becomes increasingly negative as the device is irradiated and the charge products collected. The response in the drain is of opposite polarity and of smaller magnitude than that of the gate. The neutron beam shutter was then closed, and reopened multiple times for each sample at various reactor powers (neutron fluxes). As can be observed from Figure 7.15, there is noise (shown by the arrow) in the measurement on the order of ~0.1 pA. The spikes observed in the drain current are a result of the vibrations induced by the force of the shutter movement. Additionally, a slight decrease in magnitude of the current change is observed with each successive shutter opening, which was attributed to transient behavior before the samples could reach steady state.

The magnitude of the current response in the gate and drain is shown in Table 7.4 for select GaN / AlGaN MOS-HEMTs under irradiation at reactor power of 100 kW. Samples were irradiated under the full beam which contained neutrons (n) and gamma radiation (γ-rays). Subsequently, the devices were shielded with cadmium foil which stopped 99.99% of the neutrons from passing through, creating a gamma-ray only signal. The neutron response was then calculated by subtracting the shielded response from the unshielded response in equation 7.8:

$$\Delta I_{unshielded}(n + \gamma\text{-rays}) - \Delta I_{shielded}(\gamma\text{-rays}) = \Delta I_{neutrons}(n) \qquad \text{(Amps)} \qquad \text{Eq 7.8}$$

where $\Delta I_{unshielded}$ is the current response to the full beam (neutrons and γ-rays), $\Delta I_{shielded}$ is the current response to the shielded beam (γ-rays) only and $\Delta I_{neutrons}$ is the calculated current response to neutrons.

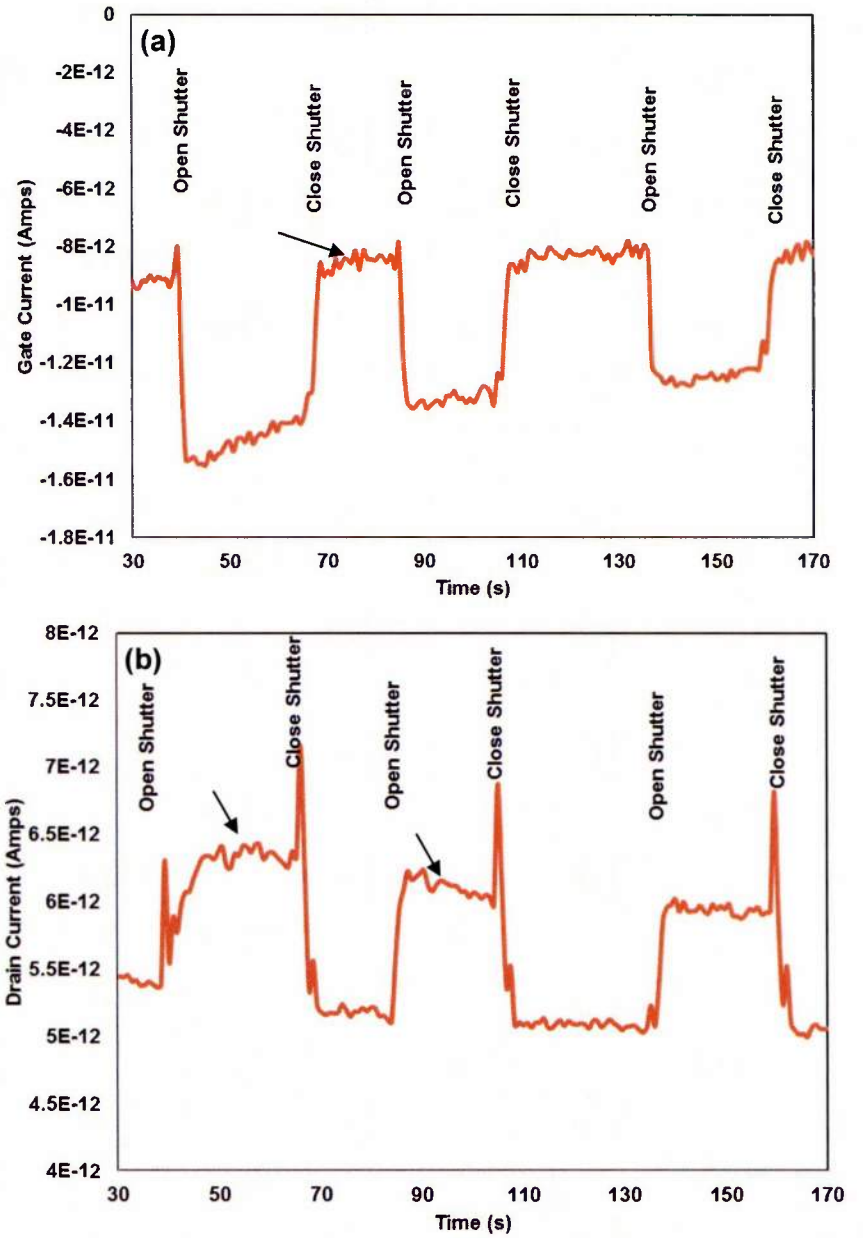

Figure 7.15. In situ current response in (a) gate and (b) drain of 1 μm mixed phase cubic Gd_2O_3 device 12F during neutron irradiation at 100kW reactor power. The arrows identify the noise in the measurement.

Table 7.2 displays the device gate response to unshielded (neutrons and γ-rays), shielded (γ-rays only) radiation, and the calculated neutron only response. For the 1 μm thick GaN / AlGaN / Gd_2O_3 MOS-HEMTs, the current increase due to neutron radiation was approximately 2.56 pA and 1.43 pA for devices with cubic Gd_2O_3 film 10A and mixed phase film 12F under electric fields of 200kV / cm and 300 kV / cm, respectively. Assuming a linear increase in current with electric field, this suggests a fairly similar current between the mixed and cubic phase films, suggesting that processing parameters did not play a large role in total charge collection. Additionally, the SiO_2 sample showed a neutron response of 1.78 pA in the gate at an applied electric field of 50 kV/cm, which suggests that SiO_2 device outperformed the Gd_2O_3 devices. Since the SiO_2 layer should not be neutron sensitive, the larger currents may come as a result of γ-rays. The small neutron response of the Gd_2O_3 films could potentially be a result of the low film thickness relative to the mean free path of neutrons in Gd_2O_3 (~7.7 μm).[5] Therefore, a 10 μm thick mixed phase film was synthesized, processed, and evaluated. With the 10 μm Gd_2O_3 overlayer, we observed a significant increase in the radiation response of the GaN / AlGaN MOS-HEMTs. At low fields of approximately 40 kV / cm, an increase in the measured neutron response up to 10 pA was observed.

The observed drain currents shown in Table 7.4 are lower in magnitude than the gate currents. Interestingly, no response was observed in the drain current for 10 μm thick Gd_2O_3 device 12G in both unshielded and shielded irradiations as shown in Table 7.4. This is likely due to the fact recombination is occurring in the thick Gd_2O_3 film, preventing charge injection into the channel during irradiation. As shown in Table 7.4, for the 1 μm thick films, we observe that the SiO_2 device resulted in a higher total

calculated neutron response than the Gd_2O_3 device. This suggests that in the thin film limit (1 μm), the Gd_2O_3 overlayer does not provide any additional benefit in detection of thermal neutrons in the drain response of the GaN/AlGaN MOS-HEMTs.

Table 7.4. Response of Gd_2O_3 and SiO_2 MOS-HEMTs to unshielded radiation (neutrons + γ-rays), shielded radiation (γ-rays only), and calculated neutron response in both the drain and the gate.

		1 μm cubic phase Gd_2O_3 film 10A	1 μm mixed phase Gd_2O_3 film 12F	10 μm mixed phase Gd_2O_3 film 12G	SiO_2 control film
	Applied field over gate oxide (kV / cm)	300	200	40	50
Gate	n + γ-ray response (pA)	4.73	1.96	26.7	1.92
	γ-ray response (pA)	2.17	0.53	16.7	0.20
	n response (pA)	**2.56**	**1.43**	**10**	**1.78**
Drain	n + γ-ray response (pA)	0.52	1.35	0	1.67
	γ-ray response (pA)	0	0.45	0	0.93
	n response (pA)	**0.52**	**0.9**	**0**	**0.74**

The experimental currents measured during neutron irradiation greatly exceed those simulated by the GEANT4 modeling by an order of magnitude.[5] For the 10 μm thick film 12G, we observed over an order of magnitude increase in the response compared to the model. Assuming that the model is correct, the excess currents may be the result of charge collection due to secondary gamma radiation, which would explain

the current response for the SiO_2 devices. Perhaps with more film optimization, it would be possible to increase the neutron current response of the Gd_2O_3 films.

7.6. Conclusions

The dielectric properties of Si(111) / Gd_2O_3 / Ti / Au MOS capacitors were investigated. Moisture absorption in Gd_2O_3 films was found to result in both increased dielectric loss (~10x) and inflated dielectric constant values (40%). Heat treatment of the films at 100 °C resulted in outgassing of moisture, reduction in dielectric constant, and excellent frequency dispersion of the dielectric constant over a range of 10 kHz – 1 MHz.

The effects of film processing and structure on the high frequency (1 MHz) dielectric constant of the Gd_2O_3 films were examined. Improvement in film crystallinity due to increased deposition temperature from 250 °C to 650 °C resulted in an increase in the dielectric constant from a value of ~11 to 17 for films 6A-6E (function of temperature, 200 sccm O_2, ~1 μm). For films 4A-4E (250 °C, function of O_2 flow, ~1 μm), dielectric constant decreased from 18 (25 sccm O_2) to 11 (200 sccm O_2) with increasing oxygen flow. This was attributed to both increased density at lower O_2 flow as well as greater monoclinic phase volume. The dielectric constants for pure cubic (film 11A) and monoclinic (film 11D) phase films were 14 and 24, respectively, agreeing well with the Claussius-Mossoti relationship. Increasing the film thickness resulted in decreased dielectric constant for sets 9 (650 °C, 200 sccm O_2, function of thickness) and 3 (250 °C, 200 sccm O_2, function of thickness) due to the increase in film porosity.

Capacitance-voltage (C-V) characteristics of GaN / AlGaN / Gd_2O_3 / Ti / Au MOS capacitors were investigated and all Gd_2O_3 films tested showed leftward threshold

voltage shift compared to the MS control sample as a result of fixed oxide charge within the film. No smearing out of the C-V curve was shown indicating good interface quality. All Gd_2O_3 devices displayed hysteresis characteristics in the C-V curves from which the concentration of trapped charge (N_t) was calculated. Conductance-voltage (G-V) measurements were performed in order to extract interface state density (D_{it}). Pure cubic phase films deposited at 650 °C with low rate were shown to have lowest D_{it} (1.05×10^{11} eV^{-1}-cm^{-2}) and N_t (6.9×10^{10} cm^{-2}). C-V measurements were also performed to test the threshold stability and charge trapping effects in the Gd_2O_3 devices. A non-volatile memory effect consistent with previous literature reports was observed for crystalline Gd_2O_3 films deposited at 650 °C, but was absent in films deposited at 250 °C. All devices showed threshold voltage instability regardless of film deposition temperature.

Conduction mechanisms in Gd_2O_3 films were studied through current-voltage-temperature (I-V-T) measurements. A wide range of mechanisms were found to govern conduction in Gd_2O_3 films across a wide temperature and electric field range. In general, at low measurement temperature under low fields, Poole-Frenkel was determined to be the dominating conduction mechanism. Trap heights of 1.03 and 1.25 eV were extracted for gate and substrate injection, respectively. In general, at high temperature under low fields, Schottky emission was found to be the dominating conduction mechanism. Schottky barrier heights for the Gd_2O_3 / Ti / Au and Si / Gd_2O_3 interfaces were found to be 0.54 eV and 0.56 eV, respectively, suggesting that the interfacial layer did not significantly affect Schottky emission. The low barrier height was attributed to the existence of a bulk trapping effect in the oxide. Finally, in the high electric field region, space charge limited current (SCLC) was responsible for conduction under gate injection.

It is important to note that in certain regions, the I-V data could not be fit to any particular mechanism, suggesting that conduction is complex and a function of multiple mechanisms.

For GaN / AlGaN / Gd_2O_3 / Ti / Au MOS capacitors, I-V-T measurements determined that the I-V characteristics were governed by Poole-Frenkel effect at temperatures of 25 – 100 °C with a trap height of 0.46 eV. Between 125 and 200 °C, the current was controlled by Schottky emission with a barrier height of 0.79 eV. The performance of GaN / AlGaN / Gd_2O_3 / Ti / Au MOS-HEMTs was investigated with emphasis on necessary device performance for radiation detection. Gd_2O_3 films deposited at 250 °C resulted in devices with poor switching characteristics and poor on/off ratios (10^6). Gd_2O_3 films deposited at 650 °C led to devices with good switching characteristics including on/off ratio of 10^9 and subthreshold swing of 88 mV. However, significant hysteresis and threshold voltage instability was observed for the Gd_2O_3 MOS-HEMTs, which is related to the effects of trapped charge identified in the C-V measurements.

Finally, the radiation response of GaN / AlGaN / Gd_2O_3 / Ti / Au MOS-HEMTs to gamma and neutron radiation was investigated and compared with a GaN / AlGaN / SiO_2O / Ti / Au control device. For devices with 1 μm thick Gd_2O_3 films, the neutron response was similar to the control device, suggesting that the Gd_2O_3 overlayer did not provide any added benefit of neutron detection. Devices with 10 μm thick Gd_2O_3 films showed significantly increased current response to neutrons (10pA at reactor power of 100 kW). However, the neutron response was larger than the expected theory, suggesting that added signal due to gamma radiation may have been collected.

Chapter 8

Conclusions and Future Work

8.1. Conclusions

The process-structure-property relationships of thick Gd_2O_3 films deposited by reactive electron-beam physical vapor deposition (EB-PVD) have been investigated. The performed work has resulted in a number of important findings that are important from both a scientific perspective as well as for development of neutron detectors incorporating micron thick Gd_2O_3 films. This section will summarize the major results of this dissertation work pertaining to the process-phase relationships (chapter 4), stress-induced phase transition and texture evolution (chapter 5), microstructure, composition, and interfacial phenomena (chapter 6), and electrical properties and radiation response of Gd_2O_3 microelectronic devices (chapter 7).

Chapter 4 – Bulleted Summary

- The effects of substrate temperature, oxygen flow, and film thickness on the phase and crystallinity of thick Gd_2O_3 films deposited by reactive electron beam-physical vapor deposition (EB-PVD) at high rates (> 5 Å / s) were examined via x-ray diffraction (XRD) and Raman spectroscopy. Quantitative phase volume calculations were performed via a Rietveld refinement technique.
    - All films were found to be fully monoclinic or mixed / cubic monoclinic phase.
    - Generally, increased deposition temperature and increased oxygen flow resulted in increased cubic phase volume.

- As film thickness increased, monoclinic phase volume increased.

- Grazing incidence x-ray diffraction (GIXRD) depth profiling analysis showed that cubic phase was only present under large incidence angle (large penetration depth into the film) measurements, and that after a certain point, only monoclinic phase was grown. The gradual transition from cubic to monoclinic phase along the film thickness was later confirmed in Chapter 6 via transmission electron microscopy (TEM) and selected area diffraction (SAD).
- The primary results from Chapter 4 show that it is possible to significantly tailor the structure (and thus properties and performance) of the Gd_2O_3 films by systematic variation of processing parameters.

Chapter 5 – Bulleted Summary

- Successful deposition of a pure cubic phase film was obtained at high deposition rates for films less than 50 nm thick under a deposition temperature of 250 °C and 200 sccm O_2 flow. However, this film was shown to be under significant compressive stress of 1.7 GPa by XRD residual stress measurements.
- Thick (1 μm) pure cubic phase films were deposited by lowering the deposition rate to < 1 Å / s and increasing the deposition temperature to 650 °C. This was attributed to both increased adatom mobility as well as reduction in compressive stress as measured by the wafer curvature technique. Based on this information, a large compressive stress was hypothesized to cause the formation of the monoclinic phase.
- An experiment was designed to introduce compressive stress into the Gd_2O_3 films via ion beam assisted deposition (IBAD). This allowed for systematic increase in

compressive stress while keeping a large adatom diffusion length on the film surface. It was shown that the films could be completely transformed from the cubic to monoclinic phase with applied compressive stress of -777 MPa for the deposition conditions considered, confirming the existence of a stress-induced phase transition in Gd_2O_3.

- At high deposition rates, it was shown that films deposited on different substrates (quartz, silicon, sapphire, and GaN) all had similar θ-2θ diffraction patterns, suggesting that films grew similarly on different substrates due to the low adatom mobility.
- Significant differences in texture were observed for films deposited at low rates (< 1 Å / s) and high temperature (650 °C) on the different substrates. For evaluation of in-plane texture in the Gd_2O_3 films, pole figure analysis was performed.
    - Mixed phase films deposited at high rates and low temperature showed weak out-of-plane texture and random in-plane texture.
    - Mixed phase films deposited at high temperatures possess a fiber texture (strong out-of-plane texture), but lack the necessary adatom mobility to develop in-plane texture.
    - For single phase cubic films grown under low rates of deposition, out-of-plane texture was observed on quartz substrates. However, weak and strong in-plane textures were observed for sapphire and GaN substrates, respectively.
    - The use of ion bombardment resulted in the formation of moderate biaxial texture for films grown on quartz. For films grown on sapphire, a very strong

biaxial texture was achieved with ion bombardment, and was attributed to the additional energy added to the system from the bombarding ions.

Chapter 6 – Bulleted Summary

- The effects of processing on the structure, composition, and interfacial chemistry of the Gd_2O_3 films was investigated via SEM, TEM, AFM, EDS, and XPS. The results showed that films primarily adhered to the structure zone models with a few exceptions. The deviation from the Structure-Zone model[15] was explained by the combined effects of columnar growth, shadowing, and adatom mobility.
    - At low deposition temperatures, decreasing oxygen flow resulted in increased film density due to higher adatom mobility. Films deposited at this temperature were characterized by small (10 – 15 nm) nanocrystalline grains with some porous disordered regions.
    - As the deposition temperature was raised to 650 °C, a dense nucleation region was observed and the films were highly crystalline with larger grain size. After the approximately 200 nm dense nucleation region, columnar growth was observed as the film grew thicker. Porosity formed between the growing columns due to shadowing effects and growth of the monoclinic (020) orientation.
- The effects of processing on the interfacial layer size of Gd_2O_3 films deposited on silicon were investigated. The size and structure of the interfacial layer was dependent upon the deposition conditions. Generally, higher oxygen flow and higher deposition temperature led to larger interfacial layer size and a more undulating

interface. The interfacial reaction was determined to proceed as a result of intermixing of the SiO_x layer with the Gd_2O_3 layer to form the Gd-Si-O interface during deposition.

- Films deposited on GaN possessed excellent interfacial characteristics with near heteroepitaxial growth and no apparent interfacial layer.
- Ion beam assisted deposition was shown to result in significant densification of the film structure and elimination of the columnar morphology.
- The O : Gd ratio of the Gd_2O_3 films was investigated using EDS and XPS, and showed that the processing conditions had significant effects on the film composition.
    - Increasing temperature was found to decrease the O : Gd ratio.
    - Increasing oxygen flow was found to increase the O : Gd ratio for films deposited at high temperatures, but had little effect for films deposited at low temperature.

Chapter 7 – Bulleted Summary

- Moisture absorption in Gd_2O_3 films was found to result in both increased dielectric loss (10x) and inflated dielectric constant values (~40 %). Heat treatment of the films at 100 °C resulted in outgassing of moisture, reduction in dielectric constant, and excellent frequency dispersion of the dielectric constant over a range of 10 kHz – 1 MHz.
- The effect of film processing on the dielectric constant was systematically investigated. Tuning of the dielectric constant from a value of 11 to a value of 24 was

possible by manipulating the structure and crystallographic phase of the material via the processing conditions.

- Capacitance-voltage (C-V) and conductance-voltage (G-V) characteristics of GaN / AlGaN / Gd_2O_3 / Ti / Au MOS capacitors were investigated. The effects of processing on fixed oxide charge, trapped oxide charge, and density of interface states were evaluated. Single phase cubic films deposited at low rates with near heteroepitaxial growth were shown to have the lowest density of trapped charge. Additionally, threshold instability in the C-V curve as well as a non-volatile charge trapping effect was observed.
- Conduction mechanisms in Gd_2O_3 films were studied through current-voltage-temperature (I-V-T) measurements. A number of mechanisms were found to govern conduction in Gd_2O_3 films across a wide measurement temperature and electric field range including ohmic conduction, Schottky Emission, Poole-Frenkel emission, and space charge limited conduction. For Poole-Frenkel emission, the trap heights of 1.03 eV and 1.25 eV were found for the cases of gate and substrate injection, respectively. Schottky barrier height at the Si (111) / Gd_2O_3 interface and Gd_2O_3 / Ti / Au interface was found to be 0.56 eV and 0.54 eV, significantly lower than the expected barrier height value.
- For GaN / AlGaN / Gd_2O_3 / Ti / Au capacitors, the Schottky barrier height at the GaN / AlGaN / Gd_2O_3 interface was found to be 0.79 eV and the Poole Frenkel trap height was 0.46 eV.
- The performance of GaN / AlGaN / Gd_2O_3 / Ti / Au high electron mobility transistors (MOS-HEMTs) was investigated with emphasis on necessary device performance for

radiation detection. Gd_2O_3 films deposited at 650 °C led to devices with good switching characteristics including an on/off ratio of ~10^9 and subthreshold swing as low as 88 mV. However, significant hysteresis and threshold voltage instability was observed for the Gd_2O_3 MOS-HEMTs.

- GaN / AlGaN / Gd_2O_3 / MOS-HEMTs devices showed sensitivity to both gamma and neutron radiation. For devices with 1 μm thick Gd_2O_3 films, the neutron response was not improved over the SiO_2-based control device. Devices with 10 μm thick Gd_2O_3 films showed significantly increased neutron detection. However, the neutron response was larger than the expected theory, suggesting that added signal due to gamma radiation may have been collected.

8.2. Future Work

The work completed in this dissertation provides the basis for a number of novel and important research directions in both fundamental and applied science. These possible research directions will be discussed in detail in this chapter. From a structural material's perspective, these topics include stabilization of thick cubic phase films with high deposition rates, stabilization of amorphous phase films, extended study of direct evaporation of Gd_2O_3 films, and further investigation into the mechanism of the stress induced phase transition. From an electrical properties perspective, detailed investigation of conduction mechanisms governing charge transport would be beneficial. Further study regarding the types of defects present in the Gd_2O_3 films is also of interest. This information can be used to improve performance of Gd_2O_3 microelectronic devices.

Finally, more work is needed to understand the neutron and gamma ray response of the Gd_2O_3 microelectronic devices.

8.2.1. Direct evaporation

The films discussed in this dissertation were deposited via reactive electron beam-physical vapor deposition (EB-PVD). This was due to the better uniformity and control obtained from the reactive evaporation process using a gadolinium metal source. During direct evaporation, dendritic growth was observed from the Gd_2O_3 source material in the crucible resulting in an uneven vapor plume and significant difficulty in maintaining a constant evaporation rate. Use of a rod-fed system (in which the source material is introduced into the chamber in rod form) could mitigate the deleterious effects of dendritic growth. A detailed investigation of the process-structure-property relationships for films deposited via direction evaporation similar to the study performed in this work would be of great interest. Additionally, it has been suggested that films deposited from an oxide source can prevent formation of interfacial SiO_x layer for Gd_2O_3 films deposited on silicon.[128]

8.2.2. Stabilization of micron thick single cubic phase films deposited at high rates

It was shown in Chapters 4 and 5 that all films deposited at high rates (> 5 Å / s) with thickness greater than 50 nm resulted in mixed phase films. The cubic phase was only stabilized for thick films (1 μm) when the deposition temperature was increased to 650 °C and the deposition rate was lowered to less than 1 Å / s resulting in a deposition time of ~ 6 hours. This is problematic for applications where single phase cubic films

with even larger thicknesses are needed. For instance, in Chapter 7, we showed that 10 μm thick Gd_2O_3 films showed better response to neutron detection than 1 μm thick films due to the large mean free path of neutrons in the material. The long deposition time required to grow a 10 μm thick film at such a low rate is not feasible or cost efficient. Therefore, other methods of stabilizing the cubic phase, yet maintaining a high deposition rate would be attractive. One possible pathway to achieve this goal would be to raise the deposition temperature. In chapter 4, we showed that increasing the deposition temperature from 250 to 650 °C increased the cubic phase volume due to the higher adatom mobility and increased tensile stress. However, 650 °C was the substrate temperature upper limit of the vacuum chamber used in this work. It would be of interest to raise the deposition temperature to a higher temperature to see if single phase cubic films could be deposited at higher rates. The added tensile stress due to the CTE mismatch between the materials as well as the higher mobility of adatoms has potential to stabilize the cubic phase.

Another possible method for stabilizing the cubic phase at high deposition would be through the incorporation of tensile stress within the Gd_2O_3 films. This can be done through doping the films with other lanthanide oxide elements. Many of the lanthanide oxide elements are isomorphic miscible within one another. Based on the size of the substituted species, it would be possible to tune the lattice spacing and resulting stress state of the films.

8.2.3. Stabilization of amorphous Gd_2O_3 films

It would be of great interest to deposit thick amorphous Gd_2O_3 films since they possess no grain boundaries, which could result in better electrical properties and less leakage current. Since it was shown in this work that the crystallinity of Gd_2O_3 films deposited by reactive EB-PVD increased with increasing deposition temperature, synthesis of amorphous films would require low deposition temperatures. Gd_2O_3 films crystallize (although poorly) quite easily via reactive EB-PVD even at ambient temperature, and are not structurally stable. We showed in chapter 3 that films deposited at ambient temperature were prone to cracking once a critical thickness was reached (typically ~4 μm). Films thinner than 4 μm could be deposited at ambient without cracking, but the films cracked upon heat treatment even at low temperatures of 100 °C. Preventing this failure would be a critical step towards the synthesis of amorphous Gd_2O_3 films which would likely require even lower substrate temperatures (through liquid nitrogen cooling).

8.2.4. Further investigation of stress induced phase transition in Gd_2O_3 films

We have shown the existence of a stress induced cubic to monoclinic phase transition by bombarding the Gd_2O_3 films with low energy oxygen ions (500 eV) during film deposition. It would be interesting to determine if it is possible to induce this transition by ion bombardment after film deposition. This could potentially allow for direct manipulation of film phase volume based on ion fluence. Indeed, a very recent study, has shown that bulk Gd_2O_3 cubic pellets can be transformed to the monoclinic phase with swift heavy ion irradiation (2.25 GeV Au ions).[36] If the phase change is

possible with low energy ions such as the one used in our study, this would yield further information on the mechanism of the phase change. Further experimental investigation into the mechanism for the stress induced phase transition presented in chapter 5 is also desirable. For instance, in situ TEM during ion irradiation would assist in determining what is physically happening to the structure of the material under irradiation. Additionally, in-situ wafer curvature measurements during film deposition would yield significant information about the role of stress in phase formation. A theoretical approach towards calculating the necessary stress needed to drive the phase transition would be of interest as well. However, this requires knowledge of the elastic constants of both cubic and monoclinic Gd_2O_3 which have not been reported in the literature.

8.2.5. Development of dry etch for Gd_2O_3 device processing

For device fabrication of the Gd_2O_3 metal-oxide-semiconductor (MOS) capacitors and transistors, an etch step was necessary as discussed in chapter 3. Unfortunately, Gd_2O_3 dry etching (via reactive ion etching) is a prohibitively slow process[129] with an etch rate of less than 1 nm / s. Therefore, wet etching based on sulfuric acid solution was employed. However, wet etching was shown to result in uneven etch rate and undercutting of the protecting photoresist, which may result in degradation of film structure and properties. Therefore, development of a dry etch with increased rate would be beneficial towards device processing.

8.2.6. Electrical properties and device performance

This work opens up many possibilities for further study into the electrical properties of thick Gd_2O_3 films. The current-voltage-temperature (I-V-T) measurements performed on the Si / Gd_2O_3 / Ti / Au capacitors showed that numerous conduction mechanisms govern charge transport over a wide electric field and measurement temperature range. However, the costs and time associated with performing I-V-T measurements on all the deposited samples was prohibitive. Nonetheless, it would be of significant interest to further explore the effects of film processing and structure on the conduction mechanisms in the Gd_2O_3 films. Deposition of thinner films (< 500 nm) would allow for investigation of the thickness dependency of the space charge limited conduction mechanism in the Gd_2O_3 films. These measurements coupled with a TEM study of the size and structure of the interfacial layer, would enable extraction of the interfacial layer contribution to charge transport. Additionally, we have shown through both C-V and I-V-T measurements that electronic defects are present within the Gd_2O_3 films. These defects have adverse effects on device properties such as threshold voltage shift, threshold instability, and non-volatile charge trapping effects. Possible techniques to study these traps in more detail are thermally stimulated current (TSC) spectroscopy and deep level transient spectroscopy (DLTS).

8.2.7. Radiation detection

We have shown that Gd_2O_3 is sensitive to both gamma and neutron radiation. However, more investigation is needed to determine the efficiency limits of the Gd_2O_3 detectors and the effects of film thickness on radiation detection. Optimizing the film

and device properties could lead to enhanced charge collection and response. Additionally, developing ways of attenuating the gamma response is necessary to meet detector requirements and avoid generation of false positives.

References

1. Knoll, G. F. *Radiation Detection and Measurement*. 1–802 (John Wiley, 2010).

2. Caruso, A. N. The physics of solid-state neutron detector materials and geometries. *J. Phys. Condens. Matter* **22,** 443201 (2010).

3. Zinkle, S. J. & Hodgson, E. R. Radiation-induced changes in the physical properties of ceramic materials. *J. Nucl. Mater.* **191-194,** 58–66 (1992).

4. Ambacher, O., Smart, J., Shealy, J. R., Weimann, N. G., Chu, K., Murphy, M., Schaff, W. J., Eastman, L. F., Dimitrov, R., Wittmer, L., Stutzmann, M., Rieger, W. & Hilsenbeck, J. Two-dimensional electron gases induced by spontaneous and piezoelectric polarization charges in N- and Ga-face AlGaN/GaN heterostructures. *J. Appl. Phys.* **85,** 3222 (1999).

5. Personal communication from E. Cazalas.

6. Kwo, J., Hong, M., Kortan, A. R., Queeney, K. L., Chabal, Y. J., Opila, R. L., Muller, D. A., Chu, S. N. G., Sapjeta, B. J., Lay, T. S., Mannaerts, J. P., Boone, T., Krautter, H. W., Krajewski, J. J., Sergnt, A. M. & Rosamilia, J. M. Properties of high κ gate dielectrics Gd2O3 and Y2O3 for Si. *J. Appl. Phys.* **89,** 3920 (2001).

7. Kwo, J., Hong, M., Kortan, A. R., Queeney, K. T., Chabal, Y. J., Mannaerts, J. P., Boone, T., Krajewski, J. J., Sergent, A. M. & Rosamilia, J. M. High ε gate dielectrics Gd2O3 and Y2O3 for silicon. *Appl. Phys. Lett.* **77,** 130 (2000).

8. Yue, S., Wei, F., Wang, Y., Yang, Z., Tu, H. & Du, J. Phase control of magnetron sputtering deposited Gd2O3 thin films as high-κ gate dielectrics. *J. Rare Earths* **26,** 371–374

9. Wolfe, D. E., Singh, J., Miller, R. A., Eldridge, J. I. & Zhu, D.-M. Tailored microstructure of EB-PVD 8YSZ thermal barrier coatings with low thermal conductivity and high thermal reflectivity for turbine applications. *Surf. Coatings Technol.* **190,** 132–149 (2005).

10. Senthilkumar, M., Sahoo, N. K., Thakur, S. & Tokas, R. B. Reactive electron beam evaporated gadolinia films at ambient substrate temperature: optical properties and morphology studies. *Appl. Surf. Sci.* **245,** 114–127 (2005).

11. Sahoo, N. K., Senthilkumar, M., Thakur, S. & Bhattacharyya, D. Correlation of optical and microstructural properties of Gd2O3 thin films through phase-modulated ellipsometry and multi-mode atomic force microscopy. *Appl. Surf. Sci.* **200,** 219–230 (2002).

12. Bhattacharyya, D., Biswas, A. & Sahoo, N. K. Investigation on dispersion of optical constants of Gd2O3 films by phase modulated spectroscopic ellipsometry. *Appl. Surf. Sci.* **233,** 155–162 (2004).

13. Raut, H. K., Ganesh, V. A., Nair, A. S. & Ramakrishna, S. Anti-reflective coatings: A critical, in-depth review. *Energy Environ. Sci.* **4,** 3779 (2011).

14. Yi, S., Bae, J. S., Shim, K. S., Jeong, J. H., Park, J.-C. & Holloway, P. H. Enhanced luminescence of Gd2O3:Eu3+ thin-film phosphors by Li doping. *Appl. Phys. Lett.* **84,** 353 (2004).

15. Messier, R. Revised structure zone model for thin film physical structure. *J. Vac. Sci. Technol. A Vacuum, Surfaces, Film.* **2,** 500 (1984).

16. Batchelor, R., Aves, R. & Skyrme, T. H. R. Helium-3 Filled Proportional Counter for Neutron Spectroscopy. *Rev. Sci. Instrum.* **26,** 1037 (1955).

17. Uher, J., Pospisil, S., Linhart, V. & Schieber, M. Efficiency of composite boron nitride neutron detectors in comparison with helium-3 detectors. *Appl. Phys. Lett.* **90,** 124101 (2007).

18. ENDFPLOT-2 at http://atom.kaeri.re.kr/index.html.

19. Munter, A. http://www.ncnr.nist.gov/resources/n-lengths/. *National Institute of Standards and Technology (NIST), Center for Neutron Research* (2009).

20. McGregor, D. S., Hammig, M. D., Yang, Y.-H., Gersch, H. K. & Klann, R. T. Design considerations for thin film coated semiconductor thermal neutron detectors—I: basics regarding alpha particle emitting neutron reactive films. *Nucl. Instruments Methods Phys. Res. Sect. A Accel. Spectrometers, Detect. Assoc. Equip.* **500,** 272–308 (2003).

21. Birks, J. B. *The Theory and Practice of Scintillation Counting*. 662 (Pergamon Press, 1964).

22. McGregor, D. S., Klann, R. T., Sanders, J. D., Lindsay, J. T., Linden, K. J., Gersch, H. K., De Lurgio, P. M., Fink, C. L. & Ariesanti, E. Recent results from thin-film-coated semiconductor neutron detectors. in *International Symposium on Optical Science and Technology* (eds. James, R. B., Franks, L. A., Burger, A., Westbrook, E. M. & Durst, R. D.) 164–182 (International Society for Optics and Photonics, 2003). doi:10.1117/12.455697

23. Peurrung, A. . Recent developments in neutron detection. *Nucl. Instruments Methods Phys. Res. Sect. A Accel. Spectrometers, Detect. Assoc. Equip.* **443,** 400–415 (2000).

24. Berdermann, E., Ciobanu, M., Connell, S. H., da Costa, A. M. O. D., Fernandez-Hernando, L., Oh, A. & Sellschop†, J. P. F. Charged particle detectors made of single-crystal diamond. *Phys. status solidi* **201,** 2521–2528 (2004).

25. Nava, F., Castaldini, A., Cavallini, A., Errani, P. & Cindro, V. Radiation Detection Properties of 4H-SiC Schottky Diodes Irradiated Up to 10^16 n/cm^2 by 1 MeV Neutrons. *IEEE Trans. Nucl. Sci.* **53,** 2977–2982 (2006).

26. Personal communication from Cree Inc. Raleigh, NC. (2009).

27. Hodgson, E. R. Radiation-enhanced electrical breakdown in fusion insulators. *J. Nucl. Mater.* **179-181,** 383–386 (1991).

28. Ishii, M., Kuwano, Y., Asai, T., Asaba, S., Kawamura, M., Senguttuvan, N., Hayashi, T., Kobayashi, M., Nikl, M., Hosoya, S., Sakai, K., Adachi, T., Oku, T. & Shimizu, H. M. Boron based oxide scintillation glass for neutron detection. *Nucl. Instruments Methods Phys. Res. Sect. A Accel. Spectrometers, Detect. Assoc. Equip.* **537,** 282–285 (2005).

29. Chernov, V. M., Belyakov, V. A., Bryuzgin, A. M., Cherednichenko, Y. G., Ievleva, J. I., Khorasanov, G. L., Plaksin, O. A., Stepanov, V. A., Vizgalov, A. V., Zherebtsov, V. A. & Zrodnikov, A. V. Investigations on radiation-induced processes in dielectric materials. *J. Nucl. Mater.* **233-237,** 1304–1309 (1996).

30. Fowler, J. F. Radiation-induced Conductivity in the Solid State, and Some Applications. *Phys. Med. Biol.* **3,** 395–410 (1959).

31. Castor, B. & Hedrick, J. B. in *Industrial Minerals and Rocks* 769–792 (2006).

32. Atwood, D. A. *The Rare Earth Elements : Fundamentals and Applications*. 1–624 (Wiley, 2013).

33. Nowick, A. S. *Rare Earth Permanent Magnets*. 214 (Elsevier Science, 2012).

34. Eyring, L. *Synthesis of Lanthanide and Actinide Compounds*. 187 (Springer Science & Business Media, 1991).

35. Adachi, G. & Imanaka, N. The Binary Rare Earth Oxides. *Chem. Rev.* **98,** 1479–1514 (1998).

36. Lang, M., Zhang, F., Zhang, J., Tracy, C. L., Cusick, A. B., VonEhr, J., Chen, Z., Trautmann, C. & Ewing, R. C. Swift heavy ion-induced phase transformation in Gd2O3. *Nucl. Instruments Methods Phys. Res. Sect. B Beam Interact. with Mater. Atoms* **326,** 121–125 (2014).

37. Bai, L., Liu, J., Li, X., Jiang, S., Xiao, W., Li, Y., Tang, L., Zhang, Y. & Zhang, D. Pressure-induced phase transformations in cubic Gd2O3. *J. Appl. Phys.* **106,** 073507 (2009).

38. Atou, T., Kusaba, K., Fukuoka, K., Kikuchi, M. & Syono, Y. Shock-induced phase transition of M2O3 (M = Sc, Y, Sm, Gd, and In)-type compounds. *J. Solid State Chem.* **89,** 378–384 (1990).

39. Zhang, F., Lang, M., Wang, J., Becker, U. & Ewing, R. Structural phase transitions of cubic Gd2O3 at high pressures. *Phys. Rev. B* **78,** 064114 (2008).

40. Mattox, D. M. *Handbook of Physical Vapor Deposition (PVD) Processing*. 792 (William Andrew, 2010).

41. Lüth, H. *Solid Surfaces, Interfaces and Thin Films*. 1–580 (Springer Berlin Heidelberg, 2010).

42. Movachan, B. A. & Demchishin, A. V. Study of the Structure and Properties of Thick Vacuum Condensates of Nickel, Titanium, Tungsten, Aluminum Oxide and Zirconium Dioxide Fiz. *Met. Met.* **28,** 83–90 (1969).

43. Thornton, J. A. High Rate Thick Film Growth. *Annu. Rev. Mater. Sci.* **7,** 239–260 (1977).

44. Ohring, M. *Materials Science of Thin Films : Deposition and Structure*. 1–794 (Elsevier, 2002).

45. Grave, D. A., Hughes, Z. R., Robinson, J. A., Medill, T. P., Hollander, M. J., Stump, A. L., Labella, M., Weng, X. & Wolfe, D. E. Process–structure–property relations of micron thick Gd2O3 films deposited by reactive electron-beam physical vapor deposition (EB-PVD). *Surf. Coatings Technol.* **206,** 3094–3103 (2012).

46. Cao, L., Sozontov, E. & Zegenhagen, J. Cubic to Tetragonal Phase Transition of SrTiO3 under Epitaxial Stress: An X-Ray Backscattering Study. *Phys. status solidi* **181,** 387–404 (2000).

47. Shaw, T. M., Suo, Z., Huang, M., Liniger, E., Laibowitz, R. B. & Baniecki, J. D. The effect of stress on the dielectric properties of barium strontium titanate thin films. *Appl. Phys. Lett.* **75,** 2129 (1999).

48. Liu, K.-C., Tsai, J.-R., Li, C.-S., Chien, P.-H., Chen, J.-N. & Feng, W.-S. Characteristics of Transparent ZnO-Based Thin-Film Transistors with High- k Dielectric Gd 2 O 3 Gate Insulators Fabricated at Room Temperature. *Jpn. J. Appl. Phys.* **49,** 04DF21 (2010).

49. Singh, M. P., Thakur, C. S., Shalini, K., Banerjee, S., Bhat, N. & Shivashankar, S. A. Structural, optical, and electrical characterization of gadolinium oxide films deposited by low-pressure metalorganic chemical vapor deposition. *J. Appl. Phys.* **96,** 5631 (2004).

50. Niinistö, J., Petrova, N., Putkonen, M., Niinistö, L., Arstila, K. & Sajavaara, T. Gadolinium oxide thin films by atomic layer deposition. *J. Cryst. Growth* **285,** 191–200 (2005).

51. Li, Y., Chen, N., Zhou, J., Song, S., liu, L., Yin, Z. & Cai, C. Effect of the oxygen concentration on the properties of Gd2O3 thin films. *J. Cryst. Growth* **265,** 548–552 (2004).

52. Laha, A., Osten, H. J. & Fissel, A. Influence of interface layer composition on the electrical properties of epitaxial Gd2O3 thin films for high-K application. *Appl. Phys. Lett.* **90,** 113508 (2007).

53. Laha, A., Osten, H. J. & Fissel, A. Impact of Si substrate orientations on electrical properties of crystalline Gd2O3 thin films for high-K application. *Appl. Phys. Lett.* **89,** 143514 (2006).

54. Hong, M. Epitaxial Cubic Gadolinium Oxide as a Dielectric for Gallium Arsenide Passivation. *Science* **283,** 1897–1900 (1999).

55. Johnson, J. W., Luo, B., Ren, F., Gila, B. P., Krishnamoorthy, W., Abernathy, C. R., Pearton, S. J., Chyi, J. I., Nee, T. E., Lee, C. M. & Chuo, C. C. Gd[sub 2]O[sub 3]/GaN metal-oxide-semiconductor field-effect transistor. *Appl. Phys. Lett.* **77,** 3230 (2000).

56. Chang, W. H., Lee, C. H., Chang, P., Chang, Y. C., Lee, Y. J., Kwo, J., Tsai, C. C., Hong, J. M., Hsu, C.-H. & Hong, M. High κ dielectric single-crystal monoclinic Gd2O3 on GaN with excellent thermal, structural, and electrical properties. *J. Cryst. Growth* **311,** 2183–2186 (2009).

57. Chang, W. H., Lee, C. H., Chang, Y. C., Chang, P., Huang, M. L., Lee, Y. J., Hsu, C.-H., Hong, J. M., Tsai, C. C., Kwo, J. R. & Hong, M. Nanometer-Thick Single-Crystal Hexagonal Gd 2 O 3 on GaN for Advanced Complementary Metal-Oxide-Semiconductor Technology. *Adv. Mater.* **21,** 4970–4974 (2009).

58. Le Luyer, C., Garcia-Murillo, A., Bernstein, E. & Mugnier, J. Waveguide Raman spectroscopy of sol-gel Gd2O3 thin films. *J. Raman Spectrosc.* **34,** 234–239 (2003).

59. Wu, X., Landheer, D., Sproule, G. I., Quance, T., Graham, M. J. & Botton, G. A. Characterization of gadolinium and lanthanum oxide films on Si (100). *J. Vac. Sci. Technol. A Vacuum, Surfaces, Film.* **20,** 1141 (2002).

60. Gupta, J. A., Landheer, D., Sproule, G. I., McCaffrey, J. P., Graham, M. J., Yang, K.-C., Lu, Z.-H. & Lennard, W. N. Interfacial layer formation in Gd2O3 films deposited directly on Si(0 0 1). *Appl. Surf. Sci.* **173,** 318–326 (2001).

61. Molle, A., Wiemer, C., Bhuiyan, M. N. K., Tallarida, G., Fanciulli, M. & Pavia, G. Cubic-to-monoclinic phase transition during the epitaxial growth of crystalline Gd2O3 films on Ge(001) substrates. *Appl. Phys. Lett.* **90,** 193511 (2007).

62. Chang, W. H., Wu, S.-Y., Lee, C.-H., Lai, T.-Y., Lee, Y.-J., Chang, P., Hsu, C.-H., Huang, T.-S., Kwo, J. R. & Hong, M. Phase transformation of molecular beam epitaxy-grown nanometer-thick Gd2O3 and Y2O3 on GaN. *ACS Appl. Mater. Interfaces* **5,** 1436–41 (2013).

63. Chiang, T.-H., Wu, S.-Y., Huang, T.-S., Hsu, C.-H., Kwo, J. & Hong, M. Single crystal Gd2O3 epitaxially on GaAs(111)A. *CrystEngComm* **16,** 8457 (2014).

64. Schwendt, D., Osten, H. J., Shekhter, P. & Eizenberg, M. Strain-induced effects on the dielectric constant for thin, crystalline rare earth oxides on silicon. *Appl. Phys. Lett.* **100,** 232905 (2012).

65. Singh, M. P., Thakur, C. S., Shalini, K., Banerjee, S., Bhat, N. & Shivashankar, S. A. Structural, optical, and electrical characterization of gadolinium oxide films deposited by low-pressure metalorganic chemical vapor deposition. *J. Appl. Phys.* **96,** 5631 (2004).

66. Bentarzi, H. *Transport in Metal-Oxide-Semiconductor Structures*. 1–106 (Springer Berlin Heidelberg, 2011).

67. Pollak, M. A percolation treatment of dc hopping conduction. *J. Non. Cryst. Solids* **11,** 1–24 (1972).

68. Rose, A. Space-Charge-Limited Currents in Solids. *Phys. Rev.* **97,** 1538–1544 (1955).

69. Simmons, J. Poole-Frenkel Effect and Schottky Effect in Metal-Insulator-Metal Systems. *Phys. Rev.* **155,** 657–660 (1967).

70. Schottky, W. Uber kalte und warme Elektronenentladungen. *Zeitschrift fur Phys.* **14,** 63–106 (1923).

71. Fòwler, R. H. & Nordheim, L. Electron Emission in Intense Electric Fields. *Proc. R. Soc. London. Ser. A, Contain. Pap. a Math. Phys. Character* **119,** pp. 173–181 (1928).

72. Patterson, A. The Scherrer Formula for X-Ray Particle Size Determination. *Phys. Rev.* **56,** 978–982 (1939).

73. Plawsky, J. L., Achanta, R., Cho, W., Rodriguez, R., Saxena, R. & Gill, W. N. in *Dielectric Films for Advanced Microelectronics* (eds. Baklanov, M. R., Green, M. L. & Maex, K.) 152 (John Wiley & Sons, Ltd, 2007).

74. Stoney, G. The Tension of Metallic Films deposited by Electrolysis. *Proc. R. Soc. Lond. A* **82,** 172 (1909).

75. (n.a). International Center for Diffraction Data (ICDD), Card 00–42–1465, (1994).

76. (n.a). International Center for Diffraction Data (ICDD), Card 00–43–1014, (1994).

77. Ostwald, W. Z. Studien uber die Bildung und Umwandlung fester Korper. *Phys. Chem.* **22,** 289–330 (1897).

78. Gaboriaud, R. J., Pailloux, F., Guerin, P. & Paumier, F. Yttrium oxide thin films, Y2O3 , grown by ion beam sputtering on Si. *J. Phys. D. Appl. Phys.* **33,** 2884–2889 (2000).

79. Kim, Y. I., Nahm, S. H. & Jung, M.-J. Structural refinement of SnO2 thin film prepared by plasma-enhanced chemical vapor deposition. *Mater. Lett.* **57,** 3653–3659 (2003).

80. Johnson, Q. & Zhou, R. S. Checking and estimating RIR values. *Adv. X-ray Anal.* **42,** 287–296 (2000).

81. Dollase, W. A. Correction of intensities for preferred orientation in powder diffractometry: application of the March model. *J. Appl. Crystallogr.* **19,** 267–272 (1986).

82. Ahtee, M., Nurmela, M., Suortti, P. & Järvinen, M. Correction for preferred orientation in Rietveld refinement. *J. Appl. Crystallogr.* **22,** 261–268 (1989).

83. Chrysochoou, M. & Dermatas, D. Application of the Rietveld method to assess chromium(VI) speciation in chromite ore processing residue. *J. Hazard. Mater.* **141,** 370–7 (2007).

84. Zarembowitch, J., Gouteron, J. & Lejus†, A. M. Raman spectrum of single crystals of monoclinic B-type gadolinium sesquioxide. *J. Raman Spectrosc.* **9,** 263–265 (1980).

85. Whitney, E. D. Kinetics and mechanism of the transition of metastable tetragonal to monoclinic zirconia. *Trans. Faraday Soc.* **61,** 1991 (1965).

86. Gaboriaud, R. J., Lacroix, B. & Paumier, F. Ion irradiation-induced phase transformations in bixbyite-fluorite related oxides: The role of dislocation loop

nucleation. *Nucl. Instruments Methods Phys. Res. Sect. B Beam Interact. with Mater. Atoms* **277,** 18–20 (2012).

87. Noyan, I. C. & Cohen, J. B. *Residual stress: measurement by diffraction and interpretation*. 276 (Springer, 1987).

88. http://www.ceramics.nist.gov/srd/summary/Gd2O3.htm.

89. Thornton, J. A. Internal stresses in titanium, nickel, molybdenum, and tantalum films deposited by cylindrical magnetron sputtering. *J. Vac. Sci. Technol.* **14,** 164 (1977).

90. Freund, L. B. & Suresh, S. *Thin Film Materials: Stress, Defect Formation and Surface Evolution*. 1–750 (Cambridge University Press, 2004).

91. Chason, E., Sheldon, B., Freund, L., Floro, J. & Hearne, S. Origin of Compressive Residual Stress in Polycrystalline Thin Films. *Phys. Rev. Lett.* **88,** 156103 (2002).

92. Sawbridge, P. T. & Waterman, N. A. On the thermal expansion and crystallography of cubic (C) and monoclinic (B) forms of Gd2O3 in the temperature range 20 to 900 C. *J. Mater. Sci.* **3,** 15–18 (1968).

93. Okada, Y. & Tokumaru, Y. Precise determination of lattice parameter and thermal expansion coefficient of silicon between 300 and 1500 K. *J. Appl. Phys.* **56,** 314 (1984).

94. Chhowalla, M. & Unalan, H. E. Thin films of hard cubic Zr3N4 stabilized by stress. *Nat. Mater.* **4,** 317–22 (2005).

95. Piascik, J. R., Zhang, Q., Bower, C. A., Thompson, J. Y. & Stoner, B. R. Evidence of stress-induced tetragonal-to-monoclinic phase transformation during sputter deposition of yttria-stabilized zirconia. *J. Mater. Res.* **22,** 1105–1111 (2011).

96. Hémon, S., Chailley, V., Dooryhée, E., Dufour, C., Gourbilleau, F., Levesque, F. & Paumier, E. Phase transformation of polycrystalline Y2O3 under irradiation with swift heavy ions. *Nucl. Instruments Methods Phys. Res. Sect. B Beam Interact. with Mater. Atoms* **122,** 563–565 (1997).

97. Gaboriaud, R. J., Paumier, F., Jublot, M. & Lacroix, B. Ion irradiation-induced phase transformation mechanisms in Y2O3 thin films. *Nucl. Instruments Methods Phys. Res. Sect. B Beam Interact. with Mater. Atoms* **311,** 86–92 (2013).

98. Tang, M., Lu, P., Valdez, J. A. & Sickafus, K. E. Ion-irradiation-induced phase transformation in rare earth sesquioxides (Dy2O3,Er2O3,Lu2O3). *J. Appl. Phys.* **99,** 063514 (2006).

99. Lang, M., Zhang, F., Zhang, J., Tracy, C. L., Cusick, A. B., VonEhr, J., Chen, Z., Trautmann, C. & Ewing, R. C. Swift heavy ion-induced phase transformation in Gd2O3. *Nucl. Instruments Methods Phys. Res. Sect. B Beam Interact. with Mater. Atoms* **326,** 121–125 (2014).

100. Antic, B., Kremenovic, A., Draganic, I., Colomban, P., Vasiljevic-Radovic, D., Blanusa, J., Tadic, M. & Mitric, M. Effects of O2+ ions beam irradiation on crystal structure of rare earth sesquioxides. *Appl. Surf. Sci.* **255,** 7601–7604 (2009).

101. Herrero, A. M., Gila, B. P., Abernathy, C. R., Pearton, S. J., Craciun, V., Siebein, K. & Ren, F. Epitaxial growth of Sc2O3 films on GaN. *Appl. Phys. Lett.* **89,** 092117 (2006).

102. Jur, J. S., Wheeler, V. D., Lichtenwalner, D. J., Maria, J.-P. & Johnson, M. A. L. Epitaxial growth of lanthanide oxides La2O3 and Sc2O3 on GaN. *Appl. Phys. Lett.* **98,** 042902 (2011).

103. Botton, G. A., Gupta, J. A., Landheer, D., McCaffrey, J. P., Sproule, G. I. & Graham, M. J. Electron energy loss spectroscopy of interfacial layer formation in Gd2O3 films deposited directly on Si(001). *J. Appl. Phys.* **91,** 2921 (2002).

104. Landheer, D., Gupta, J. A., Sproule, G. I., McCaffrey, J. P., Graham, M. J., Yang, K.-C., Lu, Z.-H. & Lennard, W. N. Characterization of Gd2O3 Films Deposited on Si(100) by Electron-Beam Evaporation. *J. Electrochem. Soc.* **148,** G29 (2001).

105. Thornton, J. A. The microstructure of sputter-deposited coatings. *J. Vac. Sci. Technol. A Vacuum, Surfaces, Film.* **4,** 3059 (1986).

106. Merckling, C., Saint-Girons, G., Delhaye, G., Patriarche, G., Largeau, L., Favre-Nicollin, V., El-Kazzi, M., Regreny, P., Vilquin, B., Marty, O., Botella, C., Gendry, M., Grenet, G., Robach, Y. & Hollinger, G. Epitaxial growth of high-κ oxides on silicon. *Thin Solid Films* **517,** 197–200 (2008).

107. Gottlob, H. D. B., Stefani, A., Schmidt, M., Lemme, M. C., Kurz, H., Mitrovic, I. Z., Werner, M., Davey, W. M., Hall, S., Chalker, P. R., Cherkaoui, K., Hurley, P. K., Piscator, J., Engström, O. & Newcomb, S. B. Gd silicate: A high-k dielectric compatible with high temperature annealing. *J. Vac. Sci. Technol. B Microelectron. Nanom. Struct.* **27,** 249 (2009).

108. Hubbard, K. J. & Schlom, D. G. Thermodynamic stability of binary oxides in contact with silicon. *J. Mater. Res.* **11,** 2757–2776 (2011).

109. Ghosh, R., Basak, D. & Fujihara, S. Effect of substrate-induced strain on the structural, electrical, and optical properties of polycrystalline ZnO thin films. *J. Appl. Phys.* **96,** 2689 (2004).

110. Gupta, J. A., Landheer, D., McCaffrey, J. P. & Sproule, G. I. Gadolinium silicate gate dielectric films with sub-1.5 nm equivalent oxide thickness. *Appl. Phys. Lett.* **78,** 1718 (2001).

111. Schwan, H. P. Complex permittivity of water at 25 °C. *J. Chem. Phys.* **64,** 2257 (1976).

112. Jeon, S. & Hwang, H. Effect of hygroscopic nature on the electrical characteristics of lanthanide oxides (Pr2O3, Sm2O3, Gd2O3, and Dy2O3). *J. Appl. Phys.* **93,** 6393 (2003).

113. Tomida, K., Kita, K. & Toriumi, A. Dielectric constant enhancement due to Si incorporation into HfO2. *Appl. Phys. Lett.* **89,** 142902 (2006).

114. Goetzberger, A. & Irvin, J. C. Low-temperature hysteresis effects in metal-oxide-silicon capacitors caused by surface-state trapping. *IEEE Trans. Electron Devices* **15,** 1009–1014 (1968).

115. Grovenor, C. R. M. *Microelectronic Materials*. 544 (CRC Press, 1989).

116. Hill, W. A. & Coleman, C. C. A single-frequency approximation for interface-state density determination. *Solid. State. Electron.* **23,** 987–993 (1980).

117. Rozen, J., Dhar, S., Dixit, S. K., Afanas'ev, V. V., Roberts, F. O., Dang, H. L., Wang, S., Pantelides, S. T., Williams, J. R. & Feldman, L. C. Increase in oxide hole trap density associated with nitrogen incorporation at the SiO2/SiC interface. *J. Appl. Phys.* **103,** 124513 (2008).

118. Chang, L. B., Das, A., Lin, R. M., Maikap, S., Jeng, M. J. & Chou, S. T. An observation of charge trapping phenomena in GaN/AlGaN/Gd2O3/Ni–Au structure. *Appl. Phys. Lett.* **98,** 222106 (2011).

119. Chiu, F.-C. A Review on Conduction Mechanisms in Dielectric Films. *Adv. Mater. Sci. Eng.* **2014,** 1–18 (2014).

120. Li, P. & Lu, T.-M. Conduction mechanisms in BaTiO3 thin films. *Phys. Rev. B* **43,** 14261–14264 (1991).

121. Gottlob, H. D. B., Echtermeyer, T. J., Schmidt, M., Mollenhauer, T., Wahlbrink, T., Lemme, M. C. & Kurz, H. Leakage Current Mechanisms in Epitaxial Gd2O3 High-k Gate Dielectrics. *Electrochem. Solid-State Lett.* **11,** G12 (2008).

122. Michaelson, H. B. The work function of the elements and its periodicity. *J. Appl. Phys.* **48,** 4729 (1977).

123. Lipp, E., Shahar, Z., Bittel, B. C., Lenahan, P. M., Schwendt, D., Osten, H. J. & Eizenberg, M. Trap-assisted conduction in Pt-gated Gd2O3/Si capacitors. *J. Appl. Phys.* **109,** 073724 (2011).

124. Gupta, R. K., Ghosh, K. & Kahol, P. K. Junction characteristics of pulsed laser deposition grown Gd2O3 on p-silicon. *Phys. E Low-dimensional Syst. Nanostructures* **41,** 1201–1203 (2009).

125. Lipp, E., Eizenberg, M., Czernohorsky, M. & Osten, H. J. Effect of oxide structure on the Fermi-level pinning at metal/Gd2O3 interfaces. *Appl. Phys. Lett.* **93,** 193513 (2008).

126. Joung, D., Chunder, A., Zhai, L. & Khondaker, S. I. Space charge limited conduction with exponential trap distribution in reduced graphene oxide sheets. *Appl. Phys. Lett.* **97,** 093105 (2010).

127. Hsu, S. S. H. AlGaN/GaN HEMTs With Low Leakage Current and High On/Off Current Ratio. *IEEE Electron Device Lett.* **31,** 102–104 (2010).

128. Bierwagen, O., Proessdorf, A., Niehle, M., Grosse, F., Trampert, A. & Klingsporn, M. Oxygen-Deficient Oxide Growth by Subliming the Oxide Source Material: The Cause of Silicide Formation in Rare Earth Oxides on Silicon. *Cryst. Growth Des.* **13,** 3645–3650 (2013).

129. Vitale, S. A., Wyatt, P. W. & Hodson, C. J. Plasma-enhanced atomic layer deposition and etching of high-k gadolinium oxide. *J. Vac. Sci. Technol. A Vacuum, Surfaces, Film.* **30,** 01A130 (2012).

Appendix A. GaN / AlGaN device fabrication and mask layouts

Appendix A.1. Device fabrication procedure

1000	**LOT START**
A	Move-in 1000
B	Inscribe wafer ID's
C	Inspect for scratches, cracks, poor surface, edge chips, etc.
D	Solvent clean: ACE 2 min, IPA 2 min, DI rinse
E	Move-out 1000
1010	**ISOLATION PHOTOLITHOGRAPHY**
A	Move-in 1010
B	Pre-bake: Dehydration at 95 °C for 1 min
C	Resist coat: 3012 @ 5000 rpm for 45 s
D	PAB: 95°C for 60 s
E	Expose first level (no alignment): **Mask "ISO"** Exposure time: 7.0 s
F	Develop: CD-26 for 60s, DI rinse; N2 blow dry
G	Mask clean: soak in ACE, IPA, DI or Remover PG, IPA, DI
H	Microscope inspection _____
I	Move-out 1010
1020	**ISOLATION ETCH**
A	Move-in 1020
B	Sample mount: 150-mm Si carrier wafer, w/green Revalpha tape
C	ICP/RIE: Recipe "AEOC_GN2": BCl_3/Ar, Flow: 6/11 sccm; Pres.: 2 mTorr;
D	60W; RF power: ____ W; Etch time: 104 s (Target 80 nm)
E	Sample demount: Hotplate @127 °C for 20 s
F	Deskin M4L_225w_ 2min_8sccm Ar_100sccm O2_10mTorr
G	Resist strip: 95°C Remover PG, Sonicate 5 sec to remove redep, IPA 2 min, DI 2 min, N2 blow dry
H	Microscope inspection _Profilometer_____
I	Move-out 1020
2010	**OHMIC CONTACT PHOTOLITHOGRAPHY**
A	Move-in 2010
B	Pre-bake: Dehydration at 95 °C for 1 min
C	Resist coat: LOR5A @6000 rpm for 45 s
D	PAB: 180°C for 10 min
E	Resist coat: 3012 @6000 rpm for 45 s
F	PAB: 95°C for 60 s
G	Align & expose: **Mask "OHMIC"** Exposure time: 6.5 -7.0 s (check last trav
H	Develop: CD-26 for 60s, DI rinse; N2 blow dry
I	Mask clean: soak in ACE, IPA, DI or Remover PG, IPA, DI
J	Microscope inspection _____
K	Move-out 2010
2020	**OHMIC METAL EVAPORATION**
A	Move-in 2020
B	Descum: M4L @150 W, O2/He flow: 150/50 sccm, 600 mTorr, for 60 s
C	**Oxide etch: BOE: DI = 1:10 for 60 s, DI rinse, N2 blow dry**
D	LOAD IMMEDIATELY INTO EVAPORATOR
E	Evaporate Ti/Al/Ni/Au: 150/1000/500/500Å Dep rates: ___/___/___/___
F	Move-out 2020
2030	**OHMIC METAL LIFTOFF**
A	Move-in 2030
C	Liftoff soak: Ace_15min_IPA_2min (to remove patterning resist)
D	Liftoff: PRS-3000 at 90 °C for 20 min_Sonicate in *new* IPA_2sec blasts
E	DI rinse, N2 blow dry
F	Move-out 2030

2040	OHMIC CONTACT ALLOY
A	Move-in 2040
B	RTA: Dummy run with Recipe P875_60
	The recipe in Big Bertha is pictured
C	RTA: Contact alloy run run with Recipe P875_60
D	Microscope inspection _____
E	Move-out 2040

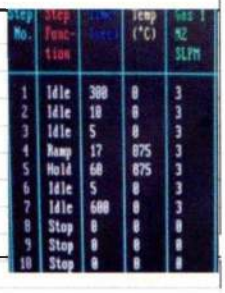

Step No.	Step Function	Time (sec)	Temp (°C)	Gas 1 N2 SLPM
1	Idle	300	0	3
2	Idle	10	0	3
3	Idle	5	0	3
4	Ramp	17	875	3
5	Hold	60	875	3
6	Idle	5	0	3
7	Idle	600	0	3
8	Stop	0	0	0
9	Stop	0	0	0
10	Stop	0	0	0

2050	OHMIC CONTACT TEST
A	Move-in 2050
B	I-V test: Probe TLM test structures and characterize ohmic contacts
C	Move-out 2050

3010	DIELECTRIC DEPOSITION
A	Move-in 3010
	(TBD)
n	Move-out 3010

4010	DIELECTRIC PATTERNING PHOTOLITHOGRAPHY
A	Move-in 4010
B	Pre-bake: Dehydration at 95 °C for 60 s
C	SPR 955 tri-layer:
	1) coat @ 3000rpm for 45s (D09_30_45) PAB: 105°C_10min
	2) coat @ 3000rpm for 45s (D09_30_45) PAB: 105°C_5min
	3) coat @ 3000rpm for 45s (D09_30_45) PAB: 105°C_1min
	Apply each layer quickly, new resist removes the previous layer if left to sit
D	Align & Expose: **Mask "DIELECTRIC"** Exposure time: 7.0 s
E	Develop: CD-26 for 60s, DI rinse; N2 blow dry
F	Mask clean: soak in ACE, IPA, DI or Remover PG, IPA, DI
G	Microscope inspection _____
H	Move-out 4010

4020	DIELECTRIC ETCH
A	Move-in 4020
B	TBD: depends on dielectric --->
C	
D	DI rinse & N2 blowdry
G	Resist strip: Gd2O3:PRS3000 @ 80C for 10 min, IPA 2 min, DI 2 min, N2 d
	Resist strip: BN:EKC830 @ 60C for 10 min, IPA 2 min, DI 2 min, N2 blow d
H	Microscope inspection _____
I	Move-out 4020

5010	GATE METAL PHOTOLITHOGRAPHY
A	Move-in 5010
B	Pre-bake: Dehydration at 95 °C for 1 min
C	Resist coat: LOR5A @5000 rpm for 45 s
D	PAB: 180°C for 10 min
E	Resist coat: 3012 @5000 rpm for 45 s
F	PAB: 95°C for 60 s
G	Align & expose: **Mask "_5um_"** Exposure time: _7s
H	Develop: CD-26 for 60s, DI rinse; N2 blow dry
I	Microscope inspection _____
J	Move-out 5010

5020	GATE METAL DEPOSITION
A	Move-in 5020
B	Descum: M4L @150 W, O2/He flow: 150/50 sccm, 600 mTorr, for 60 s
C	LOAD IMMEDIATELY INTO EVAPORATOR
D	Evaporate Ti/Au: 200/2800 Å Dep rates: _____/_____Å/s
E	Move-out 4020

5030	GATE METAL LIFTOFF
A	Move-in 5030
B	Liftoff soak: PRS-3000 at 80 °C for 10 min,
C	Liftoff: IPA for 1 min + 5 sec sonicate, DI rinse, N2 blow dry
D	Microscope inspection _____
E	Move-out 5030

Appendix A.2. Mask layouts

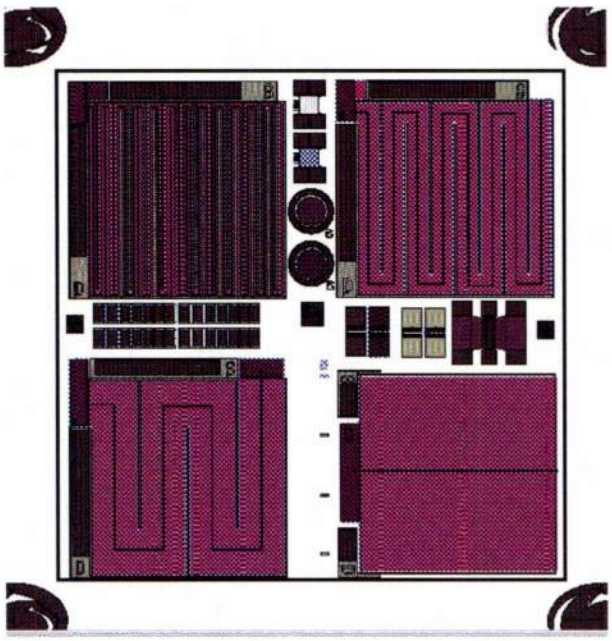

Figure A.1. Overall mask layout for GaN / AlGaN rad sensor device fabrication.

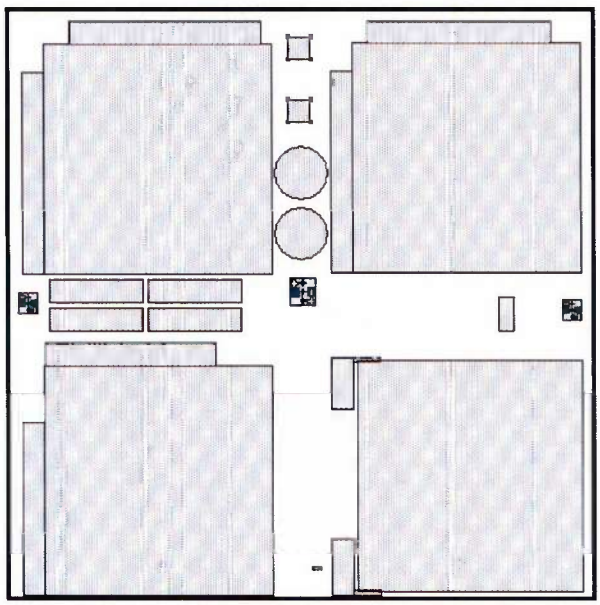

Figure A.2. Isolation layer mask layout for GaN / AlGaN rad sensor device fabrication.

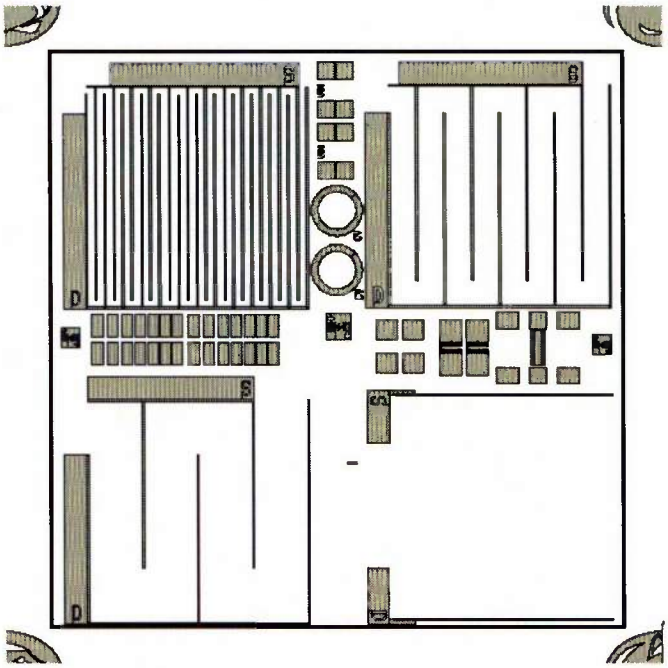

Figure A.3. Ohmic level mask layout for GaN / AlGaN rad sensor device fabrication.

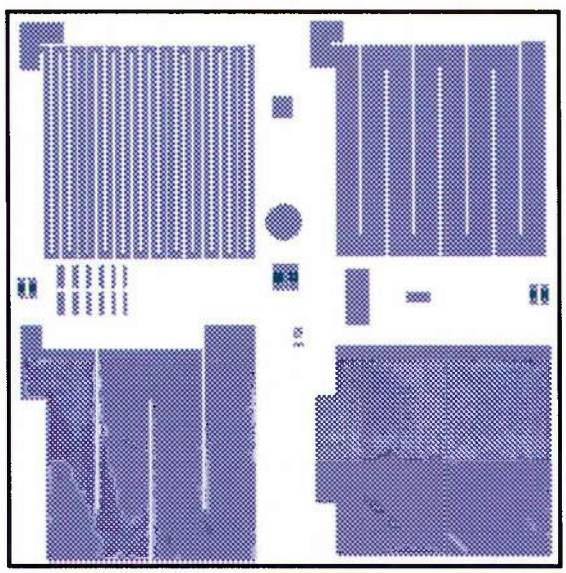

Figure A.4. Dielectric etch level mask layout for GaN / AlGaN rad sensor device fabrication.

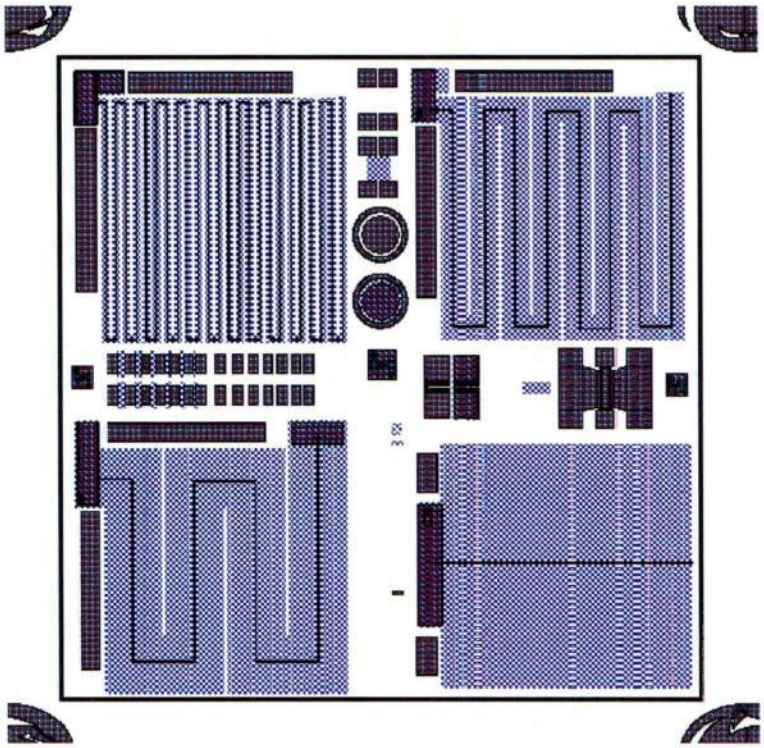

Figure A.5. Schottky level mask layout for GaN / AlGaN rad sensor device fabrication.

Appendix B. Optical properties of Gd_2O_3 films

Appendix B.1. Optical band gap measurements

The optical properties of select Gd_2O_3 films, approximately 1 μm in thickness, deposited on quartz substrates were investigated by UV–Vis spectroscopy. Preliminary optical transmittance measurements of the Gd_2O_3 films were made as shown in Figure B.1. From this data, $(\alpha h\upsilon)^2$ as a function of $h\upsilon$ was plotted, where α is the absorption coefficient and $h\upsilon$ is the photon energy.

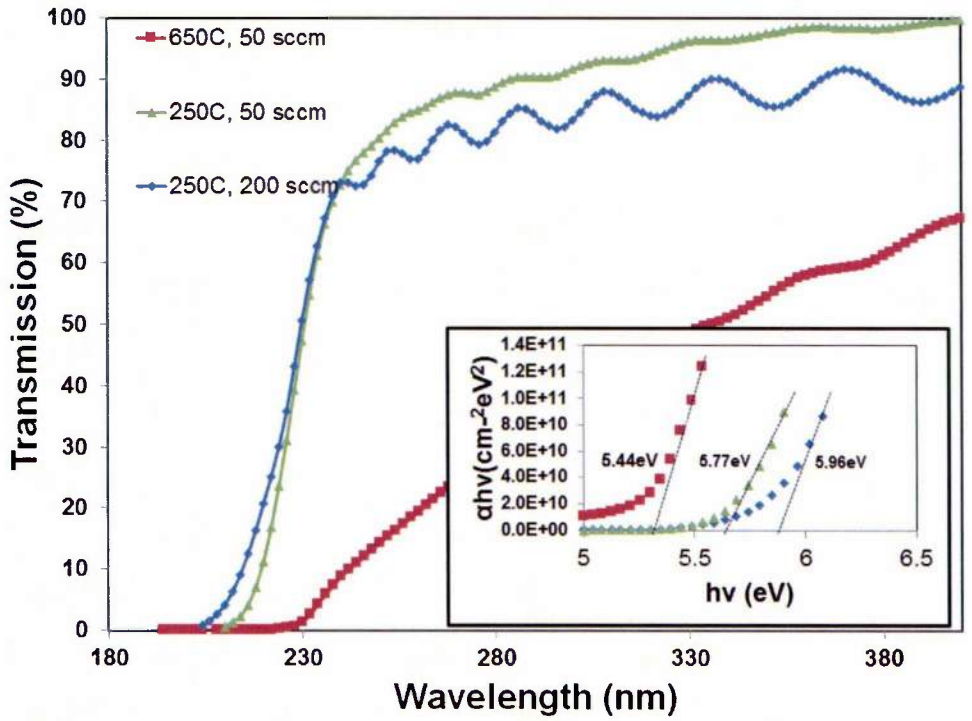

Figure B.1. UV-Vis transmission measurements for Gd_2O_3 films 6A (250 °C, 200 sccm, 1.07 μm), 6E (650 °C, 200 sccm, 0.87 μm), and 7A (250 °C, 50 sccm O_2, 1.11 μm) deposited on quartz. The inset shows optical band gap extraction via the Tauc method.

A tangential line to the absorption edge was drawn to obtain the band gap value. Increasing the deposition temperature from 250 °C to 650 °C at an O_2 flow rate of

200 sccm resulted in a significant decrease in the band gap value from 5.96 eV to 5.44 eV. This is most likely due to the increased crystallinity of the Gd_2O_3 films at elevated temperatures. Decreasing the oxygen flow rate into the deposition chamber from a value of 200 sccm to 50 sccm at a deposition temperature of 250 °C resulted in only a slight decrease in the band gap value from 5.96 to 5.77 eV.

Additional effects of processing on the optical band gap of the Gd_2O_3 films were investigated. The thickness dependence on the optical band gap for set 9 (650 °C, 200 sccm O_2, function of thickness) is shown in Figure B.2. Film 9A (380 nm) has the highest light transmission percentage. As the film thickness increases, the transmission percentage through the film decreases as a result of scattering.

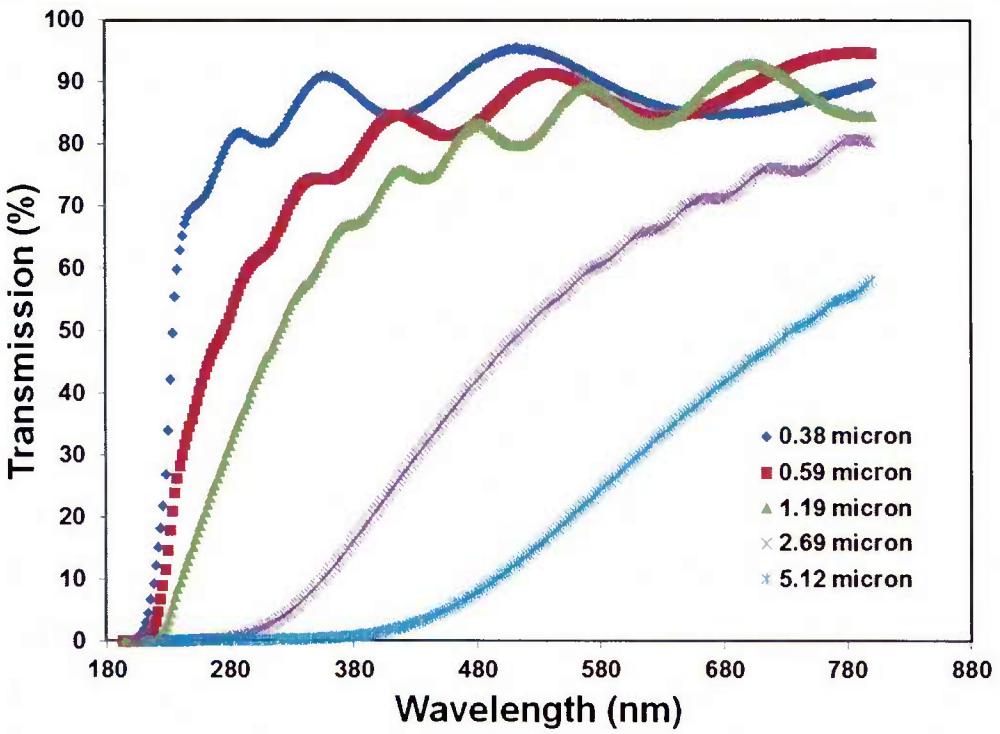

Figure B.2. UV-Vis transmission measurements for Gd_2O_3 films from set 9 (650 °C, 200 sccm O_2, function of thickness) deposited on quartz.

Appendix B.2. Refractive index measurements

Ellipsometry was used to determine Gd_2O_3 film refractive index. The refractive index was taken from the average of five locations across the wafer. Refractive index measurements for select films are shown in Table B.1. Depending on deposition conditions, the refractive index varied between 1.4 and 2.1.

Table B.1. Refractive index for select films measured by ellipsometry.

Film	Refractive index
11A	1.76 ± 0.01
11B	1.92 ± 0.11
11C	1.94 ± 0.16
11D	2.08 ± 0.18
12G	2.15± 0.02
12C	1.45 ± .05

VITA

Daniel A. Grave [redacted]. He was the [redacted]. He obtained his bachelor's degree in Materials Science and Engineering in May 2009 from Johns Hopkins University. Under the guidance of Dr. Douglas Wolfe, he continued his studies at Penn State University where he received his Ph.D. in Materials Science and Engineering in December of 2014.

Distribution List

(a) Applied Research Laboratory
The Pennsylvania State University
Attn: Dr. Douglas E. Wolfe
PO Box 30
University Park, PA 16804
Email: dew125@arl.psu.edu

(b) Defense Technical Information Center (DTIC)
Attn: DTIC-BSC
8725 John J. Kingman Road, Suite 0944
Fort Belvoir, VA 22060-0944
Email: TR@dtic.mil